Timing Jitter and Electron-Phonon Interaction in Superconducting Nanowire Single-Photon Detectors (SNSPDs)

DISSERTATION

zur Erlangung des akademischen Grades
doctor rerum naturalium (Dr. rer. nat.)
im Fach: Physik
Spezialisierung: Experimentalphysik

eingereicht an der
Mathematisch-Naturwissenschaftlichen Fakultät
der Humboldt-Universität zu Berlin

von

Mariia Sidorova, M.Sc.

Präsidentin der Humboldt-Universität zu Berlin:
Prof. Dr.-Ing. Dr. Sabine Kunst

Dekan der Mathematisch-Naturwissenschaftlichen Fakultät:
Prof. Dr. Elmar Kulke

Gutachter:
1. Prof. Dr. Heinz-Wilhelm Hübers
2. Prof. Dr. Stephan Reitzenstein
3. Prof. Dr. Wolfram Pernice

Tag der mündlichen Prüfung: 1. Dezember 2020

Preface

This dissertation is submitted for the degree of Doctor rerum naturalium at Humboldt-Universität zu Berlin (HU Berlin). The research described herein was conducted under the supervision of Prof. Dr. Heinz-Wilheim Hübers and Prof. Dr. Alexej Semenov at the Institute of Optical Sensor Systems of German Aerospace Center (DLR), Berlin.

This work is original to the best of my knowledge, except where acknowledgments and references to previous works have been made. I additionally would like to thank Dr. D. Henrich for providing raw experimental data which I analyzed in Section 3.2.3 of the presented dissertation.

Partial results of the presented dissertation have been published in:

- **Mariia Sidorova**, Alexej Semenov, Heinz-Wilhelm Hübers, Konstantin Ilin, Michael Siegel, Ilya Charaev, Maria Moshkova, Natalia Kaurova, Gregory N. Goltsman, Xiaofu Zhang, Andreas Schilling, "Electron energy relaxation in disordered superconducting NbN films", *arXiv:1907.05039*, 2019, (submitted to Phys. Rev. B)

- **Mariia Sidorova**, Alexej Semenov, Heinz-Wilhelm Hübers, Artem Kuzmin, Steffen Doerner, K. Ilin, Michael Siegel, Ilya Charaev, Denis Vodolazov, "Timing jitter in photon detection by straight superconducting nanowires: Effect of magnetic field and photon flux", *Phys. Rev. B* 98, 134504, 2018.

- **Mariia Sidorova**, Alexej Semenov, Artem Kuzmin, Ilya Charaev, Steffen Doerner, M. Siegel, "Intrinsic Jitter in Photon Detection by Straight Superconducting Nanowires", *IEEE Transactions on Applied Superconductivity*, Vol. 28, No. 7, 2018.

- **Mariia Sidorova**, Alexej Semenov, Heinz-Wilhelm Hübers, Ilya Charaev, Artem Kuzmin, Steffen Doerner, and Michael Siegel, "Physical mechanisms of timing jitter in photon detection by current-carrying superconducting nanowires", *Phys. Rev. B* 96, 184504, 2017.

Mariia Sidorova
June 2, 2020

Kurzfassung

Die vorliegende Doktorarbeit beschäftigt sich mit der experimentellen Studie zweier miteinander verbundener Phänomene: Dem intrinsischen Timing-Jitter in einem supraleitendenden Nanodraht-Einzelphotonen-Detektor (SNSPD) und der Relaxation der Elektronenenergie in supraleitenden Filmen. Supraleitende Nanodrähte auf einem dielektrischen Substrat als mikroskopische Grundbausteine jeglicher SNSPDs stellen sowohl für theoretische als auch für experimentelle Studien komplexe Objekte dar. Die Komplexität ergibt sich aus der Tatsache, dass SNSPDs in der Praxis stark ungeordnete und ultradünne supraleitende Filme verwenden, die eine akustische Fehlanpassung zu dem zugrundeliegenden Substrat aufweisen und einen Nichtgleichgewichts-Zustand implizieren.

Die Arbeit untersucht die Komplexität des am weitesten in der SNSPD Technologie verbreiteten Materials, Niobnitrid (NbN), indem verschiedene experimentelle Methoden angewandt werden. Mittels Magnetoleitfähigkeit wird die inelastische Elektron-Phonon-Streuzeit in einem Temperaturbereich von 14-30 K über der Übergangstemperatur bestimmt. Die aus den Magnetoleitfähigkeitsmessungen extrahierten Daten werden außerdem dafür verwendet, um die bei den jeweiligen Übergangstemperaturen experimentell bestimmten Photoresponse anhand des Zwei- bzw. Drei-Temperaturmodells zu beschreiben. Für dicke Filme kann auf die klassischen Drude- und Debye-Modelle bzw. auf das Modell der akustischen Fehlanpassung zurückgegriffen werden, um die Elektronen- und Phononen-Wärmekapazitäten zu berechnen bzw. das Entkommen der Phononen durch die Film-Substrat-Grenzfläche zu beschreiben. Bei dünnen Filmen wird jedoch für die Beschreibung der experimentellen Photoresponses eine geringere Wärmekapazität der Phononen benötigt. Dieses Ergebnis wird der verringerten Phononen-Zustandsdichte in dünnen Filmen bei niedrigen Temperaturen zugeschrieben.

Durch die Entwicklung eines experimentellen Ansatzes zur Messung des Timing-Jitter in NbN-Nanodrähten ist es möglich, sämtliche Beiträge zum Jitter des Systems zu untersuchen und den intrinsischen Jitter zu quantifizieren. Letzterer wird bei verschiedenen Wellenlängen, Bias-Strömen, Magnetfeldern und Photonenflüssen evaluiert. Die Ergebnisse werden außerdem im Rahmen des mikroskopischen zweidimensionalen Hot-Spot-Modells analysiert. Bei der Beschreibung der Photonendetektion in einem SNSPD erklärt das Modell zwei bekannte Jitter-Mechanismen: Die Abhängigkeit der Verzögerungszeit von der Position der Photonenabsorption auf dem Nanodraht und Fano-Fluktuationen. Obwohl das Modell die experimentellen Beobachtungen qualitativ gut beschreibt, legt der quantitative Vergleich die Präsenz einer zusätzlichen Jitter-Quelle nahe. Eine fehlende Jitter-Quelle sollte nicht nur die Stärke des Jitters beschreiben, sondern auch die spektrale Verbreiterung die Stromabhängigkeit der Sensitivität von SNSPDs, was offene Fragestellungen in der SNSPD-Forschung bleiben. Als eine mögliche Anwendung der SNSPD-Technologie wird ein Prototyp eines dispersiven Raman-Spektrometers mit Einzelphotonen-Sensitivität demonstriert.

Abstract

This PhD thesis is based on the experimental study of two mutually interconnected phenomena: intrinsic timing jitter in superconducting nanowire single-photon detectors (SNSPDs) and relaxation of the electron energy in superconducting films. Microscopically, a building element of any SNSPD device, a superconducting nanowire on top of a dielectric substrate, represents a complex object for both experimental and theoretical studies. The complexity arises because, in practice, the SNSPD utilizes strongly disordered and ultrathin superconducting films, which acoustically mismatch with the underlying substrate, and implies a non-equilibrium state.

This thesis addresses the complexity of the most conventional superconducting material used in SNSPD technology, niobium nitride (NbN), by applying several distinct experimental techniques. The inelastic electron-phonon scattering time in a temperature range from 14 - 30 K above the transition temperature is defined with the magnetoconductance technique. The extracted data from magnetoconductance measurements is further used to describe the experimental photoresponse with either the two-temperature or three-temperature models. For thick films, it is done by invoking the classical Drude and Debye models for computing electron and phonon heat capacities and also the acoustic mismatch model for describing phonon escape through the film/substrate interface. However, for thin films, a description of the experimental photoresponse requires a smaller heat capacity of phonons. This finding is attributed to the reduced density of phonon states in thin films at low temperatures.

Developing an experimental approach for measuring the timing jitter in NbN nanowires allowed us to evaluate all contributions to the system jitter and quantify the intrinsic jitter. The latter is studied at different wavelengths, bias currents, magnetic fields, and photon fluxes. The results are further analyzed in the framework of the microscopic two-dimensional hot-spot model. Describing the photon detection in the SNSPD, this model accounts for two known mechanisms of the intrinsic jitter: the dependence of the delay time on the position of the photon absorption site across the nanowire and Fano fluctuations. Although the model qualitatively well describes experimental observations, the quantitative comparison suggests the presence of an additional jitter source. A missing source of the intrinsic jitter should explain not only the jitter magnitude but also the broadening in the wavelength and current dependences of the sensitivity of SNSPDs which remain open questions in the field of SNSPD research. As an emerging application of the SNSPD technology, we demonstrate a prototype of the dispersive Raman spectrometer with single-photon sensitivity.

To my grandmother, to whom I owe everything...

Contents

List of Abbreviations

2-T	two-temperature
2-d	two-dimensional
3-T	three-temperature
3-d	three-dimensional
AL	Aslamazov-Larkin
AMAR	Absorption of Modulated (Amplitude) sub-THz Radiation
AMM	acoustic mismatch model
BCS	Bardeen-Cooper-Schrieffer
BKT	Berezinskii-Kosterlitz-Thouless
CCD	Charge Coupled Device
DOS	density of electron states
FDAM	photoresponse in the Frequency Domain to Amplitude-Modulated radiation
FWHM	Full Width at Half Maximum
GL	Ginzburg-Landau
LM	London-Maxwell
MT	Maki-Thomson
NbN	niobium nitride
PDF	Probability Density Function
SEM	scanning electron microscope
SM	Sergeev-Mitin
SNSPD	Superconducting Nanowire Single-Photon Detector
TDP	photoresponse in the Time Domain to Pulsed excitation
WAL	weak anti-localization
WL	weak localization
e-e	electron-electron

e-ph	electron-phonon
rms	root mean square
std	standard deviation

Symbols

A_{mean}	mean amplitude of a voltage transient
B	magnetic field
B_{C2}	second critical magnetic field
D	diffusion coefficient of electrons
D_m	material dispersion coefficient
E_F	Fermi energy
G_0	Drude conductance
H	discriminator level
I_B	bias current
I_C	critical current
I_{DEP}	depairing current
I_{det}	detection current
L	nanowire length
L_T	thermal length
L_f	fiber length
L_ϕ	phase-breaking length
$N(0)$	electron two spin density of states
$N(x)$	Bose–Einstein distribution function
R	resistance
R_S	square resistance
R_{SN}	square resistance above the superconducting transition
T	temprerature
T_0	bath temprerature
T_{BKT}	BKT transition temprerature
T_C	BCS mean-field transition temprerature
T_e	temperature of electron subsystem
T_{ph}	temperature of phonon subsystem
U_{th}	threshold voltage
a_0	unit cell size
c	speed of light in vacuum
c_e	heat capacity of electrons
c_{ph}	heat capacity of phonons
d	film thickness

e	elementary charge
f	frequency
f_0	roll-off frequency
$\hbar$	reduced Planck constant
k_B	Boltzmann constant
k_F	Fermi wavevector
l_e	elastic electron mean free path
m_e	electron mass
$n(x)$	Fermi–Dirac distribution function
n_1	refractive index of the fiber core
n_2	refractive index of the fiber cladding
n_g	group refractive index
p_F	Fermi momentum
q_T	wavevector of a thermal phonon
w	nanowire width
u	phonon velocity
y	photon absorption position across a nanowire
$\Gamma(x)$	gamma function
ΔG	dimensionless quantum correction to the Drude conductance
Θ	angle of incidence
Θ_{max}	angle of total phonon reflection
Λ_{PE}	mean free path for electron-phonon scattering
Λ_{bulk}	mean free path for bulk phonon losses
Ω	phonon circular frequency
δG	dimensionless magnetoconductance
η	phonon transmission coefficient at film/substrate interface
λ	wavelength
λ_0	central wavelength in free space
λ_F	Fermi wavelength
$\xi(0)$	Ginzburg-Landau coherence length at zero temperature
ξ_C	distance scale
ρ	mass density
$\varsigma(x)$	Riemann zeta function
σ_N	noise jitter
σ_{U_A}	amplitude fluctuations of a voltage transient
σ_{U_N}	rms value of the noise amplitude in the base line
σ_{U_Σ}	rms value of the noise amplitude in the to part of a voltage transient
σ_{amp}	amplitude jitter
σ_{ins}	instrumet jitter
σ_{loc}	local jitter
σ_{opt}	optical jitter

σ_s	noise-free system jitter
σ_{sys}	system jitter
σ_t	temporal width of an optical pulse
σ_λ	spectral width of an optical pulse
τ_C	time scale
τ_D	delay time
τ_{EP}	*e-ph* energy relaxation time
τ_{PE}	*ph-e* energy relaxation time
τ_{esc}	phonon escape time
τ_{e-ph}	inelastic (single-particle) *e-ph* scattering time
τ_{rise}	duration of the rising edge of a voltage transient
τ_ε	photoresponse decay time
τ_ϕ	electron dephasing time
$\psi(x)$	digamma function
ω	circular frequency

Chapter 1

Motivation and aims of this work

Owing to reduced dimensionality, thin and narrow superconducting nanowires exhibit strong modifications in their microscopic and transport properties as compared to bulk superconductors. Besides the importance of these modifications for fundamental physics, they paved the way to one of the most promising modern technologies allowing for detecting single photons. Sub-micron-wide strips, commonly denoted as nanowires, from thin superconducting films, became the key elements of superconducting nanowire single-photon detectors (SNSPDs, or also known as SSPDs). This detector technology has been unambiguously proved to be advantageous for laboratory experiments as well as for commercial applications [1]. Due to their record performance metrics, SNSPDs have been successfully demonstrated to improve the quality of instruments, e.g. in dispersive Raman spectroscopy [2], quantum key distribution [3], characterization of single-photon sources [4], optical communication with satellites [5], and tracking space debris [6]. Moreover, on-chip integration of SNSPDs with nanophotonic waveguides [7, 8] has allowed for replacing bulk optics and opened new opportunities for the application of SNSPDs in quantum simulation and quantum computation [9]. Common for all these applications is the importance of high timing accuracy in determining the arrival time of a photon at the detector. In practice, a performance metric responsible for the timing accuracy of an SNSPD is the timing jitter. Large jitter means poor accuracy. For instance, at tracking space debris, the jitter restricts the accuracy of orbit reconstruction for mid-size fragments.

A basic idea of single-photon detection by an SNSPD is briefly described as follows. A single photon is absorbed into a current-carrying superconducting nanowire. If the photon energy well exceeds the binding energy of the Cooper pair ($\sim$ meV), this creates a hot spot, a small volume of the nanowire with heated electrons and phonons where superconductivity is locally suppressed. If the current that flows around the hot spot exceeds the critical value, a cross section in the nanowire becomes normal (resistive). Influenced by Joule heating, the normal domain grows producing a non-zero voltage drop. The voltage drop is further read out and associated with a detection event. To date, the exact microscopic mechanism of photon detection by an SNSPD remains a challenging task.

Although impressive progress has been achieved in SNSPD technology since the demonstration of the first device in 2001, the performance of these detectors is still improving. During the past decades, the timing jitter of SNSPDs has been minimizing on the "try-and-see" basis rather than by understanding the underlying physics. However, further progress is hardly possible without a thorough understanding of how different physical mechanisms contribute to the jitter magnitude.

This open issue inspired the present thesis. Since the work began, numerous theoretical and experimental studies devoted to understanding the jitter mechanism have appeared. It is now realized that in a practical SNSPD system, there are various extrinsic sources of timing jitter that hide the intrinsic jitter inherent in the detector itself. The microscopic mechanism and physical sources of the intrinsic jitter were addressed in theoretical studies [10, 11]. There, the jitter appears as a variation of the time delay between the absorption of a photon and the emergence of the corresponding normal domain. These theoretical studies revealed a link between the intrinsic jitter and the energy relaxation time. Bearing in mind that a photon-detection process implies a non-equilibrium state, studying jitter requires understanding the peculiarities of energy relaxation. Among other energy relaxation mechanisms, electron-phonon scattering is the most sensitive to impurities and reduced dimensionality typical for superconducting films utilized by SNSPDs.

This Ph.D. thesis aims to identify physical mechanisms building up the intrinsic timing jitter and evaluate the electron-phonon scattering time. The objects under study are niobium nitride (NbN) thin superconducting films and straight nanowires. NbN is the most conventional material utilized in SNSPD technology, and as well as other materials, which are used for fabricating SNSPD (NbTiN, WSi, MoSi), it represents a disordered system. Physical parameters in such systems can hardly be predicted and rather should be evaluated experimentally. Straight and short nanowires were chosen as convenient objects for measuring jitter. In this geometry, the wire has the same thickness and width as straights in a meander-shaped nanowire and is free of bends that minimizes current crowding.

The Ph.D. thesis includes five chapters. In Chapter 1, "Motivation and aims", the motivation and the importance of the work are formulated. In Chapter 2, "Introduction: Photon detection in superconducting nanowires", a phenomenological description of the single-photon detection mechanism in accordance with the state-of-the-art microscopic models is presented. This chapter contains main background information, which is of importance for the rest of the thesis. It includes the description of experimental techniques for measuring the jitter, electron-phonon scattering time, and energy relaxation time together with models applied for data analysis. Chapter 2 includes several sections and paragraphs, which are the result of the author's work and, therefore, this is specified in the main text. Such sections and paragraphs are mostly related to models for the analysis of experimental data. We intentionally placed them there for the sake of completeness of Chapter 2, which serves as a guide for the rest of this Ph.D. thesis. Chapter 3, "Experimental results: Electron-energy relaxation and timing jitter", contains the main experimental data obtained in the framework of this Ph.D. study. The chapter starts

with a comprehensive characterization of the object under study, that is necessary for further comparison with theory. The analysis of the experimental electron-phonon scattering time and energy relaxation time reveals peculiarities of the phonon spectrum in thin films at low temperatures. Chapter 3 continues with the experimental study of timing jitter. It is very challenging to measure the intrinsic jitter directly because of the picosecond timescales involved. Hence we developed a formalism aiming to extract the intrinsic jitter from the analysis of raw experimental data. The chapter includes a discussion with regards to the applicability of the developed formalism and data reliability. The intrinsic jitter evaluated under different experimental conditions is further qualitatively compared with theoretical predictions that allows us to conclude about the physical sources of the intrinsic jitter. Chapter 4, "On-chip dispersive Raman spectrometer with single-photon sensitivity", focuses on the potential application, a Raman spectrometer based on a multi-pixel SNSPD array. The prototype of the on-chip dispersive Raman spectrometer and preliminary results are described. In the last Chapter 5, the conclusions are presented, and remaining problems are formulated. Each chapter contains a summary.

The main results of this work were given in oral and poster presentations at more than ten international conferences oriented on superconductivity, superconducting devices and technologies, low-temperature physics and nonlinear optics, and in three publications in peer-reviewed journals.

Chapter 2

Photon detection in superconducting nanowires

This chapter contains the background information that forms the starting point for the rest of this work and helps for a more precise formulation of the research task. A comprehensive overview of all existing models describing the detection mechanism in SNSPD is intentionally omitted here since it can be found in many other works (for a review see [12]). Instead, a phenomenological description is given along with some details of the state-of-the-art microscopic models which support it. The chapter, therefore, begins with a description of the process of single-photon detection in SNSPD. On the phenomenological level, the detection process is split into several key stages. At each stage, we reveal the processes and material parameters involved in building up the timing jitter. Among those, electron-phonon scattering and phonon escaping are main processes which affect the timing jitter. The chapter provides a description of experimental techniques and theoretical models in the frameworks of which electron-phonon scattering, phonon escaping, and timing jitter will be further studied experimentally. Finally, the chapter concludes with a summary.

2.1   Detection mechanism and metrics of an SNSPD

The first realization of an SNSPD device was done in 2001 at Moscow State Pedagogical University by Goltsman et al. [13]. At the same time, in 2001, the first and simplest model describing the detection process in a current-carrying superconducting nanowire has been proposed by Semenov et al. [14]. Despite its simplicity, the model has correctly revealed key parts of the detection process, one of which is a "hot" spot created by an absorbed photon. Today, in the advanced microscopic models [15], the hot spot is an essential step in describing single-photon detection.
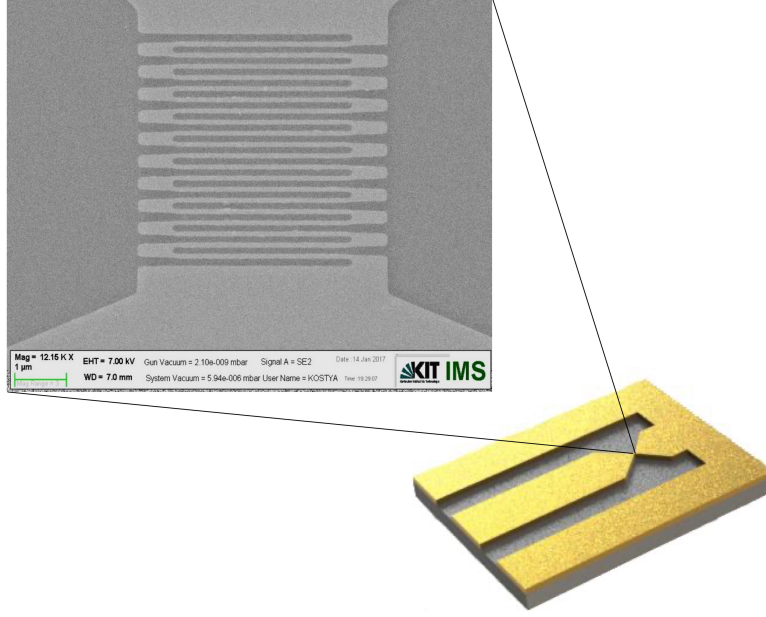
Figure 2.1: Topology of an SNSPD chip and the SEM (scanning electron microscope) image of the meander-shaped nanowire. Dark color represents the substrate while light color represents the film. The nanowire is patterned from a 5 nm thick superconducting film on top of a dielectric substrate and connected to contact pads on a chip designed as a 50 Ω coplanar line.

A conventional SNSPD utilizes a thin ($\sim$ 5 nm) superconducting strip on a dielectric substrate. Such strips with a width of a few tens of nanometers are commonly denoted as nanowires. Depending on the application, the nanowire can be straight or shaped in different forms. A straight and short nanowire is a better object for research because the effect of current crowding [16], i.e. non-uniform current density, is reduced to a minimum as compared to other layouts. However, the straight nanowires are useless from an application point of view due to inefficient optical coupling restricted by their very small active area. In contrast, a meander-shaped nanowire, shown in Fig. 2.1, is used a lot in practical devices because it covers a large area providing efficient coupling with light. However, the meander-shaped wire suffers from the current crowding effect, which arises near sharp bends. Typical superconducting materials for SNSPDs are polycrystalline films such as NbN [13], NbTiN [17], TaN [18], and amorphous films such as WSi [19], MoSi [20], MoGe [21]. Critical temperatures of these materials fall in the range from 16 to 5 K. Operating conditions require to cool the superconducting nanowire below its critical temperature, $T < T_C$, where the resistance is zero, and to bias with direct current below its critical current, $I_B \leq I_C$, therefore, the voltage drop along the nanowire is zero (the initial stage in Fig. 2.2). A common method for cooling an SNSPD is to immerse it in liquid helium (He) or, differently, to mount it in a closed-cycle refrigerator.

The detection process in the nanowire can be split into several key stages illustrated in Fig. 2.2. The first stage (i) starts with the absorption of an incident photon in the nanowire. The photon energy in the visible or near-infrared wavelength range, around 1 eV, is a few orders of magnitude larger than the superconducting gap of conventional SNSPD materials. Such a
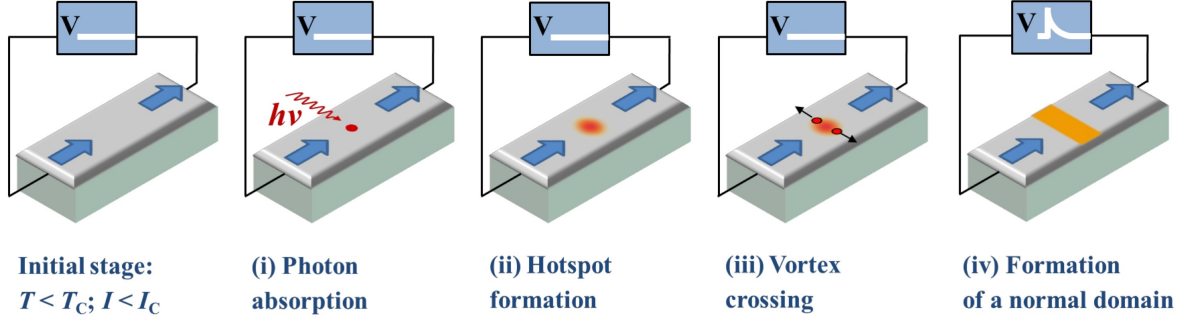
Figure 2.2: Key stages of the photon detection process in a current-carrying superconducting nanowire on a dielectric substrate.

photon breaks a Cooper pair and creates quasiparticles triggering the second stage. At the second stage, (ii) via a cascade of scattering events, the quasiparticles multiply, thermalize, and diffuse out of the absorption site, forming a hot spot. This process takes time, which is called thermalization time. The hot spot itself has a lifetime strongly dependent on the definition of the hot spot. It can be defined in terms of the quasiparticle concentration or the temperature inside. During the lifetime, before the hot spot disappears, the third stage begins, (iii) crossing the nanowire by either a magnetic vortex nucleated near to the edge of the wire or a vortex-antivortex pair nucleated inside the hot spot. Moving under the Lorentz force, vortices dissipate energy and form a normal domain (slab) across the nanowire. Due to Joule heating by the current, the normal domain grows in length diverting the current from the nanowire to the load resistance (50 Ω). Note here that the square resistance of the nanowire (usually > 300 Ω/sq) is much larger than the load resistance. A decrease in the current through the nanowire and heat flow into the substrate, further, cause the domain to shrink and disappear, and current to return to the nanowire. As a result, a voltage transient emerges in the readout that is identified as the detection of the photon. The arrival of the voltage transient at the amplifier is the fourth and last stage (iv). Cooling of the normal domain is controlled by relaxation of the electron energy via phonon escape into the underlying substrate (see subsections 2.4.4 and 2.4.3).

Modeling of the entire detection process in different regimes of photon energy and current is still challenging. However, several attempts have been made to describe some of the stages microscopically. The first two stages, namely the energy down-conversion cascade and hot-spot formation, were modeled under different assumptions by Kozorezov et al. in [22] and by Vodolazov in [15]. The third stage, the vortex-assisted formation of the normal domain, was described by Hofherr et al. in [23] and by Bulaevskii et al. in [24]. At present, Vodolazov's model qualitatively reproduces many experimental results. However, this model is limited to the case when the nanowire responds deterministically, i.e. when the absorbed photon produces a photon count with 100 % probability.

SNSPD metrics

One of the crucial performance metrics of SNSPDs is the detection efficiency. The system detection efficiency of the SNSPD is defined as the ratio between the number of counted photons

to the number of photons incident at the optical input of the detector system. Modern devices demonstrated 93 % system efficiency for SNSPD from WSi material [25], 94 % for SNSPD from NbN material [26], and 92 % for the SNSPD from NbTiN material [27]. The system detection efficiency is proportional to the efficiency of optical coupling, the absorbance of the nanowire, and the intrinsic detection efficiency, i.e. the probability that the absorbed photon produces a photon count. The intrinsic detection efficiency is determined by the intrinsic photon-detection process of the nanowire itself, and it strongly depends on energy of incident photons [28], bias current [22], and temperature. At a fixed current and temperature, the efficiency saturates for photons with high energies and monotonously decays with decreasing photon energy. At a fixed photon energy and temperature, the efficiency saturates at high currents (close to depairing current) and monotonously decays with decreasing current.

Another important performance metric of the SNSPD is its intrinsic noise known as dark counts. Even if the SNSPD is not illuminated by photons, it still generates counts, dark counts. The voltage response caused by dark counts is identical to that caused by photon counts. The number of dark counts exponentially increases with the bias current. It is generally accepted that qualitatively dark counts occur when a magnetic vortex (or a vortex/antivortex pair) crosses the nanowire overcoming the energy barrier due to thermal fluctuations. However, the value of the barrier is still open to debate [24, 29].

Perhaps the most crucial metric of SNSPDs and also the subject of the present work is the *timing jitter*. The timing jitter quantifies the timing accuracy of SNSPD in defining the arrival time of the detected photon. The origin of the intrinsic timing jitter is addressed in microscopic studies [10, 11], where it is defined as the variance in the delay time (also known as latency) between the photon absorption and the formation of the normal domain. The delay time scales with the relaxation time of the electron energy, and the same does the variance. The next section is devoted to extrinsic and intrinsic sources of the timing jitter present in a practical SNSPD device.

2.2   Timing jitter

In SNSPDs, timing jitter limits the accuracy in determining the arrival time of a photon, which caused the detection event. Nowadays, commercial detectors offer jitter on the picoseconds time scale what is of importance for a large number of applications, which require high timing accuracy. A measure of timing jitter is a standard deviation of a statistical distribution of delay times between the appearance of the photon at the optical input of the SNSPD device and the arrival of the corresponding voltage transient at the readout electronics. Numerous sources contribute to the timing jitter of the SNSPD, which roughly can be split into extrinsic and intrinsic. The extrinsic jitter is caused by readout electronics, instruments, optics, etc. The intrinsic jitter originates from the nanowire itself. Minimization of the extrinsic jitter is an engineering challenge, while the reduction of the intrinsic jitter requires understanding the

physical details of the detection mechanism in the nanowire. It was found experimentally that the statistical distribution of delay times has one unique peculiarity, namely, non-Gaussian profile. Its form is well described by exponentially-modified Gaussian distribution (Gaussian statistics at small delays and exponential at large delays). Moreover, such non-Gaussian statistics was observed for different materials NbN [30], NbTiN [27], WSi [31], MoSi [32], and by use of different experimental approaches [33, 34, 30]. Hence it is believed that non-Gaussian statistics is inherent in the detection process itself, and therefore contributes to the intrinsic jitter. In this section, we summarize what is already known about the timing jitter in SNSPD. We will start with the description of jitter sources, which undesirably attend any photon-detection event. Further, we will describe a microscopic mechanism of the intrinsic jitter and its physical source proposed by advanced microscopic models of photon detection in SNSPD.

2.2.1 Typical experimental technique: System jitter

Quantifying the timing jitter in SNSPDs is typically done via measuring a delay time between the arrivals of the reference signal and the SNSPD response. Fig. 2.3(a) schematically shows a typical experimental setup comprised of a pulsed light source, an SNSPD device, a reference signal, and readout electronics (amplifier, scope). A beam-splitter splits the laser beam into two beams. One is coupled to the SNSPD through an optical fiber and the other to a low-jitter fast photodiode. The fast photodiode provides the reference signal, which is coupled to the trigger channel of the scope. Voltage transients generated by SNSPD are amplified and sent to the readout channel of the scope (here we omitted the description of biasing SNSPD and division of rf and dc electrical paths with a bias-tee). Fig. 2.3(b) schematically shows the rising edge of the transient recorded by the scope (the green curve). The arrival time of the transient with respect to the reference is determined at the trigger level. It varies from one detection event to another. Performing many measurements enables one to build a statistical distribution of arrival times, that is schematically illustrated in Fig. 2.3(b) (the horizontal distribution). Such a statistical distribution is also known as a *probability density function* (PDF), instrument response function, or histogram. In our study, we will refer to it as PDF. A measure of the timing jitter is the standard deviation of the PDF of arrival times. The standard deviation for an experimental (raw) PDF gives a *system jitter*. A typical setup (Fig. 2.3(a)) contains numerous sources of the jitter which are considered below.

2.2.2 Sources of timing jitter

Noise jitter
Electrical noise distorts the shape of the transient and, consequently, contributes to the jitter. The main source of noise is an amplifier operated at room temperature. Noise showing up in the baseline of the acquired voltage transient results in uncertainty in the time of crossing the discriminator level by the transient (Fig. 2.3(b)). The noise contribution to the system jitter
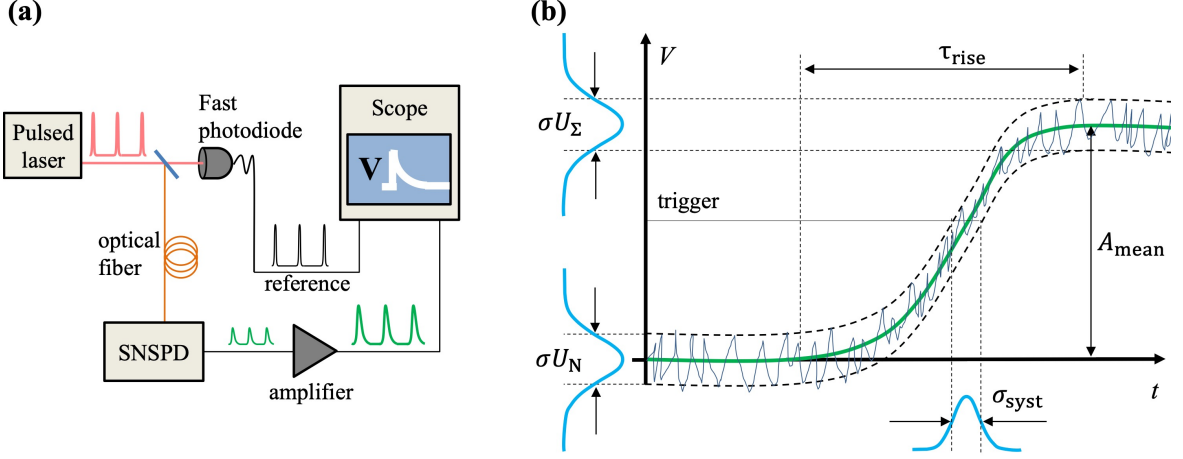
Figure 2.3: a) Schematic block diagram of a typical experimental setup for measuring the timing jitter of an SNSPD. A beam of a pulsed laser is split into two beams one of which is coupled to the SNSPD through an optical fiber and the other to a fast photodiode. A reference provided by the diode is sent to the trigger channel of a scope. Voltage transients generated by the SNSPD are amplified and sent to the readout channel of the scope. b) Schematic representation of the rising edge of the recorded voltage transient.

can be estimated as [35], [36]

$$\sigma_N = \sigma_{U_N} \frac{\tau_{rise}}{A_{mean}}, \tag{2.1}$$

where A_{mean} is the mean amplitude of the transient, τ_{rise} is the duration of the rising edge of the transient, and σ_{U_N} is the *rms* (root mean square) value of the noise amplitude in the baseline. The noise jitter depends on the signal-to-noise ratio. It can be minimized by operating at larger bias currents, I_B, and by using a low-noise amplifier at the first stage. The PDF of the noise amplitude has a Gaussian distribution.

Amplitude jitter

Another source which causes an additional jitter is amplitude fluctuations of the voltage transient [37]. An absorbed photon results in the formation of a normal domain. The size of the domain depends on the absorption site. For instance, in meander layouts, the detection event can occur either in straights or bends. Obviously, normal domains formed in straights and bends will differ in size. Amplitude fluctuations are caused by different sizes of normal domains associated with each voltage transient. Fig. 2.4 schematically shows two voltage transients arriving at the same time. These transients have different amplitudes but identical rising times. If one measures arrival times at the fixed discriminator level H from the baseline, then the difference in amplitudes will add to this time. In other words, it will broaden the measured PDF producing an artificial jitter σ_{amp} which can be estimated as

$$\sigma_{amp} = \sigma_{U_A} \frac{\tau_{rise} H}{A_{mean}^2}, \tag{2.2}$$

where $\sigma_{U_A} = \sqrt{\sigma_{U_\Sigma}^2 - \sigma_{U_N}^2}$, σ_{U_Σ} is the *rms* value of the noise amplitude in the top part of the transient (see Fig. 2.3(b)). The jitter σ_{amp} can be minimized by using bend-free SNSPD
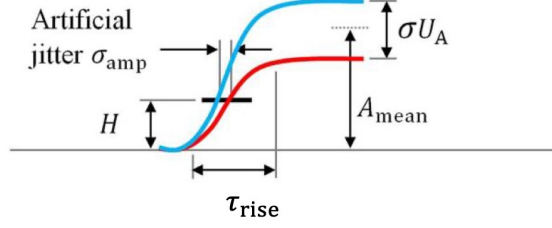
Figure 2.4: Artificial jitter, σ_{amp}, is caused by the difference in amplitudes of two voltage transients if their arrival times are determined at a fixed discriminator level H from the base line. The figure is taken from [38].

layouts such as straight or spiral nanowires. Differently the amplitude jitter can be eliminated by defining the arrival times of transients at a fixed fractional level for each pulse (analogous to constant fraction discrimination) [34].

Optical jitter

The optical fiber delivering light to an SNSPD causes an additional jitter. Being Fourier-transform-limited, an optical pulse of a Gaussian shape in free space is characterized by its duration, σ_t, and finite spectral width, σ_λ. They are connected as

$$\sigma_t = \frac{\lambda^2}{2\pi c \sigma_\lambda}, \tag{2.3}$$

where σ stands for *std* for the corresponding Gaussian distribution, λ is the central wavelength in free space, and c is the speed of light in vacuum. Traveling through the fiber, an optical pulse of a finite spectral width spreads in time. Because the material refractive index, n_1, is wavelength-dependent, photons of different wavelengths propagate within the fiber with different phase velocities. While, the whole optical pulse propagates with the group velocity. As a result, the optical pulse broadens in time. The phenomenon causing group velocity dispersion is known as chromatic or material dispersion. The variance of traveling times of the photon through the fiber gives an optical jitter, which is expressed as

$$\sigma_{opt} = D_m \sigma_\lambda L_f, \tag{2.4}$$

where $D_m = \left| -\frac{\lambda}{c} \frac{d^2 n_1}{d\lambda^2} \right|$ is the material dispersion coefficient, L_f is the fiber length. At some wavelength, the optical contribution to the system jitter can be crucial. For instance, an optical Gaussian pulse with $\sigma_t = 10$ fs will acquire the optical jitter 2, 1.9, and 6.8 ps/m after passing one meter of a single-mode fiber at wavelengths 1550, 1064, and 532 nm, respectively. To minimize the optical jitter, one needs to use zero-dispersion shifted fibers for which the zero-dispersion wavelength is shifted to a desired one. Besides chromatic dispersion, there is also waveguide dispersion. It arises from the wavelength dependence of the group velocity due to specific fiber geometry, i.e. a ratio between the diameter of the fiber core and the propagated wavelength. Waveguide dispersion is much less than the chromatic one and plays a role only at those wavelengths where chromatic dispersion is very small. If the fiber is out of the single-mode regime, the modal (or intermodal) dispersion arises due to differences in group velocities

of the propagating modes. Pulse broadening in single-mode fibers almost entirely arises from chromatic dispersion. It is worth mentioning that for multimode fibers and very long (a few kilometers) single-mode fibers, the distribution of photon traveling times deviates from the Gaussian one exhibiting a slower tail at larger times [39]. For a short single-mode fiber, however, the distribution is expected to be Gaussian.

Instrumental jitter

Other instruments may also contribute to the system jitter by introducing the uncertainty in the arrival time of the transient, the so-called instrumental jitter. The instrumental jitter is caused by the timing inaccuracy of the scope, the jitter in the reference signal from the photodiode, or undesirable optical reflections. In contrast, coaxial cables rather introduce a delay than a jitter. In Section 3.3.3.3, we will show that the instrumental jitter can be evaluated experimentally in the bolometric (uniform), multi-photon detection regime in which other jitter contributions are eliminated.

Intrinsic jitter: geometric and local

Once the contributions of external sources to the system jitter are minimized, the intrinsic jitter inherent in the detection process itself becomes measurable. The intrinsic jitter consists of longitudinal geometric and local jitters. The local jitter originates from the microscopic physics of photon detection in the nanowire itself. The geometric jitter is caused by position-dependent traveling times of the voltage transient, which propagates with the finite speed from an absorption site along the nanowire to the input of readout electronics. It was shown that increasing the nanowire length introduces the geometric jitter [30]. Here we will consider only the geometric jitter, while in Section 2.2.4, the focus will shift to the local jitter.

There are two different methods to read out the SNSPD response. In the *conventional readout*, a nanowire builds a part of the central strip in the shortened coplanar line. One end of the nanowire is connected to the ground plane of the line and another to the central strip of the line, so that the nanowire has one common output connected to an amplifier. In the *differential readout* (or dual readout) introduced in [30], the nanowire builds a part of the central strip of the coplanar line as well. However, in this case, both ends of the line serve as outputs connected to two different amplifiers. In both cases, the nanowire can be treated as a transmission line [30].

At the photon absorption site after the formation of the normal domain, two current steps are generated. They have opposite polarities and propagate to opposite directions along the nanowire with velocity $v \approx 12$ μm/ps. This propagation velocity was obtained for the 5 nm-thick, 100 nm-wide NbN nanowire on a sapphire substrate in [40]. In the case of the *differential readout*, the maximum difference between arrival times of two current steps at the input of the amplifier is $|t_1 - t_2| = L/v$, where L is the nanowire length. For a uniformly distributed probability of photon absorption and in the absence of noise, the PDF of intervals $|t_1 - t_2|$ is also uniform with the *std* $\sigma = L/(2\sqrt{3}v)$. Estimations of the geometric jitter in the conventional readout are given in Section 3.3.3.1.

11

2.2.3 Asymmetry of experimental probability density function

Numerous experimental studies of the timing jitter reported asymmetries in the profile of experimental PDFs [30, 27, 31, 32]. The asymmetry appears as a deviation from a Gaussian profile exhibiting a long tail at large delay times. Such non-Gaussian PDFs were observed for different superconducting materials, detector layouts, and readout methods [33, 34, 30]. The non-Gaussian PDF is well fitted with an exponentially-modified Gaussian distribution [33, 41]. Such a distribution exhibits a Gaussian profile at small times $\leq t_0$ and an exponential tail at large times $\geq t_0$, where t_0 is the time position of the PDF peak. This unique feature, the non-Gaussian distribution of delay times, is attributed to the intrinsic detection process.

2.2.4 Microscopic mechanism and physical sources of intrinsic timing jitter

Recently, several theoretical attempts have been made to determine the fundamental limit of the intrinsic jitter. These models neglect the geometric jitter, and therefore, the intrinsic jitter is reduced to the local jitter. Vodolazov [10] suggested that at a current close to the depairing current, the jitter is limited to the shortest relaxation time of the superconducting order parameter that may reach about 0.8 ps for an NbN nanowire. Allmaras et al. in [11] obtained a very similar value by assuming that Fano fluctuations set the jitter limit. Fano fluctuations randomize the amount of energy retained in the electron system due to energy loss via phonon escape from the film to the substrate. In [42], Wu et al. suggested that the jitter is limited to the variance in the time needed for a vortex to cross the nanowire that roughly results in 1 ps. Below we describe the mechanism of the intrinsic jitter in the framework of the microscopic two-dimensional (2-d) hot-spot model developed by Vodolazov in [10]. The impact of Fano fluctuations will be discussed in detail in Section 3.3.5.

The 2-d hot-spot model is based on a modified time-dependent Ginzburg-Landau (TDGL) equation for the superconducting order parameter, together with a two-temperature model, and a current continuity equation (for details see [15]). It is assumed that each system of electrons and phonons is instantly in internal thermal equilibrium within itself, i.e. at any time, distribution functions of electrons and phonons represent Fermi-Dirac and Bose-Einstein distributions, respectively, with their effective temperatures, T_e and T_{ph}, larger than the bath temperature. In [15], it was shown that this simple model is capable to qualitatively explain the voltage response of a superconducting nanowire to the absorption of a single photon. The model accounts for such important physical effects as finite relaxation time of the superconducting order parameter, heating of electrons due to Joule dissipation, and growth of the normal domain. The model defines a detection threshold beyond which a photon with particular energy cannot be detected, and therefore it is a deterministic model. Such a threshold is the so-called detection current, I_{det}, i.e. a threshold current in the presence of the hot spot. Because the hot spot causes spacial variations of the order parameter, the detection current appears to be smaller than the depairing current, I_{DEP} (the theoretical pair-breaking current). In the model, a detection event
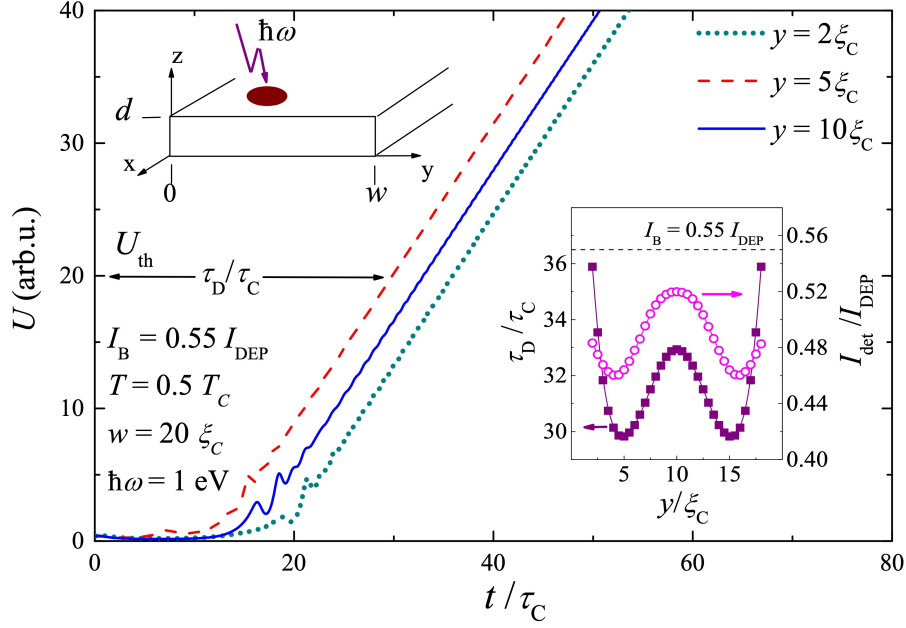
Figure 2.5: Time-dependent voltage response of the superconducting nanowire after absorption of the photon at different distances y across the nanowire. The inset in the upper left corner presents the nanowire geometry. The distances are specified in the legend (upper right corner) in units of ξ_C from the nanowire edge. Another legend (lower left corner) specifies bias current, bath temperature, the strip width, and the photon energy. Time is given in units τ_C. The delay time τ_D is defined at the threshold level $U_{th} = 20$ arb.u. The inset in the lower right corner shows the detection current in units of the depairing current and the relative delay time as a function of the hot-spot position across the wire. The absorption of the photon was modelled by instantaneous heating of both electrons and phonons at $t = 0$ in the area $2\xi_C \times 2\xi_C$ with temperature $T_e = T_{ph}$ inside. Here distance is measured in units $\xi_C = \sqrt{\hbar D/(k_B T_C)}$, voltage in units $k_B T_C/(2e)$, where e is the electron charge, and time in units $\tau_C = \hbar/(k_B T_C)$. Numerical calculations were done by Vodolazov, the figure is taken from [44].

is assisted by vortices. In the presence of the hot spot, vortex nucleation occurs at the place where the velocity of the superconducting condensate locally reaches its critical value [43]. If the hot spot is located close to the edge of the wire, the velocity of the superconducting condensate is maximal at the edge, and a vortex enters through the edge. If the hot spot is located far from the edge, the velocity of the superconducting condensate is maximal inside the hot spot and a vortex/antivortex pair nucleates inside the hot spot. For bias currents $I_B \geq I_{det}$, the entry barrier for vortices is zero, and vortices appear 'naturally'.

This 2-d hot-spot model results in the position-dependent detection current, $I_{det}(y)$, shown in the inset (lower right corner) of Fig. 2.5, where y is the coordinate of the photon absorbtion site across the nanowire. Similar dependences $I_{det}(y)$ were reported in [43, 15]. The position dependence of the detection current was theoretically predicted by Zotova et al. in [43], and experimentally observed as the position-dependent detection sensitivity by Renema et al. in [45]. The local detection current is the smallest current through the nanowire required to achieve a 100 % probability to detect a photon absorbed at that particular location. If at any location across the nanowire $I_B > I_{det}$, the detection regime is deterministic (100 % detection probabil-
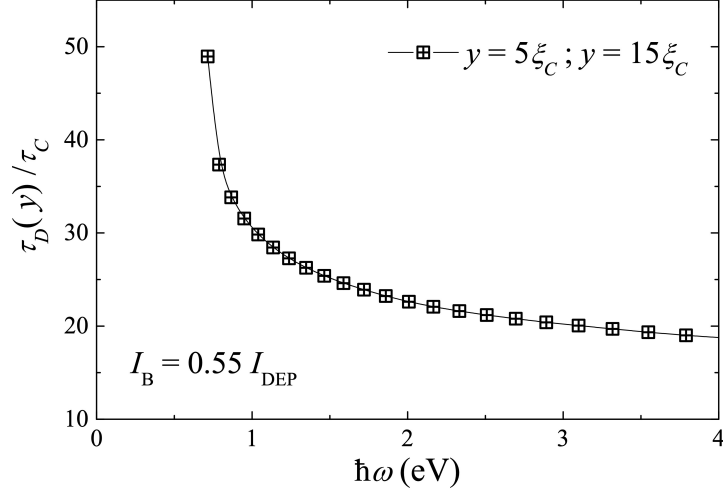
Figure 2.6: Relative delay time as function of the photon energy at zero magnetic field for the bias current $0.55\,I_{\text{DEP}}$, $T = 0.5T_C$, and the photon absorption site $y = 5\xi_C = 15\xi_C$ across the wire. The solid curve is to guide the eyes. Here distance is measured in units $\xi_C = \sqrt{\hbar D/(k_B T_C)}$, and time in units $\tau_C = \hbar/(k_B T_C)$. Numerical calculations are done by Vodolazov, the figure is taken from [44].

ity). Contrarily, if at any location $I_B < I_{\text{det}}$, the detection regime is purely probabilistic. For bias currents smaller than the maximal detection current and larger than the minimal detection current, the detection regime is a mixture of the deterministic and probabilistic regimes.

The described model allows for simulating the time dependence of the voltage drop along the nanowire caused by the formation of the growing normal domain after the photon absorption. Fig. 2.5 shows the time-dependent voltage response and illustrates the definition of the delay time, τ_D. The delay time between photon absorption and the formation of the normal domain is defined at that time when the voltage response crosses the threshold level. Because of the linear increase of the voltage response, a choice of the threshold does not add variance to τ_D, i.e. does not contribute to the jitter. The delay time in the model is a composite time comprised of the hot-spot formation time and the vortex crossing time. At a fixed current and photon energy, the delay time depends on the location of an absorption site across the nanowire. Such a dependence occurs because of the position dependence of the detection current. In the inset (lower right corner) of Fig. 2.5, we show the position dependence of $\tau_D(y)$ dictated by $I_{\text{det}}(y)$: $\tau_D(y)$ is minimal where $I_{\text{det}}(y)$ is minimal, and it has a maximum in the middle of the wire where $I_{\text{det}}(y)$ is maximal. It can also be seen that $\tau_D(y)$ monotonously decreases with the increase in the ration $I_B/I_{\text{det}}(y)$. In [10] (see Fig. 3a there), it was shown that $\tau_D(y)$ monotonously decreases and flattens with the increase of the bias current. As a result, the jitter, i.e. the variance in τ_D, will monotonously decrease with the increase of the bias current.

In Fig. 2.6, we show the delay time as a function of the energy $\hbar\omega$ of the incident photon at the fixed bias current $I_B = 0.55I_{\text{DEP}}$ and the photon absorption site $y = 5\xi_C = 15\xi_C$ (ξ_C is determined in the caption). As seen in the figure, the delay time decreases with increasing photon energy.

14

To summarize, Vodolazov's model [15, 10] allows for calculating the delay time between the absorption of a photon and the formation of the corresponding normal domain. The hot-spot formation contributes a large part to the delay time. The *e-ph* scattering time and photon escape time governing the hot-spot formation play a dominant role in determining the delay time. The intrinsic timing jitter appears in the model as a variation of the delay time. The source of such a variation is different types of fluctuations. These are fluctuations in the deposited photon energy, in the energy delivered to the electron system [11], or in the position of the photon absorption site across the wire. Both the delay time and its variation monotonically decrease either with increasing bias current at a fixed photon energy or with increasing photon energy at a fixed bias current. Hence, the variation, i.e. the intrinsic jitter, scales with the delay time. Exactly this model will be further used for comparison with experimental results in Section 3.3.5. However, to be able to realize this, we first define physical parameters of interest in the next section.

2.3   Important physical parameters

In this section, we define what material and transport parameters are essential for the further interpretation of experimental results of jitter measurements in the context of the microscopic two-dimensional model of the hot spot. First of all, the jitter is intrinsically linked with time scales of the hot-spot formation. Being a non-equilibrium, the process of hot-spot formation is governed by the energy relaxation time scales. Among those electron-phonon energy relaxation time, τ_{EP}, and phonon escape time, τ_{esc} are the most important. Hence, the rest of Chapter 2 is entirely devoted to theoretical models and experimental techniques that allow for evaluating these time scales and studying the peculiarities of electron energy relaxation in thin films.

The role of the electron diffusion coefficient, D, on hot-spot formation has been demonstrated by the experimental study of photon detection performance in NbN and NbC [46] SNSPDs. A very large D in NbC ($D = 4.45$ cm^2/s) as compared to NbN ($D = 0.7$ cm^2/s) leads to the fast diffusion of electrons out of the photon absorption site. As a result, the hot spot in SNSPDs from NbC has a much smaller temperature inside than from NbN and turns to be insufficient for detecting photons with the same energy.

The ratio between the experimental critical and theoretical depairing currents, I_C/I_{DEP}, is an important parameter in the 2-d hot-spot model (Section 2.2.4) because of the current dependence of the delay time. Usually, I_C of a superconducting nanowire is much less than I_{DEP} for several reasons. The main reason is constrictions, i.e. geometrical (sharp bends) or structural (non-uniform thickness and edges) defects in the nanowire. More specifically, constrictions cause current crowding [16], i.e. they make the current density non-uniform, larger in areas where the constriction is localized. Current crowding restricts the theoretical I_{DEP} to the experimental I_C, and in straight, bend-free nanowires also emphasizes the properties of the edges, which generally are less perfect and even non-superconducting [47]. Therefore, the ratio I_C/I_{DEP} additionally enables an estimation of the quality of a superconducting nanowire. All

these parameters, together with the critical temperature, T_C, as the most basic parameter of a superconductor, will be derived in Section 3.1.

2.4 Electron-phonon scattering and phonon escaping: experimental techniques and models

The use of SNSPDs implies a non-equilibrium state. In a metallic film (on a dielectric substrate) driven out of equilibrium, the relaxation of the electron energy is supported by two major processes. These are inelastic electron-phonon (*e-ph*) scattering and phonon escaping from the film to the substrate. The characteristic times of these processes, together with the heat capacities of electrons and phonons, define the relaxation time of the electron energy to the equilibrium value and, consequently, the timing performance of the practical device. Escape of isotropic, 3-d Debye phonons through the metal/substrate interface is described by the acoustic mismatch model (AMM) [48] as well as *e-ph* scattering in bulk and clean metals is thoroughly described theoretically [49]. Finally, the heat capacities of electrons and phonons are well defined in the framework of the Drude and Debye models, respectively. However, practical devices utilize thin and disordered superconducting films rather than bulk clean metals. For instance, the most used material for SNSPD is a disordered NbN film of 5-10 nm thickness deposited on top of an acoustically rigid substrate. The theory of *e-ph* scattering developed for bulk clean metals is irrelevant for such films. Hence in our study, we applied the theory of *e-ph* scattering in disordered metals developed by Sergeev and Mitin (SM). It predicts modification of *e-ph* scattering by disorder and impurities (see Section 2.4.2). Another challenge is the description of phonons because the phonon spectrum in thin films can undergo strong modifications as compared to the bulk material. In thin films, at low temperatures, the phonon wavelength becomes comparable or greater than the film thickness. This imposes restrictions on phonon wavevectors in the direction perpendicular to the film surface. The situation is complicated by the acoustical mismatch between the film and the underlying substrate. The restricted geometry of the material leads to the reduction in the phonon density of states [50], and acoustic mismatch reduces the ability of phonons to pass through the film/substrate interface. All these definitely affect the *e-ph* scattering and phonon escape rates and, as a result, the thermal transport.

Due to the described complexity of the system, the parameters of interest (*e-ph* scattering time, phonon escape time) should be rather evaluated experimentally than theoretically. There are two distinct experimental techniques providing these parameters, photoresponse and magnetoconductance. The main difference between these techniques is that the former implies electron heating, while the latter does not. The analysis of data in magnetoconductance measurements is based on the theory of quantum corrections to the classical Drude conductance. It allows for extracting the *e-ph* scattering rate at the temperature range above T_C. The photoresponse technique provides direct information on the effective relaxation time, the decay time of the photoresponse. The data analysis of photoresponse measurements can be done in terms

of thermal flow by applying two- or three-temperature models, and also in terms of geometric acoustic propagation of phonons by applying the phonon ray-tracing model. It allows for finding the *e-ph* energy relaxation rate or, alternatively, may reveal the properties of phonons in the film (details are in Section 2.4.4). The photoresponse technique operates at temperatures close to T_C ($T \geq T_C$) and can be extended to lower temperatures by applying a magnetic field. It is important to mention here that the magnetoconductance technique provides a value of the *e-ph* scattering rate at the Fermi level (single-particle), which can be directly compared with one predicted by the microscopic theory. However, the photoresponse technique, which implies electron heating, provides the *e-ph* energy relaxation rate (see subsection 2.4.2). In the current section, both experimental techniques are considered in detail, including models used for the data analysis. Further, in Section 3.2, both techniques will be applied.

2.4.1 Magnetoconductance technique: Electron dephasing time

The superconducting films used for fabricating SNSPD represent a disordered system. In such films at low temperatures, the electron transport is in a quantum diffusive regime. The diffusive regime denotes that a conduction electron traveling through a disordered medium experiences many scattering events. This implies that the electron mean free path, the average distance between elastic scattering centers, l_e, is much smaller than the size of the system. The wave behavior of an electron is described by the electron wave function with the amplitude and the phase. The quantum diffusive regime additionally implies that l_e is much smaller than the phase-breaking length, L_ϕ. The length scale L_ϕ corresponds to the distance between inelastic (phase-breaking) scattering centers, i.e. the distance a conduction electron can travel before the phase of its wave function becomes randomized. In contrast to inelastic scattering, after the elastic scattering event, the phase is (partially) preserved. Preservation of the phase maintains quantum interference of the electron waves that can be illustrated as follows. An electron moving from one point to another (over a distance shorter than L_ϕ) is presented as a set of partial waves with their amplitudes and phases. Each wave corresponds to a different path along which the electron experiences many elastic scattering events. The probability of finding the electron at the final point is equal to the square of the modulus of a sum of the partial waves, i.e. it includes the amplitudes, as well as the phases acquired while traveling along the corresponding paths. There is a certain probability for the electron to make a loop, i.e. to return to the initial point. It arises because two partial waves corresponding to clockwise and counter-clockwise paths along the same loop acquire the same phase. Consequently, such waves interfere constructively. Constructive interference implies that an electron tends to remain at its initial position, it is "localized", resulting in a reduction of the conductance. This effect is known as weak localization (WL). Externally, the quantum interference can be affected by applying a magnetic field. The presence of the magnetic field adds different (positive and negative) phase shifts to clockwise and counter-clockwise wave functions along the same loop. The constructive interference becomes destructive, and the conductance increases. Without a field, the largest length of a loop is limited to L_ϕ. What limits the phase-breaking length L_ϕ by destroying the phase of the wave function

are inelastic scattering events. These are scattering at other electrons, phonons, exchange of superconducting fluctuations, and also extrinsic sources as magnetic impurities or two-level systems. Hence, the field which eliminates the longest active loop allows one to estimate L_ϕ and, consequently, the associated with it dephasing time τ_ϕ. Although the mechanisms of dephasing are all due to inelastic scattering, the dephasing time is, in general, different from the inelastic time (see Subsection 2.4.1.2).

The magnetoconductance technique is based on transport measurements in the magnetic field. From these measurements one can extract the dimensionless change in the conductance (reciprocal resistance per sample square) induced by the magnetic field at a fixed temperature T as follows

$$\delta G(B,T) = \frac{2\pi^2 \hbar}{e^2} \left[\frac{1}{R_S(B,T)} - \frac{1}{R_S(0,T)} \right],$$
(2.5)

where $2\pi^2 \hbar / e^2$ has the dimension of Ω.

The experimentally obtained magnetoconductance, $\delta G(B,T)$, is further analyzed in terms of the theory of quantum corrections to the classical Drude conductance. The Drude model does not account for the quantum effects relying on the assumption that after an elastic scattering event, the information on the initial velocity and direction of an electron is completely lost. The conductance of the film in the quantum diffusive regime differs from the Drude conductance by the value of the quantum correction. We use the following notation. Dimensionless quantum corrections to the Drude conductance we denote as ΔG. Theoretical dimensionless magnetoconductance can be expressed as $\delta G(B,T) = \left[\frac{2\pi^2 \hbar}{e^2} G_0 + \Delta G(B,T) \right] - \left[\frac{2\pi^2 \hbar}{e^2} G_0 + \Delta G(0,T) \right]$, where G_0 is the Drude conductance. Computing the change in the conductance allows for excluding the term with the Drude conductance, and we arrive at $\delta G(B,T) = \Delta G(B,T) - \Delta G(0,T)$.

All quantum corrections could be divided into two main groups [51], namely single-particle and two-particle corrections. The single-particle corrections are caused by the quantum interference between waves from one electron (electron interferes with itself). They are known as weak-localization (WL) corrections. The two-particle corrections are caused by the quantum interference between waves from different electrons, responsible for the electron-electron interaction. This group can be further divided into electron-electron interaction in the cooper channel and the diffusive channel. The quantum correction from interaction in the diffusive channel is negligibly small [52] in the range of magnetic fields (0 – 9 T) and temperatures (10 – 30 K) considered in this thesis (see Section 3.2), therefore we neglect it. The quantum corrections from electron interaction in the cooper channel include superconducting fluctuations described by Aslamazov and Larkin, and Maki and Thompson, and fluctuations due to the suppression of the electronic density of states. All these corrections are considered below.

2.4.1.1 Quantum corrections

The theory of quantum corrections was developed for degenerate electron gas at the limit $k_F l_e > 1$. Each quantum correction exhibits its inherent magnetic field and temperature behaviors. These behaviors strongly depend on the dimensionality of the electron gas with respect to the characteristic scales of the theory. NbN films under the present study fall into the category of a quasi-two-dimensional system (the dimensionality is examined in Section 3.1.1). A film is treated as a quasi-2-d system if $l_e, \lambda_F < d < L_\phi, L_T$, where d is the thickness of the film and $L_T = \sqrt{2\pi\hbar D/(k_B T)}$ is the thermal coherence length. Consequently, the analytical expressions of quantum corrections, which are necessary for the further analysis of the experimental data (presented in Section 3.2.1), will be given only for the 2-d limit.

Weak Localization (WL)

In the quantum diffusive regime, scattering of non-interacting electrons on elastic impurities yields the effects of quantum interference. As was discussed above, quantum interference results in a higher probability of finding an electron at the initial point. Such an effect, the weak-localization effect, provides a negative correction to the classical Drude conductance, the amplitude of which increases with lowering the temperature. So far, the electron spin was ignored. However, in the presence of strong spin-orbit (s.o.) scattering, the former illustration of quantum interference becomes different. Two partial waves, corresponding to the clockwise and counterclockwise paths of the loop and interfering constructively (in the absence of the external magnetic field) at the initial point, have the fixed spin +1/2 or -1/2. Spin-orbit scattering rotates the spins of the partial waves in the opposite directions resulting in destructive interference. This leads to the positive correction to the Drude conductance. This effect is contrary to (normal) weak localization and known as weak anti-localization (WAL). The amplitude of the WAL correction increases with lowering the temperature.

The total correction to the Drude conductance caused by the weak-localization effect including spin-orbit scattering and magnetic impurities scattering is given by [53, 54]:

$$\Delta G^{WL}(B,T) = -\left[\psi\left(\frac{1}{2}+\frac{B_1}{B}\right) - \psi\left(\frac{1}{2}+\frac{B_2}{B}\right) + \psi\left(\frac{1}{2}+\frac{B_3}{B}\right) - \psi\left(\frac{1}{2}+\frac{B_4}{B}\right)\right], \quad (2.6)$$

where $\psi(x)$ is the digamma function and fields are:

$$B_1 = B_e + B_{s.o.} + B_s,$$
$$B_2 = \frac{4}{3}B_{s.o.} + \frac{2}{3}B_s + B_{in},$$
$$B_3 = 2B_s + B_{in}, \quad (2.7)$$
$$B_4 = B_2.$$

Here the characteristic fields, B_j, are connected with the characteristic scattering times, τ_j, as $B_j = \hbar/(4eD\tau_j)$, where indices stand for the following scattering processes: 'e' is elastic scattering, 'in' - inelastic scattering, 's' - magnetic scattering, and 's.o.' - spin-orbit scattering. Although the index 'in' denotes inelastic scattering, the corresponding time to the field B_{in} is the
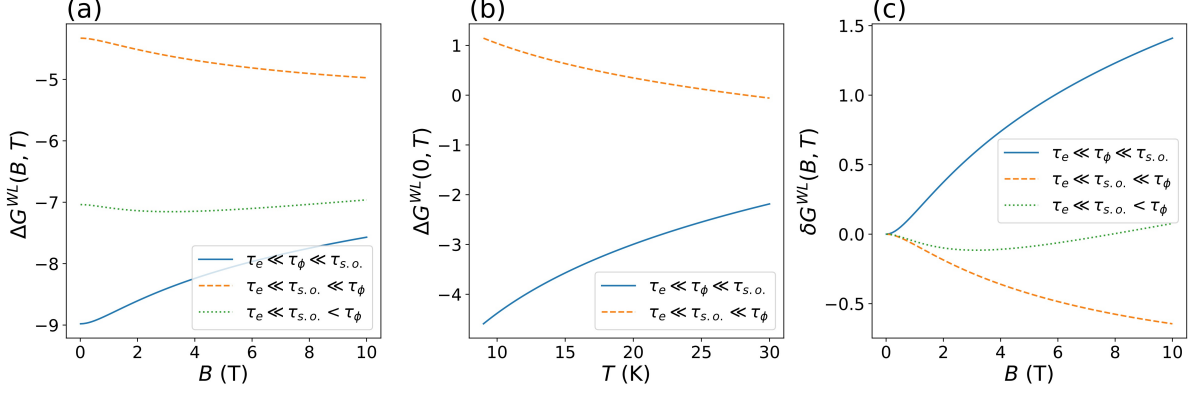
Figure 2.7: Simulated quantum corrections to the Drude conductance caused by the weak localization (WL) effect. Solid curves correspond to WL in the absence of spin-orbit and magnetic impurities scattering. Dashed curves correspond to WAL in the presence of strong spin-orbit scattering and the absence of magnetic impurities scattering. Dotted curves correspond to the weak spin-orbit scattering ($\tau_{s.o.} < \tau_\phi$) and the absence of scattering on magnetic impurities. a) Dimensionless weak-localization correction vs. magnetic field and b) vs. temperature at zero magnetic field. c) Dimensionless weak-localization magnetoconductance vs. magnetic field. For each curve we fixed the parameters $\tau_\phi = 8$ ps, $\tau_e = 1$ fs and $D = 0.5$ cm^2/s (D enters the expression for the characteristic fields); in the panels a) and c) the solid, dashed and dotted curves were simulated with $\tau_{s.o.} = 2$ ns, 0.5 ps, and 4 ps respectively. In the panel b) τ_ϕ was taken to scale with the temperature as $\tau_\phi \sim T^{-2}$, for the dashed curve, $\tau_{s.o.} = 2$ ns.

electron dephasing time τ_ϕ which is, in general, different from the inelastic electron scattering time τ_{in} (see Subsection 2.4.1.2). The term $B_s \propto 1/\tau_s$ is zero for non-magnetic materials due to the absence of magnetic impurities. NbN films studied in this thesis (Section 3.1) are not a magnetic material. Therefore, we exclude the term B_s from consideration. Consequently, Eqs. (2.7) reduce to $B_1 = B_e + B_{s.o.}$, $B_2 = B_4 = \frac{4}{3}B_{s.o.} + B_{in}$ and $B_3 = B_{in}$. Further, since τ_e is the shortest time scale, i.e $\tau_e \ll \tau_{s.o.}, \tau_\phi$, therefore $B_1 = B_e$ and the first digamma function in Eq. (2.6) can be approximated by its asymptotic limit, $\ln(B_e/B)$, which is valid for large arguments ($B_e/B \gg 1$). Eq. (2.6) consequently becomes:

$$\Delta G^{WL}(B,T) = -\left[\ln\left(\frac{B_e}{B}\right) - \frac{3}{2}\psi\left(\frac{1}{2} + \frac{\frac{4}{3}B_{s.o.} + B_{in}}{B}\right) + \frac{1}{2}\psi\left(\frac{1}{2} + \frac{B_{in}}{B}\right)\right]. \qquad (2.8)$$

In the limit $x \to 0$, the digamma function $\psi(1/2 + 1/x)$ has the asymptotic $ln(1/x)$. Hence, in the zero field limit, $B \to 0$, Eq. (2.8) becomes:

$$\Delta G^{WL}(0,T) = -\lim_{B \to 0}\left[\ln\left(\frac{B_e}{B}\right) - \frac{3}{2}\ln\left(\frac{\frac{4}{3}B_{s.o.} + B_{in}}{B}\right) + \frac{1}{2}\ln\left(\frac{B_{in}}{B}\right)\right]. \qquad (2.9)$$

In the absence of spin-orbit scattering, $\tau_{s.o.} \to \infty$ and $\tau_{s.o.} \gg \tau_\phi$, and magnetic scattering, the quantum correction is given by $\Delta G(0,T) = -\ln(B_e/B) = -ln(\tau_\phi/\tau_e)$. Since $1/\tau_\phi$ decreases with the temperature and $\tau_e < \tau_\phi$ at any temperature, the correction is negative and its magnitude increases with the decrease of temperature (solid curve in Fig. 2.7(b)). At a fixed temperature, its magnitude decreases with the increase of the magnetic field (solid curve

in Fig. 2.7(a)). In the presence of very strong spin-orbit scattering (weak-antilocalization), $\tau_e \ll \tau_{s.o.} \ll \tau_\phi$, the correction is given by $\Delta G(0,T) \propto \frac{1}{2} \ln(B_{s.o.}/B_{in}) = \frac{1}{2} \ln(\tau_\phi/\tau_{s.o.})$. Here, the inequality $\tau_e \ll \tau_{s.o.}$ holds because not every elastic-scattering event is accompanied by a spin flip. Since $\tau_{s.o.}$ is temperature-independent, for $\tau_{s.o.} \ll \tau_\phi$ the WAL correction to the Drude conductance is positive, its magnitude increases with the decrease of the temperature (dashed curve in Fig. 2.7(b)). At the fixed temperature the magnitude of the WAL correction increases with the magnetic field (dashed curve in Fig. 2.7(a)). Spin-orbit scattering arises due to interaction between the spin magnetic moment of an electron and the magnetic field generated at the electron by a moving nucleus around the electron, in the electron rest frame. This interaction is proportional to the charge of the nucleus. Therefore, spin-orbit scattering is more pronounced in materials containing heavy atoms, $1/\tau_{s.o.} \propto Z^4$ [55], where Z is the atomic number. For NbN films studied in this thesis, we expect the spin-orbit coupling to be weak, even if Nb is relatively heavy, $Z = 41$, however, N has small atomic number $Z = 7$. Moreover these films are characterized by higher content of nitrogen (see Section 3.1).

If the spin-orbit interaction is weak and in the absence of magnetic scattering, the dimensionless magnetoconductance (dotted curve in Fig. 2.7(c)) is given by:

$$\delta G^{WL}(B,T) = \left[\frac{3}{2}\psi\left(\frac{1}{2} + \frac{\frac{4}{3}B_{s.o.} + B_{in}}{B}\right) - \frac{1}{2}\psi\left(\frac{1}{2} + \frac{B_{in}}{B}\right) \right.$$
$$\left. - \frac{3}{2}\ln\left(\frac{\frac{4}{3}B_{s.o.} + B_{in}}{B}\right) + \frac{1}{2}\ln\left(\frac{B_{in}}{B}\right) \right]. \quad (2.10)$$

Or in the notation of the universal function $Y(x) = \ln(1/x) + \psi(1/2 + 1/x)$, it becomes:

$$\delta G^{WL}(B,T) = \left[\frac{3}{2}Y\left(\frac{B}{\frac{4}{3}B_{s.o.} + B_{in}}\right) - \frac{1}{2}Y\left(\frac{B}{B_{in}}\right) \right].$$

The behavior of the magnetoconductance with the magnetic field is shown in Fig. 2.7(c) for different limiting cases.

Aslamazov-Larkin (AL) fluctuations
Superconducting fluctuations, i.e. stochastic formation of Cooper pair above T_C, lead to the opening of a "new channel" for charge transfer and contribute to the conductivity. This causes broadening of the superconducting transition at $T > T_C$. The effect is commonly denoted as the Aslamazov-Larkin (AL) correction to the conductance. The AL correction is positive and its magnitude increases with lowering the temperature and the magnetic field. In the 2-d limit, in the immediate vicinity of T_C, where the AL contribution dominates, it has the form [56]

$$\Delta G^{AL}(B,T) = \frac{\pi^2}{2\ln(T/T_C)}\left\{ \frac{B_C}{B}\left(1 - 2\frac{B_C}{B}\left[\psi\left(1 + \frac{B_C}{B}\right) - \psi\left(\frac{1}{2} + \frac{B_C}{B}\right)\right]\right)\right\}. \quad (2.11)$$

Here B_C is the characteristic field defined by the relation $B_C = C^* \frac{2k_B T}{\pi e D}\ln(T/T_C)$ or differently $B_C = C^*\hbar/(4eD\tau_{GL})$, where $\tau_{GL} = (\pi\hbar)/(8k_B T\ln(T/T_C))$ is the Ginzburg-Landau time representing the lifetime of Cooper pairs. In different publications the numerical factor C^* was
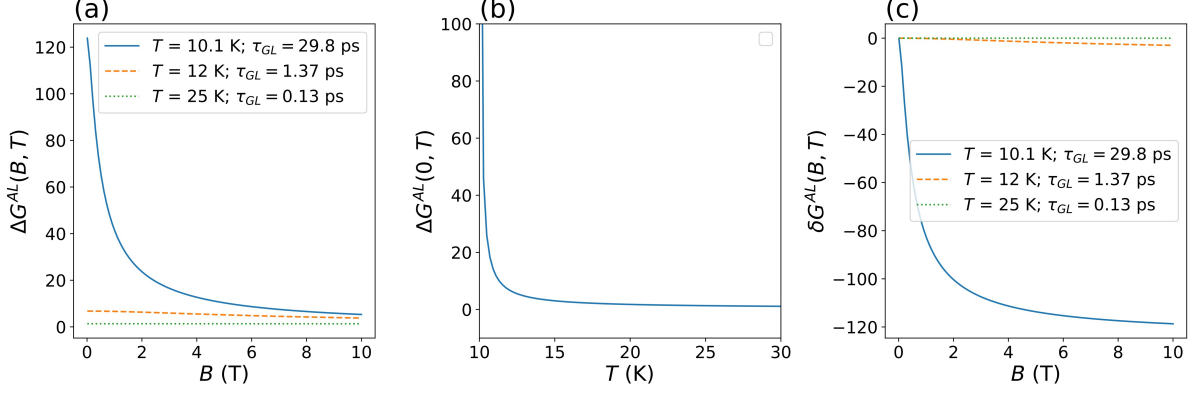
Figure 2.8: Simulated quantum corrections to the Drude conductance caused by Aslamazov-Larkin (AL) fluctuations. a) Dimensionless correction AL vs. magnetic field and b) vs. temperature at zero magnetic field. c) Dimensionless AL magnetoconductance vs. magnetic field. Three different curves in a) and c) correspond to different values of τ_{GL} as it is indicated in the legends. For each computed curve, we fixed the following parameters: $T_C = 10$ K, $\tau_\phi = 8$ ps, and $D = 0.5$ cm^2/s (D enters the expression for the characteristic field).

assigned values from 1 to 3 [54, 57, 58, 59]. In the limit, $B \to 0$, the term in curly brackets approaches a value $1/4$, therefore the AL correction becomes:

$$\Delta G^{AL}(0,T) = \left(\frac{2\pi^2 \hbar}{e^2}\right) \frac{e^2}{16\hbar \ln(T/T_C)}. \tag{2.12}$$

This correction is positive and its magnitude rapidly increases with decreasing temperature (Fig. 2.8(b)). In the vicinity of T_C, the AL correction exhibits temperature singularity. The magnetoconductance caused by the AL corrections is given by:

$$\delta G^{AL}(B,T) = \frac{\pi^2}{2\ln(T/T_C)} \left\{ \frac{B_C}{B} \left(1 - 2\frac{B_C}{B} \left[\psi\left(1 + \frac{B_C}{B}\right) - \psi\left(\frac{1}{2} + \frac{B_C}{B}\right)\right]\right) - \frac{1}{4} \right\}. \tag{2.13}$$

The behavior of the magnetoconductance with magnetic field is shown if Fig. 2.8(c) at different fixed temperatures.

Maki-Thomson (MT) fluctuations

The Maki-Thompson correction to the Drude conductance accounts for stochastic, for a time shorter than τ_ϕ, pairing of two electrons, which are about to simultaneously (coherently) scatter at the same impurity. Pairing eliminates scattering that effectively increases the electron mean free path and weakens the effect of localization. Numerous experimental studies [60, 61, 62, 63] demonstrate that the MT correction gives the main contribution to the magnetoconductance at $T > T_C$. The MT correction [64, 65] for the 2-d limit was elaborated by Larkin [66] for large temperatures and further modified by Lopes dos Santos and Abrahams (LSA) [67] for lower temperatures close to T_C, i.e. when $\ln(T/T_C) \ll 1$, as

$$\Delta G^{MT}(B,T) = -\beta_{LSA}(T,\delta) \left[\psi\left(\frac{1}{2} + \frac{B_{in}}{B}\right) - \psi\left(\frac{1}{2} + \frac{B_C}{B}\right)\right]. \tag{2.14}$$

Here, the parameter $\beta_{LSA}(T,\delta) = \pi^2/(4[\ln(T/T_C) - \delta])$ is the MT pair-breaking parameter, where $\delta = (\pi e D B_{in})/(2k_B T) = \frac{B_{in}}{B_C} \ln(T/T_C)$. Differently this parameter can be expressed as
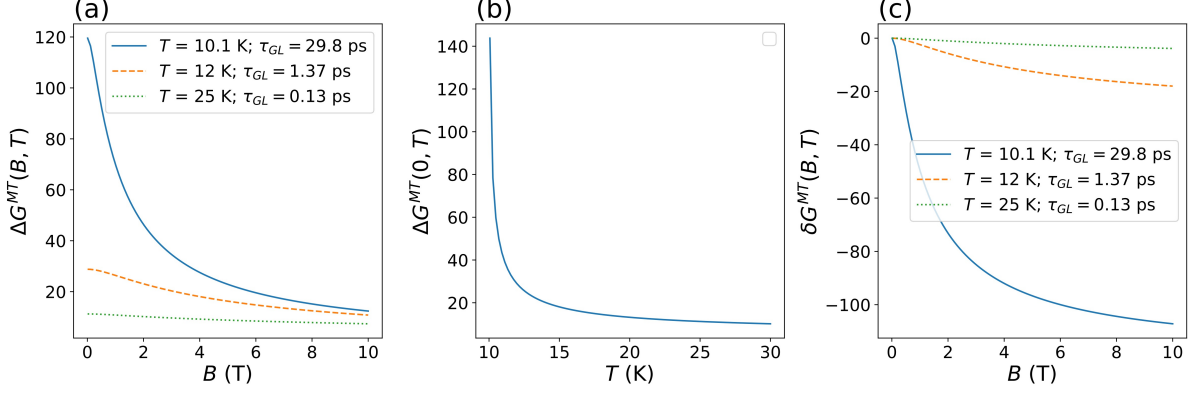
22

Figure 2.9: Simulated quantum corrections to the Drude conductance caused by Maki-Thomson (MT) fluctuations. a) Dimensionless MT correction vs. magnetic field and b) vs. temperature at zero magnetic field. c) Dimensionless MT magnetoconductance vs. magnetic field. Three different curves in a) and c) correspond to different values of τ_{GL} as it is indicated in the legends. For each computed curve, we fixed the following parameters: $T_C = 10$ K, $\tau_\phi = 8$ ps, and $D = 0.5$ cm^2/s (D enters the expression for the characteristic field).

$\beta_{LSA}(T, \delta) = \frac{2\pi k_B T}{\hbar} \frac{\tau_{GL}}{1 - \tau_{GL}/\tau_\phi}$. In the zero field limit, $B \to 0$, the MT correction becomes:

$$\Delta G^{MT}(0, T) = -\beta_{LSA}(T, \delta) \ln\left(\frac{B_{in}}{B_C}\right). \tag{2.15}$$

In contrast to the (normal) WL correction, the MT correction is positive and has temperature singularity. The magnitude of the MT correction increases with the decrease of the temperature (Fig. 2.9(b)) and decreases with the increase of the magnetic field (Fig. 2.9(a)). Finally, the magnetoconductance caused by the MT correction (Fig. 2.9(c)) is given by:

$$\delta G^{MT}(B, T) = -\beta_{LSA}(T, \delta) \left[\psi\left(\frac{1}{2} + \frac{B_{in}}{B}\right) - \psi\left(\frac{1}{2} + \frac{B_C}{B}\right) + \ln\left(\frac{B_C}{B_{in}}\right)\right]. \tag{2.16}$$

In the notation of the universal function it becomes:

$$\delta G^{MT}(B, T) = -\beta_{LSA}(T, \delta) \left[Y(B/B_{in}) - Y(B/B_C)\right].$$

Density of states (DOS) fluctuations

Because above T_C some electrons are involved in stochastic formation of Cooper pairs, the electron density of states decreases. The pairing electrons cannot simultaneously participate in charge transfer, the effective number of carriers taking part in charge transfer reduces. This results in the decrease of the normal state (Drude) conductance. This indirect fluctuation correction to the Drude conductance is known as the density of states (DOS) correction and it appears side by side with the AL correction. The DOS correction has the opposite (negative) sign and is less singular in the vicinity of T_C as compared to the AL correction (Fig. 2.10(a) and (b)). The DOS correction is given by [68, 69]:

$$\Delta G^{DOS}(B, T) = \frac{28\varsigma(3)}{\pi^2} \left[\ln\left(\frac{B}{B_C} \ln(T/T_C)\right) + \psi\left(\frac{1}{2} + \frac{B_C}{B}\right)\right], \tag{2.17}$$
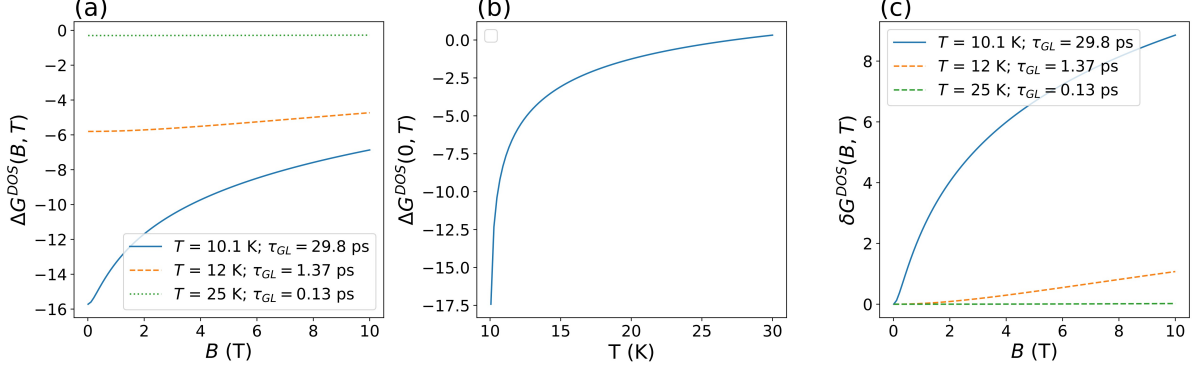
23

Figure 2.10: Simulated quantum corrections to the Drude conductance caused by fluctuations of the electron density of states (DOS). a) Dimensionless DOS correction vs. magnetic field and b) vs. temperature at zero magnetic field. c) Dimensionless DOS magnetoconductance vs. magnetic field. Three different curves in a) and c) correspond to different values of τ_{GL} as it is indicated in the legends. For each computed curve, we fixed the following parameters: $T_C = 10$ K, $\tau_\phi = 8$ ps, and $D = 0.5$ cm^2/s (D enters the expression for the characteristic field).

where $\varsigma(3) = 1.202$ is Riemann zeta function. In the limit of zero magnetic field, it becomes

$$\Delta G^{DOS}(0, T) = \frac{28\varsigma(3)}{\pi^2} \ln\left[\ln(T/T_C)\right]. \tag{2.18}$$

The DOS correction (Fig. 2.10(b)) has the opposite sign with respect to the AL and MT corrections and is less singular in temperature than those. Its magnitude decreases with increase of the temperature and of the magnetic field. The dimensionless magnetoconductance due to the DOS correction is

$$\delta G^{DOS}(B, T) = \frac{28\varsigma(3)}{\pi^2} \left[\ln\left(\frac{B}{B_C}\right) + \psi\left(\frac{1}{2} + \frac{B_C}{B}\right)\right]. \tag{2.19}$$

In the notation of the universal function it becomes $\delta G^{DOS}(B, T) = \frac{28\varsigma(3)}{\pi^2} Y(B/B_C)$. It is worth mentioning that δG^{MT} expression given by Eq. (2.16) includes the same field dependence as δG^{DOS} (Eq. (2.19)) with the accuracy of the prefactor $\beta_{LSA}(T, \delta)$.

Total magnetoconductance

Here, we simulate the contribution of each quantum correction to the total magnetoconductance at different temperatures. The total magnetoconductance is a sum of magnetoconductances caused by each quantum correction considered above: $\delta G(B, T) = \delta G^{WL}(B, T) + \delta G^{AL}(B, T) + \delta G^{MT}(B, T) + \delta G^{DOS}(B, T)$. The WL term was computed with Eq. (2.10) which corresponds to the case of weak spin-orbit scattering and the absence of magnetic impurity scattering. For computing AL, MT and DOS terms, Eqs. (2.13), (2.16) and (2.19) were used, respectively. The total magnetoconductance as well as each term are shown in Fig. 2.11 at three different temperatures 10.1, 12, and 25 K. Values of other parameters were chosen to be similar to those for studied here NbN films (see Section 3.2.1) as $T_C = 10$ K, $\tau_\phi = 8$ ps, and $D = 0.5$ cm^2/s. Fig. 2.11(a) corresponds to the vicinity of the superconducting temperature, $\ln(T/T_C) \ll 1$,
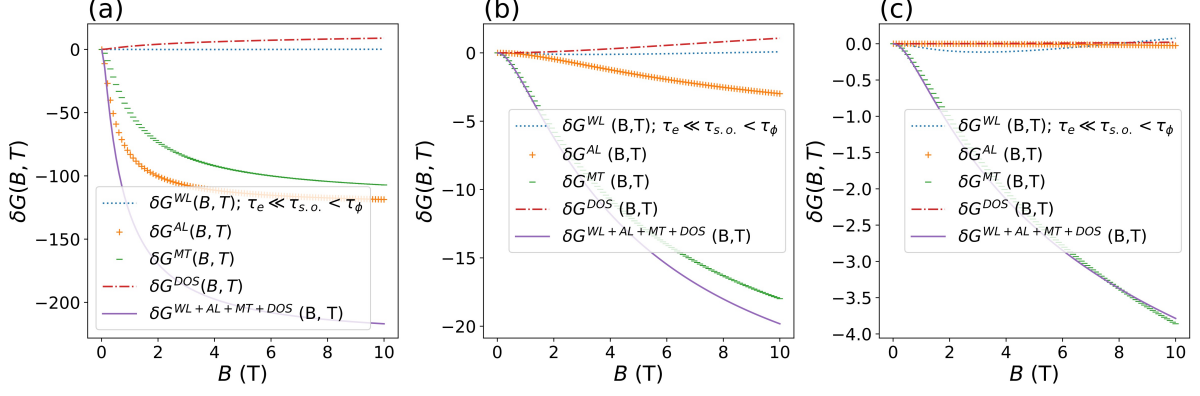
Figure 2.11: Simulated magnetoconductance caused by different quantum corrections to the Drude conductance vs. magnetic field. a) Total magnetoconductance was computed as $\delta G(B,T) = \delta G^{WL}(B,T) + \delta G^{AL}(B,T) + \delta G^{MT}(B,T) + \delta G^{DOS}(B,T)$. Simulation were done at three different temperatures a) 10.1 K, b) 12 K, c) 25 K. Simulations were done with the following parameters: $T_C = 10$ K, $\tau_\phi = 8$ ps, $D = 0.5$ cm^2/s and $\tau_{s.o.} = 4$ ps.

where the AL correction is the dominant term. However, already for $\ln(T/T_C) < 1$ (Fig. 2.11(b)) the MT term dominates over others. Fig. 2.11(c) corresponds to the temperature far above T_C, $\ln(T/T_C) \approx 1$, the total change in conductance, $\delta G(B,T)$, is almost completely determined by the MT term.

Further in Section 3.2.1, we will fit the experimental data with the total change in conductance as

$$\delta G(B,T) = \delta G^{WL}(B,T) + \delta G^{AL}(B,T) + \delta G^{MT}(B,T).$$

Here the DOS term is intentionally omitted to simplify the fitting procedure. To account for DOS fluctuations, the prefactor $\beta_{LSA}(T,\delta)$ in the MT term can be used as a fitting parameter because the MT term includes the same expression as the DOS term with the accuracy of the prefactor. To summarise, the following fitting parameters will be used: C^*, $B_{s.o.}$ and B_{in}. The dephasing rate will be found from the magnetic field as $\tau_\phi = \hbar/(4eDB_{in})$.

2.4.1.2 Electron dephasing and inelastic scattering times

Theory predicts that, in the absence of extrinsic phase-breaking sources, the total dephasing rate is a sum of the rates affiliated with independent inelastic scattering events in which electrons are involved. They are electron-electron scattering (e-e) [70], electron-phonon scattering (e-ph) and electron-fluctuation scattering (e-fl) [71]. The latter is associated with losses of the electron energy and phase coherence due to the recombination of electrons into superconducting pairs [71]. Hence, the total dephasing rate is

$$\frac{1}{\tau_\phi} = \frac{1}{\tau_{e-e}} + \frac{1}{\tau_{e-ph}} + \frac{1}{\tau_{e-fl}}. \tag{2.20}$$

Although the dephasing rate $1/\tau_\phi$ is governed by inelastic processes, in principle, $1/\tau_\phi$ may differ from the inelastic scattering rate $1/\tau_{in}$. The difference is most pronounced for scattering processes in which the change in the electron energy is smaller than thermal energy. With respect to e-e scattering, at low temperatures, the dephasing rate is dominated by Nyquist noise, i.e. scattering events with small-energy transfer [72, 70]. This is equivalent to the interaction of a conduction electron with electromagnetic fluctuations produced by the environment, i.e. other electrons. In the 2-d limit, Altshuler and Aronov [72, 70] showed that the dephasing (Nyquist) e-e rate is given by

$$\frac{1}{\tau_{e-e}} = \frac{k_B T}{\hbar} \frac{1}{2C_1} \ln(C_1), \tag{2.21}$$

where $C_1 = \pi\hbar/(R_{SN}e^2)$. At temperatures larger than the crossover temperature $\hbar/(k_B\tau_e)$, the e-e dephasing rate is dominated by Landau scattering, i.e., scattering events with large energy transfer. In this latter case the rate has a different temperature dependence $\propto T^2 \ln(T^{-1})$ [73] (for strongly disordered NbN films the crossover is expected to occur at temperatures $> 10^3$ K). With respect to e-ph scattering, the processes with small-energy transfer are suppressed [74] and typical energy exchange is $\sim k_B T$. Therefore, the e-ph dephasing rate is identical to e-ph inelastic scattering rate [75]. In a general form, the e-ph scattering rate can be described as

$$\frac{1}{\tau_{e-ph}} = C_2 \left(\frac{T}{T_C}\right)^n, \tag{2.22}$$

where C_2 is a constant. According to the theory of e-ph scattering in disordered conductors [76], the exponent n in Eq. (2.22) depends on the degree of disorder and the kind of impurities and around a fixed temperature may have any value between 2 and 4 (see Section 2.4.2). In superconducting materials, at temperatures close to T_C, the dephasing rate due to superconducting fluctuations is given by [71]

$$\frac{1}{\tau_{e-fl}} = \frac{k_B T}{\hbar} \frac{1}{2C_1} \frac{2\ln(2)}{\ln(T/T_C) + C_3}, \tag{2.23}$$

where $C_3 = 4\ln(2)/[\sqrt{\ln(C_1)^2 + 128C_1/\pi} - \ln(C_1)]$ [71].

Fig. 2.12 illustrates the contribution of the e-e, e-ph, and e-fl dephasing rates to the total dephasing rate for three values of the exponent $n = 4$, 3, and 2. Simulations were done according to Eqs. (2.21 - 2.23) with parameters $R_{SN} = 530$ Ω/sq, $T_C = 10$ K, and $C_2 = 10^{-13}$ s^{-1}, which are close to those of NbN films studied in Chapter 3. The total dephasing rate is shown with dashed curves. It is clearly seen that at $T \gg T_C$ (T_C was taken to be 10 K), for $n = 3$ and 4, the term τ_{e-ph}^{-1} dominates and defines both the temperature dependence and the magnitude of the dephasing rate (Fig. 2.12 (a) and b). Contrarily, close to T_C, the term τ_{e-fl}^{-1} dominates and controls the upturn in the $\tau_\phi^{-1}(T)$ dependence.

To conclude, the magnetoconductance technique allows for finding the dephasing time. For e-ph interaction, the dephasing time due to this interaction and the inelastic (single-particle) e-ph scattering time are identical [75]. In disordered conductors and at low temperatures, the latter is predicted by the SM model, to which we devote the next section.
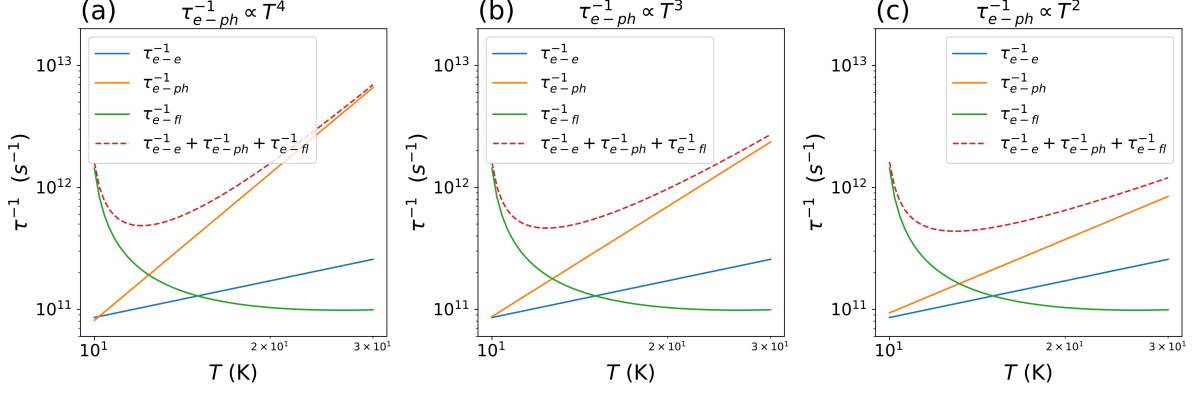
Figure 2.12: Simulated total electron dephasing rate (dashed curves) and contributing rates vs. temperature for different values of the exponent in $\tau_{e-ph}^{-1} \propto T^n$ a) $n = 4$, b) $n = 3$, c) $n = 2$. For simulations Eqs. (2.21 - 2.23) were used with the following parameters $R_{SN} = 530 \ \Omega/\text{sq}$, $T_C = 10$ K, and $C_2 = 10^{-13}$ s^{-1}. These parameters were chosen to be similar to those for NbN films studied in this thesis (see Section 3.2.1)

2.4.2 Sergeev-Mitin (SM) model: Inelastic electron-phonon scattering time

In clean metals at low temperatures, the inelastic *e-ph* scattering rate obeys a power-law temperature dependence, $1/\tau_{e-ph} \propto T^n$, with the exponent $n = 3$ [49]. In disordered metals, *e-ph* scattering is modified by disorder and impurities that makes n temperature-dependent. Models of *e-ph* scattering in disordered metals were developed by Pippard [77], Schmid [78], and Rammer and Schmid [75]. In these models, the scattering centers are always taken to vibrate in phase with the lattice atoms. Later, Sergeev and Mitin [76] generalized the Pippard-Schmid-Rammer model accounting for the presence of "static" (non-vibrating) scattering centers. Today, the Sergeev-Mitin (SM) model is the most advanced model describing *e-ph* scattering in disordered conductors.

The SM model predicts inelastic (single-particle) scattering rate of electrons at the Fermi level on 3-d Debye phonons. At low temperatures, the rate of *e-ph* scattering obeys power law temperature dependence, $\tau_{e-ph}^{-1} \propto T^n$. The magnitude of τ_{e-ph}^{-1} and the exponent n are controlled by the degree of disorder and the property of elastic scattering centers, which are presented by vibrating or heavy impurities, rigid boundaries, and defects. *E-ph* scattering is a non-local process with a characteristic size of the interaction region of the order of $1/q_T$ ($q_T = k_B T/\hbar u$ is the wave vector of a thermal phonon and u is the sound velocity). The product $q_T l_e$ characterizes the degree of disorder. The limit $q_T l_e \ll 1$ corresponds to a strongly disordered regime, and $q_T l_e \gg 1$ to a clean regime. In the regime of strong disorder, the exponent n can take a value between 2 and 4 that depends on the property of electron scattering centers. Scattering centers vibrating together with the host lattice lead to $\tau_{e-ph}^{-1} \propto T^4$. In the presence of static scattering centers, which are not dragged by phonons, $\tau_{e-ph}^{-1} \propto T^2$.

The inelastic scattering rate of an electron at the Fermi surface via interaction with *longi-*

tudinal phonons is given by

$$\tau_{e-ph(l)}^{-1} = \frac{7\pi\zeta(3)}{2\hbar} \frac{\beta_l(k_B T)^3}{(p_F u_l)^2} F_l(q_{T(l)} l_e).$$ (2.24)

We use indices 'l' and 't' to denote values associated with longitudinal and transverse phonon modes. Here, $\beta_{l(t)} = (2E_F/3)^2 (N(0)/(2\rho u_{l(t)}^2))$ is the dimensionless coupling constant, where $E_F = p_F^2/(2m_e)$ is the Fermi energy, $N(0)$ is the electron two spin density of states, $p_F = N(0)\pi^2\hbar^3/m_e$ is the Fermi momentum, m_e is the electron mass, ρ is the mass density, u is the phonon velocity for a particular phonon mode, and $\zeta(x)$ is the Riemann zeta function. The effect of disorder on the scattering rate is controlled by the integral

$$F_l(z) = \frac{2}{7\zeta(3)} \int_0^{A_l} dx\, \Phi_l(xz)[N(x) + n(x)]x^2,$$

where $N(x)$ and $n(x)$ are Bose and Fermi distribution functions, and

$$\Phi_l(x) = \frac{2}{\pi} \left(\frac{x\arctan(x)}{x - \arctan(x)} - \frac{3}{x}k \right)$$

is the Pippard function. The upper limit of the integral $F_l(z)$ is $A_{l(t)} = (6\pi^2)^{1/3}(a_0\, q_{T,l(t)})^{-1}$, where a_0 is the size of the unit cell. The parameter $1 \geq k \geq 0$ reveals the property of electron scattering centers. It is defined by the ratio between the fractions of vibrating and static scattering centers. $k = 1$ corresponds to scattering centers vibrating in the same way as the host lattice, $k = 0$ corresponds to the static ('non-vibrating') scattering centers such as heavy impurities and rigid boundaries. Differently, the role of k can be illustrated as follows. One can take $k = 1 - l_e/l^*$ where l_e is the total mean free path, and l^* is the average distance an electron can travel between static-impurity scattering centers. Therefore, if all scattering centers are static, then $l^* \to l_e$ and $k = 0$. In contrast, if there is no static scattering center then $l^* \to \infty$ and $k = 1$.

The inelastic scattering rate of an electron at the Fermi surface interacting with *transverse* phonons (two polarizations are taken into account) is given by

$$\tau_{e-ph(t)}^{-1} = 3\pi^2 \frac{\beta_t(k_B T)^2}{(p_F u_t)(p_F l_e)} k F_t(q_{T(t)} l_e),$$ (2.25)

where

$$F_t(z) = \frac{4}{\pi^2} \int_0^{A_t} dx\, \Phi_t(xz)[N(x) + n(x)]x,$$

and the Pippard function

$$\Phi_t(x) = 1 + k\frac{3x - 3(x^2 + 1)\arctan(x)}{2x^3}.$$

The total inelastic *e-ph* scattering rate is a sum of the two rates

$$\tau_{e-ph}^{-1} = \tau_{e-ph(l)}^{-1} + \tau_{e-ph(t)}^{-1}.$$ (2.26)

Effect of the degree and the property of disorder on τ_{e-ph}

In order to illustrate the effect of the degree and the property of disorder on the τ_{e-ph} we compute

28

τ_{e-ph} with Eqs. (2.24 - 2.26) for different parameters. Fig. 2.13(a) shows τ_{e-ph} as a function of temperature for different values of k and fixed values of other parameters a_0, l_e, $u_{t(l)}$, ρ, $N(0)$ and m_e (these values were taken for the specimen M-2259 from the present study, see Section 3.2.1). As seen in the figure, the value of k drastically changes both the magnitude and the temperature dependence of τ_{e-ph}, i.e. the exponent n. Complete vibrating scattering centers ($k = 1$) result in $\tau_{e-ph} \propto T^4$. However, the dependence T^2 appears already for $k = 0.99$ at low temperatures. Furthermore, if scattering centers are static ($k = 0$) then only longitudinal phonons interact with electrons, while already for $k > 0.15$ (not shown in the figure) the transverse phonons dominate over a wide temperature range. For the fixed $k = 1$, the temperature dependence of the e-ph scattering rate changes from T^4 to T^2 where the transition region ($q_T l_e \approx 1$) between two asymptotics corresponds to the transition temperature $\hbar u/(k_B l_e)$. Therefore for a fixed k, the model allows to adjust the temperature dependence of τ_{e-ph} by varying the ratio $u l_e^{-1}$. In Fig. 2.13(b) we plotted the computed τ_{e-ph} as a function of the electron mean free path, l_e, for two temperatures (1 and 15 K) and different k specified in the legend, while other parameters remained the same. The dependence $\tau_{e-ph}(l_e, T)$ illustrates the effect of disorder. In the case of vibrating scattering centers ($k = 1$), the scattering time $\tau_{e-ph} \propto 1/l_e$ in the dirty limit (short l_e and low temperatures). On the other hand, in the presence of static scattering centers ($k < 1$), the dependence changes to $\tau_{e-ph} \propto l_e$. The difference between scattering times for these two cases becomes more pronounced with lowering the temperature that corresponds to increasing disorder.
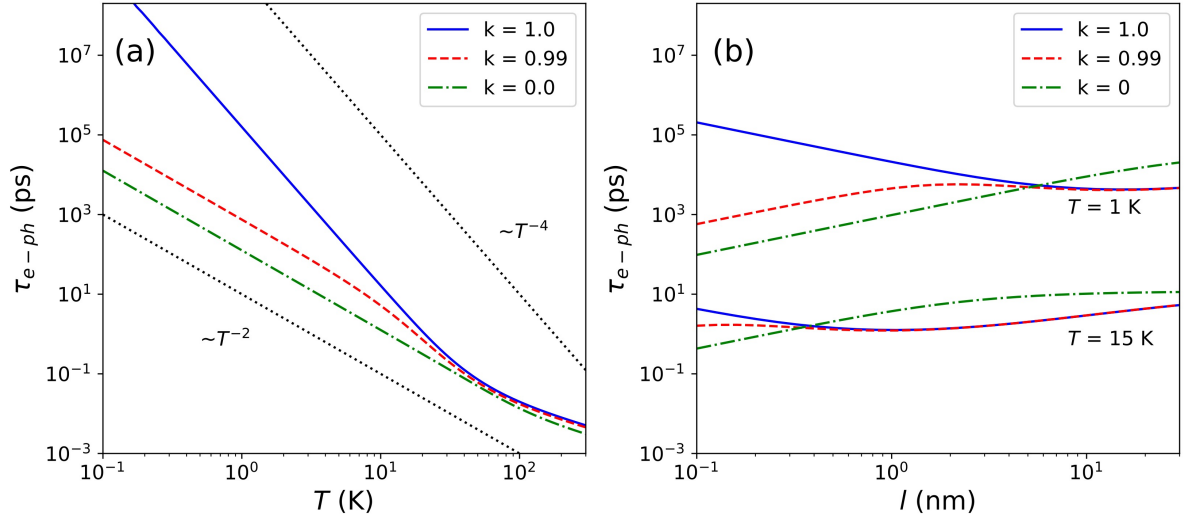

Figure 2.13: Computed e-ph scattering time as a function of a) temperature and b) electron mean free path with Eqs. (2.24-2.26). Each curve was computed with the same fixed parameters $a, l_e, u_{t,l}, \rho, N(0)$ and m_e taken from Section 3.2.1 for specimen M-2259. Dotted curves on the panel (a) are simple power functions of T with exponents specified in the figure. Other curves correspond to different values of k, where $k = 1$ corresponds to completely vibrating scattering centers, while $k < 1$ stands for the presence of 'non-vibrating', static scattering centers. In the panel (b), three upper curves were calculated for $T = 1$ K, and three lower for $T = 15$ K.

The _e-ph_ energy relaxation time (τ_{EP})

Since the photon-detection process implies a non-equilibrium state, it is rather described by the relaxation time of electron energy via _e-ph_ interaction, τ_{EP}, which is proportional but not equal to the inelastic (single-particle) _e-ph_ scattering time τ_{e-ph} used in the SM model. The proportionality coefficient between these times depends on the exponent n at a given temperature. The energy relaxation rate τ_{EP}^{-1} is an average of τ_{e-ph}^{-1} over an electron ensemble from the energy layer $\sim k_B T$. The relationship between these two rates was obtained in [79] as follows

$$\frac{\tau_{EP}^{-1}}{\tau_{e-ph}^{-1}} = \frac{3(n+2)\Gamma(n+2)\zeta(n+2)}{2\pi^2(2-2^{1-n})\Gamma(n)\zeta(n)}, \tag{2.27}$$

where $\Gamma(n)$ is the gamma function, n is the exponent in the power law dependence $\tau_{e-ph}^{-1} \propto T^n$ around a fixed temperature, and $\zeta(n)$ is the Riemann zeta function. This ratio is computed in Table 2.1 for several values of the exponent n. The photoresponse technique, which provides the τ_{EP}, will be described in Section 2.4.4.

Table 2.1: The ratio between the _e-ph_ energy relaxation rate (measured in experiments with electron heating) and the inelastic (single-particle) _e-ph_ scattering rate (Eq. 2.27) for different values of the exponent n in the power law $\tau_{e-ph}^{-1} \propto T^n$

n	2	2.5	3	3.5	4
$\tau_{EP}^{-1}/\tau_{e-ph}^{-1}$	1.6	2.9	4.5	6.6	9.1

2.4.3 Acoustic mismatch model: Phonon escape time

Total reflection of phonons at an unmatched interface between the film and the substrate allows for different definitions of the phonon escape time, τ_{esc}. Here, we compute phonon transparency for the interfaces studied in the present work and discuss different definitions of τ_{esc} in the framework of a two-temperature and three-temperature models which will be introduced in Section 2.4.4.1 and 2.4.4.2, respectively.

Escape of from the superconducting film to the underlying substrate is one of the mechanisms of energy relaxation. For the case of isotropic 3-d Debye phonons it is well described by the acoustic mismatch model (AMM), which was first proposed by Little [80] and then reviewed by Kaplan [48]. We use this model to compute transmission coefficients for certain film/substrate interfaces. In the framework of the model, one considers a phonon flux as acoustic (elastic) plane waves propagating through an interface between two media. These media are assumed to be isotropic, semi-infinite, and lossless for waves of all polarizations. Incident waves of different polarizations are associated with different phonon modes, these are one longitudinal (l) and two transversal (t), namely, vertical (SV) and horizontal (SH), with respect to the plane of incidence. The model takes into account mode conversion and total reflection at the interface. For instance, either l or SV wave incident at the solid/solid interface generates four outgoing waves: reflected and transmitted pairs of l and SV waves. The calculation of the transmission coefficient for this case results in four coupled equations with four boundary conditions. Applied

boundary conditions require the parallel and perpendicular components of strain and stress vectors to be continuous at the interface. An incident SH wave does not generate waves of other polarizations. Therefore the calculation of the transmission coefficient for this case is straightforward. Transmission coefficients were defined separately for each phonon mode as the ratio of the energy flux of all transmitted modes to the energy flux of the incident mode $P_i \propto u_i \rho A_i^2 \cos(\Theta)$. Here, index 'i' denotes the phonon mode, A is the amplitude of the incident mode, Θ is the angle of incidence, ρ is the mass density of the medium, and u is the propagation velocity. The product $u_{1(2)i}\rho_{1(2)}$ is the acoustic impedance, where indices '1' and '2' refer to the film and the substrate, respectively. As a result, transmission coefficients depend on the angle of incidence and the difference between acoustic impedances and sound velocities.

Fig. 2.14 shows transmission coefficients $\eta_{\Theta i}$ computed for longitudinal and two transverse modes vs. angle of incidence Θ for two interfaces NbN/SiO$_2$ and NbN/Al$_2$O$_3$. For calculations, we used the following parameters. For NbN we took $u_{1t} = 2400$ m/s, $u_{1l} = 2u_{1t}$, $\rho = 7.5$ g/cm^3; for SiO$_2$, $u_{2t} = 4090$ m/s, $u_{2l} = 6090$ m/s, $\rho = 2.66$ g/cm^3; and for Al$_2$O$_3$, $u_{2t} = 6450$ m/s, $u_{2l} = 1090$ m/s, $\rho = 3.99$ g/cm^3. Parameters for NbN were taken from the present study (Section 3.2), and for substrates from [48]. As it is seen from Fig. 2.14(a), for NbN/SiO$_2$ the incident l-wave exhibits only one critical angle $\Theta_{max,l} = \arcsin(u_{1l}/u_{2l}) = 52°$. Below this angle, the l-wave is transmitted as l- and SV-waves, and above this angle, the transmitted l-wave disappears, and only the transmitted SV-wave remains. For the incident SV-wave, there are two critical angles. Above the first angle $\arcsin(u_{1t}/u_{2l}) = 23.2°$, the transmitted l-wave disappears and the incident SV-wave is transmitted only as SV-wave. The second angle $\Theta_{max,t} = \arcsin(u_{1t}/u_{2l}) = 35.9°$ is the angle of total reflection.

To define the phonon escape time we consider a phonon flux propagating within a film of thickness d. The film has two boundaries with the surrounding, one is with the substrate and the other is either the vacuum boundary or contact to liquid helium, depending on experimental
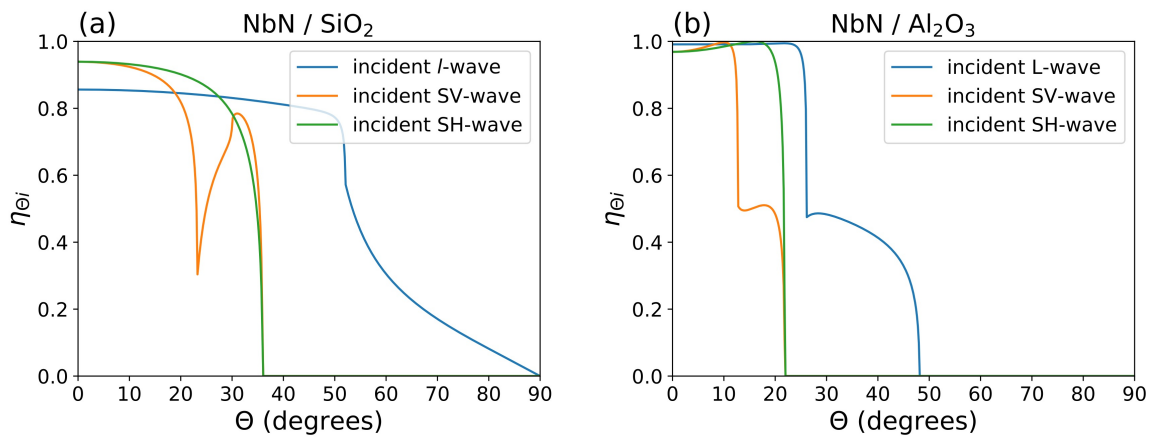

Figure 2.14: Computed transmission coefficients vs. angle of incidence in the framework of the acoustic mismatch model a) for NbN/SiO$_2$ and b) for NbN/Al$_2$O$_3$ interfaces. Different colors correspond to the certain polarization of an incident phonon wave specified in the legends.

conditions. The propagating phonon flux emitted by electrons undergoes reflections at these two interfaces. The film/vacuum (or film/helium) interface is assumed to be zero transparent. Reaching it, the flux is fully specular reflected. By reaching the film/substrate interface, the phonon flux is partly reflected and partly transmitted with transmission coefficients shown in Fig. 2.14. The remaining phonons undergo reflection at the other interface. Therefore the escape time of a particular phonon mode is defined as $\tau_{esc}(\Theta)_i = P(t)(dP(t)/dt)^{-1}$ where $P(t)$ is the phonon flux remaining in the film. After each reflection at the film/substrate interface, $P(t)$ decreases by the factor $1 - \eta_{\Theta i}$. After the q-th reflection, a relative amount of the remaining phonon flux is $1 - \eta_{\Theta i} \sum_{q=1}^{N}(1 - \eta_{\Theta i})^{q-1}$. Two sequential reflections are separated by the time $(2d)/(u_i \cos \Theta)$ that results in the dimensionless rate of the decrease in the phonon flux $\tau_{esc}(\Theta)_i^{-1} = u_i \eta_{\Theta i} \cos \Theta/(2d)$. Integration over the solid angle gives the escape time per mode $\tau_{esc,i}^{-1} = u_i \eta_i/(4d)$ with the angle-averaged transmission coefficient for a particular mode $\eta_i = 2 \int_0^{\Theta_{max,i}} \eta_{\Theta i} \sin \Theta \cos \Theta \, d\Theta$. The total decay rate of the phonon flux energy is a sum of the decay rates of the phonon energy through particular phonon mode, which in turn is proportional to the heat capacity of the mode. According to the Debye model the heat capacity is proportional to the cube of the propagation velocity of the mode. Hence, the total weighted escape rate is $\tau_{esc,g}^{-1} = \dfrac{\overline{\eta u}}{4d}$, where $\overline{\eta u} = \dfrac{\sum_i u_i^{-2} \eta_i}{\sum_i u_i^{-3}}$. The index g means *general* rate and is related to all phonons.

In Fig. 2.15 we show the products $\eta_{\Theta i} u_i$ for each particular phonon mode taken with its weight, i.e. $\dfrac{\sum_i u_i^{-2} \eta_{\Theta i}}{\sum_i u_i^{-3}}$, and also a sum of these products (dashed curve) for both interfaces NbN/SiO$_2$ and NbN/Al$_2$O$_3$. As seen in the figure, energy transfer from the film to the substrate is primarily dominated by the transverse phonons for both interfaces NbN/SiO$_2$ and NbN/Al$_2$O$_3$. Therefore, for simplicity, describing the energy transfer one can consider only transverse phonons. Another approximation is to simplify the total weighted product $\overline{\eta u}$ by a product of weighted values for the transmission coefficients, $\overline{\eta} = \dfrac{\sum_i u_i^{-3} \eta_i}{\sum_i u_i^{-3}}$, and mode velocities, $\overline{u} = \dfrac{\sum_i u_i^{-2}}{\sum_i u_i^{-3}}$, as $\overline{\eta}\,\overline{u}$. It has to be mentioned that formally calculated $\overline{\eta u} \neq \overline{\eta}\,\overline{u}$, although the difference for two mentioned interfaces remains less than ten per cent. One can use another approximation. The total weighted product $\overline{\eta u}$ can be approximated as $\eta_0 \overline{u}(\sin \overline{\Theta}_{max})^2$, where η_0 is the transmission coefficient at zero degrees and $\overline{\Theta}_{max}$ is the angle of total reflection for SH phonon mode. Here the sum of weighted products (dashed curves in Fig. 2.15) is approximated by a step function.

As a result the phonon escape rate can be defined differently. One approach is the total weighted phonon escape rate defined as $\tau_{esc,g}^{-1} = \overline{\eta u}/(4d) \approx \overline{\eta}\,\overline{u}/(4d) \approx \eta_0 \overline{u}(\sin \overline{\Theta}_{max})^2/(4d)$. Here, the same transparency is assigned to phonons with all incident angles. This approach is applied in the two-temperature model (Section 2.4.4.1). For instance, for NbN/Al$_2$O$_3$, $\overline{\eta} = 0.12$. Another approach is to split all phonons into two groups with respect to their angles of incidence. For phonons with $\Theta > \overline{\Theta}_{max}$, the transparency is zero and $\tau_{esc} \to \infty$. For phonons with $\Theta < \overline{\Theta}_{max}$, the interface transparency is defined at zero angle of incidence η_0 ($\eta_0 \approx 0.92$ for NbN/Al$_2$O$_3$) and, consequently, $\tau_{esc}^{-1} = \eta_0 \overline{u}/(2d)$. This approach is applied in the three-temperature model [81] (Section 2.4.4.2) and in the phonon ray-tracing model [82] (Sec-
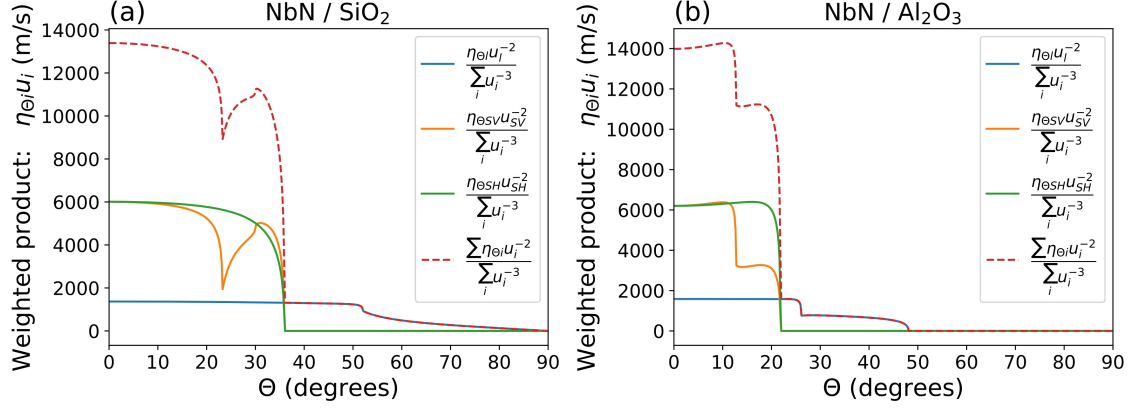
Figure 2.15: Computed products of transmission coefficients and sound velocities taken with their weight vs. angle of incidence (a) for NbN/SiO$_2$ and (b) for NbN/Al$_2$O$_3$ interfaces. Different colors correspond to the certain polarization of an incident phonon wave specified in legends. Dashed curves correspond to a sum of weighted products.

tion 2.4.4.3).

We found for NbN/SiO$_2$ interface $\overline{\eta} = 0.28$, $\overline{u_1} = 2.54 \times 10^3$ m/s, $\overline{u_2} = 4.35 \times 10^3$ m/s. For NbN/Al$_2$O$_3$ interface $\overline{\eta} = 0.12$, $\overline{u_2} = 6.87 \times 10^3$ m/s. Here indexes 1 and 2 are referred to the NbN film and to the substrate, respectively. For NbN/SiO$_2$ we obtained $\tau_{esc,g}$ [ps] $= 5.9$ d [nm] and for NbN/Al$_2$O$_3$, $\tau_{esc,g}$[ps]$=12.3$ d [nm], these values of phonon escape times are used in Section 3.2.

2.4.4 Photoresponse technique: Energy relaxation time

Measurements of the sample photoresponse to electromagnetic radiation with varying intensity allows for finding the relaxation rate of the electron energy. Depending on whether the intensity of radiation is modulated periodically or by forming short pulses, the photoresponse is measured in the time domain or the frequency domain, respectively. Corresponding experimental techniques are usually referred to as the photoresponse in the frequency domain to amplitude-modulated radiation (FDAM) and the time domain to a short pulse (TDP) excitation. Measurements of the photoresponse to radiation in the sub-THz range are sometimes referred to as AMAR technique (Absorption of Modulated (Amplitude) sub-THz Radiation) [83], while to radiation in the optical range as FDAM.

Schematically FDAM and TDP techniques are illustrated in Fig. 2.16. Operating conditions for these techniques are similar. A superconducting microbridge is biased with a small direct current (dc), kept at the superconducting transition temperature, and illuminated by radiation with varying intensity. The planar sizes (width and length) of a microbridge are designed in a way that minimizes diffusion cooling compared to phonon cooling and matches the electrical impedances between a readout circuit and the microbridge at the operating condition. A directly
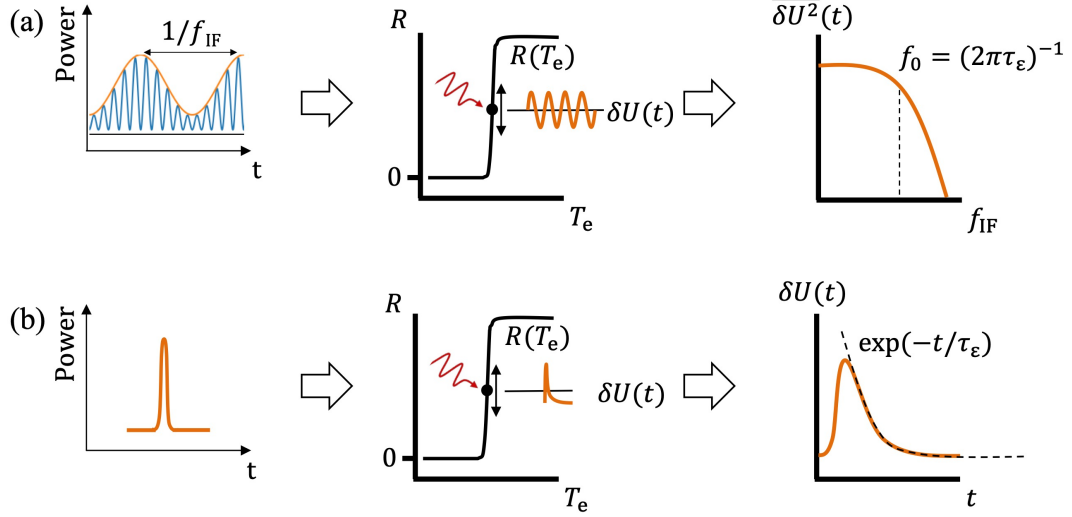
Figure 2.16: Schematic illustration of the photoresponse measurements a) in the frequency domain (FDAM technique) and b) in the time domain (TDP technique). In both techniques, the sample, microbridge, is kept in the vicinity of the superconducting transition. (a) The power of incident radiation alternates periodically and causes modulation of the electron temperature. This leads to periodic sinusoidal variations in the voltage across the microbridge, $\delta U(t) \propto \delta T_e(t)$. The magnitude of the photoresponse, $\overline{\delta U^2}(t)$, is measured at the beating frequency, f_{IF}, with a spectrum analyzer (is not shown here). At a certain roll-off frequency, f_0, the magnitude $\delta U^2(f)$ decreases to one half of its value at small frequencies $1/2\,\delta U^2(0)$. The decay time of the photoresponse, τ_ε, is extracted from the roll-off frequency as $f_0 = (2\pi\tau_\varepsilon)^{-1}$. (b) In the TDP technique, the intensity of incident radiation is modulated by forming short pulses. The photoresponse represents a voltage transient in the time domain measured with an oscilloscope. The decay time of the photoresponse can be found by fitting the falling edge of the voltage transient with an exponent, $\exp(-t/\tau_\varepsilon)$. In both techniques, the photoresponse is initially amplified.

measured parameter in the experiment is a change in the voltage drop caused by the flow of the bias current through the microbridge with changing resistance. It is implied here that the change in the resistance is induced by intensity-varied radiation. This is not immediately obvious because the radiation energy transferred to the electrons increases its temperature, but it does not change the resistance. The resistance is determined by the size of the normal domain or by the density of free vortices. It is assumed that the size of the domain or the vortex density instantly follows the electron temperature, which quickly adjusts itself to the absorbed energy. The small absorbed power is of crucial importance in these techniques because it ensures exponential relaxation of the electron temperature and linearity of the photoresponse. In Fig. 2.16, τ_ε denotes the decay time of the photoresponse.

Although the resistance is determined by either the vortex density occurring in the BKT (Berezinskii-Kosterlitz-Thouless) theory or the normal domain along the current path, the photoresponse is described in terms of quasiparticles and Cooper pairs (the theory of non-equilibrium superconductivity). The analysis of experimental photoresponse can be done with the two-temperature (2-T) model (see Section 2.4.4.1) and the three-temperature (3-T) model (see Section 2.4.4.2). There is another model, the phonon ray-tracing model, which was developed in

[82] from the Rothwarf-Taylor model [84] and applied for decay pulse experiments at the temperatures well below T_C. In this thesis, we extend the phonon ray-tracing model to temperatures at the superconducting transition (Sec. 2.4.4.3).

2.4.4.1 Two-temperature (2-T) model

The 2-T model is the most frequently applied model for the analysis of the photoresponse to electromagnetic radiation measured with FDAM, AMAR, and TDP techniques. At temperatures close to $T \geq T_C$, the concentration of Copper pairs is very low, and the superconductor is treated as a normal metal. The 2-T model was first developed by Kaganov, Lifshitz, and Tanatarov in 1957 [85]. The model implies that after absorption of incident radiation, electrons and phonons are instantly in the internal equilibrium and described by their distribution functions with two different effective temperatures, which slightly exceed the bath temperature. For electrons, it is valid because the time required for them to thermalize is much less than the time required for establishing equilibrium between electrons and phonons. Since the phonon-phonon scattering time is very long, the thermalization of phonons occurs only via electron-phonon and phonon-electron relaxation. The 2-T model provides time evolution of electron and phonon temperatures. Qualitatively, the 2-T model describes the energy transfer as it is schematically shown in Fig. 2.17. The energy absorbed in the electronic subsystem increases the electron temperature, T_e according to the electron heat capacity, c_e. The electron energy flows to the phonon subsystem via e-ph relaxation, on a time scale τ_{EP}. The energy transferred to phonons increases the phonon temperature, T_{ph}, according to the heat capacity of phonons, c_{ph}. Energy from phonons flows to the surrounding via phonon escaping on a time scale $\tau_{esc,\,g}$, and also back to electrons via ph-e relaxation on a time scale τ_{PE}. Forward e-ph and backward ph-e energy flows are connected through the principle of detailed balance. In equilibrium, it requires the forward energy flow from electrons to phonons to be equal to the backward flow, $c_e/\tau_{EP} = c_{ph}/\tau_{PE}$. The equations of the 2-T model in dimensionless form look as follows:

$$\begin{cases} \dfrac{dT_e(\xi)}{d\xi} = -\Gamma_1[T_e(\xi) - T_{ph}(\xi)] + \dfrac{\tau_0}{dc_e}P_{RF}(\xi) + \dfrac{\tau_0}{c_e}P_{dc}, \\ \dfrac{dT_{ph}(\xi)}{d\xi} = \Gamma_2[T_e(\xi) - T_{ph}(\xi)] - \Gamma_3[T_{ph}(\xi) - T_0], \end{cases} \tag{2.28}$$

where T_e and T_{ph} are temperatures of the electron and phonon subsystems, T_0 is the bath temperature, d is the film thickness. $\Gamma_1 = \tau_0/\tau_{EP}$, $\Gamma_2 = \Gamma_1 c_e/c_{ph}$, $\Gamma_3 = \tau_0/\tau_{esc,\,g}$, $\xi = t/\tau_0$ is the dimensionless time, P_{dc} is the Joule power dissipated in the unit volume of the film. Usually in measurements with TDP, AMAR, and FDAM techniques, the magnitude of P_{dc} is kept extremely small and therefore can be neglected. $P_{RF}(t)$ describes the power (the shape) of the excitation incident on the unit area of the film. Eqs. (2.28) are written for small deviations from equilibrium: $P(t) = P_0 + \delta P(t)$, $T_e(t) = T_{e,0} + \delta T_e(t)$, $T_{ph}(t) = T_{ph,0} + \delta T_{ph}(t)$, $T_{e,0} \approx T_{ph,0}$, and $|\delta T_e(t)| \to 0$, $|\delta T_{ph}(t)| \to 0$. Depending on the form of the excitation $P_{RF}(t)$ the solution of Eqs. (2.28) is different. Below the solution will be given for short-pulsed (used in TDP technique) and periodic excitations (used in AMAR and FDAM techniques).
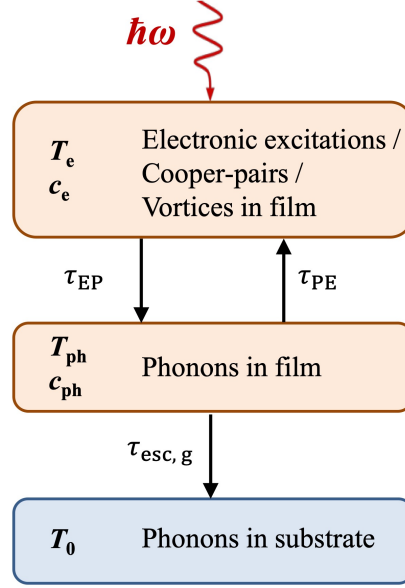
Figure 2.17: Energy balance diagram in a thin metal film (or superconducting film in the resistive state) on a dielectric substrate. The film is presented by two systems electrons and phonons, which are characterized by their temperatures and heat capacities T_e, c_e and T_{ph}, c_{ph}, respectively. The electron and the phonon systems are coupled through *e-ph* scattering. The underlying substrate is presented by phonons which are characterized by the bath temperature, T_0.

The 2-T model accounts for the critical angle of total phonon reflection at the interface between a film and a substrate by assigning to all phonons the same escape rate $\tau_{esc,\,g}^{-1}$ (see Section 2.4.3). This mean escape rate is less than the escape rate for phonons with incident angles $\Theta < \Theta_{max}$. In the 3-T model (Sec. 2.4.4.2) and the ray-tracing model (Sec. 2.4.4.3) total phonon reflection is accounted differently.

2-T model: Short-pulsed excitation

The solution of Eqs. (2.28) in time domain to short-pulsed excitation was derived in [86, 87]. The analytical expression describing instantaneous power (the shape) of the excitation pulse is given by $P_{RF}(t) = m^3 \xi^2 e^{-m\xi} E_0 / \tau_0$. For $m = 3.4$, τ_0 represents the full width at half maximum and E_0 represents the total pulse energy absorbed by the unit area of the film. With $P_{RF}(t)$ in this form, Eqs. (2.28) is a system of non-homogeneous differential equations of the first order. The solution of the system is a sum of homogeneous and non-homogeneous solutions. Solving Eqs. (2.28) we obtain time-dependent $T_e(\xi)$ and $T_{ph}(\xi)$ in the form

$$\frac{T_e(\xi) - T_0}{T_0} = A_1 \frac{\chi_1 + \Gamma_2 + \Gamma_3}{\Gamma_2} \exp(\chi_1 \xi) + A_2 \frac{\chi_2 + \Gamma_2 + \Gamma_3}{\Gamma_2} \exp(\chi_2 \xi) + Q_1(\xi) \exp(-m\xi),$$

$$\frac{T_{ph}(\xi) - T_0}{T_0} = A_1 \exp(\chi_1 \xi) + A_2 \exp(\chi_2 \xi) + Q_2(\xi) \exp(-m\xi), \tag{2.29}$$

with parameters given by

$$\chi_{1,2} = \frac{1}{2}\left(\Sigma_i^3 \Gamma_i \mp \sqrt{(\Sigma_i^3 \Gamma_i)^2 - 4\Gamma_1\Gamma_3}\right),$$

$$A_{1,2} = \pm\frac{\Gamma_2 E_0 m^3}{dc_e T_0}\frac{1}{(\chi_1 - \chi_2)(m + \chi_{1,2})^3},$$

$$Q_2 = \frac{\Gamma_2 E_0 m^3}{dc_e T_0}(a\xi^2 + b\xi + c), \tag{2.30}$$

$$Q_1 = \frac{E_0 m^3}{dc_e T_0}[(\Gamma_2 + \Gamma_3 - m)(a\xi^2 + b\xi + c) + 2a\xi + b],$$

$$a = \frac{1}{2\gamma_1\gamma_2}; \ b = \frac{\gamma_1 + \gamma_2}{(\gamma_1\gamma_2)^2}; \ c = \frac{\gamma_1^2 + \gamma_1\gamma_2 + \gamma_2^2}{(\gamma_1\gamma_2)^3}; \ \gamma_{1,2} = m + \chi_{1,2}.$$

Here in the case of double sign $\mp$ or $\pm$, the first index corresponds to the upper sign while the second to the lower. The voltage transient at the film, $U_{in}(\xi)$, is proportional to the change in the electron temperature, $T_e(\xi) - T_0$. The photoresponse measured with the TDP technique is unavoidably modified by the readout electronics (amplifiers, bias-T, cables, and oscilloscope) with the finite bandpass. It is represented by the transient $U_{out}(\xi)$. These two transients are connected through the Duhamel's integral as

$$U_{out}(\xi) = \int_0^\xi \dot{U}(\xi')h(\xi - \xi')\mathrm{d}\xi', \tag{2.31}$$

where $h(\xi)$ is the unit-step response function, i.e. the response of a readout system to a unit vertical voltage step at the input. This function characterizes the readout and can be adequately described as:

$$h(\xi) = \exp(2\sqrt{2}f_0\xi)\left[1 - \exp\left(-2\sqrt{2}f_C\xi\frac{P}{Q}\right)\right]\left[1 + \exp\left(-2\sqrt{2}f_C\xi\frac{Q}{P} + \frac{P}{Q}\right)\right]^{-1}, \tag{2.32}$$

where f_C and f_0 are upper and lower band-pass frequencies, respectively, P and Q are constants. The form of the unit-step response function is shown in Fig. 2.18. The inset in Fig. 2.18 zooms the rising edge. The parameter Q controls the delay of the function, $Q = 0$ corresponds to a zero delay. The parameter P controls the rise time of the function, at $P \to \infty$, the rise time $\to 0$.

Another important fact to be accounted for is the impedance mismatch between the sample and the readout line. The impedance mismatch results in ringing due to multiple reflections of the voltage transient. It can be simply simulated by adding a series of equidistant transients with identical shapes and decreasing magnitudes U_{in}, as

$$U_{in}(t) = (1 - r)\left[U(t) + \Sigma_{i=1}^N r^i U(t + i\Delta t)\right], \tag{2.33}$$

where $r = (R - R_0)/(R + R_0)$ is the reflection coefficient, R is the impedance of the sample, and $R_0 = 50\ \Omega$ is the impedance of the readout line. The interval Δt is defined by traveling time of the voltage transient between the sample and a plane of reflection in the transmission line (for instance, it can be an amplifier). We further use the formalism described by Eqs. (2.28 - 2.33) in Section 3.2.2 to fit voltage transients obtained with the TDP technique.
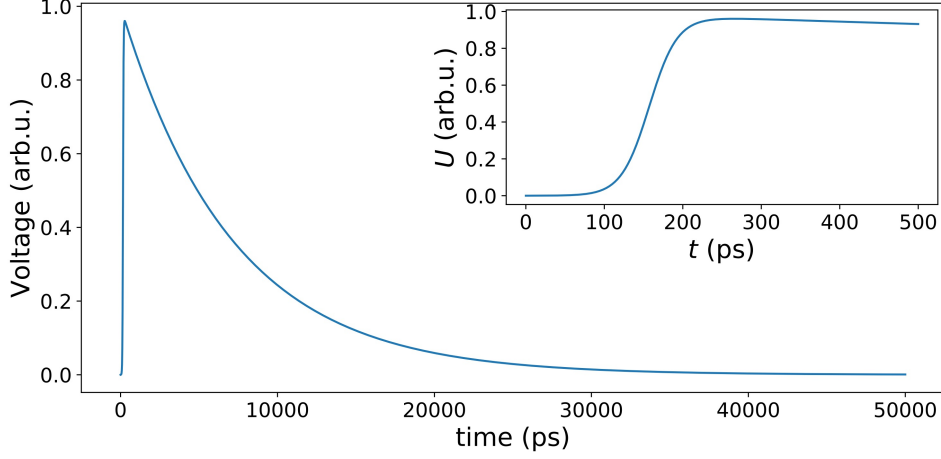
Figure 2.18: The transient characteristic of conventional electronics given by Eq. (2.32) with following parameters $f_C = 4.5$ GHz, $f_0 = 50$ MHz, $P = 4.4$ and $Q = 2.0$.

2-T model: Periodic excitation

Periodic excitation used in the AMAR and FDAM techniques can be mathematically described as $P_{RF}(t) = P_0 e^{-j\omega t}$. Here $\omega = 2\pi f$ is the circular frequency and P_0 is the radiation power absorbed per unit area of the film. The solution of Eq. (2.28) in the frequency domain in the form $\delta T_e(t) = \delta T_e(\omega)e^{-j\omega t}$ (here $\delta T_e(t)$ is the alternating part of the electron temperature) was obtained by Perrin and Vanneste in [88] as

$$\delta T_e(\omega) = P_0 \frac{1}{dc_e} \frac{\tau_2 \tau_3}{\tau_1} \left| \frac{(1 + j\omega\tau_1)}{(1 + j\omega\tau_2)(1 + j\omega\tau_3)} \right|, \tag{2.34}$$

with the characteristic times $\tau_1 = \tau_0/(\Gamma_2 + \Gamma_3)$ and $\tau_{2(3)} = \tau_0/\chi_{1(2)}$. Parameters $\Gamma_{2,3}$ are defined in the text after Eq. (2.28), and $\chi_{1,2}$, is given in Eq. (2.30). The spectrum of the sample photoresponse (Eq. (2.30)) crucially depends on the specific heat ratio c_e/c_{ph}. For instance, if $(c_e/c_{ph} + \tau_{EP}/\tau_{esc,\,g}) \gg 1$, Eq. (2.34) reduces to $\delta T_e(\omega) \approx P_0\tau_2(dc_e)^{-1}|(1 + j\omega\tau_2)^{-1}|$, with $\tau_2 \approx \tau_{EP} + \tau_{esc,\,g}\, c_e/c_{ph}$. Exactly this limiting case is valid for thin Nb films [89]. Although this limiting case was also used for thin NbN films in several works [90, 91], the required inequalities are not satisfied for NbN material. Indeed, the ratios c_e/c_{ph} obtained in [92] (for 5.5 nm NbN film at T_C) as well as in [93] all give $c_e < c_{ph}$. For NbN, the use of the limiting case would overestimate τ_{EP}. Therefore further in our study (Section 3.2.3) we use the full solution given by Eq. (2.34).

2.4.4.2   Three-temperature (3-T) model

As well as the 2-T model, the 3-T model is applied for data analysis in photoresponse measurements. Qualitatively, the 3-T model describes the energy transfer as follows (the energy diagram is schematically shown in Fig. 2.19). The energy absorbed in the electronic subsystem increases the electron temperature according to the electron heat capacity, c_e. The electron energy flows to two phonon subsystems via *e-ph* scattering, on a time scale τ_{EP}. Phonons are divided into
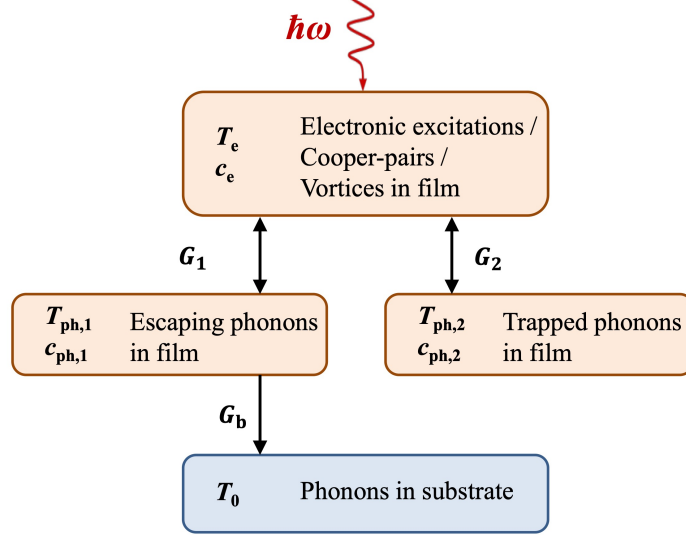
38

Figure 2.19: Energy balance diagram in a thin metal film (or superconducting film in the resistive state) on a dielectric substrate. The film is presented by three subsystems, electrons and two groups of phonons. Each subsystem is characterized by its temperature and heat capacity, T_e, c_e and T_{ph}, c_{ph}, respectively. The electron and phonon subsystems are coupled through *e-ph* scattering. Phonon subsystems are different in terms of their coupling to the substrate (ability directly to leave to the substrate). The phonon subsystem (1) is coupled to the substrate and is called the escaped phonons, the subsystem (2) is decoupled from the substrate and called the trapped phonons. The underlying substrate is presented by phonons which are characterized by the bath temperature, T_0.

two subsystems by their ability to pass through the film/substrate interface (see Section 2.4.3). We refer to phonons inside the cone defined by the critical angle as escaped phonons (group 1). Phonons outside the cone are referred to as trapped phonons (group 2). The energy transferred to phonons increases the temperature, T_{ph}, of a corresponding phonon subsystem according to its heat capacity, c_{ph}. Each phonon subsystem is characterized by its temperature and heat capacity. Only escaped phonons are coupled to the substrate, while trapped phonons are decoupled from the substrate. We neglect conversion between two phonon groups. Energy from escaped phonons flows to the surrounding via phonon escaping on a time scale τ_{esc}, and also back to electrons via *ph-e* scattering on a time scale τ_{PE}. Energy from trapped phonons flows out of the film only indirectly via sequential *ph-e* and *e-ph* scattering events. Forward *e-ph* and backward *ph-e* energy flows are connected through the principle of detailed balance. The principle of detailed balance requires in equilibrium the equality between forward and backward energy flows, $c_e/\tau_{EP} = c_{ph}/\tau_{PE}$. The equations of the 3-T model in a general form can be written as

$$
\begin{cases}
c_e \dfrac{dT_e(t)}{dt} = -G_1[T_e(t) - T_{ph,1}(t)] - G_2[T_e(t) - T_{ph,2}(t)] + \dfrac{1}{d}P_{RF}(t) + P_{dc} \\
c_{ph,1} \dfrac{dT_{ph,1}(t)}{dt} = G_1[T_e(t) - T_{ph,1}(t)] - G_b[T_{ph,1}(t) - T_0] \\
c_{ph,2} \dfrac{dT_{ph,2}(t)}{dt} = G_2[T_e(t) - T_{ph,2}(t)]
\end{cases}
\tag{2.35}
$$

The total thermal conductance for *e-ph* scattering is $G = G_1 + G_2 = c_e/\tau_{EP}$, where $G_1 = G\frac{c_{ph,1}}{c_{ph}}$ and $G_2 = G\frac{c_{ph,2}}{c_{ph}}$. The ratio $c_{ph,1}/c_{ph}$ defines the fraction of escaped phonons with angles

$\Theta > \Theta_{max}$. A simple calculation of this fraction yields $c_{ph,1}/c_{ph} = 1 - \cos(\Theta_{max})$. The total heat capacity of phonons is $c_{ph} = c_{ph,1} + c_{ph,2}$, $G_b = c_{ph,1}/\tau_{esc}$ is the thermal conductance describing the energy exchange between escaped phonons (group 1) and the thermal bath. T_e, $T_{ph,1}$, $T_{ph,2}$, and T_0 are temperatures of the corresponding systems. Eqs. (2.35) are written for small deviations from equilibrium: $P(t) = P_0 + \delta P(t)$, $T_e(t) = T_{e,0} + \delta T_e(t)$, $T_{ph,1}(t) = T_{ph,10} + \delta T_{ph,1}(t)$, $T_{ph,2}(t) = T_{ph,20} + \delta T_{ph,2}(t)$, $T_{e,0} \approx T_{ph,10} \approx T_{ph,20} \approx T_0$, and $|\delta T_e(t)| \to 0$, $|\delta T_{ph,1}(t)| \to 0$ and $|\delta T_{ph,2}(t)| \to 0$. The solution of Eqs. (2.35) depends on the excitation form P_{RF}.

In a similar form, the 3-T model was developed in [94] and, without neglecting the phonon conversion, was proposed in [81]. In [95], authors also developed a 3-T model, where phonons were divided into two groups: acoustic and optical phonons.

3-T model: Periodic excitation

Here, we consider the system of Eqs. (2.35) with periodic excitation in the form $P_{RF}(t) = P_0 e^{-j\omega t}$, where $\omega = 2\pi f$ is the circular frequency and P_0 is the radiation power absorbed per unit area of the film. Usually in measurements the magnitude of P_{dc} is kept extremely small and therefore can be neglected. With redefined constants, Eq. (2.35) can be written as

$$
\begin{cases}
\dfrac{dT_e(t)}{dt} = -Q_1 Q_4 [T_e(t) - T_{ph,1}(t)] - Q_1(1 - Q_4)[T_e(t) - T_{ph,2}(t)] + \dfrac{1}{dc_e} P_{RF}(t) \\
\dfrac{dT_{ph,1}(t)}{dt} = Q_2 [T_e(t) - T_{ph,1}(t)] - Q_3 [T_{ph,1}(t) - T_0] \\
\dfrac{dT_{ph,2}(t)}{dt} = Q_2 [T_e(t) - T_{ph,2}(t)]
\end{cases}
\tag{2.36}
$$

where $Q_1 = 1/\tau_{EP}$, $Q_2 = Q_1 c_e/c_{ph}$, $Q_3 = 1/\tau_{esc}$ and $Q_4 = c_{ph,1}/c_{ph}$. This system can be solved using Fourier transformation which turns the system of coupled differential equations into a system of linear algebraic equations. The solution of the system (2.36) in the form $\delta T_e(t) = \delta T_e(\omega) e^{-j\omega t}$, where $\delta T_e(t)$ is the alternating part of the electron temperature is given by

$$
\delta T_e(\omega) = P_0 \frac{1}{dc_e} \left| \left(j\omega + Q_1 - \frac{Q_1 Q_2 Q_4}{j\omega + Q_2 + Q_3} - \frac{Q_1 Q_2 (1 - Q_4)}{j\omega + Q_2} \right)^{-1} \right|.
\tag{2.37}
$$

This solution depends on four independent parameters: the *e-ph* energy relaxation time, τ_{EP}, the escape time of escaped phonons (group 1), τ_{esc}, the ratio between electron and phonon heat capacities, c_e/c_{ph}, and the ratio of heat capacity of escaped phonons to the total phonon heat capacity, $c_{ph,1}/c_{ph}$. Taking in Eq. (2.35) $c_{ph,1}/c_{ph} = 1$, one arrives at $G_1 = G$ and $G_2 = 0$, that corresponds to the conventional 2-T model.

2.4.4.3 Phonon ray-tracing model

Here we describe a phonon ray-tracing model which was developed by Eisenmenger et al. [82] for temperatures well below T_C. For the first time, to the best of our knowledge, we extended the phonon ray-tracing model to the temperature range in the vicinity of T_C. This section is placed here for the sake of completeness of Chapter 2.
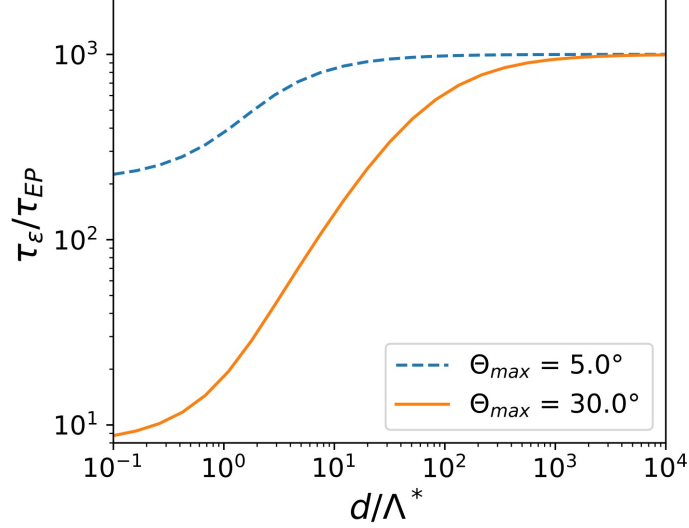
Figure 2.20: Computed ratios $\tau_\varepsilon/\tau_{EP}$ as a function of d/Λ_{PE} with Eq. (2.38). Both curves were computed with the same $\Lambda_{PE} = 10$ and $\Lambda_{bulk}/\Lambda_{PE} = 1000$ and different angles of total phonon reflection, $\overline{\Theta}_{max} = 5°$ (blue dashed curve) and $\overline{\Theta}_{max} = 30°$ (orange solid curve).

The reduced ability of phonons to transfer the energy from electrons to the substrate, the so-called phonon trapping effect, was considered by Eisenmenger et al. [82]. The effect of phonon trapping slows down the relaxation rate of the electron energy. The authors of [82] aimed to describe the difference between the experimental recombination lifetime of quasiparticles measured at temperatures well below T_C and the intrinsic recombination lifetime. The following approach was used. The authors found the mean lifetime of a phonon flux within the film by tracing the flux over several scattering events with the film/substrate boundary. Assuming specular boundary reflection, phonons reflected at angles larger the angle of total reflection, $\Theta > \overline{\Theta}_{max}$, propagate within the film. These phonons can leave the film via sequential reabsorption and reemission within the cone defined by the critical angle. Phonons can be absorbed either by Cooper pairs or phonon losses in the bulk material. The authors of [82] considered two mean free paths of phonons with energies exceeding the binding energy of a Cooper pair. They are the mean free path for reabsorption of a phonon by a Cooper pair and a mean free path for phonon losses in the bulk of the film. For temperatures close to the transition temperature, the binding energy of a Cooper pair (energy gap) is negligibly small that eliminates the difference between scattering rates of phonons on pairs and quasiparticles. The intrinsic recombination time of quasiparticles appears as the *e-ph* energy relaxation time, τ_{EP}, while the experimental recombination time becomes the decay time of the photoresponse, τ_ε. Correspondingly, the mean free path for reabsorption of the phonon by a Cooper pair becomes the mean free path for *ph-e* scattering, Λ_{PE}, and Λ_{bulk} denotes the mean free path for bulk phonon losses.

According to our redefinitions, Eq. (51) from [82], which is valid for critical angles

41

$\overline{\Theta}_{max} \leqslant 30°$, becomes

$$\frac{\tau_\varepsilon}{\tau_{EP}} = \left(1 + \frac{\Lambda_{bulk}}{\Lambda_{PE}}\right)\left(1 + \frac{1}{4}\frac{\Lambda_{bulk}}{\Lambda_{PE}}\frac{\Lambda^*}{d}H_{av}\right)^{-1}, \qquad (2.38)$$

where $1/\Lambda^* = 1/\Lambda_{PE} + 1/\Lambda_{bulk}$, $H_{av} = (sin\overline{\Theta}_{max})^2\overline{\eta}_\Theta(1-z)/(1-[1-\overline{\eta}_\Theta]z)$ and $z = \exp(-2d/\Lambda^*)$. The inequality $\Lambda_{bulk} \gg \Lambda_{PE}$ holds for NbN films studied in the present work, that results in the equality $\Lambda^* = \Lambda_{PE}$. In Fig. 2.20 we illustrate the dependence $\tau_\varepsilon/\tau_{EP} = f(d/\Lambda_{PE})$ for two critical angles $\overline{\Theta}_{max} = 30°$ (typical for many film/substrate pairs) and $\overline{\Theta}_{max} = 5°$ (implies very bad acoustic matching). As it is seen in Fig. 2.20, one can define three characteristic ranges of the thickness dependence of the experimental decay time $\tau_\varepsilon(d)$. For very small d as compared to Λ_{PE}, the ratio $\tau_\varepsilon/\tau_{EP}$ saturates and reaches a value defined by $\overline{\Theta}_{max}$. Further, in the limit $d > \Lambda_{PE}$, τ_ε grows linearly with d. Finally, for very large d, $d \gg \Lambda_{bulk}$, the ratio $\tau_\varepsilon/\tau_{EP}$ saturates and reaches the value defined by Λ_{bulk}. It is important to mention here that the ray-tracing model in the form of Eq. (2.38) is valid for $\tau_{EP} \gg \tau_{PE}$ (applying the principle of detailed balance it results in $c_e \gg c_{ph}$).

2.4.4.4   Comparison between 2-T, 3-T, and phonon ray-tracing models

This section is devoted to a comparative analysis of the 2-T, 3-T, and phonon ray-tracing models, which were described in subsections 2.4.4.1, 2.4.4.2 and 2.4.4.3, respectively. To the best of our knowledge, such a comparison has not been done before. However, we place this section here for the sake of completeness of Chapter 2. All three models take into account the effect of total internal reflection occurring for phonons incident at the film/substrate interface. The critical angle for total internal reflection $\overline{\Theta}_{max}$, together with the transmission coefficient η_0, is described in the framework of the acoustic mismatch model (AMM) (see Section 2.4.3).

The 2-T model accounts for the effect of total phonon reflection via the total weighted escape time, $\tau_{esc,g} = 4d/(\overline{\eta}\,\overline{u})$, where the same transmission coefficient $\overline{\eta}$ is assigned to phonons with all incident angles (see Section 2.4.3). The solution of the 2-T problem for periodic excitation (Eq. (2.34)) is a decay function in the frequency domain, $\delta T_e(\omega)$, of three independent parameters $\tau_{esc,g}$, τ_{EP}, and c_e/c_{ph}. The decay time τ_ε of the function $\delta T_e(\omega)$ can be found using the relation $\delta T_e^2(1/\tau_\varepsilon) = \frac{1}{2}\delta T_e^2(0)$ (for an example see the right graph in Fiq. 2.16(a)). One can differently define $\tau_{esc,g} = 4d/(\eta_0\overline{u}\sin(\overline{\Theta}_{max})^2)$, where η_0 is the transmission coefficient at zero angle. (see Section 2.4.3). Therefore the decay time τ_ε provided by the 2-T model depends on the following parameters $\tau_\varepsilon = f(\tau_{EP};\ c_e/c_{ph};\ \eta_0;\ \overline{\Theta}_{max};\ d;\ \overline{u})$.

The 3-T model differently accounts for the effect of total phonon reflection. Phonons with angles of incidence $< \overline{\Theta}_{max}$ can quickly leave the film. The escape time for them is $\tau_{esc} = 2d/(\eta_0\overline{u})$. For phonons with angles of incidence $> \overline{\Theta}_{max}$ the transmission coefficient is zero and, consequently, $\tau_{esc} \to \infty$. The 3-T model in the form of Eqs. (2.35) neglects conversion between phonons. The solution of the 3-T problem for periodic excitation (Eq. (2.37)) is a decay function $\delta T_e(\omega)$ in the frequency domain of the following parameters τ_{esc}, τ_{EP}, c_e/c_{ph} and $c_{ph,1}/c_{ph}$. We
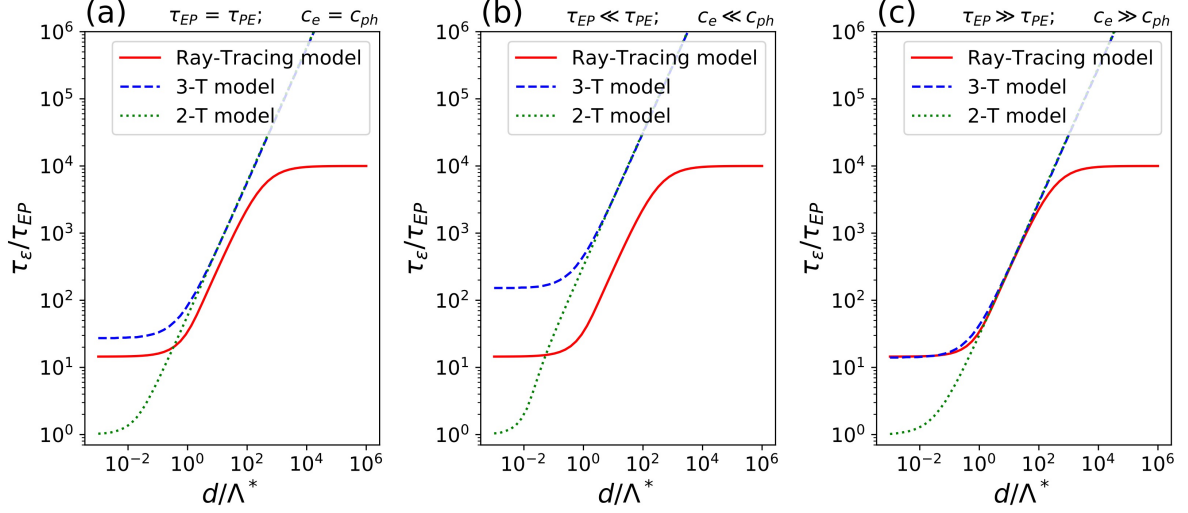
Figure 2.21: Calculated ratio $\tau_\varepsilon/\tau_{EP}$ as a function of d/Λ^* for fixed $\Lambda^* \approx \Lambda_{PE} = 1$ nm, $\Lambda_{bulk} = 10^5$ nm, $\overline{\Theta}_{max} = 21.8°$, $\eta_0 = 0.985$, $\overline{u} = 2.5$ nm/ps, $\overline{\eta} \approx \eta_0 \sin(\overline{\Theta}_{max})^2$, $\tau_{PE} = 0.4$ ps, and different τ_{EP} a) 0.4 ps, b) 0.04 ps, c) 4 ps.

define the ratio $c_{ph,1}/c_{ph}$ as a fraction of escaped phonons inside the critical cone, that is given by $1 - \cos\overline{\Theta}_{max}$. The decay time τ_ε of $\delta T_e(\omega)$ can be found in the same way as for the 2-T model. In analogy to the 2-T model, the decay time in the 3-T model depends on the very same parameters $\tau_\varepsilon = f(\tau_{EP};\ c_e/c_{ph};\ \eta_0;\ \overline{\Theta}_{max};\ d;\ \overline{u})$.

The phonon ray-tracing model accounts for the effect of phonon trapping and neglects phonon conversion. The model additionally accounts for phonon losses in the bulk of the film via the corresponding mean free path Λ_{bulk}. The solution of the ray-tracing model is the decay time (Eq. (2.38)) which is a function of τ_{EP}, η_0, $\overline{\Theta}_{max}$, d, $\overline{u}$, Λ_{bulk} and Λ_{PE}. The mean free path for *ph-e* relaxation is given by $\Lambda_{PE} = \overline{u}\tau_{PE}$. Applying the principle of detailed balance, we arrive at $\Lambda_{PE} = \overline{u}\tau_{EP}/(c_e/c_{ph})$. If the film thickness is small enough one can neglect the bulk losses (it is the case of the present study). Therefore, the decay time depends on the very same parameters for all three models

$$\tau_\varepsilon = f\left(\tau_{EP};\ \frac{c_e}{c_{ph}};\ \eta_0;\ \overline{\Theta}_{max};\ d;\ \overline{u}\right). \tag{2.39}$$

In Fig. 2.21 we show the calculated ratio $\tau_\varepsilon/\tau_{EP}$ vs. d/Λ^* for all three models. The used parameters are specified in the caption. In the limit $\Lambda_{PE} \ll \Lambda_{bulk}$, we arrive at $\Lambda^* \approx \Lambda_{PE}$ (we remind that $1/\Lambda^* = 1/\Lambda_{PE} + 1/\Lambda_{bulk}$, see subsection 2.4.4.3).

Peculiarities of these three models can be summarized as follows. (i) The ray-tracing model in the form of Eq. (2.38) is valid in the limit $\tau_{EP} \gg \tau_{PE}$ (equivalently, $c_e \gg c_{ph}$) and $\overline{\Theta}_{max} \leq 30°$. In this limit, the solution coincides with the solution of the 3-T model for small and middle thicknesses (Fig. 2.21(c)). (ii) In the limit of very thick films where bulk losses are dominant, $d \geq \Lambda_{bulk}$, the phonon ray-tracing model results in saturation of the ratio $\tau_\varepsilon/\tau_{EP}$, while the
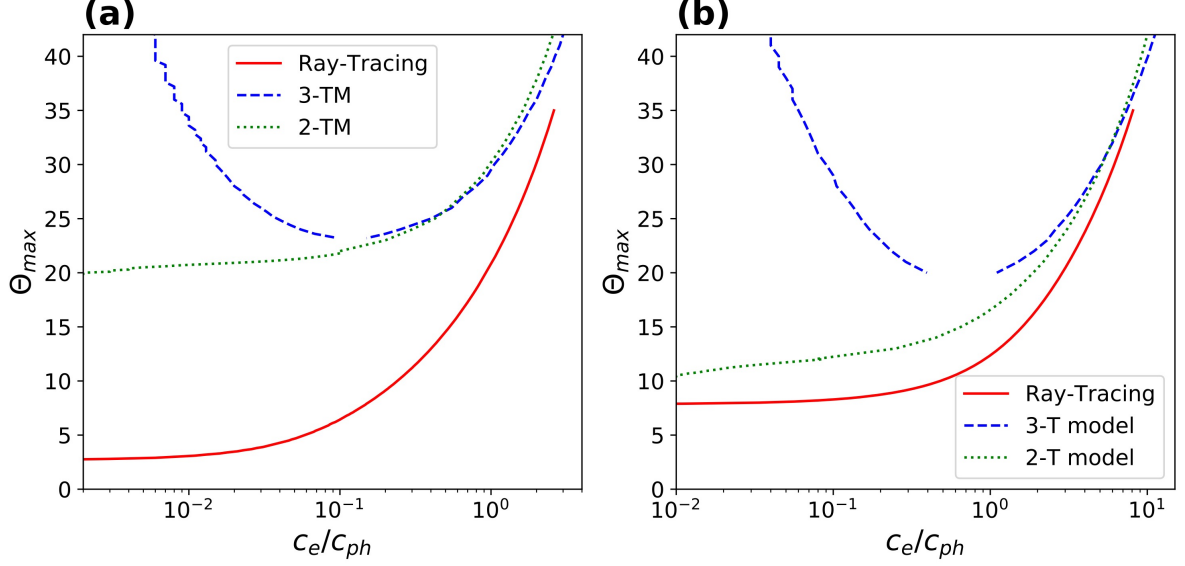
Figure 2.22: Calculated pairs of c_e/c_{ph} and $\overline{\Theta}_{max}$ for fixed parameters τ_ε, τ_{EP}, η_0, d and $\overline{u}$ obtained via Eq. (2.39) for three models specified in the legend. (a) $\tau_\varepsilon = 421$ ps, $\tau_{EP} = 0.46$ ps, $\eta_0 = 0.985$, $d = 33.2$ nm. (b) $\tau_\varepsilon = 124.3$ ps, $\tau_{EP} = 1.16$ ps, $\eta_0 = 0.985$, $d = 3.15$ nm. In both cases $\overline{u} = 2.54$ nm/ps. These parameters correspond to the thickest (a) and the thinnest (b) films of K-series studied in Section 3.2.3.

2-T and 3-T models result in the linear thickness dependence. This is because the 2-T and 3-T models do not account for bulk losses. (iii) In the limit of very thin films, $d/\Lambda^* \ll 1$, and in the presence of the critical angle, the 2-T model results in $\tau_\varepsilon \to \tau_{EP}$, while the 3-T and ray-tracing models lead to a saturated value of $\tau_\varepsilon > \tau_{EP}$. This is because the 2-T model neglects implicitly phonon trapping which occurs when the mean free path of phonons becomes larger than the film thickness. (iv) In the limit of relatively thick films, $d \geq \Lambda^*$, the solutions of the 2-T and 3-T model coincide.

We continue our analysis of the models with the following. In accordance with Eq. (2.39), for each model we find such pairs c_e/c_{ph} and $\overline{\Theta}_{max}$ that satisfy the fixed values of τ_ε, τ_{EP}, η_0, d, and $\overline{u}$. Fig. 2.22(a) and (b) shows to two sets of fixed parameters τ_ε, τ_{EP}, d, $\overline{u}$ for different pairs of c_e/c_{ph} and $\overline{\Theta}_{max}$. Values of the parameters are specified in the caption, they were taken for the thickest and thinnest films of K-series studied in Section 3.2.3. As seen in Fig. 2.22, the 3-T model provides two ratios c_e/c_{ph} for the same $\overline{\Theta}_{max}$. The reason for this is the following. Fig 2.23 shows two solutions $\delta T_e(\omega)$ obtained in the framework of the 3-T model (Eq. (2.37)), which differ only by the ratio c_e/c_{ph}. The difference between the computed curves is pronounces at small magnitudes $\delta T_e(\omega)$, while τ_ε is defined at -3 dB level, where the curves coincide exhibiting the same decay time. As seen in Fig. 2.22, in the limit $c_e \gg c_{ph}$, the pairs of c_e/c_{ph} and $\overline{\Theta}_{max}$ for the phonon ray-tracing model are similar to those for the 2-T model and one solution of the 3-T model. This is because the ray-tracing model is valid in this limit. For the same $\overline{\Theta}_{max}$, the 3-T model offers two c_e/c_{ph} solutions which cannot be distinguished. At large $\overline{\Theta}_{max}$, the pairs of c_e/c_{ph} and $\overline{\Theta}_{max}$ for the 2-T model and for the 3-T model are approximately equal. This is because the increase of $\overline{\Theta}_{max}$ results in the decrease of the fraction of trapped
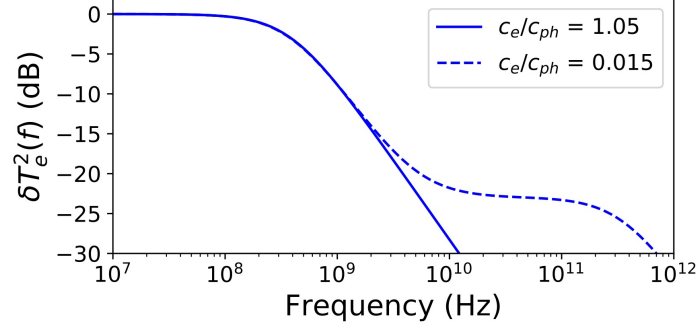
Figure 2.23: Calculated pairs of c_e/c_{ph} and $\overline{\Theta}_{max}$ for fixed parameters τ_ε, τ_{EP}, η_0, d, $\overline{u}$, and $\overline{\Theta}_{max}$ obtained via Eq. (2.39) for three models specified in the legend. (a) $\tau_\varepsilon = 421$ ps, $\tau_{EP} = 0.46$ ps, $\eta_0 = 0.985$, $d = 33.2$ nm. (b) $\tau_\varepsilon = 124.3$ ps, $\tau_{EP} = 1.16$ ps, $\eta_0 = 0.985$, $d = 3.15$ nm. In both cases $\overline{u} = 2.54$ nm/ps. These parameters correspond to the thickest (a) and the thinnest (b) films of K-series studied in Section 3.2.3.

phonons which are not accounted for in the 2-T model. Consequently, the solution of the 2-T model approaches one solution of the 3-T model.

2.5   Summary

In this chapter, we presented the phenomenological description of the single-photon detection mechanism in a superconducting nanowire. We introduced a definition of the timing jitter in SNSPD and discussed extrinsic and intrinsic sources of the jitter. We considered the microscopic mechanism of the intrinsic jitter in the framework of the microscopic 2-d model of the hot spot. The use of the superconducting nanowire in SNSPDs implies a non-equilibrium state. The microscopic mechanism of the intrinsic jitter points out on the internal link between the jitter and the *e-ph* energy relaxation and phonon escape times, which are responsible for the relaxation of the electron energy. These and other physical parameters present in the model were determined. Two appropriate experimental techniques, magnetoconductance and photoresponse, were chosen for the further study of inelastic electron-phonon scattering and energy relaxation in NbN films. A detailed description of these techniques was given. This includes a description of standard setups, requirements for the sample (geometrical size, electrical impedance, etc.), and also models which are used for the analysis of experimental data. The equations derived in the analytical form will be further used to fit experimental data in Chapter 3.

Chapter 3

Experimental results: Electron-energy relaxation and timing jitter

The delay time between the photon absorption and the formation of the normal domain varies from one detection event to another resulting in jitter. Microscopic models show that the intrinsic jitter and the delay time are connected, i.e. the longer the delay, the larger the jitter. The hotspot formation contributes a long part to the delay time. Among the parameters that control the emergence time of the hot spot, the most important are the electron-phonon scattering time and the phonon escape time. Therefore, understanding the details of electron energy relaxation is of importance here. This chapter contains the experimental results and interpretation regarding electron energy relaxation (Section 3.2) and timing jitter (Section 3.3). To compare our results with theoretical predictions, we also provide a comprehensive characterization of the object under study. Thin (< 10 nm) and narrow (~ 100 nm) NbN nanowires studied here are fabricated from disordered superconducting films with high square resistance (> 300 Ω/sq), small diffusion coefficient (~ 0.5 cm^2/s), and reduced dimensionality. We address the complexity of the films, that definitely modifies their microscopic properties, in Section 3.1. Section 3.2 is devoted to an experimental study of electron energy relaxation. We investigate the processes of inelastic scattering and evaluate their strengths by means of magnetoconductance (see Section 3.2.1). Among those, we focus on electron-phonon scattering. Then in Section 3.2.2, we study the relaxation of the electron energy by means of photoresponse. Applying several experimental techniques and models, we reveal how the nanowire thickness affects the energy outflow that is discussed in Section 3.2.4. The chapter continues with an experimental investigation of the jitter (Section 3.3) and concludes with a summary.

3.1   Specimens and parameters

Specimens

We studied NbN films from two series (M- and K0-series). The films of M-series were fabricated on Si/SiO$_2$ substrate by magnetron sputtering. Their thicknesses ranged from 5 to 9.5 nm. Magnetoconductance measurements (Section 3.2.1) were carried out with non-structured approximately squared 1×1 cm^2 films. Photoresponse measurements to pulsed excitation (Section 3.2.2) were carried out with the same films which were shaped in the form of microbridges. A film of K0-series was fabricated on an Al$_2$O$_3$ substrate by magnetron sputtering. This film was structured in a nanowire with a length of 40 μm, a nominal width of 100 nm, and a thickness of 5 nm. The width and thickness of the wire were chosen to be similar to those utilized by a practical SNSPDs. Patterning was done by the electron-beam lithography over a standard positive-tone PMMA (Polymethyl Methacrylate) resist in the negative lithographic process. This process results in the improvement of the fabrication quality and superconducting characteristics of nanowires [96]. Jitter measurements were carried out with the nanowire of K0-series (see Section 3.3).

Physical parameters of described specimens were derived by carrying out magneto-transport measurements. The measurements were performed in a Physical Property Measurement System (PPMS from Quantum Design). The applied bias currents were extremely small to avoid heating. The square resistance, R_S, was measured with a four-point van der Pauw method [97]. This method is generally used to measure R_S of arbitrary shaped two-dimensional samples, to eliminate geometric differences between them. Additionally, to eliminate the inhomogeneity of samples, the resistances measurements were repeated by changing current and voltage terminals clockwise four times.

Fig. 3.1 shows with symbols experimental dependences $R_S(T)$ for four NbN films of M-series of different thicknesses recorded in zero magnetic field. As seen in the inset, the R_S of each film increases with lowering the temperature from 300 K down to 20 K. Such an increase in the resistance is most likely due to due to Anderson localization. At approximately 20 K, the square resistance reaches its maximum value. We refer to this value as R_{SN}. With further lowering of the temperature, the R_S drops to zero within a finite transition region. The finite transition region is caused by superconducting fluctuations (see subsection 2.4.1).

The temperature dependence of R_S at zero magnetic field in the vicinity of the superconducting transition is well described by the theory of fluctuation conductivity of Aslamazov and Larkin (AL) [56] and Maki and Thompson (MT) [64, 65]. For 2-d films (the dimensionality of the films under study is examined in Section 3.1.1), it is given by

$$R_S(T) = \left[\frac{1}{R_{SN}} + A_{2d} \frac{1}{16} \frac{e^2}{\hbar \ln(T/T_C)} \right]^{-1},$$ (3.1)

where $\hbar$ is the reduced Planck constant, e is the elementary charge. We fit the experimental dependences $R_S(T)$ with Eq. (3.1) in a very narrow temperature range where the inequality
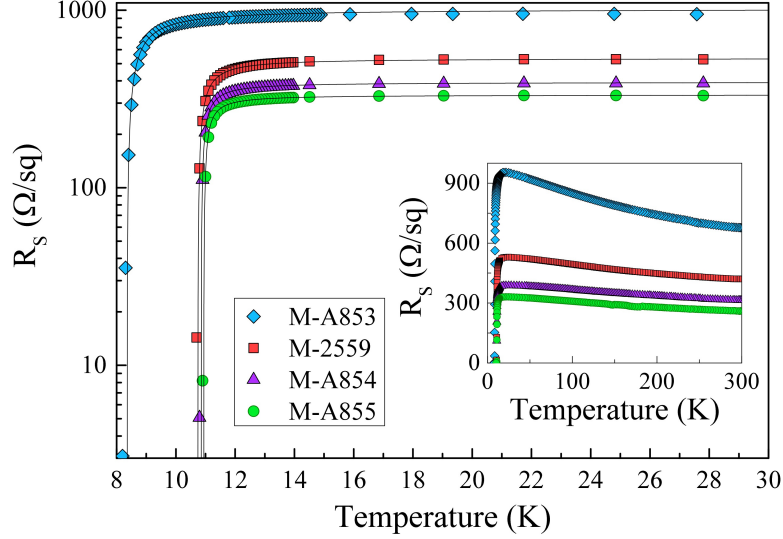
Figure 3.1: Temperature variation of the square resistance around the superconducting transition for four exemplary films with different thicknesses. Experimental data are shown with symbols. Solid lines represent extrapolations of the best fits obtained with Eq. (3.1). The inset shows resistances in a larger temperature range up to 300 K.

$\ln(T/T_C) \leq 1$ holds. Parameters T_C, R_{SN}, and A_{2d} were used as fitting parameters. Solid curves shown in Fig. 3.1(a) are extrapolations of the obtained fit to a broader temperature range. The best fit values of the normal state resistance are 540.1 Ohm/sq for M-2559, 1032 Ohm/sq for M-A853, 395.2 Ohm/sq for M-A854, and 335.2 Ohm/sq for M-A855. These values are slightly larger than those measured at 20 K. The fitting parameter A_{2d} for all films varies between 1.9 – 2.6. The best fit values of T_C are listed in Table 3.1 which also contains the values of R_{SN} measured at 20 K. Highly resistive 2-d films exhibit two transition temperatures due to the presence of two types of excitation: topological (magnetic vortices) and electronic (quasiparticles). The resistance of a superconducting film appears when there are free vortices which move under the Lorentz force imposed by the current perpendicular to the direction of the current. The emergence of free vortices sets in at the BKT (Berezinskii-Kosterlitz-Thouless) temperature, T_{BKT}. With increasing the temperature, the density of free vortices increases resulting in an exponential rise of the resistance beyond the T_{BKT}. In general, the T_{BKT} is close to but below the BCS mean-field transition temperature, T_C. The mean-field transition temperature controls the energy gap and does not cause the emergence of resistance. A larger value of R_{SN} leads to a lower value of the T_{BKT} compared to T_C. For NbN film of $R_{SN} = 431$ Ohm/sq these temperatures are related as $T_{BKT} = 0.85 T_C$ [98]. Anyway, right above the superconducting transition, our experimental $R_S(T)$ dependences are well described by AL and MT fluctuations.

We applied an external magnetic field perpendicularly to the film surface and recorded $R_S(T)$ at a set of fields for each specimen (Fig. 3.2). The preset field was taken as the second critical magnetic field, B_{C2}, at the temperature at which $R_S = R_{SN}/2$. From these measurements, we obtained temperature dependences of the B_{C2} at temperatures $T < T_C$. The linear part of the
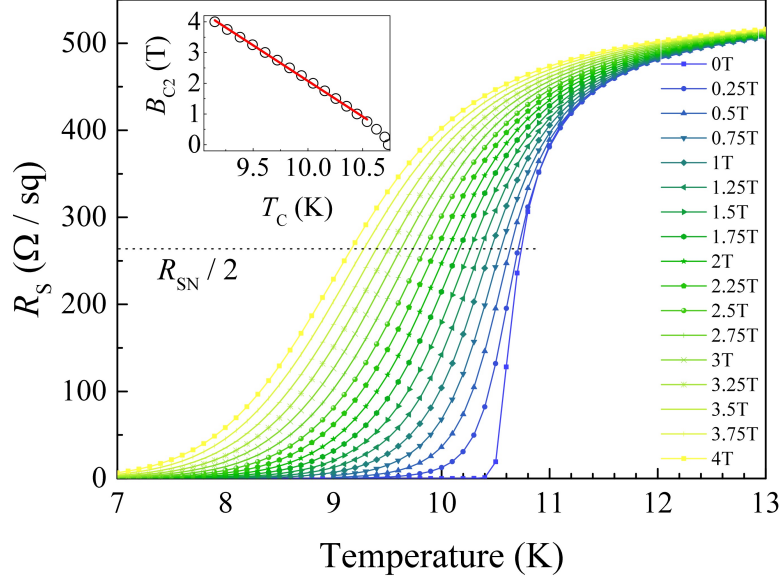
Figure 3.2: Temperature variation of the square resistance at different magnetic fields for specimen M-2259. Solid lines are to guide the eyes. The dotted line shows the $R_{SN}/2$ level which was used to determine the temperature dependence of the second critical magnetic field, B_{C2}. The inset shows the $B_{C2}(T)$ dependence, a linear part of which was used to compute the diffusion coefficient D with Eq. (3.2) and $B_{C2}(0)$ at zero temperature.

$B_{C2}(T)$ dependence was used to compute the electron diffusion coefficient as

$$D = \frac{4k_B}{\pi e} \left(\frac{\mathrm{d}B_{C2}}{\mathrm{d}T} \right)^{-1}, \tag{3.2}$$

where k_B is the Boltzmann constant.

The total density of electron states (two spin density) at the Fermi level, $N(0)$, can be derived from the Einstein-Smoluchowski equation [99, 100] as follows

$$N(0) = \frac{1}{e^2 R_{SN} dD}. \tag{3.3}$$

Values of D and $N(0)$ are listed in Table 3.1.

The second critical magnetic field at zero temperature, $B_{C2}(0)$, can be obtained by linear extrapolation of the experimental $B_{C2}(T)$ dependences to zero temperature. However, this certainly overestimates the real second critical field at zero temperature. To obtain more realistic values in the dirty limit, $B_{C2}(0)$ must be multiplied with a factor of 0.69 [101, 102]. According to the Ginzburg-Landau (GL) model, the second critical field is connected with the superconducting coherence length, ξ, and the magnetic flux, $\Phi_0 = h/2e$, as follows

$$B_{C2}(T) = \frac{\Phi_0}{2\pi\xi^2(T)}. \tag{3.4}$$

Therefore, the GL coherence length at zero temperature is

$$\xi(0) = \sqrt{\frac{\Phi_0}{2\pi 0.69 B_{C2}(0)}}, \tag{3.5}$$

Table 3.1: Parameters of studied NbN films. R^{300K}/R^{20K} is the ratio of square resistances at 300 and 20 K, $N(0)$ is the total (two spin) density of states for electrons at the Fermi level.

Sample (film)	d (nm)	T_C (K)	R_{SN} (Ω/sq)	D (cm^2/s)	$N(0)$ (eV^{-1}m^{-3})	R^{300K}/R^{20K}	$B_{C2}(0)$ (T)	$\xi(0)$ (nm)
M-2259	5.0	10.74	529.5	0.474	4.98×10^{28}	0.793	25.24	4.35
M-A853	6.4	8.35	954.0	0.339	3.02×10^{28}	0.709	27.77	4.15
M-A854	7.5	10.84	387.9	0.453	4.74×10^{28}	0.809	26.62	4.23
M-A855	9.5	10.94	330.6	0.418	4.75×10^{28}	0.788	28.99	4.06
K0	5.0	12.55	260.0	0.560	8.58×10^{28}	0.960	27.20	4.80

where $B_{C2}(0)$ was obtained by linear extrapolation. Values of $B_{C2}(0)$ and $\xi(0)$ are listed in Table 3.1.

As seen from Table 3.1, films M-2259, -A854, and -A855 have similar electron diffusion coefficients, transition temperatures, and electron densities of states. These parameters are noticeably smaller for film M-A853. Moreover, this film has a much larger square resistance (and resistivity $\rho_{SN}d$) as compared to others. Such a difference in parameters is evidence that film M-A853 is characterized by a higher degree of disorder compared to other films of M-series. The Ioffe-Regel parameter, $k_F l_e$ (k_F is the wave vector of electrons at the Fermi energy), estimated for films M-2259, M-A854, and M-A855 as $k_F l_e = 3meD/\hbar$ varies from 1.08 to 1.22. This characterizes these films as strongly disordered. It has been shown [103, 104] that with the increase of disorder, in the limit $k_F l_e \sim 1$, a homogeneously disordered superconductor becomes a granular system where superconducting grains (islands) are immersed in an insulating sea and connected by Josephson coupling. More likely, the film M-A853 with $k_F l_e = 0.88$ corresponds to this case. This film is close to the superconducting-insulator transition and may additionally have an enhanced degree of granularity. The emergence of inhomogeneities in NbN films with lowering the thickness was experimentally investigated in [105].

Although the exact composition of our NbN films is unknown, it can be estimated. In [106, 107, 108], the authors examined how the transition temperatures change with the compositions (N/Nb $= x$) of NbN$_x$ films. They found that films with nearly stoichiometric compositions (x $= 1$) exhibit higher transition temperatures and with increasing nitrogen compound, both the sheet resistance, R_S^{20K}, and the ratio R_S^{300K}/R_S^{20K} increase. The author of [109] (Chapter 3 there) investigated the influence of deposition conditions of thin NbN films, namely the discharged current, on their superconducting and transport properties (such as T_C, R_{SN}, R_S^{300K}/R_S^{20K}). Because the discharge current controls the composition (x) of NbN$_x$ films, we used the data from [106, 107, 108] to estimate their relationship. According to these studies [106, 107, 108, 109] we can conclude that our films of M-series are NbN$_x$ compositions with $x \approx 1.18$. Whereas, the film of K0-series is characterized by $x \approx 1.04$. Therefore, the films of M-series contain more nitrogen as compared to the film of K0-series.

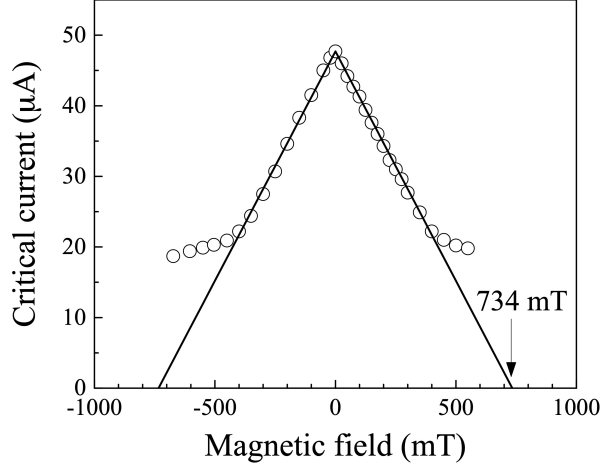The film of K0-series was used for jitter measurements. Transport measurements of non-

Figure 3.3: Critical current of the wire in external magnetic field. Straight lines approximate the linear decrease of the current at small magnetic fields. The arrow marks the field B^* discussed in the text.

structured NbN film of K0-series showed $T_C = 12.55$ K, and $R_{SN} = 260$ Ω/sq. After patterning into a nanowire, the resistance was found to be larger, $R_{SN} = 331.8$ Ω/sq. The resistivity of the wire is defined as $\rho_0 = R_{SN}d = 165.9$ $\mu\Omega\times$cm. The experimental critical current of the wire is $I_C = 50.2$ μA, and the critical current density is $j_C = I_C/(wd) = 10.4$ MA/cm^2. Although the current crowding effect is significantly minimized in straight nanowires as compared to meanders, the experimental critical current is still less than the theoretical depairing current, I_{DEP}. The reason for this is damaged nanowire edges, which suffer in the lithographic process [47], with significantly suppressed superconductivity across their width. Damaged edges turn the nanowire into a planar NSN structure, i.e. a superconducting core with non-superconducting edges on both sides of the core (NSN model in [47]). To check the quality of edges in our nanowire, we studied the suppression of the critical current by an external magnetic field applied perpendicularly to the substrate. The measured $I_C(B)$ dependence is shown in Fig. 3.3.

As seen in Fig. 3.3, the $I_C(B)$ dependence is symmetric with respect to zero magnetic field and exhibits the sharp maximum at $B = 0$. At small fields, the critical current linearly decreases with increasing the field. Then at some fields, the decrease slows down that indicates the transition from the vortex-free Meissner state to the mixed vortex state. A part where I_C depends linearly on B can be extrapolated by $I_C(B) = I_C(0)(1 - B/B^*)$, where $B^* = 734$ mT is the field at which an extrapolated straight line crosses the field axes at zero current. The transition from the Meissner state to the mixed vortex state occurs at approximately $B^*/2$. Theoretically, B^* is predicted by the London-Maxwell (LM) [110] model as

$$B_{LM}^* = \frac{\eta\Phi_0}{\mu e\pi\xi w}, \tag{3.6}$$

and by the Ginzburg-Landau (GL) [111] models as

$$B_{GL}^* = \frac{\eta\Phi_0}{\sqrt{3}\pi\xi w}, \tag{3.7}$$

where $\mu \approx 0.715$ is the ratio of the current that suppresses the potential barrier for the vortex entry and the GL depairing current [110], η is the ratio of the experimental critical current to

the depairing critical current at $B = 0$. The coherence length amounts to $\xi = 4.8$ nm. Both predictions result in B^* smaller than the experimental value. The density of the Ginzburg-Landau depairing current with the dirty-limit correction [112], $KL(T)$, is given by [93]

$$j_{\text{DEP}} = KL(T) \frac{4\sqrt{\pi} \exp(2\gamma)}{21\zeta(3)\sqrt{3}} \frac{\beta_0^2 (k_B T_C)^{3/2}}{e\rho\sqrt{D\hbar}} \left[1 - (T/T_C)^2 \right]^{3/2},$$

$$KL(T) = 0.65 \left[3 - (T/T_C)^5 \right]^{1/2}, \tag{3.8}$$

where $\gamma = 0.577$, $\zeta(3) = 1.202$, $\beta_0 = 2.05$ is the ratio between the energy gap in NbN and $k_B T_C$, and e is the electron charge. With nominal width and thickness of our nanowire, $w = 100$ nm and $d = 5$ nm, we obtained $I_{\text{DEP}} = 113$ μA at $T = 4.2$ K and the ratio $I_C/I_{\text{DEP}} \approx 0.44$. This ratio is comparable to those reported in [96] for straight wires of the same width.

A disagreement between the theoretical (Eqs. (3.6 and 3.7)) and experimental fields B^* is hardly surprising, because for computing B^* we used the nominal width w of the nanowire without accounting for the damaged edges. However, assuming that the actual width, which carries the superconducting current, is less than nominal, one can find an agreement between the model predictions and the experimental data for B^*. Such an approach has been suggested in [47], where the wire was considered as a planar NSN (normal-superconducting-normal) structure. The effective width of the superconducting core, w_S, is smaller than the nominal width of the wire, w, by a value of w_N, where w_N is the total width of two damaged edges around the core. Consequently, $w = w_S + w_N$. Such a wire can be represented by two resistors connected in parallel with different resistances. We allow the central core to have the resistance of the non-structured film $R_{SN(film)} = \rho_S/w_S$, where the resistivity is defined as $\rho_S = R_{SN(film)}d = 130$ $\mu\Omega{\times}$cm. The damaged, normal edges, consequently, have the resistance $R_N = \rho_N/w_N$. The experimental resistance of the nanowire is $R_{SN(wire)} = \rho_0/w$, where $\rho_0 = R_{SN(wire)}d = 165.9\mu\Omega{\times}$cm, or differently after algebraic transformation it becomes

$$\rho_0 = \frac{\rho_N \rho_S w}{\rho_S w_N + \rho_N(w - w_N)}. \tag{3.9}$$

Further, we assume that the experimental critical current is concentrated in the superconducting core of the nanowire. Theoretically, this current corresponds to either the depairing current of the core $I = j_{DEP} w_S d$, according to the GL model, or the current $I = \mu\, j_{DEP} w_S d$, which suppresses the barrier for vortex-entry in the core, according to the LM model. Thus, simultaneously satisfying experimental values of ρ_0, the currents given by the last expressions, and the experimental B^*, we obtained the following pairs of w_S and ρ_N. In the framework of the GL model, $w_S = 61$ nm and $\rho_N = 292\mu\Omega{\times}$cm. In the framework of the LM model, $w_S = 57.5$ nm and $\rho_N = 265\mu\Omega{\times}$cm. The evaluated widths of the superconducting core with both approaches are close to each other and almost twice as small as the nominal width. Now, knowing the actual width of the core, which carries the superconducting current, we can correct the ratio between experimental and theoretical currents. The corrected ratios are 0.57 for the the GL model and 0.84 for the LM model, that still amounts to only a fraction of the predicted current.
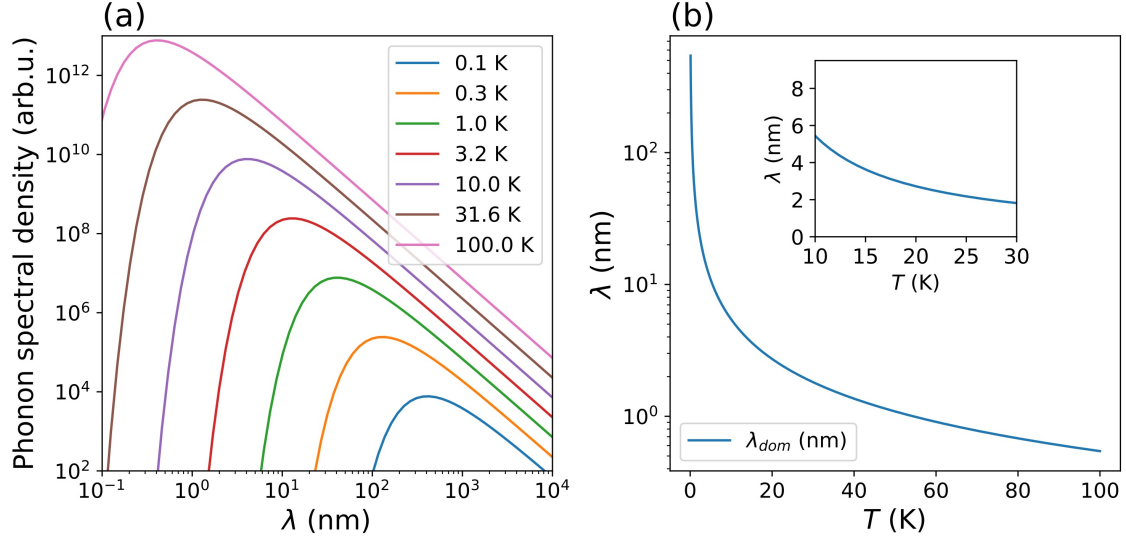
Figure 3.4: (a) Phonon spectral density in arbitrary units as a function of the phonon wavelength, $\lambda = 2\pi u/\Omega$. Various colors correspond to different temperatures. The maximum of the distribution corresponds to the dominant wavelength λ_{dom}. (b) The dominant wavelength as a function of temperature (Eq. (3.10)). Calculations were done using the averaged kinematic velocity for phonons in the film $u = 4u_{1t}/3 \approx 3.2$ nm/ps found from the analysis of magnetoconductance data in Section 3.2.1.

3.1.1 Dimensionality of studied films

In this subsection, we discuss the dimensionality of films under the present study with respect to different physical phenomena. The dimensionality is especially important in the theory of quantum corrections (see Section 2.4.1), which will be applied for the analysis of magnetoconductance data in Section 3.2.1. Magnetoconductance data will be acquired in the temperature range from a corresponding critical temperature up to 30 K. We consider the following dimensionality criterion:

- With respect to *electron-electron scattering* a film is 2-d when $d \ll L_T$, where $L_T = \sqrt{2\pi D\hbar/(k_B T)}$ is the thermal coherence length. The inequality $d < L_T$ holds for our films in the temperature range of interest. This corresponds to the quasi-two-dimensional (quasi-2-d) case. Only for the thickest film M-A855, the thickness slightly exceeds L_T at temperatures > 23 K.

- With respect to the *normal conduction* a film is three-dimensional (3-d) when $d \gg l_e$. The elastic mean free path l_e in NbN is of the order of the lattice parameter. According to [107, 113], for different compositions of NbN_x with x in the range 0.6 - 1.2, the lattice parameter approximately changes from 0.435 to 0.47 nm. Therefore, the inequality $d \gg l_e$ holds for each specimen.

- The dimensionality of the films with respect to *phonons* is more specific. The spectral density of phonons emitted isotopically covers a wide spectral range (Fig. 3.4(a)). In the

3-d limit is given by $D(\Omega)\hbar\Omega N(\Omega)$, where Ω is the phonon circular frequency, $D(\Omega) = \Omega^2/(2\pi^2 u^3)$ is the density of phonon states per each phonon mode, and $N(\omega)$ is the Bose-Einstein distribution. At temperatures below the Debye temperature, the wavelength position of the spectral maximum depends on the temperature as

$$\lambda_{dom} = \frac{2\pi\hbar u}{2.82 k_B T}. \tag{3.10}$$

λ_{dom} is known as the phonon dominant wavelength. Here $u = 4u_{1t}/3$ is the averaged kinematic velocity for phonons in the film (Section 3.2.1). We computed λ_{dom} taking $u_{1t} = 2.40$ nm/ps found from the analysis of magnetoconductance data in Section 3.2.1. Fig. 2.20(b) shows the temperature dependence of the λ_{dom}, and the inset zooms the $\lambda_{dom}(T)$ dependence for the temperature range of interest. Although the λ_{dom} is comparable with the thickness of the thinnest film, the fact that our films are in direct contact with the bulk substrate may enhance the three-dimensionality of phonons. Therefore, we conclude that phonons in our NbN films can be treated as the 3-d Debye phonons in the temperature range of interest far from T_C. However, at temperatures around T_C, the films more likely approach the 2-d - 3-d crossover. The dimensionality of phonons will be important for comparing the experimental τ_{e-ph} with the one predicted by the SM model (Section 2.4.2), because the model assumes 3-d Debye phonons.

- The commonly accepted 2-d criterion with respect to superconductivity is : $d < \xi$, where ξ is the superconducting coherence length. Our NbN films (see Table 3.1) approach the vicinity of the 2-d - 3-d crossover.

3.2 Electron-phonon scattering and phonon escape times

3.2.1 Magnetoconductance measurements

As discussed in Section 2.4.1, magnetoconductance measurements allow for funding the electron dephasing time τ_ϕ. The measurements were carried out with non-structured NbN films of M-series (Table 3.1). We measured resistance at different fixed temperatures in the range from a corresponding T_C up to 30 K by varying magnetic field applied perpendicular to the sample surface in the range from 0 to 9 T. The measurements were performed in a Physical Property Measurement System (PPMS from Quantum Design) by applying very small bias currents to prevent heating. The square resistance was found for each sample by means of the four-point van der Pauw method. Fig. 3.5 shows R_S as a function of the magnetic field at various fixed temperatures indicated by different colors. Since $R_S(B,T)$ dependences are monotonous and look pretty similar for all studied specimens, we plot in Fig. 3.5 data for only one representative NbN film with the thickness 5 nm (specimen M-2259 in Table 3.1). At high temperatures, the change in the resistance due to the magnetic field is relatively small. At temperatures near T_C, the effect of magnetic field on R_S is very pronounced.
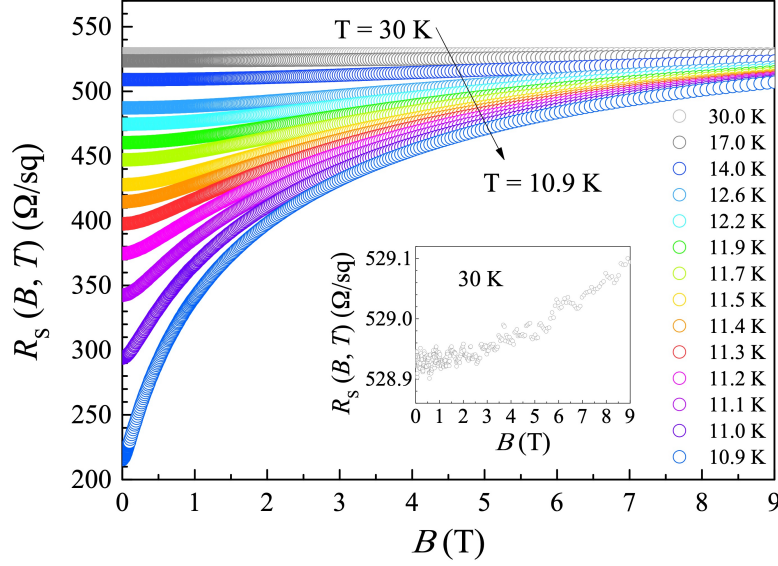
Figure 3.5: Square resistance as a function of magnetic field at different temperatures for 5 nm thick NbN film (specimen M-2259). Various colours correspond to different temperatures specified in the legend. The inset shows $R_S(B)$ data recorded at 30 K.

Fitting procedure

The magnetoconductance is the change in the reciprocal resistance caused by the magnetic field. The dimensionless magnetoconductance is computed according to Eq. (2.5) as $\delta G(B,T) = \frac{2\pi^2\hbar}{e^2}\left[\frac{1}{R_S(B,T)} - \frac{1}{R_S(0,T)}\right]$. Here $2\pi^2\hbar/e^2$ has the dimension of Ω. From the measurements of $R_S(B,T)$, we extract the experimental magnetoconductance per sample square, which is shown for the representative specimen M-2559 in Fig. 3.6 with symbols. In the low-temperature range near T_C, where superconducting fluctuations are strong, the square resistance considerably changes with the magnetic field. With increasing temperature, the change in the resistance induced by the magnetic field decreases. At temperature 30 K far from T_C (Fig. 3.6, inset), the change in the resistance is small.

For the analysis of experimental data, we apply the theory of quantum corrections described in subsection 2.4.1. We fit the experimental $\delta G(B,T)$ with a sum of magnetoconductances caused by weak-localization (WL, Eqs. (2.10)), Aslamazov-Larkin (AL, Eqs. (2.13)), and Maki-Thomson (MT, Eqs. (2.16)) quantum corrections, i.e. $\delta G(B,T) = \delta G^{WL}(B,T) + \delta G^{AL}(B,T) + \delta G^{MT}(B,T)$. Although we explicitly omit the magnetoconductance term caused by fluctuations of the electron density of states (DOS) from the fitting procedure. However, we indirectly account for it via the prefactor $\beta_{LSA}(T,\delta)$ present in the MT correction by using it as a fitting parameter (see paragraph "Total magnetoconductance" in subsection 2.4.1.1). As shown in Fig. 2.11 on page 25, the contribution of each quantum correction to the total magnetoconductance strongly depends on the temperature. At relatively high temperatures, for instance, 15 - 30 K, the magnetoconductance caused by AL fluctuations is negligibly small, and the total magnetoconductance is dominated by MT fluctuations. Therefore, in order to simplify the fitting procedure, we neglected the AL term at high temperatures. At low temperatures near T_C, the situation is different. The WL and MT terms alone fail to describe the experimental magneto-
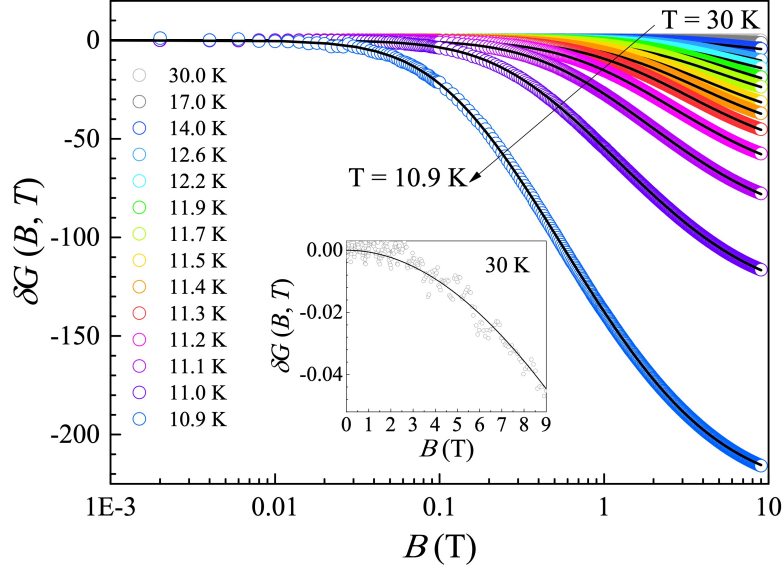
Figure 3.6: Dimensionless magnetoconductance. Symbols correspond to experimental data for 5 nm thick NbN film (specimen M-2259) obtained from resistance measurements and with Eq. (2.5). Different colours correspond to different temperatures. The solid lines are fits according to Eqs. (2.10, 2.13, 2.16).

conductance, and the AL term should be necessarily included. In the immediate vicinity of T_C, magnetoconductance is dominated by AL fluctuations. Finally, the experimental magnetoconductance was fitted with four parameters: $\beta_{LSA}(T, \delta)$, $B_{s.o.}$, C^*, and B_{in}. For temperatures 10.9 and 17 K, the typical values are $\beta_{LSA}(T, \delta) = -67.32$, $B_{s.o.} = 0.98$ T, $C^* = 2.97$, $B_{in} = 0.52$ T, and $\beta_{LSA}(T, \delta) = 6.61$, $B_{s.o.} = 0.91$ T, $C^* = 3.00$, $B_{in} = 2.69$ T, respectively. The best fits are shown in Fig. 3.6 with solid curves.

Dephasing time

The electron dephasing time τ_ϕ was extracted from the best fit values of the magnetic field B_{in} as $\tau_\phi = \hbar/(4eDB_{in})$, where the electron diffusion coefficient D was taken from Table 3.1. The obtained values of τ_ϕ are plotted with symbols in Fig. 3.7 vs temperature for four studied specimens M–2259, M–A853, M–A854, and M–A855.

Above the superconducting transition, the total dephasing rate is a sum of the electron-electron, τ_{e-e}^{-1}, electron-phonon, τ_{e-ph}^{-1}, and electron-superconducting fluctuation, τ_{e-fl}^{-1} scattering rates. In order to compute each of them we used existing theoretical predictions given in Eqs. (2.21 - 2.23). For each specimen, we took R_{SN} and T_C from Table 3.1 and computed $\tau_{e-fl}(T)^{-1}$ and $\tau_{e-e}^{-1}(T)$. The two parameters C_2 and n entering the expression for the *e-ph* scattering rate $\tau_{e-ph}^{-1} = C_2(T/T_C)^n$ are unknown. We assumed that in the given temperature range, n is temperature-independent, and used C_2 and n as fitting parameters. As it has been noted in [114], it is not possible to fit the V-shape behavior of the experimental τ_ϕ at temperatures close to T_C. The reason is not clear and goes beyond the scope of the present study. To circumvent the problem, we included in the fitting procedure only the data obtained at temperatures above 14 K. The resulting fit with $\tau_\phi^{-1} = \tau_{e-e}^{-1} + \tau_{e-ph}^{-1} + \tau_{e-fl}^{-1}$ is shown in Fig. 3.7(a). As discussed in Section 2.4.1.2 and seen in the inset of Fig. 3.7(a), in the temperature range 14 -
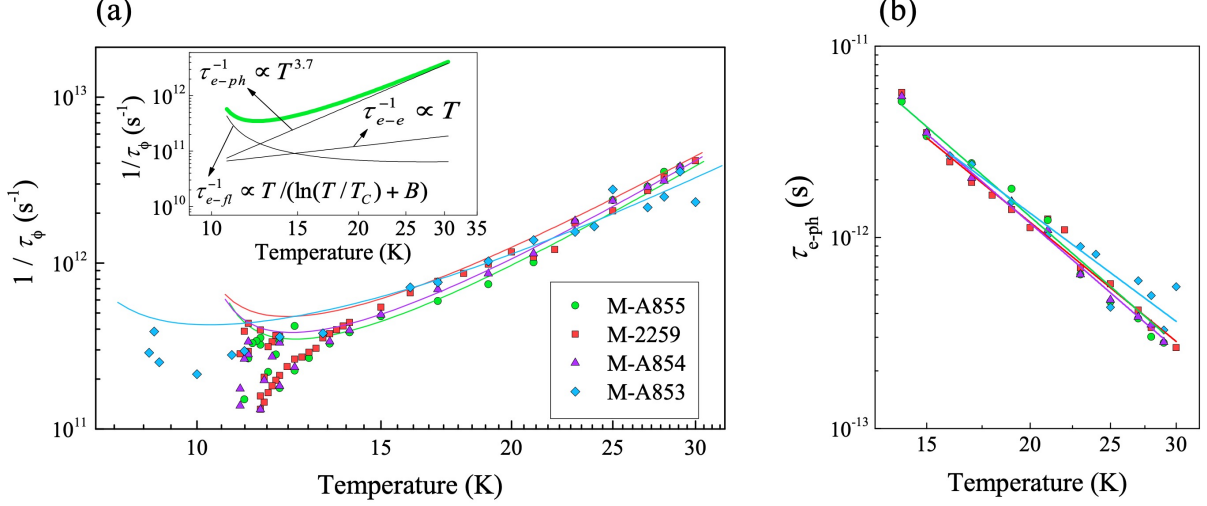
Figure 3.7: (a) Dephasing rate vs. temperature (symbols) extracted from magnetoconductance measurements in the double logarithmic scale. Various colors correspond to different specimens specified in the legend. Solid lines are fits made with a sum of the *e-e*, *e-ph*, *e-fl* scattering rates given in Eqs. (2.21 - 2.23), $\tau_\phi^{-1} = \tau_{e-e}^{-1} + \tau_{e-ph}^{-1} + \tau_{e-fl}^{-1}$. The inset shows the best fitting curve (thick green curve) for specimen M-A855 and the contribution of each scattering rate to the total rate (thin curves). In the temperature range 14 - 30 K, the contribution of τ_{e-ph}^{-1} dominates. This contribution is shown with symbols in panel (b) for each specimen. The solid lines are the best fits according to Eqs. (2.22) with fitting parameters listed in Table 3.2. The legend specifies specimens for both panels.

30 K, *e-ph* scattering is the dominant scattering mechanism that defines the magnitude and the temperature dependence of τ_ϕ^{-1}. Therefore, such a fitting procedure is consistent with the scope of the present study. The best fit values of C_2 and n are listed in Table 3.2, together with τ_{e-ph}, which were extrapolated to 10 K and the corresponding T_C. Fig. 3.7(b) shows τ_{e-ph} (symbols) extracted from experimental rates τ_ϕ^{-1} and the corresponding best fits $\tau_{e-ph}^{-1} = C_2(T/T_C)^n$ (solid lines) for four studied specimens.

As discussed in Section 2.4.1.2, with respect to *e-ph* scattering, the dephasing time is identical to the inelastic single-particle time. The later is predicted by the SM model (Section 2.4.2). Therefore, further, we analyze the derived dependences $\tau_{e-ph}(T)$ with the SM model.

Table 3.2: Parameters extracted from magnetoconductance measurements

Sample	$\tau_{e-ph}(10\text{ K})$ (ps)	$\tau_{e-ph}(T_C)$ (ps)	n	$C_2 \times 10^{10}$ (s^{-1})
M-2259	11.9 ± 0.7	9.3 ± 0.4	3.53 ± 0.19	10.80 ± 0.52
M-A853	12.4 ± 1.4	21.7 ± 3.3	3.21 ± 0.19	4.60 ± 0.69
M-A854	15.9 ± 1.1	11.8 ± 0.7	3.75 ± 0.13	8.48 ± 0.48
M-A855	17.5 ± 1.7	12.5 ± 1.0	3.77 ± 0.23	8.02 ± 0.65

Analysis of experimental dependences $\tau_{e-ph}(T)$ with the SM model

Due to $\tau_\phi \approx \tau_{in}$ with respect to *e-ph* scattering (see Section 2.4.1.2), we can directly compare τ_{e-ph} with the predictions of the theory. We analyze the τ_{e-ph} acquired with magnetoconduc-

Table 3.3: Best fit parameters present in the SM model (Eqs. 2.24 - 2.26).

Sample	l_e (nm)	ρ (g/cm^3)	u_t (m/s)	k
M-2259	0.13	7.8	2.42×10^3	1
M-A853	-	5.2	2.2×10^3	-
M-A854	0.14	7.5	2.4×10^3	1
M-A855	0.12	7.5	2.37×10^3	1

tance measurements in the temperature range 14 - 30 K in the framework of the SM model. Since the model assumes 3-d Debye phonons, we first refer to Section 3.1.1 where we concluded that phonons in the studied films can be treated as 3-d Debye phonons. We fit experimental data shown in Fig. 3.7(b) with symbols with Eqs. (2.24 - 2.26, on page 28). To do this, we used three fitting parameters: the electron mean free path l_e, the mass density ρ, and the velocity of transverse phonons u_t. Because in the temperature range where our MC data were acquired, the scattering rate of electrons via transverse phonons dominate, the parameter u_l does not affect the result of simulations. We therefore excluded u_l from the set of fit parameters and took it $u_l = 2u_t$ that is approximately valid for a large variety of materials (for an example see Table I in [48]). Other parameters which are present in the SM model were taken from Table 3.1. To compute the Fermi momentum and Fermi energy we took the effective electron mass to be equal to the mass of a free electron. For fixed k, fine tuning of the exponent n in the $\tau_{e-ph}^{-1} \sim T^n$ dependence can be achieved only by varying the transition temperature between two asymptotes. This transition temperature is given by $\hbar u_t (k_B l_e)^{-1}$. Therefore, the fine tuning of n was done by changing the ratio $u_t l_e^{-1}$. The variations in the mass density ρ affect only the magnitude of the e-ph scattering rate. The best fit values of l_e, ρ, and u_t are listed in Table 3.3.

It turned out that reasonable fits of the temperature dependence of the inelastic e-ph scattering rate could only be obtained with $k \to 1$. For specimens M-2559, M-A854, and M-A855, the best fits were obtained with $k = 1$. Fitting the data for the film M-A853 with $k = 1$ gives enormously large $l_e = 0.31$ nm that contradicts to other parameters (D and R_{SN}) found for this specimen. Although the exact reason is not clear, we have to note that using $k \sim 0.9$ results in a reasonably small l. In the SM model, $k < 1$ corresponds to the presence of static scattering centers. Since the grain boundaries act as static, non-vibrating scatterers, experimental data can be qualitatively related to enhanced granularity of the film M-A853 as compared to other films of the M-series. Recall here that the Ioffe-Regel parameter estimated for this film is $k_F l_e < 1$ that may also indicate enhanced granularity [104]. For our films in the entire temperature range from 14 to 30 K, we found $q_T l_e \ll 1$. It can be presented as $q_T l_e = \beta T$, where the coefficient β falls into the range 0.075 ± 0.005 K^{-1}. Hence, the films of the M-series are strongly disordered with a very close degree of disorder.

Comparison with previously reported data on NbN

The best fit values of mass density and sound velocity obtained for our NbN films (see Table 3.3) deviate from those reported in [115] for bulk hexagonal NbN, where $\rho = 8.5$ g/cm^3 and $u_t =$

4500 m/s. This deviation is predictable since the crystallographic structure and stoichiometry in thin films is modified as compared to bulk material. For example, excess nitrogen content with respect to the optimal stoichiometric composition reduces the mass density while the granularity and weak bounds at film surfaces reduce the sound velocity.

For all specimens (except for specimen M-A853), the best fit values of l_e are by a factor of two smaller than those obtained from Hall-effect measurements by different groups [116, 117, 118], and by a factor of 4 to 6 smaller than values reported in [101]. The data in [101] were computed as $l_e = \sqrt{3D\tau_e}$ with independently measured diffusion constant and the elastic scattering time τ_e obtained by means of spectral ellipsometry. Such a difference from previously reported data can originate from a different stoichiometry of the films studied here and in [116, 117, 118, 101]. Alternatively, the reason for such a difference can be artificial and inherent in the SM model. One of the mechanisms in the model that controls $e\text{-}ph$ scattering is disorder. If the scattering rate in the specimen under study changes due to any other reason, the only way to account for that in the framework of the model is to increase or decrease disorder, i.e. to change the value of l_e.

To the best of our knowledge, there are two published experimental studies [119, 91] where the magnitude of τ_{e-ph} and the exponent n were defined for NbN films. In Table 3.4, we list the parameters for NbN films reported in [119, 91] and for one representative NbN film M-2259 from the present study. In both studies [119] and [91], the reported exponent n differs from what we obtained for our NbN films. In order to understand the nature of such a difference, we first simulate the data in a corresponding temperature range and then describe it with the SM model.

In Fig. 3.8, with blue symbols we show the simulated data from [119], where the τ_{e-ph} was defined by means of magnetoconductance in the temperature range from 10 to 30 K. Green symbols in the figure correspond to the simulated data from [91], where the τ_{e-ph} was defined by means of photoresponse (AMAR) in the temperature range 1.6 – 10.2 K. In the same figure with red symbols, we plot $\tau_{e-ph}(T)$ acquired for specimen M-2259 in the present study. For each film, we define the electron density of states with Eq. (3.3), which enters the SM model. Further, we describe these data with the SM model using following fitting parameters ρ, u_t, l_e, and k, and taking $u_l = 2u_t$. The best fitting values of these parameters are listed in Table 3.4. The best fits are shown in Fig. 3.8 with solid curves. Since $n < 2$ cannot be achieved in the framework of the SM model (in the dirty regime), we described the simulated data with the closest value $n = 2$. We note here that in the dirty regime, $n = 2$ can be obtained only if static scattering centers are present, i.e. if $k < 1$. Because the true value of k is unknown we take $k = 0$. For both data sets, ρ and u_t are smaller than for bulk material.

Although the properties of our film are very similar to those from [91] (Table 3.4), there are noticeable differences in temperature dependences of $e\text{-}ph$ scattering times. This can be a result of different degrees of granularity caused by different deposition rates. We suppose that granules are responsible for enhanced resistivity while their boundaries act as static, non-

Table 3.4: Reported properties of NbN films and fitting parameters present in the SM model. n is the exponent in $\tau_{e-ph}^{-1} \propto T^n$.

sample	Properties of NbN sample						Best fit parameters present in the SM model			
	d	T_C	R_{SN}	D	n	τ_{e-ph}^{10K}	l_e	ρ	u_t	k
	(nm)	(K)	(Ω/sq)	(cm^2/s)		(ps)	(nm)	(g/cm^3)	(nm/ps)	
X-A[a]	200	10.3	34	0.2	1.64	7.2	0.20	7.5	3.90	0.0
X-B[b]	7	11	500	0.4	1.6[c]	5.6[c]	0.20	7.5	2.70	0.0
M-2259[d]	5.0	10.74	529.5	0.474	3.53	11.9	0.13	7.8	2.42	1.0

[a] NbN film on Si/SiO$_2$ substrate, [119]. The authors defined the *e-ph* scattering time τ_{e-ph} by means of magnetoconductance in the temperature range from 10 to 30 K.

[b] NbN film on Al$_2$O$_3$ substrate, [91]. The authors defined the decay times of the photoresponse τ_ϵ by means of photoresponse (AMAR) in the temperature range from 1.6 to 10.2 K.

[c] The authors identified measured decay times of the photoresponse, τ_ϵ, with the *e-ph* energy relaxation time, τ_{EP}. The exponent n relates to the temperature dependence of the photoresponse time. The τ_{e-ph} was computed according to Eq. (2.27).

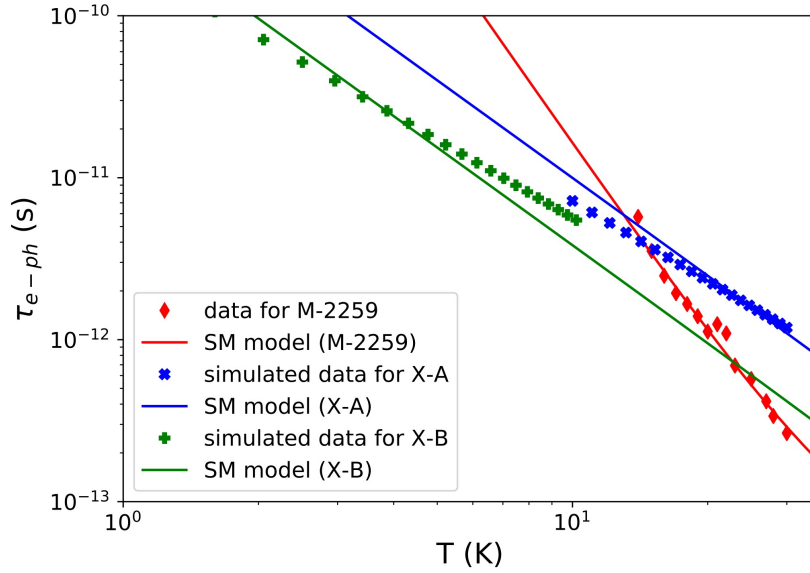[d] NbN film on Si/SiO$_2$ substrate, the present study.

Figure 3.8: *E-ph* scattering time vs temperature. Blue and green symbols correspond to the simulated $\tau_{e-ph}(T)$ from [119] and [91], respectively. Red symbols correspond to $\tau_{e-ph}(T)$ for specimen M-2259 from the present study. Solid curves correspond to the best fits with the SM model (material and fitting parameters are listed in Table 3.4).
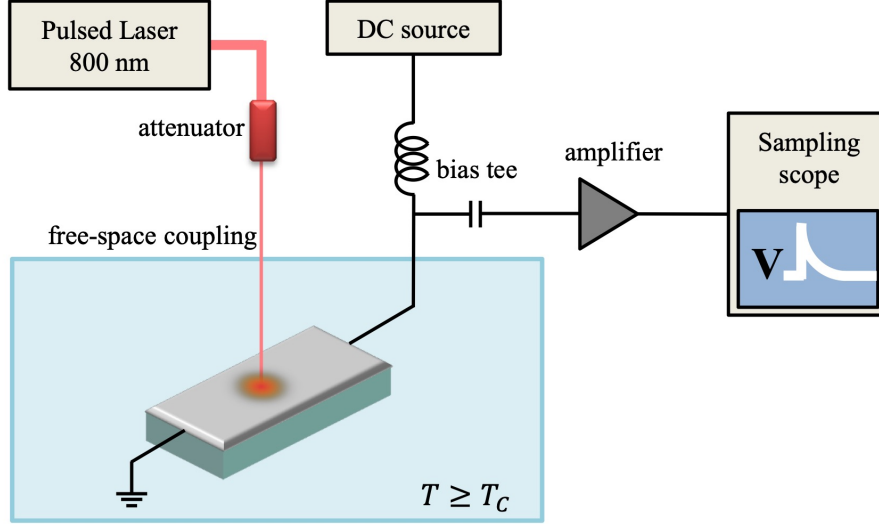
Figure 3.9: Scheme of experimental setup for photoresponse measurements in the time domain. The light from the Ti:sapphire laser (800 nm pulsed mode) in free space is sent to the sample. The RF and dc paths are de-coupled at room temperature. The voltage transients from the sample are amplified at room temperature before they are recorded by a sampling scope. The relative power of incoming light from the laser is controlled by an attenuator.

vibrating scatterers. For thick NbN films from [119], the difference in the exponent n as compared to our films is not surprising. The morphology of those films of 200 nm thick can be quite different from ours. Usually, a small value of the electron diffusion coefficient in such thick films indicates either the presence of defects (vacancies or impurities) or pronounced granularity [116]. The granular morphology of thick NbN films in the form of vertical columnar metallic grains with amorphous grain boundaries was observed in [120]. Grain boundaries can act as static, non-vibrating scattering centers. According to the SM model, the presence of static scattering centers is indicated by the parameter $k < 1$ that is consistent with our simulations.

To summarise, we ascribe the difference in the exponent n for NbN films studied in this thesis ($n = 3.53$ - 3.77) and those studied in [91, 119] ($n = 1.6$) to the difference in the degree of granularity.

3.2.2   Photoresponse measurements in the time domain

Specimens and experimental setup

Relaxation of the electron energy was studied by means of photoresponse in the time domain with microbridges patterned from NbN films of M-series described in Section 3.1 (M-2259, M-A853, M-A854, and M-A855). The widths of microbridges varied from 0.615 to 0.69 μm and the lengths from 3.6 to 7 μm. Their planar sizes with respect to thicknesses were chosen in such a way as to match the normal square resistance of each microbridge to the electrical impedance of the readout circuit 50 Ω. The experimental setup is schematically shown in Fig. 3.9. The

measurements were done using a continuous flow cryostat. Optical pulses with a duration of $\sigma_t = 0.017$ ps were generated by a Ti-sapphire laser (Femtosource, synergy 20) with the central wavelength at 800 nm at a repetition rate of 80 MHz. The light from the laser was collimated and sent into the cryostat in free space through a quartz window. The laser power was controlled by a powermeter (Thorlabs, PM100, sensor S120C) and could be adjusted by a variable attenuator placed between the laser and the cryostat. The microbridges were mounted on a holder together with the temperature sensor and the heater and were kept in the resistive state at an ambient temperature slightly larger than T_C. The temperature was controlled with a temperature controller (LakeShore, Model 331). On the holder, microbridges were connected to the coplanar line via bonding. A coaxial cable connected the line and a bias-tee, which was plugged to the SMA output of the cryostat. Samples were biased by a small direct current from a battery-powered dc source. Photoresponse of the microbridge, a voltage transient, was amplified by a low-noise amplifier connected directly to the bias-tee, and further acquired with a 50 GHz sampling scope (Keysight Infiniium DCA-X 86100D) connected to the amplifier through a coaxial cable. The resulting bandwidth of the readout setup was 0.05 - 4.5 GHz.

Fig. 3.10 shows representative voltage transients acquired by the oscilloscope for each studied microbridge. For microbridges of different thicknesses, transients look similar. They all exhibit fast rising and slow falling parts. Rising times for all microbridges regardless their thickness are identical and equal to 45 ps, which also corresponds to the upper frequency of our readout. Therefore, we conclude that the rising time is limited to the bandwidth of our readout. The falling parts of transients still contain valuable information. As seen in Fig. 3.10, the falling parts of transients exhibit ringing. This is caused by multiple reflections between the microbridge and the readout occurring due to impedance mismatch. The ringing period is approximately 250 ps
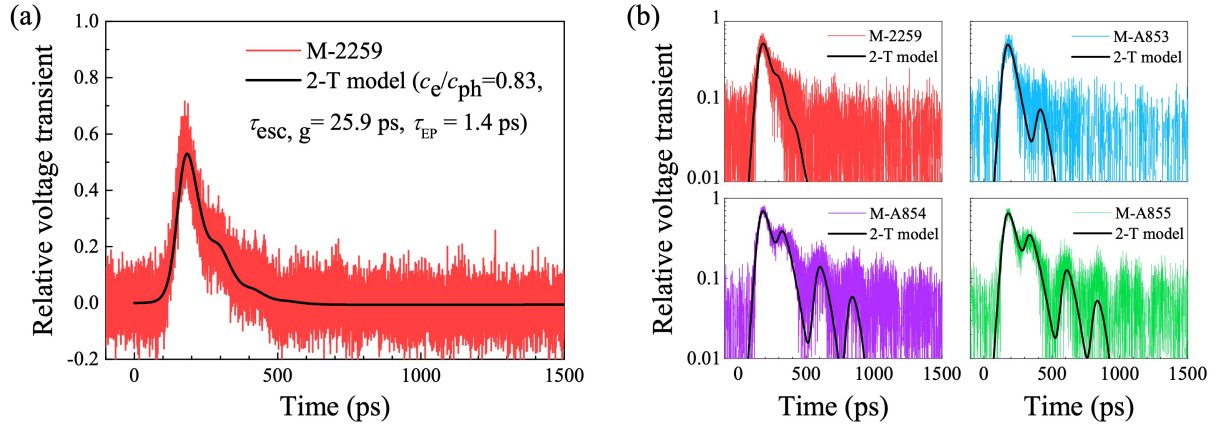

Figure 3.10: (a) Voltage transient for the microbridge with the thickness 5 nm in the linear scale. (b) Voltage transients for NbN microbridges of four different thicknesses in the semi-logarithmic scale. Black curves are best fits according to the 2-T model (Eqs. (2.29 - 2.33)) with parameters: for M-2259 $c_e/c_{ph} = 0.83 \pm 0.18$, $\tau_{esc} = 25.9$ ps; for M-A853 $c_e/c_{ph} = 0.25 \pm 0.03$, $\tau_{esc} = 39$ ps; for M-A854 $c_e/c_{ph} = 0.35 \pm 0.05$, $\tau_{esc} = 39$ ps; and for M-A855 $c_e/c_{ph} = 0.11 \pm 0.03$, $\tau_{esc} = 51.3$ ps. For each bridge $< \tau_{e-ph} >$ was fixed at the value obtained for original film from MC measurements and further averaged over the electron distribution according to Eq. (2.27). Legends specify film numbers from Table 3.1.

that corresponds to 2.5 cm electrical path between the microbridge and the first SMA connector at the microbridge holder.

Fitting procedure

We describe the photoresponse data shown in Fig. 3.10 with the 2-T model (Eq. (2.28)) and the 3-T model (Eq. 2.35). We simulate the photoresponse as $U_{out}(t)$, which we find from the solution $T_e(t)$ of the corresponding model and the formalism described by Eqs. (2.31 - 2.33). This formalism accounts for the limited bandwidth of the readout electronics and signal ringing. To compute the dependences $T_e(t)$ we used analytical solution for the 2-T model given by Eqs. (2.29) and numerically solved the system (Eq. (2.35)) for the 3-T model. The 2-T model has three independent parameters, these are the *e-ph* energy relaxation time, τ_{EP}, the ratio between electron and phonon heat capacities, c_e/c_{ph}, and the averaged phonon escape time, $\tau_{esc,g}$. The 3-T model has four independent parameters, these are τ_{EP}, c_e/c_{ph}, the phonon escape time, τ_{esc}, and the ratio between heat capacities of escaping phonons to the total phonon heat capacity, $c_{ph,1}/c_{ph}$. All these parameters can be extracted for our films from the magnetoconductance data (Section 3.2) and the data obtained with transport measurements (Section 3.1). As it was discussed in Section 2.4.2, because the photoresponse technique implies electron heating, the relaxation time τ_{EP} present in the 2-T and 3-T models is an average of the single-particle scattering rate τ_{e-ph} over the range of electron states $\sim k_B T$. For each sample, we found τ_{EP} at T_C with Eq. (2.27), which are listed in Table 3.5. The heat capacity of electrons is predicted by the Drude model, $c_{e(Drude)} = \frac{1}{3}\pi^2 k_B^2 N(0)T$, and for 3-d phonons by the Debye model, $c_{ph(Debye)} = \frac{2\pi^2 k_B}{15}[(k_B T)/\hbar]^3 \left[2/u_t^3 + 1/u_l^3\right]$. Here $u_{t(l)}$ is the propagation velocity of transverse (longitudinal) phonons within the film. The total weighted phonon escape time present in the 2-T model can be found as $\tau_{esc,g} \approx 4d/(\eta_0 \overline{u}(\sin \overline{\Theta}_{max})^2)$ (see Section 2.4.3). Both the transmission coefficient at the film/substrate interface at zero degrees η_0 and the critical angle for total internal reflection of phonons $\overline{\Theta}_{max}$ can be found with the acoustic mismatch model (AMM) (see Section 2.4.3). Their values are $\eta_0 = 0.9 - 1.0$ and $\overline{\Theta}_{max} = 32.3° - 35.5°$ To compute $\overline{u}$ we used values of u_t from Table 3.3 and took $u_l = 2u_t$. The phonon escape time in the 3-T model is $\tau_{esc} \approx 2d/(\eta_0 \overline{u})$. The ratio $c_{ph,1}/c_{ph} = 1 - \cos(\overline{\Theta}_{max})$ defines the fraction of escaping phonons. All these parameters are listed in Table 3.5.

Although all parameters present in the 2-T and 3-T models are found (Table 3.5), the experimental photoresponse can not be well described by fixing all of them. Therefore, at least

Table 3.5: Computed parameters for NbN films of M-series on SiO_2 substrates present in the 2-T and 3-T models.

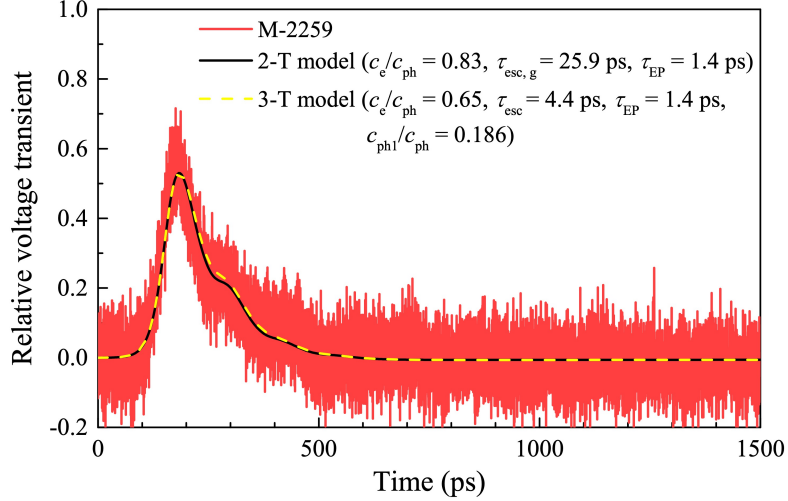| Sample	d	$\tau_{EP}(T_C)$	$\frac{c_{e(Drude)}}{c_{ph(Debye)}}$	$\tau_{esc,g}$	τ_{esc}	$\frac{c_{ph,1}}{c_{ph}}$	c_e/c_{ph}	c_e/c_{ph}
(microbridge)	(nm)	(ps)		(ps)	(ps)		(2-T model)	(3-T model)
M-2259	5.0	1.4 ± 0.2	0.28	25.9	4.4	0.19	0.83 ± 0.18	0.65 ± 0.19
M-A853	6.4	4.2 ± 1.1	0.21	39.0	5.6	0.15	0.25 ± 0.03	0.25 ± 0.03
M-A854	7.5	1.5 ± 0.2	0.25	39.0	6.6	0.19	0.35 ± 0.05	0.29 ± 0.06
M-A855	9.5	1.6 ± 0.3	0.24	51.3	8.5	0.18	0.11 ± 0.03	0.32 ± 0.04

Figure 3.11: Voltage transient for the microbridge with the thickness 5 nm in the linear scale. The black solid curve corresponds to the best fit with the 2-T model (Eqs. (2.29 - 2.33)) and the yellow dashed curve to the best fit with the 3-T model (Eqs. (2.35), Eqs. (2.31 - 2.33)). Parameters present in the models are specified in the legend.

one fitting parameter is required. Since τ_{EP} was derived from MC measurements of the original films, we fixed its value for each bridge. We also fixed the phonon escape times for each bridge and the fraction of escaping phonons according to the acoustic mismatch model. This leaves only one fitting parameter, the ratio c_e/c_{ph}. Fig. 3.11 shows the best fits of the photoresponse (the solid and dashed curves) with the 2-T and 3-T models for specimen M-2259. The fitting curves are very close to each other. Because for other specimens the best fits with both models look very similar, in Fig. 3.10 we show fits (solid curves) only for the 2-T model. The best fit ratios c_e/c_{ph} obtained with both models are listed in Table 3.5. For thicker specimens (M-A853, M-A854, M-A855), both models provide ratios c_e/c_{ph} close to those predicted by the Debye and the Drude models. However, for the thinnest specimen M-2259, the best fit ratios c_e/c_{ph} considerably deviate from the predicted one.

To summarise, the experimental photoresponse data in the time domain were described with the 2-T and 3-T models. We found that for the thinnest film the best fit ratios c_e/c_{ph} strongly deviate from the ration c_e/c_{ph} predicted by the Debye and Drude models as compared to thicker films. The discussion of such a discrepancy is presented in Section 3.2.4.

3.2.3   Photoresponse measurements in the frequency domain

In order to improve the reliability of the photoresponse analysis, we additionally analyzed the photoresponse data in the frequency domain for NbN microbridges with different thicknesses from 3.2 to 33.2 nm on Al_2O_3 substrates. We will refer to these samples as samples of K-series. The advantage of this series is that the substrate is transparent for the excitation wavelength. The combination of T_C and R_{SN} for films of K-series indicates that their compositions are
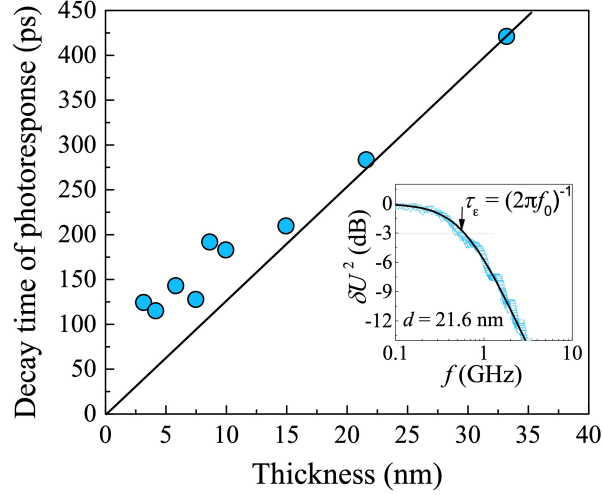
Figure 3.12: Decay time of the photoresponse, τ_ε, vs. thickness for NbN microbridges of K-series (symbols). The black line represents the linear fit $\tau_\varepsilon = 11.5d$ that corresponds to the computed phonon escape time versus film thickness. The inset shows a representative experimental photoresponse $\delta U^2(f)$ (symbols) for sample K-8 from Table 3.6. The black curve there is a fit obtained as $\delta U^2(f) = \delta U^2(0)/(1 + f^2/f_0^2)$, where f_0 is the roll-off frequency. The experimental decay time of the photoresponse is found from the roll-off frequency as $\tau_\varepsilon = (2\pi f_0)^{-1}$.

characterized by a larger relative amount of niobium (Nb) than the composition of films of M-series. The composition of films of K-series is very similar to the film of K0-series.

Raw data obtained with the frequency domain technique were partly reported in [109] and [121]. The technique in detail was described in [109]. Shortly, beams of two continuous-wave near-infrared lasers (wavelength 850 nm) with the controllable difference between radiation frequencies were overlapped on the microbridge. The microbridge was cooled down to an operating temperature on the resistive transition and biased by a small dc current I_B. The amplitude of the periodic variations of the photoresponse at the beating frequency f (the difference between frequencies of two lasers) was monitored for different beating frequencies in the interval from 10 MHz to 10 GHz. The power of the absorbed radiation, P_{RF}, alternates periodically and causes modulation of the electron temperature. This leads to periodic sinusoidal variations in the voltage $\delta U(t) = I_B \frac{dR}{dT}\delta T(t)$ which are amplified and controlled with a spectrum analyzer. The roll-off frequency f_0 in the dependence of the photoresponse magnitude $\delta U^2(f)$ on the beating frequency is the frequency at which the magnitude decreases to one half of its value at small frequencies $\frac{1}{2}\delta U^2(0)$. In the inset in Fig. 3.12 we show with symbols representative experimental data $\delta U^2(f)$ corresponding to microbridge K-8 from Table 3.6 and the solid fitting curve obtained as $\delta U^2(f) = \delta U^2(0)/(1 + f^2/f_0^2)$. For each microbridge, the roll-off frequencies were measured at $T \approx T_C$ and the response time was found as $\tau_\varepsilon = (2\pi f_0)^{-1}$. In Fig. 3.12 we plot the values of the response time τ_ε as a function of film thickness. They vary from 124 ps for the thinnest film to 421 ps for the thickest film. Generally, τ_ε decreases when d decreases. However, the rate of the decrease is noticeably less for microbridges with smaller thicknesses.

Table 3.6: Computed parameters for NbN films of K-series on Al_2O_3 substrates present in the 2-T and 3-T models.

Sample (microbridge)	d (nm)	T_C (K)	$\tau_{EP}(T_C)$ (ps)	$\frac{c_{e(Drude)}}{c_{ph(Debye)}}$	$\tau_{esc,g}$ (ps)	τ_{esc} (ps)	c_e/c_{ph} (2-T mod.)	c_e/c_{ph} (3-T mod.)
K-1	3.2	12.70	0.32	0.25	36.5	2.5	2.15 ± 0.08	2.10 ± 0.06
K-2	4.2	12.90	0.30	0.24	48.7	3.4	1.55 ± 0.07	1.52 ± 0.06
K-3	5.8	14.60	0.19	0.19	67.3	4.6	0.90 ± 0.05	0.88 ± 0.05
K-4	7.5	14.80	0.19	0.19	86.6	5.9	0.66 ± 0.06	0.62 ± 0.05
K-5	8.6	15.35	0.16	0.17	100.0	6.9	0.82 ± 0.03	0.84 ± 0.03
K-6	9.9	10.80	0.15	0.17	115.5	7.9	0.67 ± 0.04	0.68 ± 0.03
K-7	14.9	16.00	0.13	0.16	172.7	11.9	0.22 ± 0.07	0.17 ± 0.06
K-8	21.6	16.35	0.12	0.15	250.4	17.3	0.13 ± 0.06	0.10 ± 0.08
K-9	33.2	16.35	0.12	0.15	384.9	26.5	0.10 ± 0.06	0.09 ± 0.06

Fitting procedure

In our analysis we describe experimental response times, τ_ε, with the 2-T model (Eq. (2.28)) and with the 3-T model (Eq. 2.35). For this reason, we first define the parameters for the films of K-series present in the corresponding models. These are τ_{EP}, c_e/c_{ph}, and $\tau_{esc,g}$ for the 2-T model and τ_{EP}, c_e/c_{ph}, τ_{esc}, and $c_{ph,1}/c_{ph}$ for the 3-T model. As seen in Table 3.3, the best fit parameters found with the SM model (Table 3.3) for films of M-series, u_t, ρ, and l_e do not vary much with the degree of disorder. Therefore, for less disordered films K1-K9 we expect close values. We assign the mean values of the mass density ($\rho = 7.5$ g/cm^3), the phonon velocity ($u_t = 2.4 \times 10^3$ m/s) and the electron mean free path ($l_e = 0.13$ nm) found for films of M-series (except the most disordered film M-A853), and the averaged $N(0) = 6.5 \times 10^{28}$ eV^{-1}m^{-3} taken from [109] to films of K-series. By applying the SM model (Section 2.4.2) we computed values of τ_{e-ph} at the actual transition temperatures of each film of K-series. The fall into the range from 2.68 ps for the thinnest film K-1 to 1.02 ps for the thickest film K-9. At given T_C from 12.70 K to 16.35 K, the derived $\tau_{e-ph}(T_C)$ represent a power function of temperature with a mean value of the exponent $n = 3.85$. Further, from $\tau_{e-ph}(T_C)$ and $n = 3.85$, with Eq. (2.27) we compute averaged times $\tau_{EP}(T_C)$ for each film of K-series. These averaged values, $\tau_{EP}(T_C)$, are listed in Table 3.6. For NbN films of K-series on Al_2O_3 substrate, applying the acoustic mismatch model we found the critical angle $\overline{\Theta}_{max(AMM)} = 21.8°$ and the transmission coefficient $\eta_0 = 0.985$. Therefore, the ratio $c_{ph,1}/c_{ph} = 1 - \cos(\overline{\Theta}_{max(AMM)})$ for these films is 0.07. We also computed other parameters present in the 2-T and 3-T models and list them in Table 3.6.

To describe experimental response times, τ_ε, we find the theoretical response times τ_ε^* from Eq. (2.34) within the 2-T model and from Eq. (2.37) within the 3-T model using the relation $\delta T_e^2(1/\tau_\varepsilon^*) = 1/2\, \delta T_e^2(0)$. To compute the theoretical dependence $\delta T_e(\omega)$, we fixed values of τ_{EP}, $\tau_{esc,g}$ for the 2-T model and τ_{EP}, τ_{esc}, and $c_{ph,1}/c_{ph}$ for the 3-T model (Table 3.6). This approach leaves us the only one fitting parameter c_e/c_{ph}. The best fit ratios c_e/c_{ph}, i.e. those providing the theoretical response times equal to the experimental response times ($\tau_\varepsilon = \tau_\varepsilon^*$), are listed in Table 3.6. As it was shown in Section 2.4.4.4, the 3-T model offers two best fit

values of c_e/c_{ph}, both correspond to the same τ_ε (the reason of this is discussed there). One of these values is almost independent on the film thickness and $\ll 1$. Such small ratios c_e/c_{ph} for NbN are considerably different from the previously reported ones in [92] and [86]. Therefore, we exclude them from our discussion. The other value of the ratio c_e/c_{ph} offered by the 3-T model is very close to those found within the 2-T model. They monotonously vary from 0.09 for the thickest film with $d = 33.2$ nm to 2.1 for the thinnest film with $d = 3.2$ nm. In both cases, with decreasing the film thickness, the best fit ratios c_e/c_{ph} deviate stronger from those predicted by the Drude and Debye models. The reason for such a discrepancy is discussed in the next section.

3.2.4   Discussion: Effect of the phonon spectrum and film thickness

The analysis of the photoresponse in the time (Section 3.2.2) and frequency domains (Section 3.2.3) for NbN films of M- and K-series, respectively, showed that for very thin films the best fit ratios c_e/c_{ph} obtained within both the 2-T and 3-T models deviate from ratios c_e/c_{ph} predicted by the Debye and Drude models. With respect to normal conduction, the studied NbN film are 3-d (see Section 3.1.1), therefore, we assume that the electron heat capacity is described quantitatively well by the Drude model. Then from the best fit ratios c_e/c_{ph}, we derive the phonon heat capacities. The values c_{ph} computed with the Debye model are shown in Fig. 3.13 together with the best fit values. We assigned averaged values of $N(0)$ and n to films of K-series. However, as seen from Table 3.2 and [101] these parameters vary with thickness. Error bars in the right panel of Fig. 3.13 show corresponding variations in the phonon heat capacities.
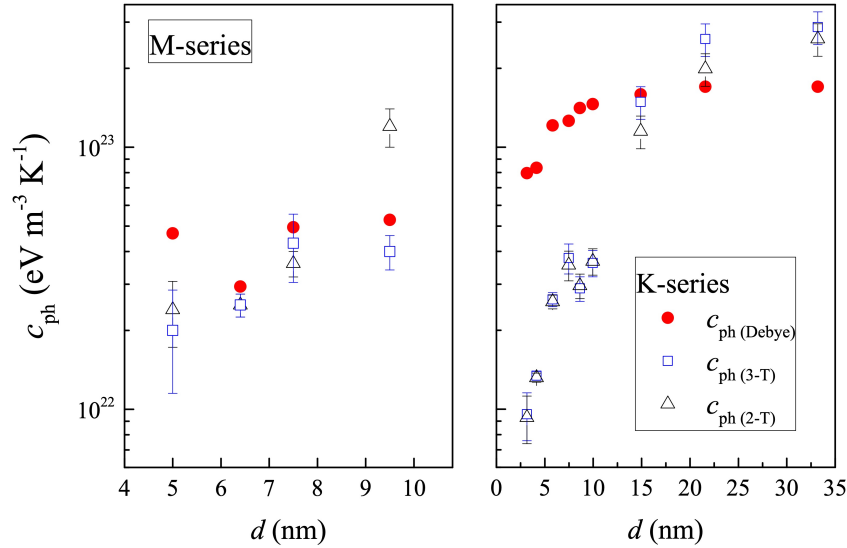

Figure 3.13: Phonon heat capacities vs. film thickness for films of M-series (left panel) and K-series (right panel) in the semi-logarithmic scale. Values $c_{ph(Debye)}$ (closed red symbols) were computed with the 3-d Debye model and phonon velocities found in Section 3.2.1. Values $c_{ph(2-T)}$ and $c_{ph(3-T)}$ were extracted from the best fit ratios c_e/c_{ph} with values of c_e predicted by the Drude model. Error bars in the right graph show the impact of variations in $N(0)$ and the exponent n between films of the K-series.

As seen in Fig. 3.13, in thin films the phonon heat capacities c_{ph} obtained within either the 2-T or 3-T models are less than those computed in the framework of the Debye model is more pronounced for thin films. We attribute such a difference to changes in the phonon spectrum. There are at least two effects which may result in a decrease in the phonon heat capacity in thin films on the substrate. One is depletion of the transverse phonon modes in thin films specifically for the mode with polarization along the normal to the film [122]. Another effect is an increase of the phonon wavelength at low temperatures. In thin films at low temperatures, the phonon wavelength becomes comparable or even larger than the film thickness. This effect eliminates low-energy phonons propagating at small angles Θ and hence destroys isotropy of the phonon spectrum and reduces the phonon density of states. The reduction in the phonon spectrum emitted perpendicularly to the film/substrate interface with the decrease of the film thickness was observed and modeled in [50]. The authors showed that in the restricted direction, the phonon spectrum is modified. Phonon states with small frequencies are forbidden, that resulted in discrete, sharp steps in the number of excited phonons. Qualitatively, this effect reduces the phonon heat capacity, however, quantitatively we cannot estimate it. (ii) Generally, transverse sound velocity is approximately as twice as small than the longitudinal one [48]. According to the Debye model $c_{ph,t(l)} \propto 1/u_{t(l)}^3$. Consequently, the heat capacity of transverse phonons is eigth times larger than of longitudinal phonons. Therefore, the absence of the transverse phonon mode will indeed result in a much lower heat capacity of phonons.

We further estimate the Debye temperature of our NbN films. In the framework of the 3-dimensional Debye model, it is given by $T_D = (\hbar(6\pi^2)^{1/3}\overline{u})/(k_B a_0)$. Assuming $a_0 = 0.44$ nm and $\overline{u} = 2.54$ nm/ps, we found $T_D = 172$ K. Such value is typical for Debye temperatures reported for similar films [123] and is a few times less than the values reported for the bulk NbN material. The reduction of the Debye temperature is usually denoted as "phonon softening" caused by granularity and weakening of ion bonds on film surfaces [124].

3.3   Timing jitter

To probe the intrinsic jitter, we first develop a formalism (Section 3.3.1) that aims to extract the intrinsic jitter from the analysis of experimental data. Then we evaluate all other jitter contributions which are unavoidably present at the experimental setup. Then, in Section 3.3.4, we study the effect of the bias current and magnetic field on the intrinsic jitter. The section contains main experimental findings that clarify and validate existing microscopic models of the photon detection process.
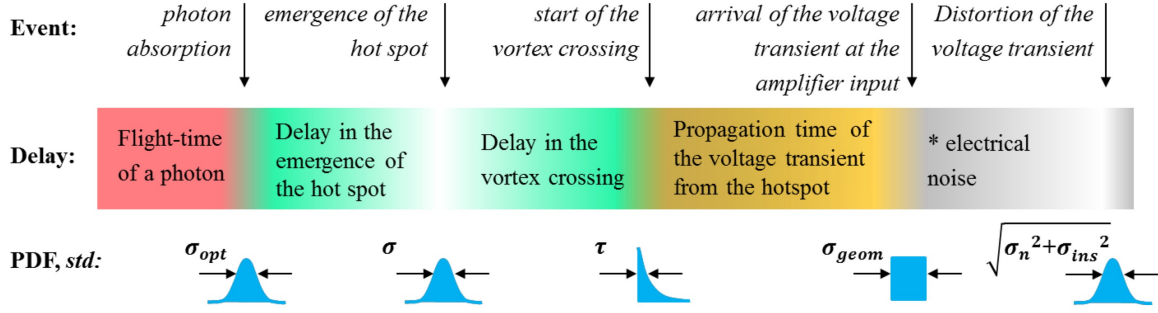
Figure 3.14: Schematic representation of a photon detection event in a nanowire. The detection event is a sequence of elementary events. Each event except for the last contributes to the total delay time and each adds uncertanty to the jitter. The standard deviation of each delay with a particular probability density function is the measure of the corresponding jitter.

3.3.1 Probability density function: Formalism

As discussed in Section 2.2.3, the experimental probability density function (PDF) of the delay time between the arrival of a photon at the optical input of a nanowire and registration of the corresponding voltage transient exhibit a non-Gaussian profile. The profile is well described by exponentially-modified Gaussian distribution. At small delays, such a distribution obeys Gaussian statistics and at large delays exponential one. Non-Gaussian statistics is attributed to intrinsic effects. Here we develop a formalism aiming to extract the intrinsic jitter from the analysis of experimental PDFs where Gaussian and exponential statistics are assigned to different stages of the photon-detection process.

The standard deviation (std), σ, of the PDF is a measure of the timing jitter. It is generally defined as follows

$$\sigma^2 = \int_{-\infty}^{\infty} (t - \mu)^2 \, f(t) \, \mathrm{d}t; \qquad \mu = \int_{-\infty}^{\infty} t \, f(t) \, \mathrm{d}t, \qquad (3.11)$$

where $f(t)$ is the PDF of the random variable t, and μ is the mean value of the PDF.

In Section 2.1, we described a photon-detection process by separating it into several stages. Here we refer to that description and represent a photon-detection event as a sequence of the following elementary events (Fig. 3.14): (1) absorption of a photon in the nanowire, (2) the emergence of the hot spot, (3) the start of vortex crossing, (4) arrival of the voltage transient at the input of the first amplifier, and (5) acquiring the voltage transient with readout electronics (amplifier, scope, timing reference from a fast photodiode, coaxial cables). Each event from (1) to (4) is associated with its time delay (Fig. 3.14). The noise of the amplifier does not introduce a delay, however, it distorts the voltage transient and adds uncertainty to the measured jitter (see Section 2.2.2). The additional instrumental jitter is caused by the timing accuracy of the scope and the timing stability of the reference from a fast photodiode. A contribution to the jitter from coaxial cables as compared to that from the amplifier is negligible. However, the cables add to the time delay. Each time delay is considered as an independent random variable. These

variables are flight time of a photon through the fiber (event 1), time delay in the emergence of the hot spot (event 2), time delay in the start of the vortex crossing (event 3), traveling time of the voltage transient from the hot spot to the amplifier (event 4), and joint contribution of electrical noise and instruments (event 5). The total delay time is a sum of delays associated with the particular events. A PDF of the total delay time or, differently, the whole set of random variables is the joint PDF. Each variable is characterized by a particular PDF. All variables enumerated above are statistically independent, however, those which are affiliated with the adjacent events (from 1 to 4) are connected via conditional probability. A conditional joint PDF for two sequential events implies that the latter event occurs only if and after the earlier has occurred. It is given by [125]

$$f(t) = \int_{-\infty}^{t} f_1(u) f_2(t-u) \mathrm{d}u, \tag{3.12}$$

where $f_1(t)$ and $f_2(t)$ are particular PDFs for two sequential events. The conditional joint PDF given in Eq. (3.12) also implies that $f_2(t) = 0$ at $t < 0$. The adjacent events (4) and (5) are not connected via conditional probability. These two events are connected via the joint PDF:

$$f(t) = \int_{-\infty}^{\infty} f_4(u) f_5(t-u) \mathrm{d}u. \tag{3.13}$$

Therefore, an experimental PDF of the total delay time is described by the joint PDF in the form of a multiple integral [125]

$$F(t) =$$
$$\int_{-\infty}^{\infty} \left\{ \int_{-\infty}^{t_4} \left[\int_{-\infty}^{t_3} \left(\int_{-\infty}^{t_2} f_1(t_1) f_2(t_2 - t_1) \, \mathrm{d}t_1 \right) f_3(t_3 - t_2) \, \mathrm{d}t_2 \right] f_4(t_4 - t_3) \, \mathrm{d}t_3 \right\} f_5(t - t_4) \, \mathrm{d}t_4. \tag{3.14}$$

Now we will describe each particular PDF which enters Eq. (3.14). The PDF of the optical delay added by flight time of a photon through a short single-mode fiber, $f_1(t)$, is Gaussian [39], in the form

$$f_1(t, \sigma_{opt}) = \frac{1}{\sigma_{opt}\sqrt{2\pi}} \exp\left[-\frac{(t-\mu)^2}{2\sigma_{opt}^2} \right], \tag{3.15}$$

where σ_{opt} is the *std* and μ is the mean value. The mean value is defined by the delay time in a setup (flight time of a photon through the fiber, traveling time of a reference signal to the scope, etc). The experimental techniques (subsection 2.2.1) for measuring jitter do not allow for finding the absolute delay time. Therefore, for simplicity of calculations, we take $\mu = 0$. Now we consider the PDF of the delay time in the emergence of the hot spot, $f_2(t)$. As shown in [11], the physical origin of the variance in this delay is Fano fluctuations [126] and spatial non-uniformity of the nanowire. Because both obey Gaussian statistics, we assign to the PDF $f_2(t, \sigma)$ the Gaussian distribution of the same form as Eq. (3.15) but with *std* σ.

Two sequential events (1 and 2) are connected via a conditional probability. Because the delay in the emergence of the hot spot is non-zero, the mean values of $f_1(t, \sigma_{opt})$ and $f_2(t, \sigma)$

are separated by a time delay, Δt. The delay time Δt is the latency in the models of Allmaras et al. [11] and Vodolazov [10]. The conditional joint PDF of two sequential events (1) and (2) (round brackets in Eq. (3.14)) can be evaluated analytically [127] as

$$p(t) = \int_{-\infty}^{t} f_1(u, \sigma_{opt}) f_2(t - \Delta t - u, \sigma) \mathrm{d}u =$$

$$\frac{1}{\sqrt{2\pi(\sigma_{opt}^2 + \sigma^2)}} \exp\left[-\frac{(t - \Delta t)^2}{2(\sigma_{opt}^2 + \sigma^2)}\right] \left(1 + (erf)\left[\frac{t - \Delta t}{\sqrt{2(\sigma_{opt}^2 + \sigma^2)}} \frac{\sigma}{\sigma_{opt}} + \Delta t \frac{\sqrt{\sigma_{opt}^2 + \sigma^2}}{\sigma_{opt}\sigma\sqrt{2}}\right]\right). \tag{3.16}$$

For $\Delta t \geq 2.5\sigma$, the function $p(t)$ is Gaussian with the standard deviation $\sqrt{\sigma_{opt}^2 + \sigma^2}$. With lowering Δt, $p(t)$ quickly becomes asymmetric and non-Gaussian.

The next PDF, $f_3(t)$, is the PDF of the start time of vortex crossing (event 3). Vortex crossing in the presence of the energy barrier is a Poisson process [125, 23]. In that, the start time of a single crossing obeys the same statistics as, e.g., nuclear decay and is described by an exponential PDF in the form

$$f_3(t, \tau) = \frac{1}{\tau} \exp\left(-\frac{t}{\tau}\right). \tag{3.17}$$

For an exponential distribution, both the mean value and the *std* are equal to τ. The conditional joint PDF of the delay times from events (2) and (3) can be analytically derived as

$$g(t, \sigma, \tau) = \int_{-\infty}^{t} f_2(u, \sigma) f_3(t - u, \tau) \mathrm{d}u =$$

$$\frac{1}{2\tau} \exp\left[\frac{1}{2\tau}\left(\frac{\sigma^2}{\tau} - 2t\right)\right]\left[1 - \mathrm{erf}\left(\frac{\frac{\sigma^2}{\tau} - t}{\sigma\sqrt{2}}\right)\right]. \tag{3.18}$$

This distribution is known as an exponentially-modified Gaussian distribution. In Fig. 3.15, we show this PDF for different ratios τ/σ. It can be shown [127] that the *std* and the mean value for this distribution are $\sqrt{\sigma^2 + \tau^2}$ and τ, respectively. This *std* $\sqrt{\sigma^2 + \tau^2}$ corresponds to the local jitter, σ_{loc} (see Section 2.2.2). The function $g(t, \sigma, \tau)$ exhibits a Gaussian shape for $t \leq t_0$ and an exponential tail at $t > t_0$, where t_0 stands for the position of the maximum value of $g(t, \sigma, \tau)$.

Further, it can be shown that the conditional joint PDF of the sequential events (1), (2), and (3) (square brackets in Eq. (3.14)) is also an exponentially-modified Gaussian distribution. It can be described by the function $g(t, \sqrt{\sigma_{opt}^2 + \sigma^2 + \tau^2}, \tau)$ in Eq. (3.18) with the *std* $\sqrt{\sigma_{opt}^2 + \sigma^2 + \tau^2}$ and the mean value τ.

In Section 3.3.3.1 it will be shown that for our experimental conditions, the geometric jitter is negligibly small. Therefore, we skip the PDF for event (4). Finally, we come to the last event in the sequence, (event 5), noise and instrumental contributions. Their PDF is Gaussian (Eq. (3.15)) with the *std* $\sqrt{\sigma_N^2 + \sigma_{ins}^2}$. As noted at the beginning of this section, the last event
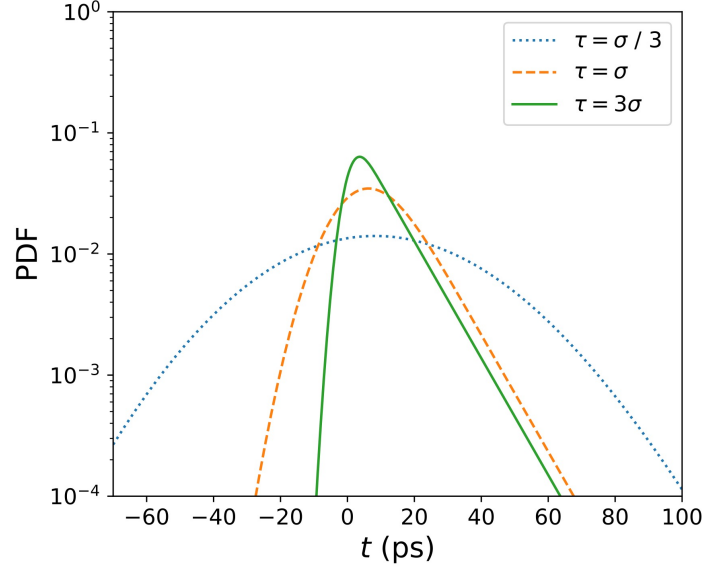
Figure 3.15: Simulated exponentially-modified Gaussian distributions given by Eq. (3.18) for different ratios between τ and σ, where $\tau = 9$ ps.

(5) does not introduce a delay, and therefore it is not connected to the previous event (4) via a conditional PDF. The total joint PDF in Eq. (3.14) is presented by the convolution integral

$$F(t) = \int_{-\infty}^{\infty} g(u, \sqrt{\sigma_{opt}^2 + \sigma^2 + \tau^2}, \tau) f(u - t, \sqrt{\sigma_N^2 + \sigma_{ins}^2}) du =$$

$$\frac{1}{2\tau} \exp\left[\frac{1}{2\tau} \left(\frac{\sigma_{sys}^2}{\tau} - 2t \right) \right] \left[1 - \mathrm{erf}\left(\frac{\frac{\sigma_{sys}^2}{\tau} - 2t}{\sigma_{sys}\sqrt{2}} \right) \right]. \quad (3.19)$$

The resulting PDF, $F(t)$, represents the exponentially-modified Gaussian distribution with the *std* given by

$$\sigma_{sys} = \sqrt{\sigma_{opt}^2 + \sigma^2 + \tau^2 + \sigma_N^2 + \sigma_{ins}^2}. \quad (3.20)$$

Further, this PDF (Eq. (3.19)) is used for fitting experimental PDFs. Experimentally, the *std* of $F(t)$ defines the system jitter.

3.3.2   Experimental approach

Specimens

Jitter measurements were carried out with an NbN nanowire of K0-series on Al_2O_3 substrate described in Section 3.1. The straight nanowire was 5 nm thick, 100 nm wide, and 40 μm long. The transport measurements of the wire showed an experimental critical current of $I_C = 50.2$ μA, a critical temperature of $T_C = 12.55$ K, and a square resistance of $R_{SN} = 260$ Ω/sq. The experimental I_C of the wire is almost twice as less as the depairing current, $I_C/I_{DEP} = 0.57$ (see Section 3.1). Fig. 3.16 shows a scanning-electron-microscope image of the film of K0-series patterned in parallel, geometrically identical nanowires. The only active nanowire was
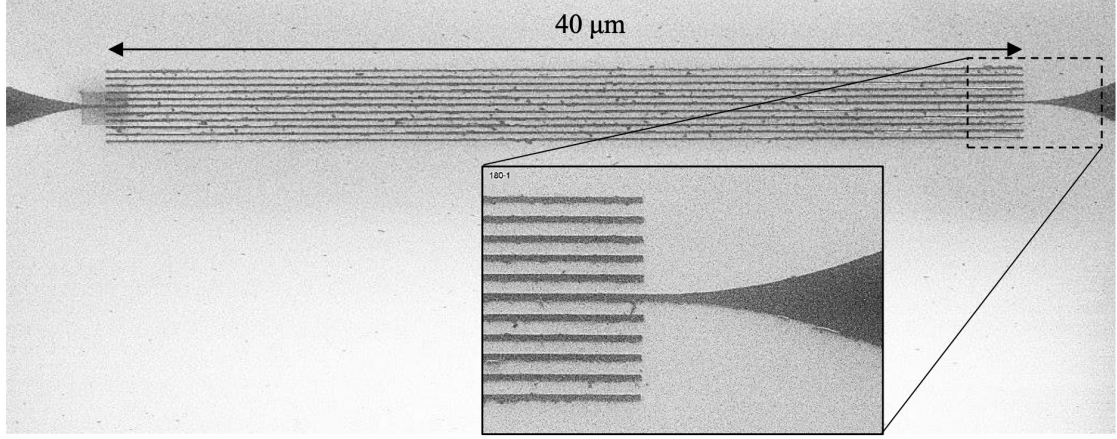
Figure 3.16: Images of the nanowire of K0-series obtained with a scanning electron microscope. The active wire is surrounded by parallel equally spaced and electrically suspended wires of the same width. Dark color represents the NbN film.

surrounded by parallel equally spaced and electrically suspended wires of the same width. It was done in order to eliminate diffraction and obtain the same optical coupling as for meandered wires.

Experimental setup

Jitter measurements were performed at 4.2 K at two wavelengths 800 nm and 1560 nm in a continuous-flow cryostat with a quartz window (either a dipstick immersed in a Dewar with liquid helium). To minimize contributions to the system jitter from optics and readout electronics, we used short-pulse light sources and low noise electrical readout. A 800 nm Ti-sapphire laser (Femtosource, synergy 20) and a 1560 nm fiber-based laser (C-Fiber, Menlo Systems) generated the optical pulses with a duration (*std*) of 17 and 27 fs at a repetition rate of 80 and 100 MHz, respectively. The laser power was controlled by a powermeter (Thorlabs, PM100 with S120UV sensor for 800 nm and PM20C for 1560 nm) and could be adjusted by a variable attenuator placed between the laser and the fiber input (either the cryostat). Fig. 3.17 schematically illustrates the experimental setup. The active nanowire was uniformly illuminated by laser pulses. The light from lasers was coupled to the nanowire either via single-mode fibers (SM980 for 800 nm and SMF28 for 1560 nm) or in free space. To ensure the uniform illumination for the fiber-coupled light between the nanowire and the fiber end, there was a distance of 15 mm. So that the light spot on the nanowire plane had a diameter of 2 mm. A chip with the nanowire was mounted on a holder together with a temperature sensor and a heater and was kept at the temperature 4.2 K. The temperature was controlled with a temperature controller (LakeShore, Model 331). We used a conventional method to read out the nanowire response where the nanowire builds a part of the central strip in a shortened coplanar line (more details in Section 3.3.3.1). On the holder, one end of the active nanowire was connected to the shortened coplanar line via bonding and the other one to the ground plane. So that the nanowire had one common output. A coaxial cable connected the coplanar line and a bias-tee. The bias-tee was plugged to the SMA output of the cryostat (either the dipstick). The wire was biased by a small direct current from a battery-
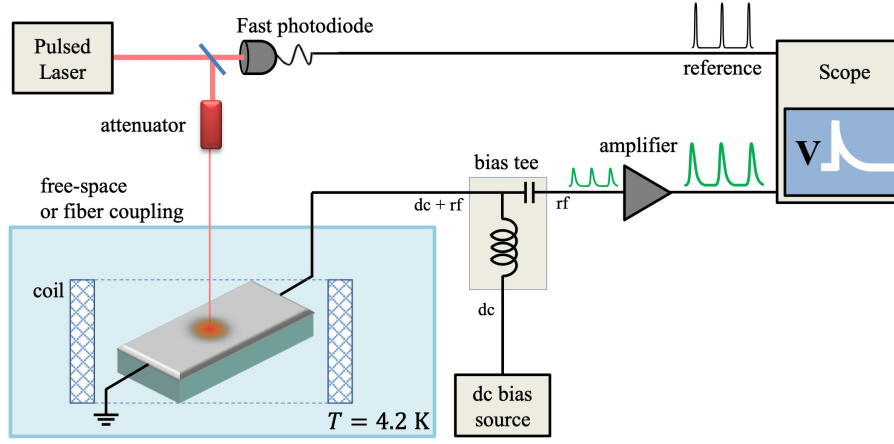
Figure 3.17: Schematic block diagram of the experimental setup for measuring the timing jitter. The light from a pulsed laser (either at 800 nm or 1560 nm) is sent to a sample via a single-mode fiber (either in free space through a quartz window of a cryostat). Rf and dc paths are de-coupled at room temperature with a bias-tee. Voltage transients from the sample are amplified at room temperature before they are recorded by a scope (either sampling or real-time). The relative power of incoming light from the laser is adjusted by an attenuator. For measuring the jitter in magnetic field, a superconducting solenoid was used to create the magnetic field perpendicularly to the sample substrate.

powered dc source. The nanowire response, a voltage transient, was amplified by a low noise amplifier with a bandwidth from 100 MHz to 8 GHz, which was connected directly to the bias-tee. Further, voltage transients were acquired with a scope connected to the amplifier through a coaxial cable. We used a sampling scope (Keysight Infiniium DCA-X 86100D) with a bandwidth of 50 GHz or, alternatively, a real-time oscilloscope (Keysight Infiniium X-series 93204A) with an effective bandwidth of 33 GHz for both active channels. The effects of the photon flux and bias currents on the jitter (Section 3.3.3.3 and 3.3.4) were studied in the cryostat. It allowed us to couple the light from lasers to the nanowire in free space and drastically minimize the optical contribution to the jitter. For measurements in the magnetic field (Section 3.3.4), we used the dipstick with a superconducting solenoid, which was immersed in a Dewar with liquid helium. In the dipstick, the laser light was coupled to the nanowire via optical fibers. The magnetic field was applied perpendicularly to the sample substrate.

Experimental PDF

We consider the time delay between the arrival of a photon at the fiber input (either directly at the nanowire when free-space coupling used) and arrival of the corresponding voltage transient to the scope as a random variable. To obtain the PDF of the arrival time, we measured the difference between arrival times of two voltage transients appearing at two different channels of the real-time scope (either the sampling scope that is discussed further). As shown in Fig. 3.17, one of the transients was generated by a fast photodiode, which was illuminated by the same laser, while the other was generated by the nanowire itself. Triggering was done at the rising edge of the voltage transient from the nanowire. To eliminate the contribution to the jitter due to amplitude fluctuations, the arrival times of the transients were measured at the 50% level of their instantaneous amplitudes. To build one PDF, we accumulated 10 000 measurements. The
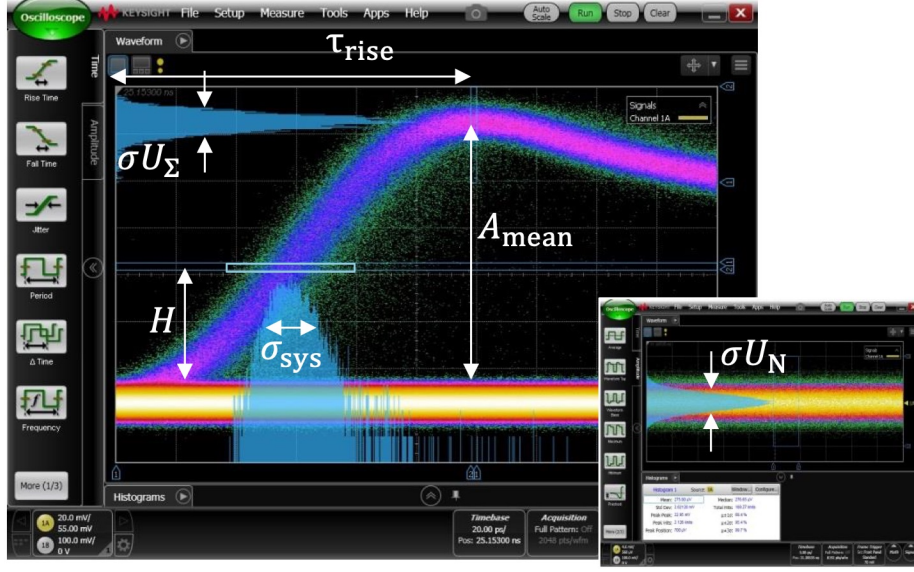
Figure 3.18: Screen shot from the sampling scope shows the rising edge of many voltage transients acquired in a persistence display mode. The inset shows the histogram of noise in the base line.

system jitter was obtained either as the numerical *std* (Eq. (3.11)) of the experimental PDF or the *std* of the fitting exponentially-modified Gaussian distribution (Eq. (3.19)). Std for the noise contribution to the system jitter was estimated as $\sigma_N = \sigma_{U_N} \tau_{rise}/A_{mean}$ (Eq. 2.1). When the sampling scope was used, triggering was done by the transient from the fast photodiode, while the transient from the nanowire was acquired. To build one PDF, we accumulated 10 000 points inside an acquisition window on the rising edge of the voltage transient from the nanowire (shown by the rectangle in Fig. 3.18). The arrival time of the transient was associated with the time when the points from this transient appear within the window. The contribution to the system jitter due to amplitude fluctuations was estimated as $\sigma_{amp} = \sqrt{\sigma_{U_\Sigma}^2 - \sigma_{U_N}^2}\, \tau_{rise}\, H/A_{mean}^2$ (the parameters are defined in Eq. (2.2) and also shown in Fig. 3.18). In our measurements, this contribution had a Gaussian distribution and amounted to only a fraction of the noise jitter $\sigma_{amp} = (0.34 - 0.51)\sigma_N$ in the range of the relative bias currents $I_B = (0.9 - 0.7)I_C$.

3.3.3 Jitter contributions

3.3.3.1 Geometric jitter

In Section 2.2.2 we gave estimations for the geometric jitter in the differential readout method. However, as it will be shown bellow, for our nanowire of 40 μm long, the geometric jitter in the conventional readout method is negligible. Moreover, this method is easier to implement as compared to the differential one. Therefore, in our measurements, we used the conventional readout method, i.e. a shortened coplanar line which is schematically illustrated in Fig. 3.19.
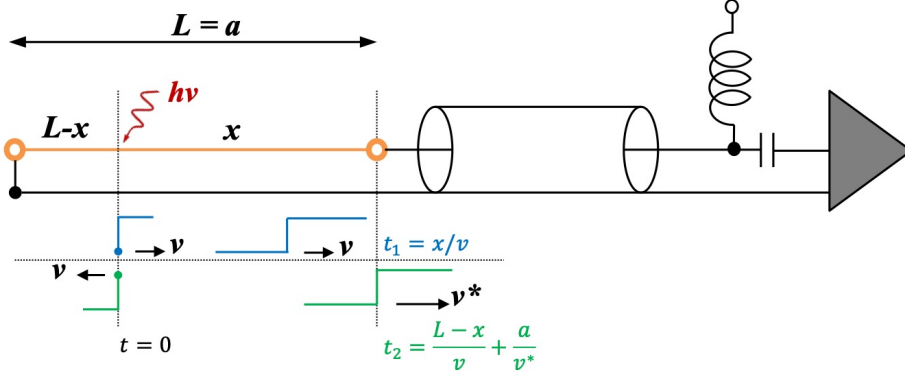
Figure 3.19: Schematic representation of the propagation of the voltage transient in a straight nanowire connected to a shortened coplanar line.

At the photon absorption site after the formation of the normal domain, two current steps are generated. They have opposite polarities and propagate to opposite directions along the nanowire of length L with velocity $v \approx 12$ μm/ps [40]. One of the current steps propagates to the shortened end, is reflected and then propagates via the outer ground plane of the coplanar line. The propagation velocity in the ground plane of the coplanar line is (on the sapphire substrate) $v^* \approx 140$ μm/ps. The outer size a between nanowire contacts depends on the layout. For meander layouts a is less than the length of a meandered nanowire, $a < L$, while for layouts with straight wires $a = L$. The maximum difference between arrival times of two current steps at the input of the amplifier is $|t_1 - t_2| = x/v + ((L - x)/v + a/v*) \sim L/v$. Here L is the nanowire length and $x \in [0; L]$ is the longitudinal random variable assigned to each photon absorption site along the nanowire. As an example, in Fig. 3.20 we show computed voltage steps before, $U_{in}(t)$, and after, $U_{out}(t)$, the amplifier for several absorption sites x along a 1000 μm long nanowire. Amplified voltage steps in Fig. 3.20(b) were computed with Eqs. (2.31 and 2.32) for the bandwidth 50 MHz – 4.5 GHz. As seen in Fig. 3.20(b), the difference in arrival times of voltage transients for such a long nanowire is resolved by the readout electronics with a given bandwidth that will result in the geometric jitter.

If the time difference is much less than the time resolution of the readout electronics, the two voltage steps cannot be resolved. This situation is shown in Fig. 3.21 for a 40 μm long nanowire and the same bandwidth of the readout electronics (50 MHz – 4.5 GHz). This corresponds to our experimental conditions. As seen in Fig. 3.21(b), all amplified voltage steps exhibit the same rising edges. Therefore, it does not introduce an additional jitter. However, in the shortened coplanar line, another source of the geometric jitter may appear. It is the difference in dispersion and losses in the superconducting nanowire and in the ground plane. This difference results in the effective propagation velocity. In [38], the effective velocity of 70 μm/ps was found for NbN meandered nanowires with parameters similar to our nanowires. This scenario results in the geometric jitter < 1 ps. Hence, further, we exclude the geometric jitter from the analysis. It is worth mentioning that in our simulations, we neglected electrical reflections at both ends of the nanowire, which occur due to impedance mismatch.
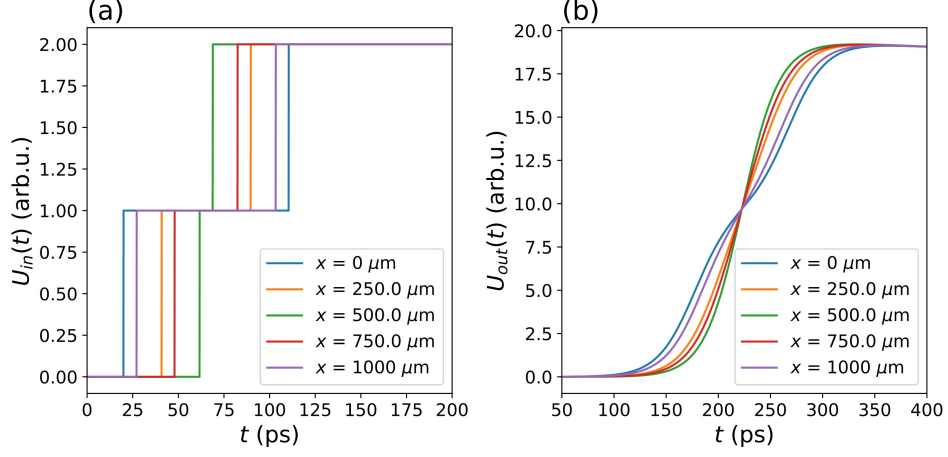
76

Figure 3.20: (a) Computed voltage steps arriving at a reference plane before amplifier for five absorption sites $x = 0$, $L/4$, $L/2$, $3L/4$, L, where $L = 1000$ μm. (b) Rising edges of amplified voltage steps were computed with Eqs. (2.31 and 2.32). In simulations reflections at both ends of the nanowire due to impedance mismatch, and also the difference in dispersion and losses in the nanowire and in the ground plane were neglected.

3.3.3.2 Fiber coupling: Optical jitter

In order to estimate the optical contribution, σ_{opt}, to the jitter due to chromatic dispersion in single-mode fibers (Eq. (2.4)), we first characterize the spectral width, σ_λ, of the optical pulses. The spectrum of the 800 nm Ti-sapphire laser in a pulsed mode was acquired with a spectrometer (OceanOptics, USB4000). Fig. 3.22(a) shows this spectrum with the central wavelength $\lambda_0 \approx$ 800 nm. This spectrum is well described by a Gaussian distribution with a *std* of $\sigma_\lambda = 19$ nm. At this central wavelength, for the fibers we used (SM980 and SMF28), the material dispersion coefficient is $D_m = $ - 120 ps/(km nm). Therefore, we expected the optical jitter per fiber length to amount to 2.3 ps/m. The spectrum for the 1560 nm fiber-based laser in a pulsed mode
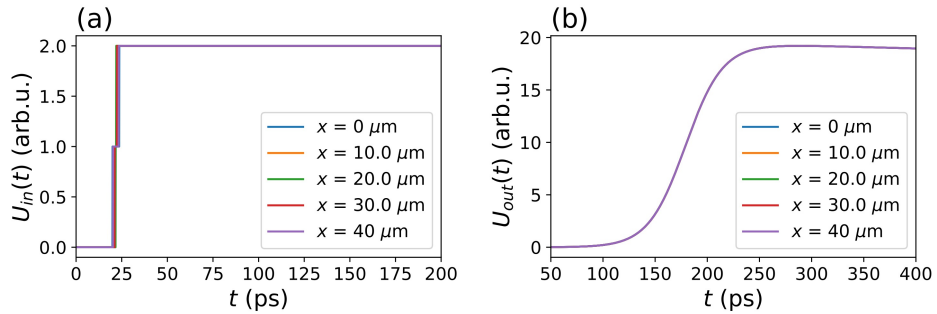

Figure 3.21: (a) Computed voltage steps arriving at a reference plane before amplifier for five absorption sites $x = 0$, $L/4$, $L/2$, $3L/4$, L, where $L = 40$ μm. (b) Rising edges of amplified voltage steps were computed with Eqs. (2.31 and 2.32). In simulations reflections at both ends of the nanowire due to impedance mismatch, and also the difference in dispersion and losses in the nanowire and in the ground plane were neglected.
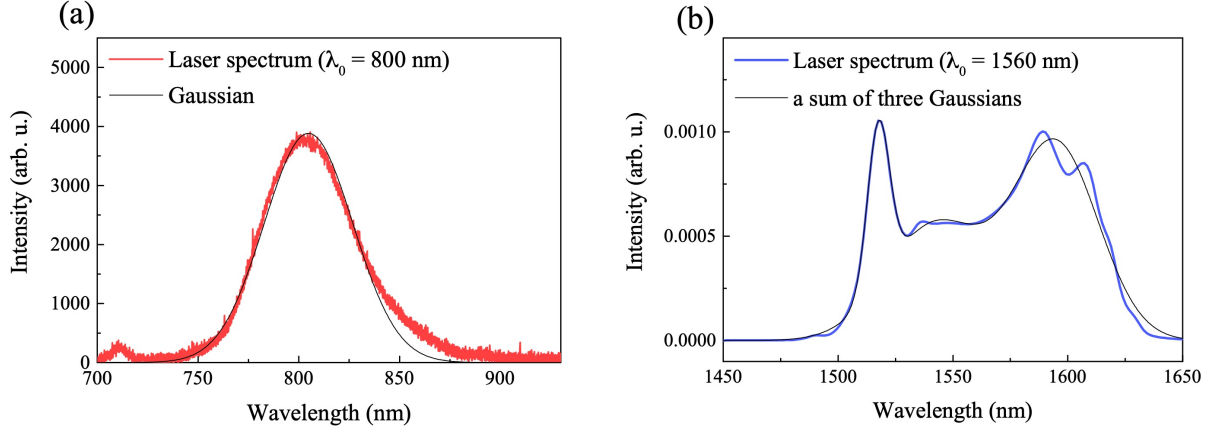
Figure 3.22: Spectra of lasers in pulsed mode with a central wavelength at (a) 800 nm and (b) 1560 nm. Solid black curves are fits with (a) one Gaussian and (b) a sum of three Gaussians.

was taken from a data sheet provided by manufacturers. Fig. 3.22(b) shows the spectrum with $\lambda_0 \approx 1560$ nm. This spectrum can be described by a sum of three Gaussians with a total *std* of $\sigma_\lambda = 28.6$ nm given by the square root of the sum of the squares of a particular *std*. For the fiber SMF28 at 1560 nm, the coefficient $D_m = $ - 18 ps/(km nm) that results in an optical jitter of 0.5 ps/m. The parameters characterizing lasers pulses are listed in Table 3.7.

The optical contributions to the jitter introduced by fibers at 800 and 1560 nm were evaluated experimentally as well. For this, we carried out several measurements by varying the length and the type of fibers placed between the laser and the nanowire, while the rest of the experimental conditions (bias current, light intensity, etc.) were the same. Some of the experimental PDFs of the delay time are plotted with symbols in Fig. 3.23. Fig. 3.23(a) shows experimental PDFs acquired at the wavelength 800 nm and the relative bias current 0.9 I_C. The PDFs are normalized to one and shifted to zero delay. The narrower PDF (open symbols) was measured with a 4 m long fiber and the wider one with a 9 m long fiber. The former PDF exhibits an almost Gaussian shape (black curve) while the latter is asymmetric with a tail extended to larger delays. Further, each measured PDF we fitted with Eq. (3.19) in the framework of the formalism described in Section 3.3.1. It allowed us to evaluate the optical contribution to the

Table 3.7: Parameters of the laser pulses and the optical jitter in the experimental setup

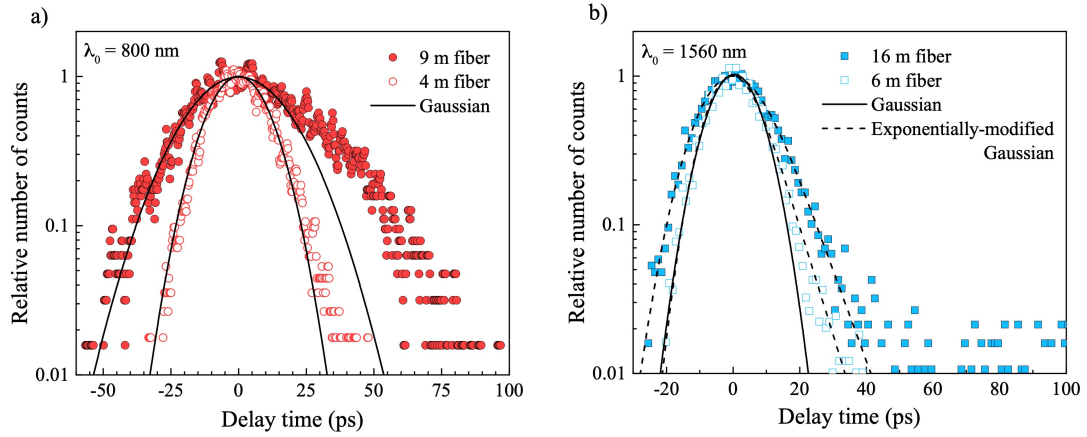| λ_0 (nm)	σ_t (fs)	σ_λ (nm)	SM980 fiber theor.	SM980 fiber exp.	SMF28 fiber theor.	SMF28 fiber exper.	σ_{opt} in the setup with the fiber-coupled light
			σ_{opt} (ps/m)	
800	17	19	2.3	2.4 ± 0.5	2.3	3.9 ± 0.5	$\sigma_{opt} = 8.0$ ps (2 m of SM980 and 2 m of SMF28 fibers)
1560	27	28.6			0.5	0.5 ± 0.1	$\sigma_{opt} = 3.0$ ps (6 m of SMF28 fiber)

Figure 3.23: PDF of the delay time obtained for a straight nanowire at 4.2 K and two wavelengths. Maxima of PDFs were normalized to one and shifted to zero delay. PDFs were obtained (a) at the relative bias current 0.9 I_C and 800 nm wavelength by use of 9 m (closed symbols) and 4 m (open symbols) long fibers (combined from two fiber types SMF28 and SM980), (b) at 0.95 I_C, 1560 nm by use of 16 m (open symbols) and 6 m (closed symbols) of SMF28 fibers. Solid curves are fits with a Gaussian distribution, and dashed curves are fits with an exponentially-modified Gaussian distribution (Eq. (3.18))

jitter that amounts to 2.4 ± 0.5 at 800 nm and 3.9 ± 0.5 ps/m in SM980 and SMF28 fibers, respectively [128]. The jitter added by the fiber SMF28 at 800 nm is larger because the fiber at this wavelength operates at the border of the single-mode regime. Fig. 3.23(b) shows with symbols two experimental PDFs acquired at 1560 nm at the relative bias current 0.95 I_C by use of 16 m and 6 m of SMF28 fiber. The evaluated optical jitter amounts to 0.5 ± 0.1 ps/nm. The optical jitters evaluated experimentally at 1560 nm in SMF28 and 800 nm in SM980 fibers agree well with estimations due to the chromatic dispersion alone. Our experimental setup with a superconducting solenoid, which unavoidably includes fibers, is characterized by the optical jitter σ_{opt} = 3 ps at 1560 nm (6 m of SMF28 fiber) and σ_{opt} = 8 ps at 800 nm (2 m of SM980 and 2 m of SMF28 fibers). All evaluated σ_{opt} are listed in Table 3.7.

3.3.3.3 Free-space optical coupling: Effect of photon flux, local jitter

The effect of photon flux was studied with free-space optical coupling in a continuous-flow cryostat. Removing optical fibers excludes the optical contribution due to chromatic dispersion in the fiber material. The only remaining contribution to the optical jitter comes from the temporal width of the laser pulses, that is negligible in our experiment (17 fs at 800 nm and 27 fs at 1560 nm). Thus optical coupling in free space eliminates the optical jitter. We carried out jitter measurements with free-space optical coupling at both wavelengths (800 nm and 1560 nm) and a relative bias current $I_B = 0.88 I_C$. Two experimental PDFs shown in Fig. 3.24 with circles and squares were measured at relatively small photon flux ($\approx 10^{-3}$ arb.u.). The
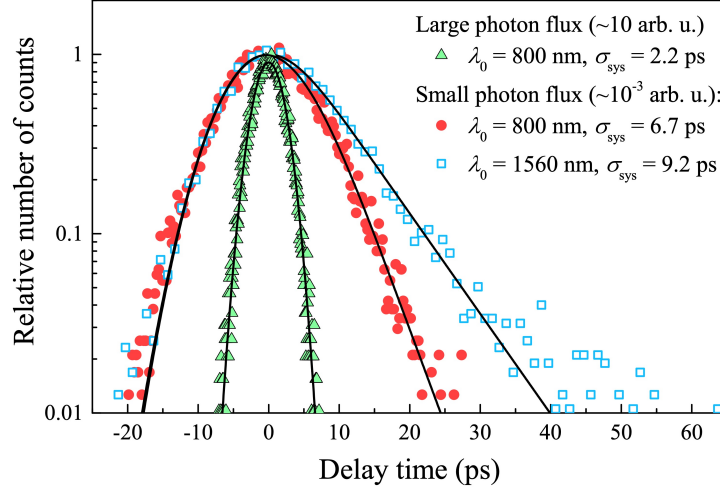
Figure 3.24: PDF of delay time measured for two wavelengths and two different photon fluxes at a fixed relative current of 0.88 I_C, at the wavelength 800 nm (circles) and 1560 nm (squares) with relatively small flux ($\approx 10^{-3}$ arb.u.) and at the wavelength 800 nm (triangles) with relatively large flux (≈ 10 arb.u.). Maxima of PDFs were normalized to one and shifted to zero delay. The solid curves show the best fits described in Section 3.3.1. The legend specifies the system jitter (numeric *std*) for corresponding PDFs.

relative photon flux incident on the nanowire was controlled with a powermeter inserted in front of the cryostat and adjusted with a variable attenuator. Then, at 800 nm, we considerably increased the photon flux (up to ≈ 10 arb.u.) by decreasing the attenuation and repeated the measurements. The PDF measured at large photon flux is shown in Fig. 3.24 with triangles. This PDF is considerably narrower as compared to two PDFs measured with small photon flux. Moreover, the narrowest PDF exhibits a pure Gaussian shape, while the other two are better discribed by an exponentially-modified Gaussian distribution (Eq. (3.18)). The corresponding distributions are shown in Fig. 3.24 with lines. The *std* of each PDF amounts to $\sigma_{sys} = 6.7$ ps for 800 nm and $\sigma_{sys} = 9.2$ ps for 1560 nm with small photon flux and $\sigma_{sys} = 2.2$ ps for 800 nm with large photon flux. These values are listed in Table 3.8.

To qualitatively characterize the difference between detection regimes at small and large photon fluxes, we carried out the following measurements. At a fixed current $I_B = 0.88 I_C$, by varying the photon flux at 800 nm, we measured the amplitude of the voltage transient and the count rate, i.e. the number of voltage transients from the nanowire that crossed a trigger value of the scope. Fig. 3.25(a) shows the amplitude of the voltage transient vs. photon flux. As seen in the figure, for relatively small photon fluxes $10^{-3} - 10^{-2}$ arb.u., the amplitude of the voltage transient remains constant and then grows with a further increase in the flux. At large fluxes, the amplitude saturates as it is shown in the inset to Fig. 3.25(a) on the linear flux scale. Fig. 3.25(b) shows a current dependence of the count rate obtained at small ($\sim 10^{-3}$ arb.u.) and large (~ 10 arb.u.) photon fluxes. Depending on the flux, the current dependence of the count rate changes significantly. At small flux, the dependence has a shape typical for the single-photon detection regime. At large photon flux, it exhibits a saturated plateau, which is equal to a laser repetition rate of 80 MHz. This rate is smaller than the fastest count rate
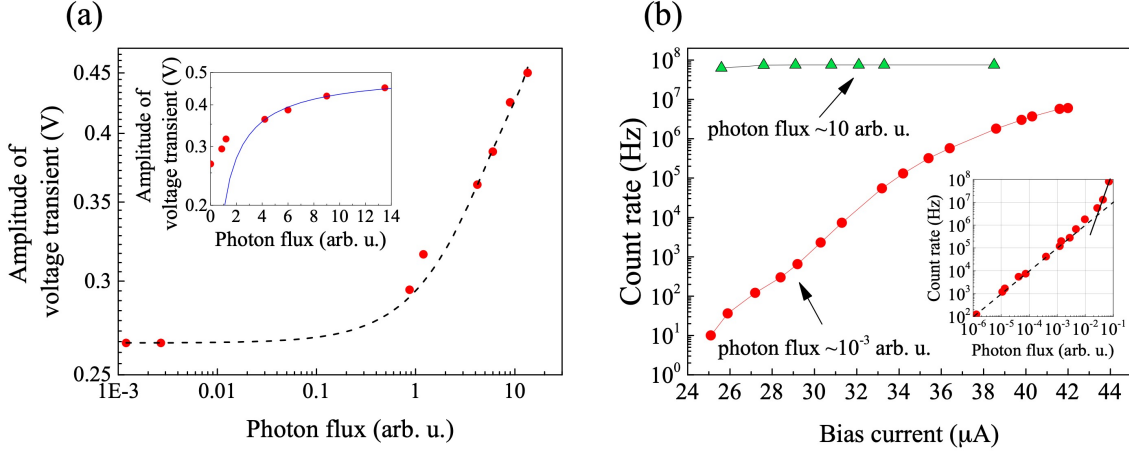
Figure 3.25: (a) Amplitude of the voltage transient at 800 nm and fixed relative current of 0.88 I_C vs. photon flux. The dashed curve is a guide to the eye. The inset shows the same data on the linear flux scale. The solid curve in the inset is the best fit described in the text. (b) Counte rate vs. bias current at 800 nm for two different relative photon fluxes $\approx 10^{-3}$ and ≈ 10 arb.u. The solid curves are guides to the eye. The inset shows the dependence of the count rate on the photon flux in the double logarithmic scale. The dashed straight line in the inset shows the best linear fit. The solid line in the inset depicts an approximately cubic increase in the count rate at large photon fluxes.

of the nanowire (500 MHz), which is defined by the reciprocal recovery time of the nanowire (2 ns). At large photon fluxes, each laser pulse contains a large number of photons in a very narrow timing frame (the width of the optical pulse). The nanowire counts optical pulses rather than photons. This leads to the saturated count rate equal to the laser repetition rate. The inset in Fig. 3.25(a) shows the count rate vs. photon flux measured at the fixed bias current 0.88 I_C. It is seen that at small fluxes, the count rate grows linearly with the flux (dashed line) that indicates the single-photon detection regime. While at large fluxes, the dependence becomes super-linear (solid line) that corresponds to the saturated plateau in the count rate vs. current. Such a saturation indicates the multi-photon detection regime at which many photons are absorbed simultaneously. With increasing photon flux, the multi-photon regime remains discrete until the number of absorbed photons becomes so large that the mean distance between adjacent hot spots equals the mean size of hot spots. The further increase in the photon flux results in uniform heating of electrons in the nanowire, i.e. the non-equilibrium state of electrons in the nanowire becomes uniform. To denote such a uniform, multi-photon detection regime, we use the term bolometric regime. The transition from the discrete, single-photon regime to the uniform, multi-photon (bolometric) regime is supported by the flux dependence of the voltage amplitude, which saturates at large fluxes (the inset in Fig. 3.25(a)). The fitting curve shown in the inset in Fig. 3.25(a) was obtained with an expression $f(x) = (a\ bx)/(Z_0 + bx)$, where $Z_0 = 50\ \Omega$ is the load impedance, bx is the resistance of the normal domain in the nanowire proportional to the photon flux x, and a and b are adjustable parameters. The best fit values of $a = 0.5$ and $b = 31$. For $b = 31$ at the photon flux $x = 10$, the resistance of the emerged domain is 310 Ω. Extrapolating to the discrete single-photon regime with the kinetic inductance of our wire 6 nH and the flux-independent rise time of the transient 70 ps, we arrive at the resistance of the normal domain in excess of 400 Ω that corresponds to the value estimated in the framework

Table 3.8: Jitter contributions for small and large photon fluxes. For free-space optical coupling the local jitter was computed as $\sigma_{loc} = \sqrt{\sigma_{sys}^2 - \sigma_{ins}^2 - \sigma_N^2}$. The σ is a component of the local jitter, the *std* of the growth time of the hot spot.

photon flux (arb. u.)	λ_0 (nm)	I_B/I_C	σ_{sys} (ps)	σ_N (ps)	σ_{loc} (ps)	σ (ps)	comments
$\sim 10^{-3}$	800		6.7	2.0	6.1	4.3	single-photon regime
	1560	0.88	9.2	3.9	8.2	3.1	
~ 10	800		2.2	1.2			bolometric regime

of the electro-thermal model [28].

The PDF measured in the bolometric detection regime (Fig. 3.24 triangles) has much smaller *std* ($\sigma_{sys} = 2.2$ ps) as compared to the PDF obtained in the discrete, single-photon regime ($\sigma_{sys} = 6.7$ ps at) at the same wavelength (see Table 3.8). This is because the bolometric, multi-photon detection regime eliminates the intrinsic jitter (see Section 2.2.2). Indeed, a large number of photon absorption sites evenly distributed over the nanowire excludes a position dependence of traveling times of the voltage transient, i.e. eliminates the geometric jitter. In the limit of a large number of absorption sites, the local jitter associated with the difference in the growth time of the hot spot, or, differently, in the energy released at different absorption sites (occurring due to Fano fluctuations) is averaged out. The same is true for the local jitter associated with the start time of vortex crossing. Hence, in the bolometric regime, the system jitter only includes an instrumental contribution (scope, laser, and cables), σ_{ins}, and a contribution from electrical noise, σ_N, i.e. $\sigma_{sys} = \sqrt{\sigma_{ins}^2 + \sigma_N^2}$. At $I_B = 0.88 I_C$ in the bolometric regime, $\sigma_N = 1.2$ ps that results in $\sigma_{ins} = 1.8$ ps. In the single-photon regime, the local and geometric jitters are present so that $\sigma_{sys} = \sqrt{\sigma_{ins}^2 + \sigma_N^2 + \sigma_{loc}^2 + \sigma_{geom}^2}$. At $I_B = 0.88 I_C$ in the single-photon regime, $\sigma_N = 2.0$ ps at the wavelength 800 nm (circles in Fig. 3.24) and $\sigma_N = 3.9$ ps at the wavelength 1560 nm (squares Fig. 3.24). Here the difference in the noise jitter is due to the difference in readout electronics. Therefore the instrument- and noise-free jitter amounts to 6.1 ps at 800 nm and 8.2 ps at 1560 nm. In the limit of negligibly small geometric jitter, which is estimated to be < 1 ps in our experiment (see Section 3.3.3.1), these values are entirely defined by the local jitter. The derived jitter contributions are listed in Table 3.8.

It is worth mentioning that *std*-s of experimental PDFs measured with and without optical fibers agree well with the system jitter expected by applying the formalism developed in Section 3.3.1, i.e. when each component of the system jitter was derived independently $\sigma_{sys} = \sqrt{\sigma_{opt}^2 + \sigma_{loc}^2 + \sigma_{ins}^2 + \sigma_N^2}$. Such an agreement verifies the applied approach.

As shown in Section 3.3.1, the local jitter can be represented as $\sigma_{loc} = \sqrt{\sigma^2 + \tau^2}$, where σ is the *std* of the growth time of the hot spot, and τ is the *std* of the start time of vortex crossing. At 0.88 I_C in the single-photon regime at 800 nm, $\sigma = 4.3$ ps and at 1560 nm $\sigma = 3.1$ ps. The ratio between these two values is very close to the reciprocal square root of the corresponding wavelengths. Exactly this ratio is expected for Fano fluctuations which

provide standard deviation in the number of excited electrons $\sigma_E = \sqrt{\varepsilon\,F\,\hbar\omega\,\Delta}$, where Δ is the superconducting energy gap, $\varepsilon \approx 0.55$ is the quantum yield, and $F = 0.2$ - 0.4 is the Fano factor. The impact of Fano fluctuations will be discussed in more details in Section 3.3.5.

To summarise, we applied the formalism described in Section 3.3.1 to analyze raw experimental PDFs. We evaluated different contributions to the jitter originated from optics, electrical noise, instruments, and the nanowire itself. We found that the system jitter computed as numerical *std* of an experimental PDF agrees well with the system jitter consisted of contributions found independently. The equality between expected and measured *std*-s holds for PDFs measured at different currents, with very different contributions from optics and electrical noise. This verifies the applied formalism (Section 3.3.1). The formalism is also used in the next section where we evaluate components of the local jitter and study the effect of current and magnetic field on it.

3.3.4   Effect of current and magnetic field on the local jitter

We start with studying a general effect of the magnetic field and the bias current on the noise-free system jitter. The noise-free system jitter we define as follows $\sigma_s = \sqrt{\sigma_{sys}^2 - \sigma_N^2}$, where σ_N is the noise contribution. Except for the local jitter, all other contributions to the noise-free system jitter are independent on the bias current and magnetic field. Therefore, we expect that current and magnetic field dependences of the noise-free system jitter reveal all characteristic features of the local jitter. Further, by applying the formalism described in Section 3.3.1, we evaluate components of the local jitter, σ and τ, at different bias currents and magnetic fields.

Fiber coupling: Jitter in magnetic fields
The effect of the magnetic field was studied with fiber coupling in a dipstick with a superconducting solenoid. The magnetic field was applied perpendicularly to the nanowire surface. In the setup with the fiber-coupled light, the optical jitter was evaluated in Section 3.3.3.2, and it amounts to 8 ps at 800 nm and 3 ps at 1560 nm. The jitter measurements were carried out at both wavelengths, different magnetic fields, and bias currents $0.63I_C$, $0.7I_C$, and $0.75I_C$ for 800 nm and $0.75I_C$, $0.8I_C$, and $0.85I_C$ for 1560 nm. Here we refer to the critical current, I_C, as the critical current at zero magnetic field. Some of the experimental PDFs are shown in Fig. 3.26 (with symbols). Fig. 3.26(a) shows PDFs measured at 800 nm and the relative bias current $0.63I_C$. Fig. 3.26(b) shows PDFs measured at 1560 nm and $I_B = 0.75I_C$. As seen in Fig. 3.26, at $B = 0$ mT, the PDFs for both wavelengths are narrower and less asymmetrical exhibiting close to Gaussian shapes. With the magnetic field, the exponential tail at large delay times appears, while at small delay times (the left part from the PDF maximum), the PDFs retain Gaussian shapes. The slope of the exponential tail decreases with the field that corresponds to an increase in the characteristic exponential time. At both wavelengths, the Gaussian part of PDFs, i.e. the left part from the PDF maximum, slowly grows with the magnetic field, while the exponential tail grows faster. The solid curves in Fig. 3.26 show the best fits according to
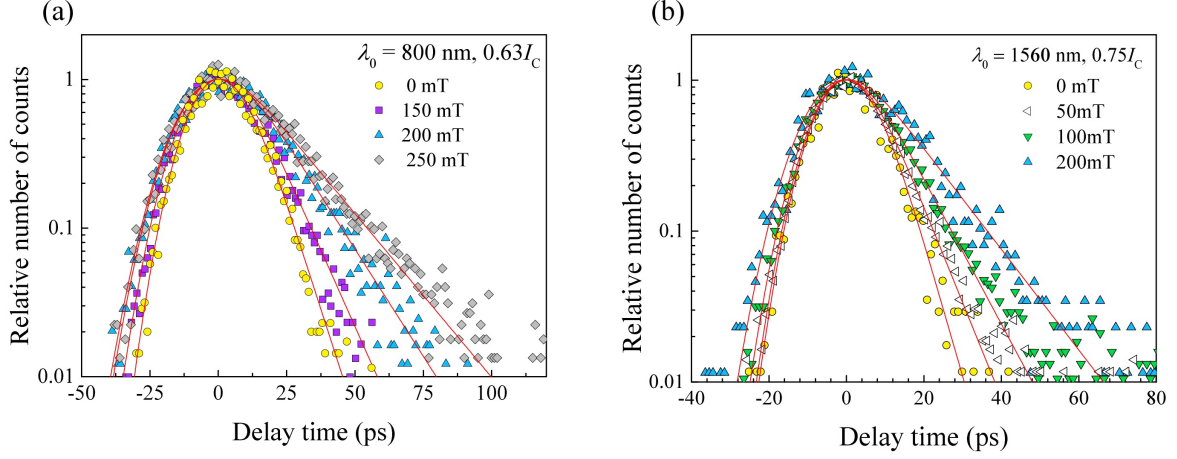
Figure 3.26: Experimental PDFs (symbols) in different magnetic fields. Maxima of PDFs were normalized to one and shifted to zero delay. (a) Data for the wavelength 800 nm were obtained at current $0.63I_C$ and magnetic fields 0, 150, 200, and 250 mT. (b) Data for the wavelength 1560 nm were obtained at $0.75I_C$ and magnetic fields 0, 50, 100, and 200 mT. Solid lines show best fits according to Eq. (3.19).

the exponentially-modified Gaussian distribution (Eq. (3.19)). For each experimental PDF, we define the system jitter and the noise jitter. Then, subtracting the noise contribution from the system jitter, we obtained a noise-free system jitter. The derived jitter contributions for both wavelengths (at some currents and magnetic fields) are listed in Table 3.9.

Fig. 3.27(a) shows the noise-free system jitter, σ_s. At both wavelengths, the σ_s increases with the magnetic field. At 800 nm, the σ_s saturates with a decrease in the magnetic field. It is because the σ_s includes the optical contribution, which is considerably larger at 800 nm
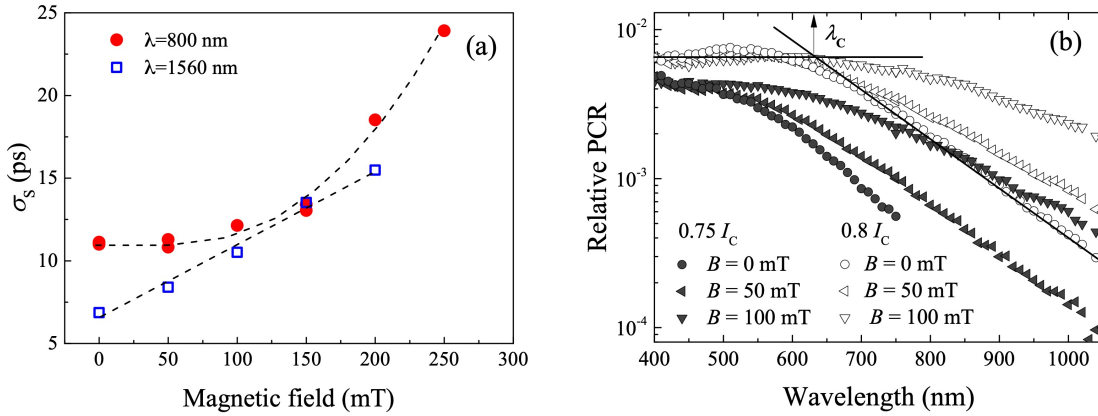

Figure 3.27: (a) Noise-free system jitter at different magnetic fields. Data were obtained for the wavelengths 800 nm at currents $0.63I_C$, $0.7I_C$, and $0.75\ I_C$ and for 1560 nm at currents $0.75I_C$, $0.8I_C$, and $0.85I_C$. The dashed lines are to guide the eyes. (b) Spectra of the relative count rate at different magnetic fields and bias currents. For $I_B = 0.8I_C$ and B = 0, the straight lines approximate the plateau and the linear decrease in the count rate (note the logarithmic scale for the count rate) and define the critical wavelength $\lambda_C \approx 630$ nm marked with the arrow.

Table 3.9: Jitter contributions for PDFs measured in magnetic field. The components of the local jitter, σ and τ, are the best fit values derived by fitting an experimental PDF with Eq. (3.19). For both wavelengths $\sigma_{ins} = 1.8$ (see Section 3.3.3.3).

λ_0 (nm)	I_B/I_C	B (mT)	σ_{sys} (ps)	σ_N (ps)	σ_{opt} (ps)	σ (ps)	τ (ps)
800	0.63	0	12.2			5.0 ± 0.4	5.0 ± 0.9
		150	14.1	4.9	8.0	5.5 ± 0.4	10.5 ± 0.8
		200	19.3			6.6 ± 0.3	15.0 ± 0.8
		250	24.5			7.3 ± 0.3	19.0 ± 0.7
1560	0.75	0	6.8			3.8 ± 0.4	4.9 ± 0.9
		50	8.4			3.9 ± 0.1	6.9 ± 0.3
		100	10.5	4.6	3.0	4.5 ± 0.1	9.1 ± 0.3
		150	13.5			4.9 ± 0.1	12.3 ± 0.3
		200	15.6			5.6 ± 0.4	14.0 ± 0.9

(8 ps) as compared to 1560 nm (3 ps). In Fig. 3.27(b), we show spectra of count rate. These spectra were obtained with a monochromator (Zolix Omni-λ 1509) at different magnetic fields and bias currents. Such spectra are typical for SNSPDs and have been reported in several publications which are reviewed in [12]. Each spectrum exhibits a plateau and a roll-off, which begins around a particular wavelength. At small wavelengths, the count rate is almost wavelength-independent, while beyond the roll-off, the count rate exponentially decreases with increasing the wavelength. For each spectrum, there is a critical wavelength [93], λ_C. The λ_C is associated with the intersection of two straight lines, which extrapolate the plateau and the decaying part of the count rate spectrum (solid lines in Fig. 3.27(b)). For $I_B = 0.8I_C$ and zero magnetic field $\lambda_C \approx 630$ nm. The critical wavelength formally demarcates two different detection scenarios. The plateau corresponds to a deterministic detection scenario, i.e. when each absorbed photon results in a counting event with a probability 100%. The wavelength range where the count rate decays exponentially corresponds to a probabilistic detection scenario [12], i.e. the probability that an absorbed photon will result in a counting event is $< 100\%$. Around the critical wavelength, there is a relatively broad spectral range where the nanowire response corresponds to a mixture of these scenarios. For all magnetic fields and currents studied here, at 1560 nm, the nanowire response obeys pure probabilistic detection scenario, while at 800 nm, the scenario is a mixture of both. As seen in Fig. 3.27(b), at fixed bias current, the increase in the magnetic field shifts the λ_C towards longer wavelengths that consequently expands the range of the deterministic detection scenario. In the microscopic 2-d model of the hot spot [43], the criterion for the deterministic and probabilistic scenarios is defined by the ratio of the bias current to the detection current (also see Section 2.2.4).

Free-space coupling: Jitter at different bias currents and zero magnetic field
In Fig. 3.28, we show the noise-free system jitter as a function of bias current for two wavelengths at zero magnetic field. These data were acquired with free-space optical coupling. The current dependence of the σ_s is entirely defined by the current dependence of the local jitter since other
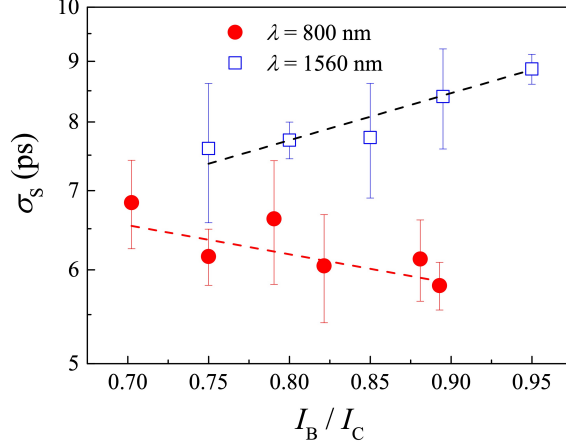
Figure 3.28: Noise-free system jitter vs. relative bias current. Jitter measurements were carried out at zero magnetoc field with free-space optical coupling.

jitter contributions are current-independent. Moreover, in the limit of negligibly small geometric jitter, which is estimated to be < 1 ps in our experiment (see Section 3.3.3.1), the magnitude of σ_s is defined by the local jitter. As seen in Fig. 3.28, the current dependences of the jitter at 800 and 1560 nm are different. At 1560 nm, which corresponds to the pure probabilistic detection scenario, the jitter grows with the current. While at 800 nm, which corresponds to a mixture between the probabilistic and deterministic detection scenarios, the jitter decreases with increasing current. Qualitatively similar current dependences were observed in [38], where the authors studied NbN meanders with very similar material parameters. It has been shown [38] that bends in the meander respond probabilistically at both photon energies (1560 and 800 nm) while straights undergo deterministic detection scenario at higher photon energy.

Components of the local jitter at different bias currents and magnetic fields

We now determine the components of the local jitter. To do this we analyze raw PDFs obtained at different magnetic fields and bias currents. Some of them are shown in Fig. 3.26 with symbols. Each raw PDF we fit with Eq. (3.19), which represents an exponentially-modified Gaussian distribution. In the fitting procedure, the following jitter contributions were fixed at their values defined experimentally σ_{sys}, σ_{opt}, σ_N, and σ_{ins} (Section 3.3.3). The components of the local jitter, σ and τ, were used as independent fitting parameters. Here, σ is the *std* of a Gaussian distribution associated with the emergence of the hot spot, and τ is the *std* of an exponential distribution associated with the start of vortex crossing. Fig. 3.29 shows the best fit values of σ and τ obtained at zero magnetic field and different wavelengths. At 800 nm (Fig. 3.29(a)), σ and τ are almost equal and both decrease with the current. At 1560 nm (Fig. 3.29(b)), τ increases with current while σ is almost current-independent. As seen in Fig. 3.29, at bias currents close to the experimental critical current ($I_B \approx 0.95 I_C$) which are typical for SNSPD applications, τ for the wavelength 1560 nm is almost twice as large for 800 nm. At longer wavelength, τ provides the major contribution to the local jitter.

In Fig. 3.30 we show the best fit values of σ and τ obtained at different magnetic fields and
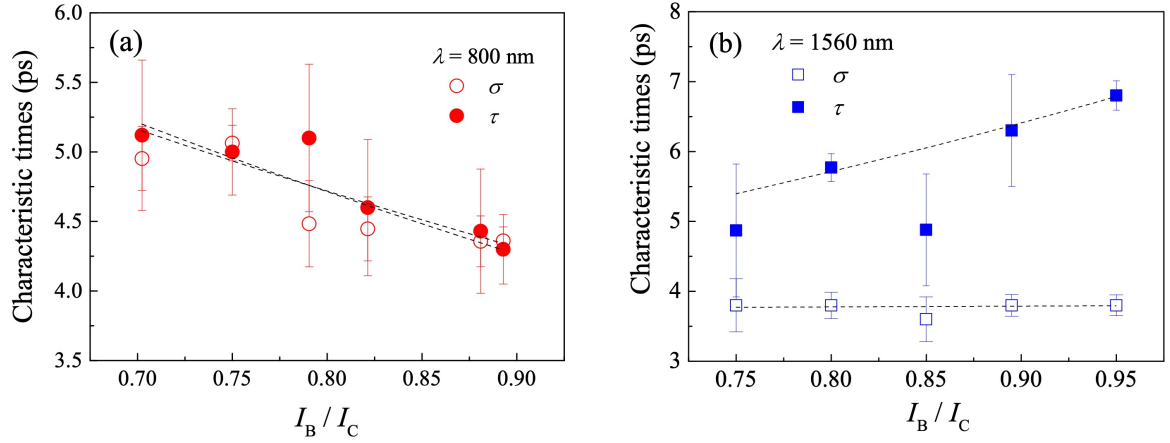
Figure 3.29: Characteristic times τ and σ of the exponentially-modified Gaussian distribution associated with the intrinsic jitter vs relative bias current for $B = 0$ and two wavelengths (a) 800 nm and (b) 1560 nm. Values τ and σ are obtained with the fitting procedure described in the text.

bias currents. Recall here that the critical current, I_C, is defined as current at zero magnetic field. As seen in the figure, both components σ and τ grow with the magnetic field at both wavelengths. The effect of the magnetic field is stronger on the exponential time τ as compared to σ. The full variation of τ in the field range from 0 to 200 mT is the same for both wavelengths.
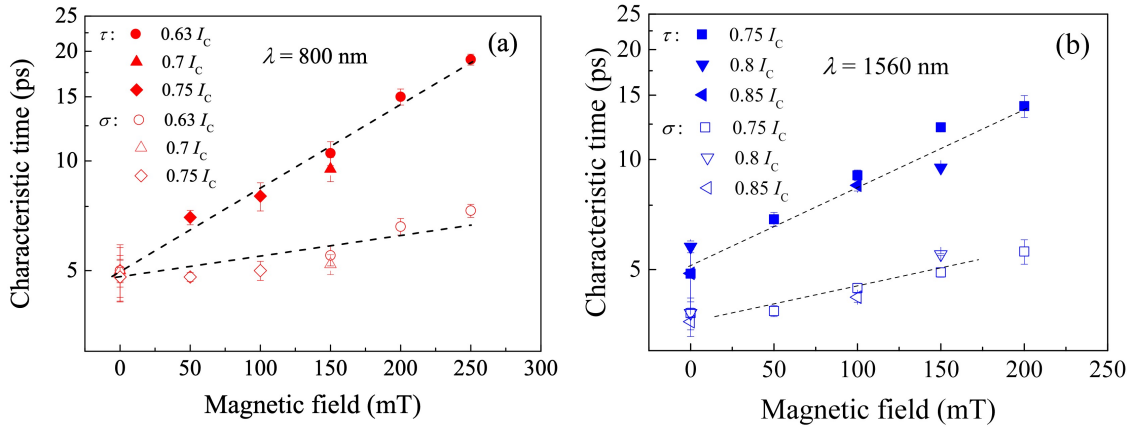
Figure 3.30: Characteristic times, τ (closed symbols) and σ (open symbols), of exponentially-modified Gaussian PDFs associated with internal detection process vs magnetic field. (a) For the wavelength 800 nm at bias currents 0.63 I_C, 0.7 I_C, and 0.75 I_C. (b) For the wavelength 1560 nm at bias currents 0.75 I_C, 0.8 I_C, and 0.85 I_C.

3.3.5 Qualitative comparison with theory

Our main experimental results contain several important findings. These are the current (at zero magnetic field) and magnetic field dependences of the components of the local jitter that are shown in Fig. 3.29 and Fig. 3.30, respectively, and the form of the experimental PDF (exponentially-modified Gaussian function). We analyze these results in the framework of the 2-d hot-spot model, which describes the microscopic mechanism of the intrinsic timing jitter (Section 2.2.4). Recall here that the model excludes the geometric jitter and, therefore, implies equality between the local jitter and the intrinsic jitter. Here we use numerical calculations, which were done by Vodolazov for our study in [44]. These calculations are also partly described in Section 2.2.4. As it was shown in Section 2.2.4, the model allows for calculating the delay time, τ_D, between the absorption of a photon and the formation of the corresponding normal domain. The timing jitter can be represented as a variation of the delay time. Basically, the model allows for translating the variation of the value of some parameter present in the model, for example, the photon energy, in the variation of the growth time of the hot spot and, consequently, the delay time. At the moment, several physical sources of such variations, intrinsic jitter, are known. One of the sources is the position (across the nanowire) dependence of the detection current, I_{det}, that was already described in Section 2.2.4. However, here, we add a non-zero magnetic field to that description. Another source is Fano fluctuations that will be considered in the second part of this section.

The nanowire geometry used in the model is shown in the inset in Fig.3.31(b), where the axis y is directed across the nanowire. Fig. 3.31(a) shows a computed ratio between the detection and depairing currents across the nanowire, $I_{\mathrm{det}}(y)/I_{\mathrm{DEP}}$. The computations were done for the photon energy $\hbar\omega = 1$ eV, bath temperature $T = 0.5T_C$, bias current $I_B = 0.55I_{\mathrm{DEP}}$. In the absence of a magnetic field, the density of the bias current across the nanowire is uniform, and therefore the dependence $I_{\mathrm{det}}(y)$ is symmetric (black curve) with respect to the center across the nanowire (position $10y/\xi_C$ in Fig.3.31). The current $I_{\mathrm{det}}(y)$ dictates a position dependence of the delay time, $\tau_D(y)$, which is shown for $B = 0$ and $I_B = 0.55I_{\mathrm{DEP}}$ in Fig.3.31(b) with a black curve. In [10] (see Fig. 3a there) it was shown that $\tau_D(y)$ monotonously decreases and flattens with the increase of the bias current. As a result, the variation of τ_D, that can be considered as a jitter, will monotonously decrease with the increase of the bias current. Qualitatively it corresponds to our experimental finding at 800 nm, the jitter decreases with increasing bias current (Fig. 3.29(a)). At 1560 nm, the experimental result is the opposite, the jitter increases with the current (Fig. 3.29(b)). The deterministic 2-d hot-spot model is not applicable in this case because the nanowire response at 1560 nm obeys pure probabilistic detection scenario. However, in [10] it was shown that at $I_{\mathrm{det}}^{min} < I_B < I_{\mathrm{det}}^{max}$ the timing jitter decreases with the decrease of the current. This is because at $I_B < I_{\mathrm{det}}^{max}$, only a part of the wire, where $I_B > I_{\mathrm{det}}^{min}$, detects photons. Therefore, with decreasing current, the variation of τ_D decreases. In the presence of a perpendicular magnetic filed, which is small enough for the nanowire to stay in the vortex-free Meisner state, the density of the bias current across the nanowire becomes non-uniform. It is because the magnetic field induces a screening current in
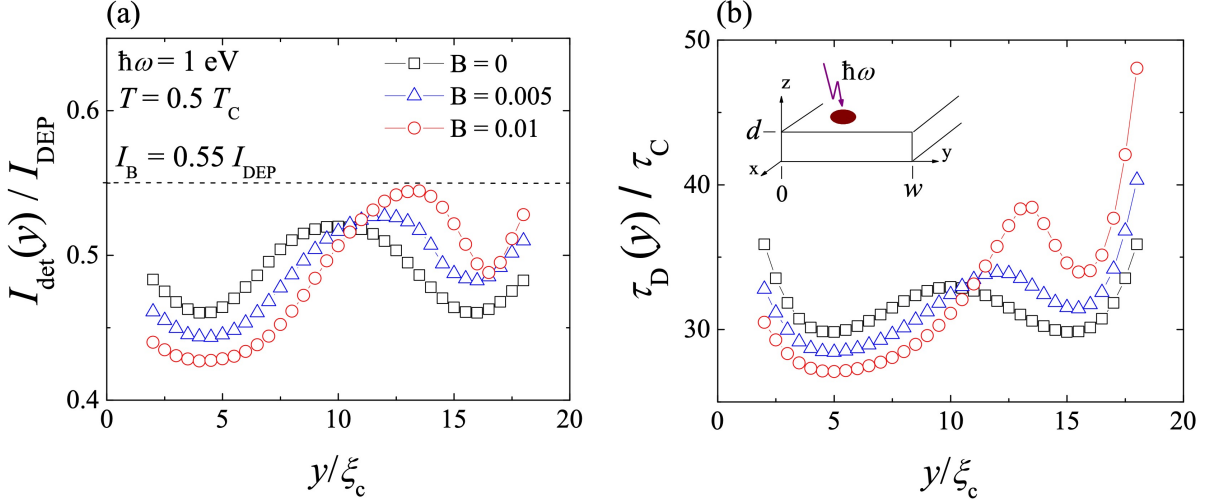
88

Figure 3.31: Position-dependent detection current (a) and delay time (b) for three different magnetic fields. The nanowire geometry is shown in the inset in the panel (b). Magnetic fields in units of B_C are specified in the legend for both panels. In both panels, the computations were done for the photon energy $\hbar\omega = 1$ eV, bath temperature $T = 0.5T_C$, and bias current $I_B = 0.55I_{\text{DEP}}$.

the wire so that the density of the local bias current is a sum of the densities of the applied bias and screening currents. The resulting tilted distribution of the bias current affects $I_{\text{det}}(y)$. The symmetric I_{det} at $B = 0$ becomes asymmetric at small $B \neq 0$ (blue and red curves in Fig.3.31). I_{det} increases at the edge, where the density of the local bias current decreases, and decreases at the opposite edge [43, 129, 15]. Such a change in $I_{\text{det}}(y)$ due to the magnetic field causes a respective change in $\tau_D(y)$ (Fig. 3.31(b)). In Fig. 3.31(b), it is clearly seen that the variation in τ_D, i.e. simply a difference between the maximum and minimum values of τ_D, increases with the field. This corresponds to our experimental finding, the increase in the local jitter with magnetic field (Fig. 3.30).

Now let us consider an effect of the deposited photon energy on $\tau_D(y)$. In [43, 129, 15], it has been shown that $I_{\text{det}}(y)$ shifts to smaller currents and flattens when the deposited photon energy increases. This affects $\tau_D(y)$ too. Fig. 3.32(a) shows dependences of the delay time on the deposited photon energy computed in the framework of the 2-d hot-spot model for three magnetic fields and two photon absorption sites. At any photon energy and zero magnetic field, τ_D at two symmetric minima $y = 5\xi_C$ and $15\xi_C$ are equal (see the black curve Fig. 3.31(b)) and decrease with increasing photon energy as shown in Fig. 3.32(a). Qualitatively we obtained the same result, i.e. the jitter at 800 nm is smaller than the jitter at 1560 nm (for a fixed current). In the presence of a magnetic field, τ_D at locations $y = 5\xi_C$ and $15\xi_C$ are different. The difference between $\tau_D(5\xi_C)$ and $\tau_D(15\xi_C)$ increases with magnetic field. This is also clearly seen in Fig. 3.31, where the calculations were done for the photon energy 1 eV. Fig. 3.32(b) shows dependences of the delay time on the deposited photon energy computed in the framework of the uniform hot-belts model [15]. For the hot-belt model, the TDGL approach was used together with an assumption that the photon instantaneously heats both electrons and phonons at $t = 0$ in the area $w \times w$. The detection current in the hot-belt model is independent on the photon
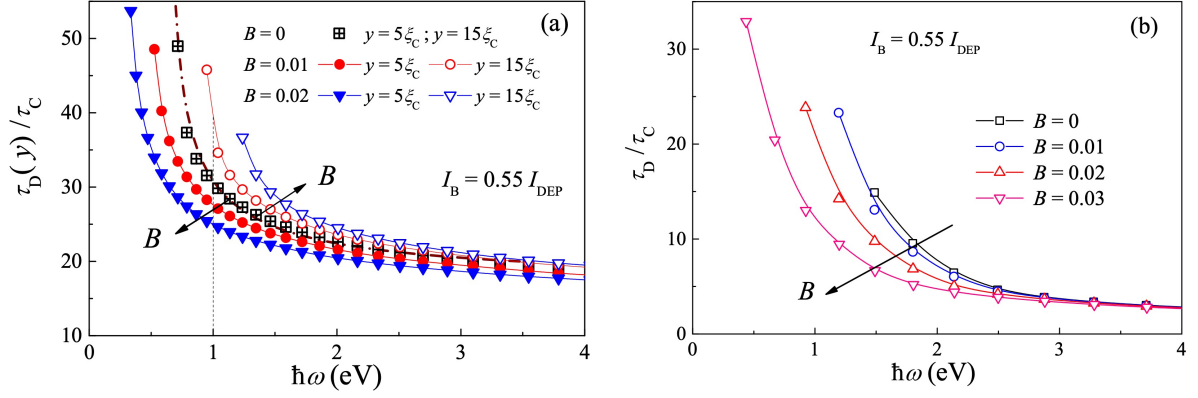
89

Figure 3.32: Relative delay time as a function of the photon energy at different magnetic fields for the bias current $0.55I_{DEP}$ and $T = 0.5T_C$. Fields are specified in insets in units of B_C. Arrows show the direction of changes when the field increases. Solid lines are to guide the eyes. (a) Delay time for different locations of the hot-spot in the framework of the hot-spot model. Distances from the strip edge are specified in units of ξ_C. The dash-dotted line is the fit described in the text. (b) Delay time in the framework of the uniform hot-belt model.

absorption site across the nanowire. As seen in Fig. 3.32(b) (hot-belt model), τ_D decreases with increasing magnetic field. However, it does not result in the variation of τ_D because both the detection current and the delay time are position-independent.

So far we have discussed only the behavior of the jitter with bias current, magnetic field, and photon energy. Now we will discuss the form of the PDF of the delay time provided by the 2-d hot-spot model with different physical souses of the jitter. The reconstruction of the PDF crucially depends on the local detection scenario (deterministic or probabilistic) and the uniformity of the absorbance across the nanowire. Consequently, we assume uniform local absorbance across the wire and deterministic scenario with constant detection efficiency. The form of the PDF expected for the position-dependent delays alone would have two maxima (one arises from minimal $\tau_D(y)$ at the locations $y = 5\xi_C$ and $y = 15\xi_C$, the other arises from $\tau_D(y)$ at the central part $y = 10\xi_C$ separated by a minimum. Such a PDF is inconsistent with the experimental PDF, which is better described by the exponentially-modified Gaussian distribution. Let us now add Fano fluctuations. Fano fluctuations randomize the amount of energy retained in the electron system that results in $\sigma_E = \sqrt{\varepsilon F \hbar\omega \Delta}$, where $\hbar\omega$ is the photon energy, ε is the quantum yield, and $F = 0.2 - 0.4$ is the Fano factor. Fano fluctuations alone, i.e. fluctuations in the retained energy, obey Gaussian distribution [126, 22] in the form

$$P(E) = \frac{1}{\sigma_E \sqrt{2\pi}} \exp\left[-\frac{(\hbar\omega - \varepsilon\,\hbar\omega)^2}{2\sigma_E^2}\right], \tag{3.21}$$

where σ_E is the *std* and $(\varepsilon\,\hbar\omega)$ is the mean value.

To reconstruct the PDF for τ_D in the presence of Fano fluctuations, we use the dependence $\tau_D(\hbar\omega)$ at a fixed location $y = 5\xi_C$ shown in Fig. 3.32(a) for $B = 0$. This dependence can be closely described by the power function $\tau_D(\hbar\omega) = a/(\hbar\omega - b) + c$. Generally, the PDF
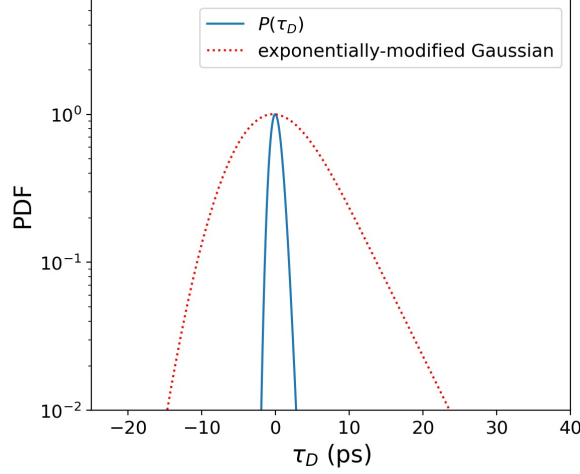
Figure 3.33: The solid curve corresponds to the PDF for the energy-dependent delay time at $B = 0$, $y = 5\xi_C$, and $I_B = 0.55 I_{\mathrm{DEP}}$ obtained in the presence of Fano fluctuations (Eq. (3.22)). The dotted curve corresponds to the exponentially-modified Gaussian distribution (Eq. (3.18)) computed for the experimental $\tau = 4.3$ and $\sigma = 4.3$ at 800 nm which were extrapolated at $I_B = 0.55 I_{\mathrm{DEP}}$.

of the random variable z, which is the function of the random variable x, i.e. $z = f(x)$, is $P(z) = P(g(z))|g(z)'|$, where $P(z)$ is the PDF of the variable z, $g(z)$ is the inverse function for $f(x)$, and $g(z)'$ is the derivative. In our notation, it corresponds to $P(\tau_D) = P(E)|E(\tau_D)'|$, where $E(\tau_D) = (\tau_D/a - c)^{-1} + b$ and $|E(\tau_D)'| = a^{-1}(\tau_D/a - c)^{-2}$. Therefore, we arrive at the PDF

$$P(\tau_D) = \frac{1}{a(\tau_D/a - c)^2} \frac{1}{\sigma_E \sqrt{2\pi}} \exp\left[-\frac{((\tau_D/a - c)^{-1} + b - \varepsilon\, h v)^2}{2\sigma_E^2}\right]. \qquad (3.22)$$

Although, the quantum yield is unknown for our nanowire, it can be estimated via the ratio $c_e/(c_e + c_{ph})$, which gives the fraction of photon energy delivered to the electron system. The experimental ratios $c_e/(c_e + c_{ph}) = 0.61$ and 0.47 were found for two similar NbN films, the 4.2 nm-thick film K-2 and the 5.8 nm-thick film K-3 (Table 3.6), respectively. For our film we take an average of these two, $\varepsilon \approx 0.55$. In Fig. 3.33 (solid curve) we plot a PDF computed with Eq. (3.22) with the following parameters $\hbar\omega = 1.55$ eV (corresponds to 800 nm), $F = 0.3$, and $\varepsilon = 0.55$. In the same figure, we show the exponentially-modified Gaussian distribution (Eq. (3.18)) for $\tau = 4.3$ ps and $\sigma = 4.3$ ps. These are the experimental values at 800 nm extrapolated at $I_B = 0.55 I_{\mathrm{DEP}}$ (Fig. 3.29(a)), to be consistent with the parameters used in numerical calculations. Numerically computed *sdt*-s are 0.68 for the theoretical PDF, $P(\tau_D)$, and 6.08 for the experimental PDF. As seen in Fig. 3.33, the form of the function $P(\tau_D)$ is closer to our experimental PDF. At the present stage, we cannot distinguish between contributions to the local jitter due to Fano fluctuations and the position-dependent delay times.

Due to the simplicity of the 2-d hot-spot model, we rather expected to obtain qualitative predictions than quantitatively correct results. Hence, the difference in *std*-s between obtained PDFs is not surprising. However, position-dependent delays, along with Fano fluctuations, result in almost one order of magnitude smaller *std* as compared to the experimental value. Therefore, neither of these two contributions can explain the magnitude of the intrinsic jitter. Although the

function $P(\tau_D)$ is closer to the experimental PDF, it deviates from a Gaussian profile at small delays (left from the PDF maximum) and an exponential profile at large delays (right from the PDF maximum). These two findings indicate that there is another source of the intrinsic jitter which has not been accounted so far.

3.4 Summary

This chapter was dedicated to the experimental results on electron-energy relaxation and timing jitter in NbN films and nanowires. First of all, the specimens under study were comprehensively characterized by means of magneto-transport measurements. The derived transport parameters within these measurements showed that the studied NbN films represent very disordered 2-d material with respect to quantum interference at impurities. The inelastic electron-phonon scattering time was derived from the electron dephasing time by means of magnetoconductance and further analyzed with the SM model. This allowed us to derive acoustic parameters for the studied NbN films, namely the phonon velocity and the mass density, which were found to be smaller than in the bulk NbN material. These parameters were used to compute the transparency and the angle of total phonon reflection for the given film/substrate interfaces and, further, to compute the phonon escape time. Relaxation of the electron energy was studied by means of photoresponse (electron heating). The data extracted from magnetoconductance measurements were used to describe the experimental photoresponse with the 2-T and 3-T models. For relatively thick films, the photoresponse data are reasonably well described without fitting parameters. However, for very thin films, the fit requires a smaller phonon heat capacity as compared to the predictions of the Debye model. We attribute this finding to the reduced density of phonon states in thin films at low temperatures. Further, on a thoroughly characterized NbN nanowire, the intrinsic jitter was studied. We developed a formalism aiming to derive the intrinsic jitter from raw experimental PDFs of delay time. This allowed us to quantify the intrinsic jitter and study its behavior with photon flux, bias current, and magnetic field at two wavelengths. Our experimental results contain several important observations. (i) The local jitter increases with the bias current in the probabilistic detection scenario and decreases in the deterministic detection scenario. (ii) The local jitter increases with the magnetic field. (iii) The experimental statistical distribution in the time of the appearance of the photon count is best described by the exponentially-modified Gaussian distribution in the range of values covering three orders of magnitude below the maximum. We analyzed these results in the framework of the 2-d hot-spot model. Qualitatively, the model does describe our experimental observations (i) and (ii). Moreover, at this stage, we compared it with the hot-belt model and concluded that the hot spot is essential in explaining the magnetic field dependence of the local jitter. The third experimental observation (iii) could not be described even including another jitter source, Fano fluctuations. We also found that position dependent delays, along with Fano fluctuations, predict much smaller magnitude of the intrinsic jitter than the experimental value. We attribute this finding to a missing source of the intrinsic jitter.

Chapter 4

On-chip dispersive Raman spectrometer with single-photon sensitivity

Raman spectroscopy is a powerful tool that provides a unique "fingerprint" (Raman spectrum) of a sample. A Raman signal is generated by inelastically scattered photons, i.e. the energy of the scattered photon is not equal to that of the incident photon. The problems associated with Raman spectroscopy include a relatively small intensity of the Raman signal. This is caused by a small cross-section of inelastic Raman scattering as compared to elastic Rayleigh scattering. To ensure a good signal-to-noise ratio, a conventional Raman spectrometer that utilizes a CCD (Charge Coupled Device) sensor requires both a high-intensity light source and long integration time. There is an alternative approach to resolve a Raman spectrum that exploits single-photon sensitivity and picosecond timing resolution of an SNSPD [2, 130]. A potential application of the SNSPD in Raman spectroscopy is a Raman spectrometer based on a multi-pixel SNSPD array. In this chapter, we present a prototype of the spectrometer. The dispersive Raman spectrometer comprises an SNSPD device and a dispersive element, an optical fiber. Conceptually, the Raman spectrum can be acquired as follows. Photons corresponding to different wavelengths in the Raman spectrum arrive at the input of the fiber at the same time. However, traveling times of these photons through the fiber are wavelength-dependent. Consequently, at the output of the fiber, they will arrive at different times. Therefore, by measuring photon arrival times, one can resolve a Raman spectrum in the time domain. Further, knowing the traveling time for photons of each wavelength, the spectrum can be reconstructed in the wavelength domain. This chapter describes in detail this approach and demonstrates a simplified prototype of the Raman spectrometer based on a multi-pixel SNSPD array.

4.1 Formalism

The measure for the Raman effect in a substance is the difference in 'wavenumbers' $\nu = 1/\lambda$ (λ is the wavelength) between the absorbed and the emitted photon. This difference is also called the Raman shift. Commonly it does not depend on the energy of the absorbed photon and is usually presented in units of inverse centimeters, cm^{-1}. The lines in the spectrum of the Raman shift are called the Raman lines. In order to convert the Raman spectrum in wavenumbers into the spectrum in wavelengths and back, the following formulas can be used:

$$\lambda_0^{(i)} = \frac{1}{1/\lambda_0^* - \Delta\nu^{(i)} \times 10^{-7}}, \tag{4.1}$$

$$\Delta\nu^{(i)} = \left(\frac{1}{\lambda_0^*} - \frac{1}{\lambda_0^{(i)}}\right) \times 10^7.$$

Here λ_0^* is the wavelength of the light exciting the Raman effect (in our case $\lambda_0^* = 785$ nm), and $\lambda_0^{(i)}$ and $\Delta\nu^{(i)}$ are the wavelength (in units of nm) and the Raman shift (in units of cm^{-1}) of the i-th Raman line, respectively. Hereinafter the subscript '0' is used to denote light characteristics in free space.

Fourier-transform-limited light pulses have a Gaussian shape in space (x), wavelength (λ), wave vector ($k = 2\pi/\lambda$) and time (t). The width of a Gaussian-shaped pulse we characterize with a corresponding *std*. For the transform-limited light pulse in free space, the *std*-s in coordinates, x, λ, k, and t are connected as follows (c is the velocity of light in free space)

$$\sigma_k = \frac{1}{\sigma_x} = \frac{2\pi}{\lambda_0^2}\sigma_\lambda, \tag{4.2}$$

$$\sigma_t = \frac{\sigma_x}{c} = \frac{\lambda_0^2}{2\pi c}\frac{1}{\sigma_\lambda}.$$

After passing a distance L_f in a transparent dispersive medium, e.g. a fiber with the refractive index n_1, the transform-limited pulse loses this property and spreads in time and coordinate. For relatively small broadening, the profile of the pulse in time and coordinate remains Gaussian, while the spectral content (σ_k) does not change. The traveling velocity of the pulse through the medium $\nu_g = d\omega/dk$ is called group velocity (ω is the circular frequency, $k = 2\pi n_1/\lambda_0$ is the wave vector in the medium, and λ_0 is the central wavelength in the wavelength profile of the pulse in free space). Generally, the group velocity differs from the phase velocity of monochromatic light in the medium, c/n_1. Furthermore, the pulse becomes chirped. This can be interpreted either as the time-dependent instantaneous frequency at any fixed coordinate or as non-evenly distributed spectral components along the coordinate at any fixed time. The above effects are controlled by the dependence of the refractive index of the medium on the wavelength $n_1(\lambda_0)$ (red dashed curve in Fig. 4.1). The traveling time of the light pulse through the fiber (delay time) is

$$\tau = \frac{L_f}{v_g}, \tag{4.3}$$

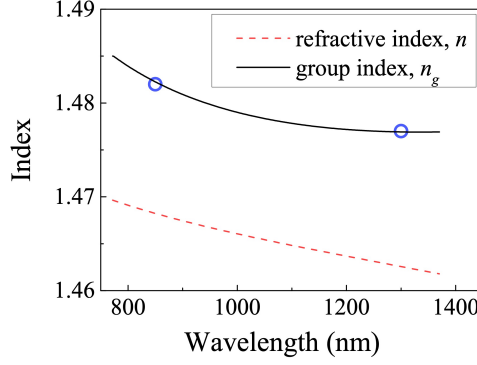$$v_g = \frac{d\omega}{dk} = \frac{c}{n_1 - \lambda_0 dn_1/d\lambda_0} = \frac{c}{n_g},$$

Figure 4.1: Index of refraction vs. wavelength. Symbols correspond to the effective group index of refraction, n_g^*, specified in the datasheet for the graded-index multi-mode fiber GIF50C. The black solid curve corresponds to the group index of refraction and the red dashed curve correspond to the refractive index. These two curves were obtained from the best fit of n_g^* values with Eqs. (4.1) and Sellmeier equation 4.7 using the following Sellmeier coefficients taken from [131] $C = 0.9993$, $A = [0.49795; 0.65295; 0.83515]$ and $B = [0.04407; 0.11754; 9.86362]$.

where L_f is the fiber length and n_g is the group index of refraction (black solid curve in Fig. 4.1). Note, that the group velocity of light pulses in free space (vacuum) equals the phase velocity and equals c. Fiber manufacturers usually specify for several wavelengths the values of the effective group index, n_g^* (symbols in Fig. 4.1). The effective index is convenient because it accounts for the wavelength-dependent penetration of the electric field of a mode into the fiber cladding. The effective index can be considered as an average over the actual refractive index of the medium (n_1 and n_2).

Commonly broadening of the light pulse in space and in time is described by the wavelength dependence of the group velocity, the so-called group velocity dispersion. In a single-mode fiber, pulse broadening is dominated by chromatic (also called material) dispersion. It occurs when the phase velocity of a spectral component propagating through a medium varies non-linearly with wavelength, i.e. when the dependence $n_1(\lambda_0)$ is non-linear, its second derivative is not zero ($dn_1^2/d\lambda_0^2 \neq 0$). This type of dispersion was already discussed in Section 2.2.2. The pulse broadening (std) due to chromatic dispersion is given by

$$\sigma_{t,chr} = D_m \sigma_{\lambda_0} L_f, \tag{4.4}$$

where $D_m = \left| -\dfrac{\lambda_0}{c} \dfrac{d^2 n_1}{d\lambda_0^2} \right|$ is the material dispersion coefficient. In Section 3.3.3.2, we have found that for single-mode fibers the pulse broadening per unit length of fiber computed with Eq. (4.4) is very close to the experimental values. Another source of pulse broadening is waveguide dispersion. It arises from the dependence of the effective refractive index on the core diameter of the fiber. This contribution is usually much less than one given by chromatic dispersion. Therefore, we will not consider it here. In a multi-mode fiber, there is an additional source of pulse broadening, which is called modal dispersion. The different modes, which constitute the pulse in the multi-mode fiber, propagate with different longitudinal components of the group velocity. Modal dispersion dominates pulse broadening in step-index multi-mode fibers.

However, it is minimized by use of multi-mode graded-index fibers where the refractive index of the fiber core has a parabolic profile. When the number of allowed modes in the fiber is large, the pulse broadening due to modal dispersion is given by [39, 132]

$$\sigma_{t,mod} = L_f \frac{n\Delta}{2\sqrt{3}c}, \tag{4.5}$$

$$\sigma_{t,mod} = L_f \frac{n\Delta^2}{20\sqrt{3}c},$$

for a step-index fiber and for a graded-index fiber, respectively. Here $\Delta = (n_1 - n_c)/n_1$ is the relative difference between refractive indices of the fiber core n_1 and cladding n_c.

For an initially transform-limited pulse with the time width σ_{t0}, the *std* in the time-profile after passing a few serially connected fibers becomes

$$\sigma_t = \sqrt{\sigma_{t0}^2 + \left(\sum_{q=1}^{q=N} \sigma_{t,chr}^{(q)}\right)^2 + \sum_{q=1}^{q=N} \left(\sigma_{t,mod}^{(q)}\right)^2}, \tag{4.6}$$

where $\sigma_{t,chr}^{(q)}$ and $\sigma_{t,mod}^{(q)}$ are time broadenings contributed by the q-th fiber due to chromatic and modal dispersions, respectively. This is the empirical expression retaining validity in the limiting cases when either chromatic or modal dispersion dominates. We note here, that at an interface between two media the *std* in the time-profile of the pulse does not change, i.e. $\sigma_t = \frac{\sigma_x^{(q)}}{v_x^{(q)}} = \frac{\sigma_x^{(q+1)}}{v_x^{(q+1)}}$ is invariant.

For further estimation of the expected system performance of the dispersive Raman spectrometer, we use experimental data everywhere where measurements could be done. Where measurements were not possible, the group velocity and the group velocity dispersion were computed with an empirical relationship between the refractive index of the fiber material and the wavelength that is given by the Sellmeier equation

$$n_1^2(\lambda_0) = C\left(1 + \frac{A_1\lambda_0^2}{\lambda_0^2 - B_1^2} + \frac{A_2\lambda_0^2}{\lambda_0^2 - B_2^2} + \frac{A_3\lambda_0^2}{\lambda_0^2 - B_3^2}\right). \tag{4.7}$$

Here $A_{1,2,3}$ and $B_{1,2,3}$ are Sellmeier coefficients for a particular transparent medium [131]. Since datasheets for different fibers contain values of the effective group refractive index, n_g^*, for just a few wavelengths, we use an additional coefficient C in order to fit the datasheet data with the Sellmeier equation. The computed broadenings and delays were also used to cross-check the measured data. The way how expected broadening has been estimated is specified for each optical element which will be used in the Raman spectrometer.

When SNSPDs are used for Raman spectroscopy, the *std* in the time-profile σ_t of incident light pulses is converted into the timing jitter which is added to the timing jitter of the detector, σ_{SNSPD}, as [128]

$$\sigma_\tau = \sqrt{\sigma_t^2 + \sigma_{\text{SNSPD}}^2}. \tag{4.8}$$
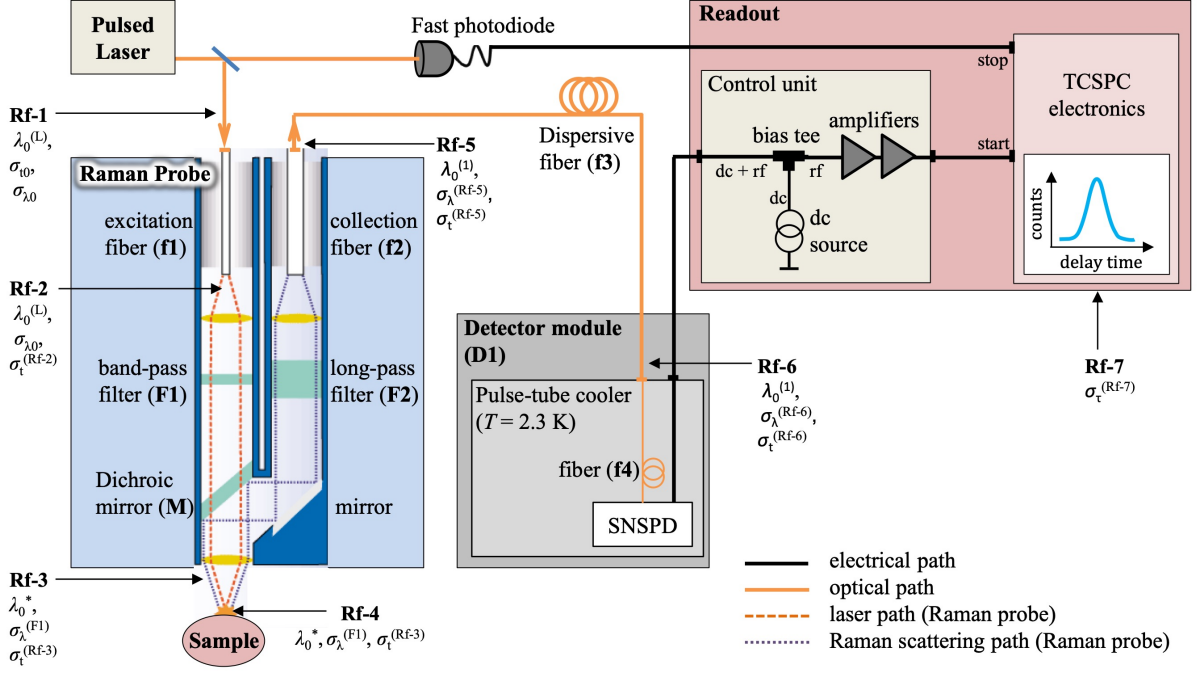
Figure 4.2: Schematics of the dispersive Raman spectrometer. Arrows specify reference planes (Rfs) which are numbered in the light-propagation sequence. Every Rf is specified by the central wavelength, the time-width, and the spectral width of light pulses. The Rf-7 is specified by the measured jitter in the SNSPD response.

4.2 Prototype of the dispersive Raman spectrometer

Here we describe the schematics and properties of the Raman spectrometer. The experimental setup is shown in Fig. 4.2. The instrument consists of the five following modules. (1) Pulsed laser (Section 4.2.1.1) for generating the Raman signal from the studied object. (2) Raman probe (Section 4.2.1.2) that shapes the incident excitation laser pulses, collects the Raman signal and filters out the reflected portion of the laser pulses (Rayleigh signal) from the Raman signal. (3) Dispersive fiber (Section 4.2.1.3) that transfers the spectrum of the Raman signal into the different arrival times of corresponding photons to the fiber output. (4) Detector module (Section 4.2.1.4) that detects single photons, and, finally, (5) readout electronics (Section 4.2.1.5) that measures and stores the arrival times of detected photons. The next section contains detail description of each module and the sample under study.
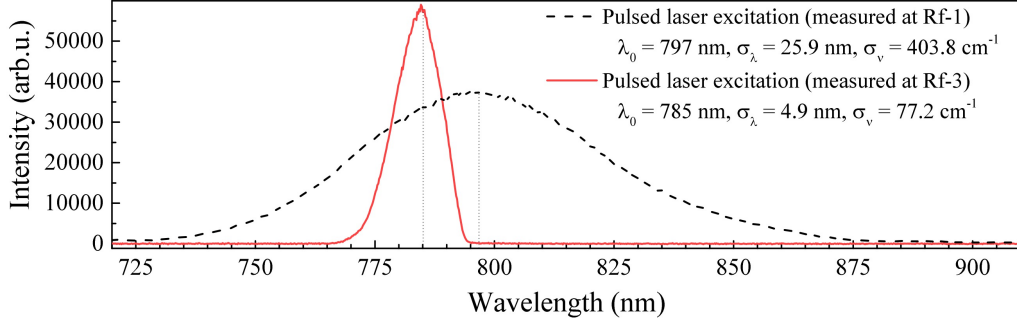
Figure 4.3: Spectra of pulsed laser excitation acquired at reference plane 1 (dashed black curve) and reference plane 3 (solid red curve) measured with a spectrometer (OceanOptics, USB4000).

4.2.1 System modules

4.2.1.1 Pulsed laser

In our setup, the excitation source is a Ti-sapphire laser (Femtosource, synergy 20). Operating in the pulsed mode, the laser generates Fourier-transform-limited pulses at the central wavelength $\lambda_0 = 797$ nm and a repetition rate of 80 MHz. Fig. 4.3 (dashed black curve) shows the spectrum of the pulsed laser excitation acquired at the laser output (**Rf-1** in Fig. 4.2) with a spectrometer (OceanOptics, USB4000). The laser pulses have a sub-picosecond duration of $\sigma_{t0} = 0.013$ ps and a spectral width of $\sigma_{\lambda_0} = 25.9$ nm ($\sigma_\nu = 403.8$ cm^{-1}). Here, the corresponding standard deviations, σ_{t0} and σ_{λ_0}, are related via Eq. (4.1). The laser pulses are coupled from free space into the excitation fiber **f1** of the Raman probe (Fig. 4.2)) by a collimator. The laser can also operate in a continuous wave (CW) mode in which it emits radiation with the central wavelength 780 nm.

4.2.1.2 Raman probe

The Raman probe (Ocean Optics, RPB785) (Fig. 4.2) is designed for the excitation wavelength 785 nm. It comprises a dichroic mirror (**M**), two filters (**F1** and **F2**), which are located in free space, and two multi-mode fibers (**f1** and **f2**). The excitation fiber **f1** is a multi-mode, step-index fiber with a length of $L_{f1} = 1.5$ m, a core diameter of 105 μm, and a numerical aperture of 0.22. This fiber adds pulse broadening per unit fiber length $\sigma_t^{(f1)}(\lambda_0^{(L)})/L_{f1} = 18.5$ ps/m. This value was measured experimentally by using another fiber (Thorlabs, FG050LGA) with the same core diameter (50 μm) and numerical aperture (0.22). After the fiber **f1**, the laser pulses pass the band-pass filter **F1**, which is centered at $\lambda_0^{(F1)} = 785$ nm with the spectral width $\sigma_\lambda^{(F1)} = 4.9$ nm (see the solid red curve in Fig. 4.3). The wavelength of the excitation $\lambda_0^* = 785$ nm is jointly defined by the spectrum of laser pulses and by the filter **F1**. Further, the laser pulses pass the dichroic mirror **M** and are focused onto the sample (the sample is described in Section 4.3) at 7.5 mm working distance from the end of the Raman probe. Further, the Raman backscattered
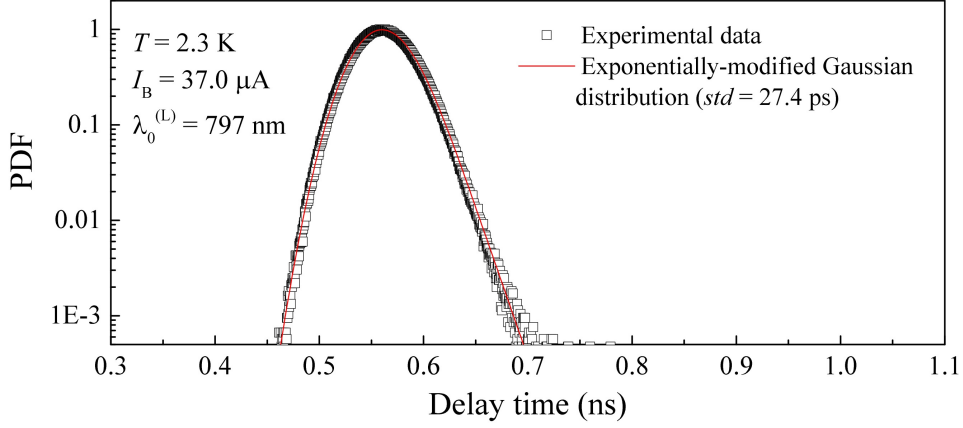
Figure 4.4: PDF of delay times measured at **Rf-7** with laser pulses coupled at **Ref-1** directly to the detector module **D1** via an additional 2 m-long SMF28 fiber.

light is collected into the Raman probe and passes the dichroic mirror (**M**). The mirror **M** filters out the excitation (laser light) and redirects the Raman signal via another mirror to the filter **F2**. The long-pass filter **F2** and the dichroic mirror together provide a spectral step centered at 806 nm. The width of the step (specified by the manufacturer) between 10 and 90 % of the full transmission is 4 nm. After the filter **F2**, the Raman light is collected into the fiber **f2**. The collection fiber **f2** is a multi-mode, step-index fiber with a core diameter of 200 μm, a numerical aperture of 0.22, and a length of L_{f2} =1.5 m. Although the datasheets for this fiber was not provided, we suppose that the fiber has the same modal dispersion as fiber **f1**. We expect that the fiber adds pulse broadening per unit fiber length $\sigma_t^{(f2)}(\lambda_0^{(L)})/L_{f2} \approx 18.5$ ps/m.

4.2.1.3 Dispersive fiber

After the collection fiber **f2**, the Raman light is coupled to the fiber **f3**, which acts as a dispersive element (Fig. 4.2). The dispersive fiber **f3** (Thorlabs, GIF50C) is a multi-mode, graded-index fiber with a germanium-doped core. The fiber has a length of $L_{f3} = 45$ m and a core diameter of 50 μm. The datasheet for this fiber specifies effective group indices of refraction $n_g^* = 1.482$ and 1.477 for two wavelengths $\lambda_0 = $ 850 and 1300 nm, respectively. For the wavelength $\lambda_0 = 850$ nm, the traveling time (delay time) of a light pulse through a unit fiber length amounts to $\tau = 4.96$ ns/m (according to Eq. (4.1)). The dispersive fiber adds pulse broadening per unit length $\sigma_t^{(f3)}(\lambda_0^{(L)})/L_{f3} = 3.5$ ps/m that was measured experimentally for the wavelength $\lambda_0^{(L)} = 797$ nm. This value agrees well with the value expected due to chromatic dispersion.

4.2.1.4 Detector module

After the dispersive fiber **f3**, the Raman light is coupled to the detector module **D1**. The detector module comprises a fiber **f4**, which is coupled to a SNSPD. The fiber **f4** (Thorlabs, SMF28) is

a step-index fiber with a length of $L_{f4} = 3$ m and a core diameter of 10 μm. Experimentally we found that the fiber **f4** adds pulse broadening per unit fiber length $\sigma_t^{(f4)}(\lambda_0^{(L)})/L_{f4} = 5.1$ ps/m. At the wavelength 797 nm, the fiber **f4** operates at the boarder of the single-mode regime; therefore the experimental $\sigma_t^{(f4)}$ is slightly larger than the expected value (3.1 ps/nm) due to the chromatic dispersion. Finally, this fiber **f4** guides the Raman light to the SNSPD device. The SNSPD chip was manufactured by Superconducting Nanotechnology (Scontel) and installed at the second stage of a two-stage pulse-tube cooler (TransMIT, PTD406), which has an optical and electrical feedthroughs. During detector operation, the temperature at the second stage was 2.3 K. At this temperature, the experimental critical current of the SNSPD amounts to 40.3 μA. The SNSPD is optically accessible through fiber **f4**. For our pulsed laser excitation $\lambda_0^{(L)} = 797$ nm, the detection system **D1** has the system jitter $\sigma_t^{(D1)} = 25.5$ ps. This value was defined from jitter measurements (see Fig. 4.4) with a bias current $I_B = 37.0$ μA and an additional 2 m-long SMF28 fiber, which was placed between the laser output and the detector module **D1**.

4.2.1.5   Readout electronics

The readout includes a control unit (bias-tee, amplifying chain, set of connecting cables), cables, and time-correlated single-photon counting electronics (TCSPC). The control unit (Scontel, CU-2SPD/P&T-005) provides dc-bias source for the detection system **D1** and comprises a bias-tee with the bandwidth 0.1 - 4200 MHz and two amplifiers with the bandwidth 0.1 - 1000 MHz and total gain $\sim$ 46 dB. The TCSPC electronics (Becker & Hickl, SPC-150NX) measures a delay time between two voltage transients with a time resolution of ≈ 0.4 ps (specified by the manufacturer). The voltage transients from the fast photodiode and from SNSPD were send to the SYNC and CFD outputs of the TCSPC electronics, respectively. The TCSPC software allows for building the PDF (histogram) of the measured time delays, which is further stored in the computer. Alternatively, for Raman measurements (see Section 4.3) we used a commercial spectrometer (OceanOptics, USB4000). The spectrometer has a 3648-pixel linear silicon CCD array with spectral sensitivity in the range 200 - 1100 nm.

4.2.1.6   Sample

In order to demonstrate a dispersive Raman spectrometer we chose a well-known object, methanol (CH_3OH). Fig. 4.5 shows a digitized image of the Raman spectrum of methanol with laser excitation of 785 nm taken from [133] (Fig. 3 there). The choice of methanol is caused by several reasons. Methanol is a colorless liquid, which can be placed in a transparent cuvette, that minimizes reflection of the light exciting the Raman effect. Another reason is that the Raman spectrum of methanol exhibits several Raman lines which are positioned at relatively small as well as relatively large distances from each other. The Raman spectrum of methanol contains four prominent Raman lines with the following Raman shifts: $\Delta\nu^{(1)} = 1034.8$ cm^{-1},

$\Delta\nu^{(2)} = 1458.7$ cm^{-1}, $\Delta\nu^{(3)} = 2835.7$ cm^{-1}, $\Delta\nu^{(4)} = 2945.0$ cm^{-1}. For the pulsed laser excitation used in our setup, $\lambda_0^* = 785$ nm, wavelengths of Raman lines (Eqs. (4.1)) become $\lambda_0^{(1)} = 855.2$ nm, $\lambda_0^{(2)} = 887.7$ nm, $\lambda_0^{(3)} = 1012.7$ nm, $\lambda_0^{(4)} = 1024.2$ nm.

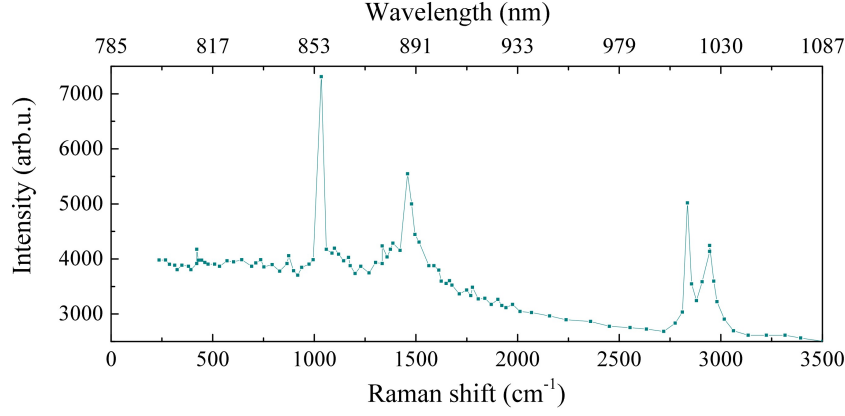**Figure 4.5:** Raman spectrum of methanol (CH$_3$OH). The data were extracted by digitizing Fig. 3 from [133], where the excitation source was a CW laser emitting at 785 nm with $\sigma_\lambda < 0.1$ nm.

Table 4.1: Temporal broadening and spectral shaping added by optical elements of the Raman spectrometer and the jitter of the detector module D1. Components are shown in Fig. 4.2.

Optical element	Central wavelength (nm)	Spectral std (nm)	Temporal std (ps)	Comments
Laser L	$\lambda_0^{(L)} = 797$	$\sigma_{\lambda_0} = 25.9$	$\sigma_{t_0} = 0.013$	Fourier-transform limited pulses, *std*-s measured experimentally
Fiber f1	$\lambda_0^{(L)} = 797$	$\sigma_{\lambda_0} = 25.9$ (chirping)	$\sigma_t^{(f1)} = 27.8$	$\sigma_t^{(f1)}$ measured experimentally
Filter F1	$\lambda_0^{(F1)} = 785$	$\sigma_\lambda^{(F1)} = 4.9$	$\sigma_t^{(F1)} \approx 5.2$	$\sigma_t^{(F1)}$ estimated as $\sigma_t^{(F1)} = [(\sigma_t^{(Rf-3)})^2 - (\sigma_t^{(f1)})^2]^{1/2}$ $\sigma_t^{(Rf-3)}$ defined in Table 4.2
Fiber f2	$\lambda_0^{(L)} = 797$	$\sigma_{\lambda_0} = 25.9$ (chirping)	$\sigma_t^{(f2)} = 27.8$	$\sigma_t^{(f2)}$ assumed to be equal to $\sigma_t^{(f1)}$
Sample	$\lambda_0^{(1)} = 855.2$	$\sigma_\lambda^{(1)} < 1.0$	$\sigma_t^{(1)} < 1.0$	$\sigma_t^{(1)}$ assumed to be Fourier-trans.-limit. $\lambda_0^{(1)}$ and $\sigma_\lambda^{(1)}$ are from [133]
Fiber f3	$\lambda_0^{(L)} = 797$	$\sigma_{\lambda_0} = 25.9$	$\sigma_t^{(f3)} = 157.4$	measured experimentally
Fiber f4	$\lambda_0^{(L)} = 797$	$\sigma_{\lambda_0} = 25.9$	$\sigma_t^{(f4)} = 15.3$	measured experimentally
detector module D1	$\lambda_0^{(L)} = 797$		$\sigma_t^{(D1)} = 25.5$	measured experimentally

4.2.2 Evaluation of the pulse broadening

To evaluate pulse broadening in the Raman spectrometer with the proposed configurations at each reference plane (see Fig 4.2), we carried out the following measurements. The initial parameters of the laser pulses were measured in the reference plane **Rf-1**. Transform-limited laser pulses were coupled into the optical path at different reference planes. We measured temporal and spectral profiles of pulses appearing at the next reference plane. The measurements were performed at the wavelength $\lambda_0^{(L)} = 797$ nm within a pair **Rf-1** $-$ **Rf-3** and **Rf-5** $-$ **Rf-6**, where the sequence, for example, **Rf-1** $-$ **Rf-3**, means that the laser light was coupled at **Rf-1** and measured at **Rf-3**. The results are presented in Table 4.1. The experimental broadening added by fiber **f3**, 157.4 ps, measured for the coupled light with $\lambda_0^{(L)} = 797$ nm and $\sigma_{\lambda_0} = 25.9$ nm agrees well with the value $\sigma_{t,chr}^{(f3)} = 156.2$ ps expected due to chromatic dispersion (Eq. (4.4)). Hence, we conclude that the pulse broadening added by the fiber **f3** is dominated by chromatic dispersion.

Table 4.2 contains either measured or expected spectral and temporal widths at reference planes from **Rf-1** to **Rf-6** and the expected jitter at **Rf-7** for the Raman line $\lambda_0^{(1)}$ of methanol. In our setup, the spectral widths of the Raman line at **Rf-4** is defined by the spectral width of laser excitation at **Rf-3**. We assumed that at **Rf-5** the Raman line $\lambda_0^{(1)} = 855.2$ nm of methanol is filtered out from the laser excitation. For the light with the central wavelength 855.2 nm and width $\sigma_\lambda = 4.9$ nm propagating through fiber **f3**, the expected pulse broadening due to chromatic dispersion (Eq. (4.4)) amounts to $\sigma_t^{(f3)} = 21.6$ ps. To estimate the jitter at **Rf-7**, we took the jitter of the detector module **D1** from Table 4.1 as an upper boundary.

4.2.3 System performance

To evaluate the system performance, we used data of light-pulse broadening (Tables 4.1 and 4.2). The 45 m-long dispersive fiber **f3** dominates the traveling time of the light pulse through the instrument. While the broadenings of the light pulse added by fibers **f1** and **f2** in the Raman Probe and the fiber **f3** are comparable. Under this condition, the resolution is set by the difference between the central wavelengths of two pulses for which the difference in traveling times equals ≈ 2.5 times the pulse broadening. In other words, to resolve the two overlapping Gaussian peaks with equal widths, the minimum separable peak–peak interval should be ≥ 2.5 its width (std) [134]. Fig. 4.6 shows the simulated timing jitter at **Rf-7** (open symbols) for the Raman line $\lambda_0^{(1)} = 855.2$ nm of methanol as a function of the length of fiber **f3**. The timing jitter for different fiber lengths was computed (Eqs. (4.6, 4.8)) as

$$\sigma_\tau(L) = \sqrt{(\sigma_\tau^{(Rf-7)})^2 + (\sigma_t^{(f3)})^2 \, [(L/L_{f3})^2 - 1]}. \tag{4.9}$$

Here $\sigma_\tau^{(Rf-7)}$ and $\sigma_t^{(f3)}$ are the jitter at **Rf-7** and the broadening of the light pulse added by the fiber **f3**, respectively, for the fiber length $L_{f3} = 45$ m. The values are specified in Tables 4.1 and 4.2. For fiber lengths < 30 m, the jitter is limited to the "setup" jitter coming

Table 4.2: Temporal and spectral widths of light pulses at different reference planes and the expected jitter at **Rf-7**. Reference planes are defined in Fig. 4.2.

Reference plane	Central wavelength (nm)	Spectral std (nm) or (cm^{-1})	Temporal std (ps)	Comments
1	$\lambda_0^{(L)} = 797$	$\sigma_{\lambda_0} = 25.9$	$\sigma_{t_0} = 0.013$	Fourier-transform limited
2	$\lambda_0^{(L)} = 797$	$\sigma_{\lambda_0} = 25.9$	$\sigma_t^{(Rf-2)} = 27.8$	$\sigma_t^{(Rf-2)} = [\sigma_{t0}^2 + (\sigma_t^{(f1)})^2]^{1/2}$, expected value
3	$\lambda_0^* = 785$	$\sigma_\lambda^{(F1)} = 4.9$ $\sigma_\nu^{(F1)} = 77.2$	$\sigma_t^{(Rf-3)} \approx 28.3$	$\sigma_\lambda^{(F1)}$, $\sigma_t^{(Rf-3)}$, measured experimentally
4	$\lambda_0^{(1)} = 855.2$	$\sigma_\lambda^{(Rf-4)} = 4.9$ $\sigma_\nu^{(F1)} = 77.2$	$\sigma_t^{(Rf-4)} = 28.3$	$\sigma_\lambda^{(Rf-4)} = [(\sigma_\lambda^{(F1)})^2 + (\sigma_\lambda^{(1)})^2]^{1/2}$, $\sigma_t^{(Rf-4)} = [(\sigma_t^{(Rf-3)})^2 + (\sigma_t^{(1)})^2]^{1/2}$, expected values
5	$\lambda_0^{(1)} = 855.2$	$\sigma_\lambda^{(Rf-5)} = 4.9$	$\sigma_t^{(Rf-5)} = 39.7$	$\sigma_t^{(Rf-5)} = [(\sigma_t^{(Rf-4)})^2 + (\sigma_t^{(f2)})^2]^{1/2}$
6	$\lambda_0^{(1)} = 855.2$	$\sigma_\lambda^{(Rf-6)} = 4.9$	$\sigma_t^{(Rf-6)} = 45.2$	$\sigma_t^{(Rf-6)} = [(\sigma_t^{(Rf-5)})^2 + (\sigma_t^{(f3)})^2]^{1/2}$
7			$\sigma_t^{(Rf-7)} = 51.8$	$\sigma_t^{(Rf-7)} = [(\sigma_t^{(Rf-6)})^2 + (\sigma_t^{(D1)})^2]^{1/2}$

from other modules of the spectrometer. The curves in Fig. 4.6 represent the difference between traveling times, $\Delta\tau$, for three pairs of pulses with different central wavelengths as a function of L_{f3}. The central wavelengths of the pairs correspond to the wavelengths of Raman lines of methanol, $\lambda_0^{(1)} - \lambda_0^{(2)}$, $\lambda_0^{(1)} - \lambda_0^{(3)}$, and $\lambda_0^{(1)} - \lambda_0^{(4)}$ (see Section 4.2.1.6). We associate the traveling time of a pulse through fibers **f1**, **f2**, **f3**, and **f4** with the delay time between the pulse launch by the laser and the arrival of the signal at the readout. The difference in delay times imposed by fibers **f1**, **f2**, and **f4** amounts to ≈ 8 ps. The difference in the delay times was computed with Eqs. (4.1). The values of n_g^* at two wavelengths were obtained via linear interpolation of the data provided by the manufacturer.

For computing delay times and pulse broadening, the following parameters were used: $n_1(\lambda_0^{(L)}) = 1.4691$, $dn_1(\lambda_0^{(L)})/d(\lambda_0^{(L)}) = -0.01853$ μm^{-1}, $dn_1^2(\lambda_0^{(L)})/d(\lambda_0^{(L)})^2 = 0.04686$ μm^{-2}, $D_m = -124.95459$ ps/(nm × km). The dependence $n_1(\lambda_0)$ was obtained from the best fit of datasheet values for n_g^* with Eqs. (4.1) and (4.7). The best fit value of the fitting parameter was $C = 0.9993$. As the seed $n_1(\lambda_0)$ dependence, the output of Eq. ((4.7)) with the Sellmeier coefficients $A = [0.49795; 0.65295; 0.83515]$ and $B = [0.04407; 0.11754; 9.86362]$ from [131] was used. The broadening added by fiber **f3** was also computed with Eq. (4.4).
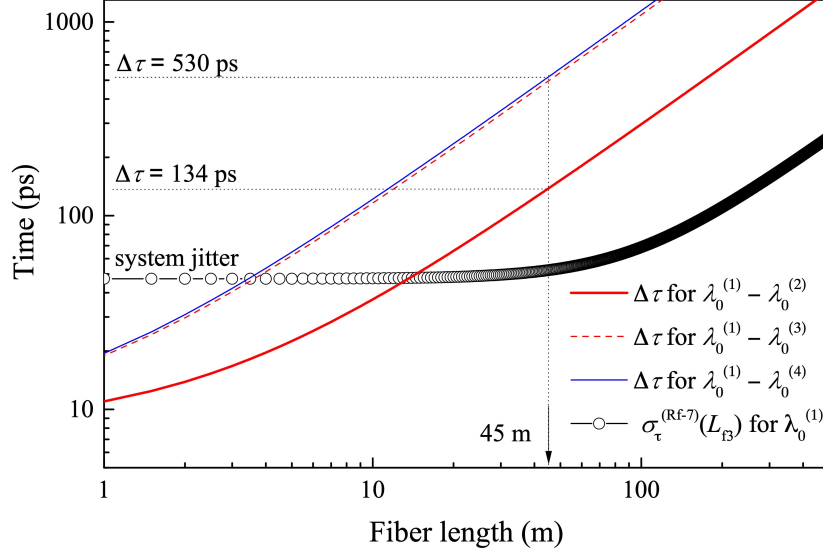
Figure 4.6: Simulation of the system performance for different lengths of the fiber **f3**. Open symbols correspond to the timing jitter (σ_τ) at the readout (Rf-7) for light pulses with the central wavelength $\lambda_0^{(L)} = 800$ nm. Curves correspond to the difference ($\Delta\tau$) between traveling times (through fibers **f1**, **f2**, **f3**, and **f4**) for pairs of light pulses with different central wavelengths specified in the legend. These wavelengths correspond to the wavelengths in the Raman spectrum of methanol (see Section 4.2.1.6).

To summarize, with the 45 m-long fiber **f3**, the difference in traveling times for two outermost Raman lines of methanol ($\lambda_0^{(1)}$ and $\lambda_0^{(4)}$) amounts to $\Delta\tau = 530$ ps (Fig 4.6). This value defines the size of an acquisition window for reconstruction of the Raman spectrum of methanol. $\Delta\tau = 530$ ps is less than a typical duration of the response transient of the SNSPD (~ 5 ns) and much less than the inverse repetition rate of laser pulses (12.5 ns). With 45 m-long fiber **f3**, the total computed jitter at **Rf-7** for $\lambda_0^{(1)} = 855.2$ nm and $\sigma_\lambda = 4.9$ nm amounts to $\sigma_\tau^{Rf-7} = 51.8$ ps. Using the resolution criterion 2.5σ, the spectral resolution of our system is 129.5 ps that corresponds to two Raman lines separated by an interval of ≈ 30 nm. Therefore, the Raman lines of methanol $\lambda_0^{(3)}$ and $\lambda_0^{(4)}$, which are separated by the interval 11.5 nm, can not be resolved with $L_{f3} = 45$ m.

4.3   Raman measurements: experimental results and discussion

We measured Raman spectra of methanol with three different approaches. One was performed with the experimental setup shown in Fig 4.2, the so-called SNSPD-based Raman spectrum (Fig. 4.7(c)). The two others, spectrometer-based Raman spectra, were obtained with a commercial spectrometer (OceanOptics, USB4000), which was connected at the reference plane 3 (**Rf-3**) to the collection fiber **f2** of the Raman probe. These two spectrometer-based measurements differ with respect to the mode of laser excitation, the CW (Fig. 4.7(a)) mode and the pulsed mode (Fig. 4.7(b)). Both spectrometer-based spectra were acquired with integration time of 10 s. As seen in Fig. 4.7(a), the Raman spectrum with CW laser excitation of 782 nm

exhibits four expected Raman shifts. We fit the acquired spectrum with a sum of four Gaussian finctions. The best fit *std*-s of the corresponding Raman lines are $\sigma_\lambda(\lambda^{(1)}) = 4.0 \pm 0.1$ nm, $\sigma_\lambda(\lambda^{(2)}) = 5.2 \pm 0.1$ nm, $\sigma_\lambda(\lambda^{(3)}) = 3.0 \pm 0.4$ nm, and $\sigma_\lambda(\lambda^{(4)}) = 5.7 \pm 2.6$ nm. The Raman lines are slightly broader than the spectral width of the CW laser excitation $\sigma_\lambda = 2.6$ nm. The spectrometer-based spectrum obtained with pulsed laser excitation (Fig. 4.7(b)) clearly exhibits only three Raman peaks at central wavelengths $\lambda^{(1)} = 854.1 \pm 0.1$ nm, $\lambda^{(2)} = 885.8.1 \pm 0.2$ nm, and $\lambda^{(3)} = 1010.0 \pm 0.3$ nm. The third peak is an overlap of two not resolved Raman lines. We fit the spectrum with a sum of three Gaussian functions. The corresponding line widths given by the best fit *std*-s are $\sigma_\lambda(\lambda^{(1)}) = 5.5 \pm 0.1$ nm, $\sigma_\lambda(\lambda^{(2)}) = 6.4 \pm 0.2$ nm, and $\sigma_\lambda(\lambda^{(3)}) = 8.9 \pm 0.9$ nm. Here, the widths of the first two resolved Raman lines slightly exceed the spectral width of the pulsed laser excitation, $\sigma_\lambda = 4.9$ nm. Because the excitation with broader spectrum results in broader Raman lines of smaller amplitude, within the same integration time (10 s), the signal-to-noise ratio for this spectrum is lower as compared to one acquired with the CW laser.

Fig. 4.7(c) shows the SNSPD-based Raman spectrum obtained with a dispersive Raman spectrometer of the proposed configuration. The spectrum represents a histogram of delay times between arrival times of voltage transients from the SNSPD and the fast photodiode. These results were obtained within the integration time 437 s. Because the traveling time through the fiber **f3** decreases with increasing wavelength, the spectrum acquired in the time domain is a mirror-reversal of the spectrum in the wavelength domain. The reconstruction of the spectrum in the wavelength domain was done by the use of a calibration curve shown in the right panel of Fig. 4.7(c). The curve was obtained with Eq. (4.1). The spectrum exhibits three Raman peaks, which appear at the positions with the expected temporal distance between them $\Delta\tau(\lambda^{(1)} - \lambda^{(2)}) = 139.1 \pm 2.8$ ps and $\Delta\tau(\lambda^{(1)} - \lambda^{(3)}) = 512 \pm 2.3$ ps. The third peak represents two overlapping not resolved Raman lines of methanol. Because the SNSPD exhibits non-Gaussian statistics of delay times, we fit the SNSPD-based spectrum with a sum of three exponentially-modified Gaussian functions (Eq. 3.18). The best fit *std*-s of the corresponding lines are $\sigma_t(\lambda^{(1)}) = 54.5 \pm 1.5$ ps, $\sigma_t(\lambda^{(2)}) = 40.0 \pm 1.6$ ps, and $\sigma_t(\lambda^{(3)}) = 62.8 \pm 1.4$ ps, that corresponds to $\sigma_\lambda(\lambda^{(1)}) = 11.5 \pm 0.3$ nm, $\sigma_\lambda(\lambda^{(2)}) = 10.7 \pm 0.5$ nm, and $\sigma_\lambda(\lambda^{(3)}) = 31.8 \pm 0.6$ nm in the wavelength domain. The temporal width of the first Raman line $\sigma_t(\lambda^{(1)}) = 54.5 \pm 1.5$ ps is slightly larger that the expected value 51.8 ps (see Table 4.2). The width of the resolved lines in the wavelength domain, $\lambda^{(1)}$ and $\lambda^{(2)}$, is almost twice as large as the width of those in the spectrometer-based spectrum measured with the same laser excitation. This is because the broadenings in time are converted into broadenings in wavelength when the SNSPD-based spectrum is reconstructed. The SNSPD-based spectrum does reproduce the difference in the peak intensities for the first two Raman lines, $\lambda^{(1)}$ and $\lambda^{(2)}$, however, the intensity of the third Raman peak is much larger than expected. We explain it by a difference in the spectral sensitivity between the SNSPD device and a silicon sensor in the spectrometer. The third Raman peak appears around 1020 nm. This wavelength is close to the edge of the spectral range 200 - 1100 nm of the silicon sensor. In contrast, because the used SNSPD was optimized for the telecommunication wavelength, the sensitivity of the SNSPD at 1020 nm is higher than at smaller wavelengths. It is worth mentioning here that we also performed the Raman measurements of cyclohexane, which has six prominent Raman shifts at the wavelengths: 835, 853, 872, 884,
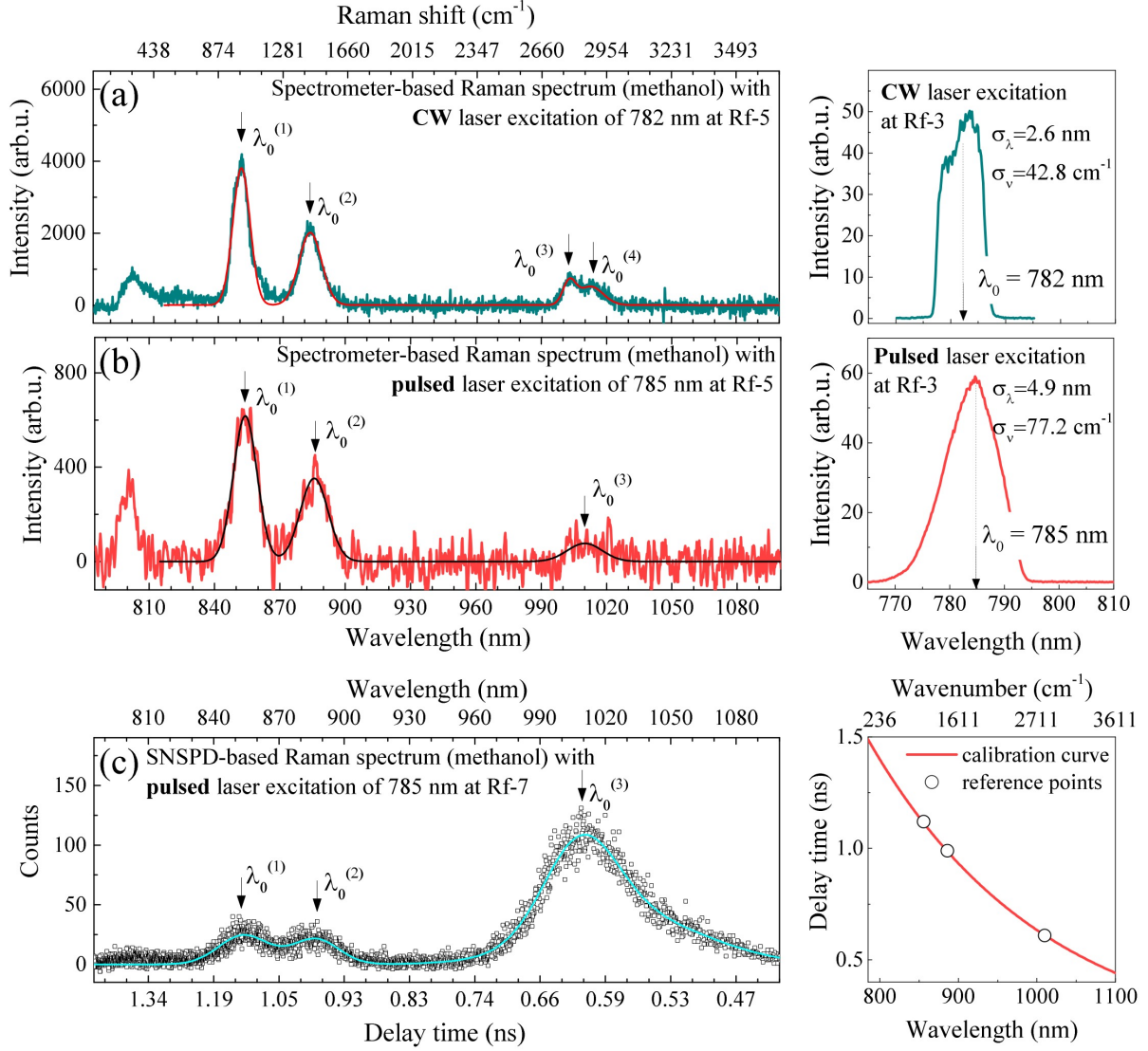
Figure 4.7: Raman spectra of methanol. (a) Spectrometer-based Raman spectrum with CW laser excitation of 782 nm and integration time 10 s (the CW laser excitation measured at Rf-3 is shown on the right panel). (b) Spectrometer-based Raman spectrum with pulsed laser excitation of 785 nm (the pulsed laser excitation measured at Rf-3 is shown on the right panel) and integration time 10 s. (c) SNSPD-based Raman spectrum with pulsed laser excitation of 785 nm. The right panel shows the calibration curve used for the reconstruction of the spectrum in either wavelengths or wavenumbers.

1015, and 1020 nm [135]. The distances between the first four lines and the last two lines of cyclohexane are beyond the resolution of the proposed spectrometer. As a result, the SNSPD-based spectrum exhibited only two peaks, one is an overall peak of the first four overlapping Raman lines, and the other is the last two overlapping Raman lines. We do not show these results here.

4.4 Summary

Here we have demonstrated a simplified prototype of a Raman spectrometer utilizing a single-pixel SNSPD device. In the present modification, the temporal resolution of the spectrometer is determined by several factors. The main factor is the spectral width of the excitation (σ_ν = 77 cm^{-1} or σ_λ = 4.9 nm), which is jointly defined by the filter **F1** in the Raman probe and the spectrum of Fourier-transform-limited pulses of the laser. Because the pulse broadening due to chromatic dispersion is proportional to a spectral width of the propagated pulse ($\sigma_\tau \propto \sigma_\lambda$), such a broad spectrum results in a large pulse broadening due to chromatic dispersion in fiber **f3**. Another limiting factor is the pulse broadening (σ_τ) added due to modal dispersion in multi-mode step-index fibers **f1** and **f2** in the Raman probe. Using the resolution criterion $\Delta\tau = 2.5\sigma_\tau$, the resolution of the proposed spectrometer is $\approx$ 29 nm. Broadenings due to chromatic and modal dispersion contribute almost evenly to the resulting resolution. There are several ways to improve the resolution. One is to use a light source with Fourier-transform-limited pulses of picosecond duration. It would result in a smaller spectral width of the laser excitation and, therefore, decrease the broadening due to chromatic dispersion. Another way is to reduce the length of fibers in the Raman probe and replace them with graded-index fibers. A relatively long acquisition time of the spectrum (437 s) is caused by non-efficient optical coupling. The Raman signal is sequentially coupled to fibers with a core diameter of 200, 50, and 10 μm. This problem can be solved by improving the optical coupling and replacing the multi-mode fibers with single-mode ones.

Chapter 5

Conclusions and outlook

In this thesis, we have presented results of an experimental study of two mutually interconnected phenomena: the intrinsic timing jitter in photon detection by an NbN superconducting nanowire and the relaxation of the electron energy in NbN superconducting films. The practical use of SNSPDs relies on a non-equilibrium state in superconducting nanowires where its relaxation is controlled by the dynamics of the electron energy. The relaxation of the electron energy, plays an essential role in the physics of such detectors. Experimental studies of the microscopic mechanism of the intrinsic jitter of a superconducting nanowire provide hints about the relationship between the jitter magnitude and the characteristic time scales of processes involved in the energy relaxation.

To reveal the processes of energy relaxation, we have studied inelastic scattering and energy relaxation of electrons by means of magnetoconductance and photoresponse, respectively, in a series of superconducting NbN films on Si/SiO_2 and Al_2O_3 substrates with thicknesses in the range from 3 to 33 nm. The main results are:

- The inelastic electron-phonon scattering rate defined by magnetoconductance technique depends on temperature as $\tau_{e-ph}^{-1} \propto T^n$ with an exponent $n \approx 3.2$ - 3.8. The magnitude of τ_{e-ph} at 10 K falls into the range 11.9 - 17.5 ps. The studied NbN films are strongly disordered. The degree of disorder $q_T l_e = \beta T \ll 1$ at T = 10 K, with $\beta = 0.075 \pm 0.005$ K^{-1} and the Ioffe-Regel parameter, $k_F l_e$, varying from 0.88 to 1.22.

- The Debye temperature in our films ($\approx$ 172 K) is noticeably smaller than the Debye temperature of bulk NbN. We attribute this to phonon softening caused by granularity and weakening of ion bonds at the film surfaces.

- Experimental photoresponse data for thicker films are described reasonably well in the framework of the 3-d Debye model and either the 2-T or 3-T models with the film parameters extracted from magnetoconductance measurements. For thin films the photoresponse

can only be described with the reduced heat capacity of phonons. We attribute this finding to the reduced density of phonon states in thin films with thicknesses comparable to or smaller than the mean free path of thermal phonons.

We have studied the timing jitter of an NbN nanowire by analyzing PDFs of delay times of the appearance of photon counts with respect to the photon absorption. To describe an experimental PDF, we have developed a formalism, which accounts for different jitter sources such as noise, optics, and the detection process in the nanowire itself and allows for extracting the intrinsic jitter. The main results are:

- Development of an experimental technique which eliminates the geometric jitter and allows separation of the instrumental, optical, and noise components of the system jitter from the intrinsic jitter.

- We have shown that increasing the photon flux turns the nanowire from a discrete, single-photon to bolometric detection regime. In the bolometric regime, the intrinsic jitter of a single-photon detection is averaged out that allows direct measurements of the instrument and noise contributions to the system jitter.

- At 800 nm, the magnitude of the intrinsic jitter increases with increasing magnetic field and decreasing bias current.

- Comparing the experimental data with the microscopic 2-d hot-spot model has shown that the "hot spot" is essential in explaining the magnetic field dependence of the jitter. In contrast, the uniform hot-belt model fails to describe it qualitatively.

- The position dependence (across the wire) of the delay time and Fano fluctuations are not sufficient to explain the experimental magnitude of the intrinsic jitter. This finding hints about a missing source of the intrinsic jitter.

In this thesis, we have also demonstrated a prototype of a Raman spectrometer utilizing an SNSPD device and a dispersive fiber. An alternative method for obtaining a Raman spectrum has been demonstrated. The Raman spectrum of methanol has been acquired with a one-pixel commercial SNSPD device. We have found two limiting factors for this spectrometer configuration: the spectral resolution and the acquisition time. They can be further improved by using only single-mode fibers and optimizing optical coupling. Compared to conventional Raman spectrometers based on CCD sensors, the SNSPD approach provides a single-photon sensitivity over a wide spectral range from visible to near-infrared wavelength range.

The study presented in this thesis reveals a few topics for further research in the field of SNSPD applications. For instance, there are remaining questions on the microscopic mechanism of single-photon detection in superconducting nanowire and specifically on the physical sources of the intrinsic jitter. So far, two sources have been considered, the dependence of the delay time

on the position of the photon absorption site and Fano fluctuations. According to our results, they do not provide a good explanation of the magnitude of the experimental intrinsic jitter. We anticipate the larger impact of thermal fluctuations and spacial non-uniformities on the intrinsic jitter and suggest them as directions for future work.

Bibliography

[1] C. M. Natarajan, M. G. Tanner, and R. H. Hadfield, "Superconducting nanowire single-photon detectors: physics and applications," *Superconductor science and technology*, vol. 25, no. 6, p. 063001, 2012.

[2] J. Toussaint, S. Dochow, I. Latka, A. Lukic, T. May, H.-G. Meyer, K. Il'in, M. Siegel, and J. Popp, "Proof of concept of fiber dispersed Raman spectroscopy using superconducting nanowire single-photon detectors," *Optics express*, vol. 23, no. 4, pp. 5078–5090, 2015.

[3] A. Glejm, A. Anisimov, L. Asnis, Y. B. Vakhtomin, A. Divochiy, V. Egorov, V. Kovalyuk, A. Korneev, S. Kynev, Y. V. Nazarov *et al.*, "Quantum key distribution in an optical fiber at distances of up to 200 km and a bit rate of 180 bit/s," *Bulletin of the Russian Academy of Sciences: Physics*, vol. 78, no. 3, pp. 171–175, 2014.

[4] R. Riedinger, S. Hong, R. A. Norte, J. A. Slater, J. Shang, A. G. Krause, V. Anant, M. Aspelmeyer, and S. Gröblacher, "Non-classical correlations between single photons and phonons from a mechanical oscillator," *Nature*, vol. 530, no. 7590, p. 313, 2016.

[5] H. Li, S. Chen, L. You, W. Meng, Z. Wu, Z. Zhang, K. Tang, L. Zhang, W. Zhang, X. Yang *et al.*, "Superconducting nanowire single photon detector at 532 nm and demonstration in satellite laser ranging," *Optics express*, vol. 24, no. 4, pp. 3535–3542, 2016.

[6] Z.-P. Zhang, F.-M. Yang, H.-F. Zhang, Z.-B. Wu, J.-P. Chen, P. Li, and W.-D. Meng, "The use of laser ranging to measure space debris," *Research in Astronomy and Astrophysics*, vol. 12, no. 2, p. 212, 2012.

[7] W. H. Pernice, C. Schuck, O. Minaeva, M. Li, G. Goltsman, A. Sergienko, and H. Tang, "High-speed and high-efficiency travelling wave single-photon detectors embedded in nanophotonic circuits," *Nature communications*, vol. 3, no. 1, pp. 1–10, 2012.

[8] S. Ferrari, C. Schuck, and W. Pernice, "Waveguide-integrated superconducting nanowire single-photon detectors," *Nanophotonics*, vol. 7, no. 11, pp. 1725–1758, 2018.

[9] J. L. O'brien, A. Furusawa, and J. Vučković, "Photonic quantum technologies," *Nature Photonics*, vol. 3, no. 12, p. 687, 2009.

[10] D. Y. Vodolazov, "Minimal timing jitter in superconducting nanowire single-photon detectors," *Physical Review Applied*, vol. 11, no. 1, p. 014016, 2019.

[11] J. P. Allmaras, A. G. Kozorezov, B. A. Korzh, K. K. Berggren, and M. D. Shaw, "Intrinsic timing jitter and latency in superconducting nanowire single-photon detectors," *Physical Review Applied*, vol. 11, no. 3, p. 034062, 2019.

[12] A. Engel, J. Renema, K. Il'in, and A. Semenov, "Detection mechanism of superconducting nanowire single-photon detectors," *Superconductor Science and Technology*, vol. 28, no. 11, p. 114003, 2015.

[13] G. Gol'Tsman, O. Okunev, G. Chulkova, A. Lipatov, A. Dzardanov, K. Smirnov, A. Semenov, B. Voronov, C. Williams, and R. Sobolewski, "Fabrication and properties of an ultrafast NbN hot-electron single-photon detector," *IEEE Transactions on applied superconductivity*, vol. 11, no. 1, pp. 574–577, 2001.

[14] A. D. Semenov, G. N. Gol'tsman, and A. A. Korneev, "Quantum detection by current carrying superconducting film," *Physica C: Superconductivity*, vol. 351, no. 4, pp. 349–356, 2001.

[15] D. Y. Vodolazov, "Single-photon detection by a dirty current-carrying superconducting strip based on the kinetic-equation approach," *Physical Review Applied*, vol. 7, no. 3, p. 034014, 2017.

[16] J. R. Clem and K. K. Berggren, "Geometry-dependent critical currents in superconducting nanocircuits," *Physical Review B*, vol. 84, no. 17, p. 174510, 2011.

[17] S. Dorenbos, E. Reiger, U. Perinetti, V. Zwiller, T. Zijlstra, and T. Klapwijk, "Low noise superconducting single photon detectors on silicon," *Applied Physics Letters*, vol. 93, no. 13, p. 131101, 2008.

[18] A. Engel, A. Aeschbacher, K. Inderbitzin, A. Schilling, K. Il'in, M. Hofherr, M. Siegel, A. Semenov, and H.-W. Hübers, "Tantalum nitride superconducting single-photon detectors with low cut-off energy," *Applied Physics Letters*, vol. 100, no. 6, p. 062601, 2012.

[19] B. Baek, A. E. Lita, V. Verma, and S. W. Nam, "Superconducting W_xSi_{1-x} nanowire single-photon detector with saturated internal quantum efficiency from visible to 1850 nm," *Applied Physics Letters*, vol. 98, no. 25, p. 251105, 2011.

[20] Y. P. Korneeva, M. Y. Mikhailov, Y. P. Pershin, N. Manova, A. Divochiy, Y. B. Vakhtomin, A. Korneev, K. Smirnov, A. Sivakov, A. Y. Devizenko *et al.*, "Superconducting single-photon detector made of MoSi film," *Superconductor Science and Technology*, vol. 27, no. 9, p. 095012, 2014.

[21] V. B. Verma, B. Korzh, F. Bussieres, R. D. Horansky, S. D. Dyer, A. E. Lita, I. Vayshenker, F. Marsili, M. D. Shaw, H. Zbinden *et al.*, "High-efficiency superconducting nanowire single-photon detectors fabricated from MoSi thin-films," *Optics express*, vol. 23, no. 26, pp. 33 792–33 801, 2015.

[22] A. Kozorezov, C. Lambert, F. Marsili, M. Stevens, V. Verma, J. Allmaras, M. Shaw, R. Mirin, and S. W. Nam, "Fano fluctuations in superconducting-nanowire single-photon detectors," *Physical Review B*, vol. 96, no. 5, p. 054507, 2017.

[23] M. Hofherr, D. Rall, K. Ilin, M. Siegel, A. Semenov, H.-W. Hübers, and N. Gippius, "Intrinsic detection efficiency of superconducting nanowire single-photon detectors with different thicknesses," *Journal of Applied Physics*, vol. 108, no. 1, p. 014507, 2010.

[24] L. Bulaevskii, M. Graf, C. Batista, and V. Kogan, "Vortex-induced dissipation in narrow current-biased thin-film superconducting strips," *Physical Review B*, vol. 83, no. 14, p. 144526, 2011.

[25] F. Marsili, V. B. Verma, J. A. Stern, S. Harrington, A. E. Lita, T. Gerrits, I. Vayshenker, B. Baek, M. D. Shaw, R. P. Mirin *et al.*, "Detecting single infrared photons with 93% system efficiency," *Nature Photonics*, vol. 7, no. 3, p. 210, 2013.

[26] K. Smirnov, A. Divochiy, Y. Vakhtomin, P. Morozov, P. Zolotov, A. Antipov, and V. Seleznev, "Nbn single-photon detectors with saturated dependence of quantum efficiency," *Superconductor Science and Technology*, vol. 31, no. 3, p. 035011, 2018.

[27] I. Esmaeil Zadeh, J. W. Los, R. B. Gourgues, V. Steinmetz, G. Bulgarini, S. M. Dobrovolskiy, V. Zwiller, and S. N. Dorenbos, "Single-photon detectors combining high efficiency, high detection rates, and ultra-high timing resolution," *Apl Photonics*, vol. 2, no. 11, p. 111301, 2017.

[28] A. Semenov, P. Haas, H.-W. Hübers, K. Ilin, M. Siegel, A. Kirste, D. Drung, T. Schurig, and A. Engel, "Intrinsic quantum efficiency and electro-thermal model of a superconducting nanowire single-photon detector," *Journal of Modern Optics*, vol. 56, no. 2-3, pp. 345–351, 2009.

[29] A. D. Semenov, M. Sidorova, M. A. Skvortsov, A. Kuzmin, K. Ilin, and M. Siegel, "Local thermal fluctuations in current-carrying superconducting nanowires," *arXiv preprint arXiv:1910.05035*, 2019.

[30] N. Calandri, Q.-Y. Zhao, D. Zhu, A. Dane, and K. K. Berggren, "Superconducting nanowire detector jitter limited by detector geometry," *Applied Physics Letters*, vol. 109, no. 15, p. 152601, 2016.

[31] B. Korzh, Q.-Y. Zhao, S. Frasca, D. Zhu, E. Ramirez, E. Bersin, M. Colangelo, A. Dane, A. Beyer, J. Allmaras *et al.*, "WSi superconducting nanowire single photon detector with a temporal resolution below 5 ps," in *CLEO: QELS_ Fundamental Science*. Optical Society of America, 2018, pp. FW3F–3.

[32] M. Caloz, M. Perrenoud, C. Autebert, B. Korzh, M. Weiss, C. Schönenberger, R. J. Warburton, H. Zbinden, and F. Bussières, "High-detection efficiency and low-timing jitter with amorphous superconducting nanowire single-photon detectors," *Applied Physics Letters*, vol. 112, no. 6, p. 061103, 2018.

[33] B. Korzh, Q. Zhao, S. Frasca, J. Allmaras, T. Autry, E. Bersin, M. Colangelo, G. Crouch, A. Dane, T. Gerrits *et al.*, "Demonstrating sub-3 ps temporal resolution in a superconducting nanowire single-photon detector," *arXiv preprint arXiv:1804.06839*, 2018.

[34] A. Kuzmin, S. Doerner, M. Sidorova, S. Wuensch, K. Ilin, M. Siegel, and A. Semenov, "Geometrical jitter and bolometric regime in photon detection by straight superconducting nanowire," *IEEE Transactions on Applied Superconductivity*, vol. 29, no. 5, pp. 1–5, 2019.

[35] Q. Zhao, L. Zhang, T. Jia, L. Kang, W. Xu, J. Chen, and P. Wu, "Intrinsic timing jitter of superconducting nanowire single-photon detectors," *Applied Physics B*, vol. 104, no. 3, pp. 673–678, 2011.

[36] J. Wu, L. You, S. Chen, H. Li, Y. He, C. Lv, Z. Wang, and X. Xie, "Improving the timing jitter of a superconducting nanowire single-photon detection system," *Applied optics*, vol. 56, no. 8, pp. 2195–2200, 2017.

[37] A. Semenov, P. Haas, B. Günther, H.-W. Hübers, K. Il'in, M. Siegel, A. Kirste, J. Beyer, D. Drung, T. Schurig *et al.*, "An energy-resolving superconducting nanowire photon counter," *Superconductor Science and Technology*, vol. 20, no. 10, p. 919, 2007.

[38] M. Sidorova, A. Semenov, H.-W. Hübers, I. Charaev, A. Kuzmin, S. Doerner, and M. Siegel, "Physical mechanisms of timing jitter in photon detection by current-carrying superconducting nanowires," *Physical Review B*, vol. 96, no. 18, p. 184504, 2017.

[39] B. E. Saleh and M. C. Teich, *Fundamentals of photonics.* John Wiley & Sons, 2019.

[40] D. F. Santavicca, J. K. Adams, L. E. Grant, A. N. McCaughan, and K. K. Berggren, "Microwave dynamics of high aspect ratio superconducting nanowires studied using self-resonance," *Journal of Applied Physics*, vol. 119, no. 23, p. 234302, 2016.

[41] N. Faraz, *Timing performance of superconducting nanowire single-photon detectors.* Massachusetts Institute of Technology, 2015.

[42] H. Wu, C. Gu, Y. Cheng, and X. Hu, "Vortex-crossing-induced timing jitter of superconducting nanowire single-photon detectors," *Applied Physics Letters*, vol. 111, no. 6, p. 062603, 2017.

[43] A. Zotova and D. Y. Vodolazov, "Intrinsic detection efficiency of superconducting nanowire single photon detector in the modified hot spot model," *Superconductor Science and Technology*, vol. 27, no. 12, p. 125001, 2014.

[44] M. Sidorova, A. Semenov, H.-W. Hübers, A. Kuzmin, S. Doerner, K. Ilin, M. Siegel, I. Charaev, and D. Vodolazov, "Timing jitter in photon detection by straight superconducting nanowires: Effect of magnetic field and photon flux," *Physical Review B*, vol. 98, no. 13, p. 134504, 2018.

[45] J. J. Renema, Q. Wang, R. Gaudio, I. Komen, K. Op't Hoog, D. Sahin, A. Schilling, M. Van Exter, A. Fiore, A. Engel *et al.*, "Position-dependent local detection efficiency in a nanowire superconducting single-photon detector," *Nano letters*, vol. 15, no. 7, pp. 4541–4545, 2015.

[46] Y. Korneeva, M. Sidorova, A. Semenov, S. Krasnosvobodtsev, K. Mitsen, A. Korneev, G. Chulkova, and G. Goltsman, "comparison of hot-spot formation in NbC and NbN single-photon detectors," *IEEE Transactions on Applied Superconductivity*, vol. 26, no. 3, pp. 1–4, 2016.

[47] I. Charaev, T. Silbernagel, B. Bachowsky, A. Kuzmin, S. Doerner, K. Ilin, A. Semenov, D. Roditchev, D. Y. Vodolazov, and M. Siegel, "Proximity effect model of ultranarrow NbN strips," *Physical Review B*, vol. 96, no. 18, p. 184517, 2017.

[48] S. B. Kaplan, "Acoustic matching of superconducting films to substrates," *Journal of Low Temperature Physics*, vol. 37, no. 3-4, pp. 343–365, 1979.

[49] A. Abrikosov, *Fundamentals of the theory of metals, 1988.* New York, NY; Elsevier Science Pub. Co. Inc., 1988.

[50] W. Frick, D. Waldmann, and W. Eisenmenger, "Phonon emission spectra of thin metallic films," *Applied physics*, vol. 8, no. 2, pp. 163–171, 1975.

[51] B. L. Altshuler and A. G. Aronov, "Electron-electron interaction in disordered conductors," in *Modern Problems in condensed matter sciences.* Elsevier, 1985, vol. 10, pp. 1–153.

[52] B. L. Altshuler, A. G. Aronov, and P. Lee, "Interaction effects in disordered fermi systems in two dimensions," *Physical Review Letters*, vol. 44, no. 19, p. 1288, 1980.

[53] S. Hikami, A. I. Larkin, and Y. Nagaoka, "Spin-orbit interaction and magnetoresistance in the two dimensional random system," *Progress of Theoretical Physics*, vol. 63, no. 2, pp. 707–710, 1980.

[54] G. Bergmann, "Quantum corrections to the resistance in two-dimensional disordered superconductors above T_C: Al, Sn, and amorphous $Bi_{0.9}Tl_{0.1}$ films," *Physical Review B*, vol. 29, no. 11, p. 6114, 1984.

[55] A. Abrikosov and L. Gor'kov, "Spin-orbit interaction and the Knight shift in superconductors," *Sov. Phys. JETP*, vol. 15, p. 752, 1962.

[56] L. Aslamasov and A. Larkin, "The influence of fluctuation pairing of electrons on the conductivity of normal metal," *Physics Letters A*, vol. 26, no. 6, pp. 238–239, 1968.

[57] M. H. Redi, "Two-dimensional fluctuation-induced conductivity above the critical temperature," *Physical Review B*, vol. 16, no. 5, p. 2027, 1977.

[58] E. Abrahams, R. Prange, and M. Stephen, "Effect of a magnetic field on fluctuations above Tc," *Physica*, vol. 55, pp. 230–233, 1971.

[59] M. Tinkham, "Introduction to superconductivity, reprinted ed," 1980.

[60] W. Brenig, M. Paalanen, A. Hebard, and P. Wölfle, "Magnetoconductance of thin-film superconductors near critical disorder," *Physical Review B*, vol. 33, no. 3, p. 1691, 1986.

[61] J. M. Gordon, C. Lobb, and M. Tinkham, "Divergent phase-breaking rate in aluminum films from magnetoconductance measurements," *Physical Review B*, vol. 29, no. 9, p. 5232, 1984.

[62] J. M. Gordon and A. M. Goldman, "Electron inelastic scattering in aluminum films and wires at temperatures near the superconducting transition," *Physical Review B*, vol. 34, no. 3, p. 1500, 1986.

[63] Z. Kvon, T. Baturina, R. Donaton, M. Baklanov, M. Kostrikin, K. Maex, E. Olshanetsky, and J. Portal, "Maki–thompson corrections in thin superconducting PtSi films nearby Tc," *Physica B: Condensed Matter*, vol. 284, pp. 959–960, 2000.

[64] K. Maki, "Critical fluctuation of the order parameter in a superconductor. I," *Progress of Theoretical Physics*, vol. 40, no. 2, pp. 193–200, 1968.

[65] R. S. Thompson, "Microwave, flux flow, and fluctuation resistance of dirty type-II superconductors," *Physical Review B*, vol. 1, no. 1, p. 327, 1970.

[66] A. Larkin, "Reluctance of two-dimensional systems," *JETP lett*, vol. 31, no. 4, pp. 219–223, 1980.

[67] J. L. dos Santos and E. Abrahams, "Superconducting fluctuation conductivity in a magnetic field in two dimensions," *Physical Review B*, vol. 31, no. 1, p. 172, 1985.

[68] A. Glatz, A. Varlamov, and V. Vinokur, "Quantum fluctuations and dynamic clustering of fluctuating cooper pairs," *EPL (Europhysics Letters)*, vol. 94, no. 4, p. 47005, 2011.

[69] A. Larkin and A. Varlamov, "Fluctuation phenomena in superconductors," in *The Physics of Superconductors.* Springer, 2003, pp. 95–231.

[70] B. L. Altshuler, A. Aronov, and D. Khmelnitsky, "Effects of electron-electron collisions with small energy transfers on quantum localisation," *Journal of Physics C: Solid State Physics*, vol. 15, no. 36, p. 7367, 1982.

[71] W. Brenig, M.-c. Chang, E. Abrahams, and P. Wölfle, "Inelastic scattering time above the superconductivity transition in two dimensions: Dependence on disorder and magnetic field," *Physical Review B*, vol. 31, no. 11, p. 7001, 1985.

[72] B. Altshuller, A. Aronov, and D. Khmelnitsky, "Suppression of localization effects by the high frequency field and the nyquist noise," *Solid State Communications*, vol. 39, no. 5, pp. 619–623, 1981.

[73] G. F. Giuliani and J. J. Quinn, "Lifetime of a quasiparticle in a two-dimensional electron gas," *Physical Review B*, vol. 26, no. 8, p. 4421, 1982.

[74] D. Belitz and S. D. Sarma, "Inelastic phase-coherence time in thin metal films," *Physical Review B*, vol. 36, no. 14, p. 7701, 1987.

[75] J. Rammer and A. Schmid, "Destruction of phase coherence by electron-phonon interactions in disordered conductors," *Physical Review B*, vol. 34, no. 2, p. 1352, 1986.

116

[76] A. Sergeev and V. Mitin, "Electron-phonon interaction in disordered conductors: Static and vibrating scattering potentials," *Physical Review B*, vol. 61, no. 9, p. 6041, 2000.

[77] A. Pippard, "CXXII. ultrasonic attenuation in metals," *The London, Edinburgh, and Dublin Philosophical Magazine and Journal of Science*, vol. 46, no. 381, pp. 1104–1114, 1955.

[78] A. Schmid, "Electron-phonon interaction in an impure metal," *Zeitschrift für Physik*, vol. 259, no. 5, pp. 421–436, 1973.

[79] K. Il'in, N. Ptitsina, A. Sergeev, G. Gol'tsman, E. Gershenzon, B. Karasik, E. Pechen, and S. Krasnosvobodtsev, "Interrelation of resistivity and inelastic electron-phonon scattering rate in impure NbC films," *Physical Review B*, vol. 57, no. 24, p. 15623, 1998.

[80] W. Little, "The transport of heat between dissimilar solids at low temperatures," *Canadian Journal of Physics*, vol. 37, no. 3, pp. 334–349, 1959.

[81] M. V. Sidorova, A. Kozorezov, A. Semenov, Y. P. Korneeva, M. Y. Mikhailov, A. Y. Devizenko, A. Korneev, G. Chulkova, and G. Goltsman, "Nonbolometric bottleneck in electron-phonon relaxation in ultrathin WSi films," *Physical Review B*, vol. 97, no. 18, p. 184512, 2018.

[82] W. Eisenmenger, K. Lassmann, H.-J. Trumpp, and R. Krauß, "Quasiparticle recombination and 2Δ-phonon-trapping in superconducting tunneling junctions," *Applied physics*, vol. 11, no. 4, pp. 307–320, 1976.

[83] A. Kardakova, A. Shishkin, A. Semenov, G. Goltsman, S. Ryabchun, T. Klapwijk, J. Bousquet, D. Eon, B. Sacépé, T. Klein *et al.*, "Relaxation of the resistive superconducting state in boron-doped diamond films," *Physical Review B*, vol. 93, no. 6, p. 064506, 2016.

[84] A. Rothwarf and B. Taylor, "Measurement of recombination lifetimes in superconductors," *Physical Review Letters*, vol. 19, no. 1, p. 27, 1967.

[85] M. Kaganov, E. Lifshitz, and L. Tanatarov, "Relaxation between electrons and the crystalline lattice," *Journal of Experimental and Theoretical Physics*, vol. 4, pp. 173–178, 1957.

[86] A. Semenov, R. Nebosis, Y. P. Gousev, M. Heusinger, and K. Renk, "Analysis of the nonequilibrium photoresponse of superconducting films to pulsed radiation by use of a two-temperature model," *Physical Review B*, vol. 52, no. 1, p. 581, 1995.

[87] K. Il'in, M. Lindgren, M. Currie, A. Semenov, G. Gol'Tsman, R. Sobolewski, S. Cherednichenko, and E. Gershenzon, "Picosecond hot-electron energy relaxation in NbN superconducting photodetectors," *Applied Physics Letters*, vol. 76, no. 19, pp. 2752–2754, 2000.

[88] N. Perrin and C. Vanneste, "Response of superconducting films to a periodic optical irradiation," *Physical Review B*, vol. 28, no. 9, p. 5150, 1983.

[89] A. Sergeev and M. Yu. Reizer, "Photoresponse mechanisms of thin superconducting films and superconducting detectors," *International Journal of Modern Physics B*, vol. 10, no. 06, pp. 635–667, 1996.

[90] S. Cherednichenko, P. Yagoubov, K. Il'In, G. Gol'tsman, and E. Gershenzon, "Large bandwidth of NbN phonon-cooled hot-electron bolometer mixers on sapphire substrates," *Proc. 8th Int. Symp. on Space Terahertz Technology*, vol. 245, 1997.

[91] Y. P. Gousev, G. Gol'Tsman, A. Semenov, E. Gershenzon, R. Nebosis, M. Heusinger, and K. Renk, "Broadband ultrafast superconducting NbN detector for electromagnetic radiation," *Journal of Applied Physics*, vol. 75, no. 7, pp. 3695–3697, 1994.

[92] E. Baeva, M. Sidorova, A. Korneev, K. Smirnov, A. Divochy, P. Morozov, P. Zolotov, Y. B. Vakhtomin, A. Semenov, T. Klapwijk *et al.*, "Thermal properties of NbN single-photon detectors," *Physical Review Applied*, vol. 10, no. 6, p. 064063, 2018.

[93] A. Semenov, A. Engel, H.-W. Hübers, K. Il'in, and M. Siegel, "Spectral cut-off in the efficiency of the resistive state formation caused by absorption of a single-photon in current-carrying superconducting nano-strips," *The European Physical Journal B-Condensed Matter and Complex Systems*, vol. 47, no. 4, pp. 495–501, 2005.

[94] A. Bezuglyj and V. Shklovskij, "Kinetics of electron cooling in metal films at low temperatures and revision of the two-temperature model," *Journal of Physics: Condensed Matter*, vol. 30, no. 29, p. 295001, 2018.

[95] D. Pan, *Time-resolved photoresponse studies of ferromagnet/superconductor nano-bilayers and nanostructures*. Citeseer, 2010.

[96] I. Charaev, T. Silbernagel, B. Bachowsky, A. Kuzmin, S. Doerner, K. Ilin, A. Semenov, D. Roditchev, D. Y. Vodolazov, and M. Siegel, "Enhancement of superconductivity in NbN nanowires by negative electron-beam lithography with positive resist," *Journal of Applied Physics*, vol. 122, no. 8, p. 083901, 2017.

[97] L. J. van der Pauw, "A method of measuring the resistivity and Hall coefficient on lamellae of arbitrary shape," *Philips technical review*, vol. 20, pp. 220–224, 1958.

[98] H. Bartolf, A. Engel, A. Schilling, K. Il'In, M. Siegel, H.-W. Hübers, and A. Semenov, "Current-assisted thermally activated flux liberation in ultrathin nanopatterned NbN superconducting meander structures," *Physical Review B*, vol. 81, no. 2, p. 024502, 2010.

[99] A. Einstein, "On the theory of the Brownian movement," *Ann. Phys*, vol. 19, no. 4, pp. 371–381, 1906.

[100] M. Von Smoluchowski, "Zur kinetischen theorie der brownschen molekularbewegung und der suspensionen," *Annalen der physik*, vol. 326, no. 14, pp. 756–780, 1906.

[101] A. Semenov, B. Günther, U. Böttger, H.-W. Hübers, H. Bartolf, A. Engel, A. Schilling, K. Ilin, M. Siegel, R. Schneider *et al.*, "Optical and transport properties of ultrathin NbN films and nanostructures," *Physical Review B*, vol. 80, no. 5, p. 054510, 2009.

[102] E. Helfand and N. Werthamer, "Temperature and purity dependence of the superconducting critical field, H_{c2}. II," *Physical Review*, vol. 147, no. 1, p. 288, 1966.

[103] Y. Dubi, Y. Meir, and Y. Avishai, "Nature of the superconductor-insulator transition in disordered superconductors," *Nature*, vol. 449, no. 7164, p. 876, 2007.

[104] A. Ghosal, M. Randeria, and N. Trivedi, "Inhomogeneous pairing in highly disordered s-wave superconductors," *Physical Review B*, vol. 65, no. 1, p. 014501, 2001.

[105] C. Carbillet, S. Caprara, M. Grilli, C. Brun, T. Cren, F. Debontridder, B. Vignolle, W. Tabis, D. Demaille, L. Largeau *et al.*, "Confinement of superconducting fluctuations due to emergent electronic inhomogeneities," *Physical Review B*, vol. 93, no. 14, p. 144509, 2016.

[106] G.-i. Oya and Y. Onodera, "Transition temperatures and crystal structures of single-crystal and polycrystalline nbn x films," *Journal of applied physics*, vol. 45, no. 3, pp. 1389–1397, 1974.

[107] K. Tanabe, H. Asano, Y. Katoh, and O. Michikami, "Ellipsometric and optical reflectivity studies of reactively sputtered NbN thin films," *Journal of applied physics*, vol. 63, no. 5, pp. 1733–1739, 1988.

[108] D. Bacon, A. English, S. Nakahara, F. Peters, H. Schreiber, W. Sinclair, and R. Van Dover, "Properties of nbn thin films deposited on ambient temperature substrates," *Journal of applied physics*, vol. 54, no. 11, pp. 6509–6516, 1983.

[109] D. Henrich, *Influence of material and geometry on the performance of superconducting nanowire single-photon detectors.* KIT Scientific Publishing, 2013, vol. 10.

[110] L. N. Bulaevskii, M. J. Graf, and V. G. Kogan, "Vortex-assisted photon counts and their magnetic field dependence in single-photon superconducting detectors," *Physical Review B*, vol. 85, no. 1, p. 014505, 2012.

[111] G. Maksimova, N. Zhelezina, and I. Maksimov, "Critical current and negative magnetoresistance of superconducting film with edge barrier," *EPL (Europhysics Letters)*, vol. 53, no. 5, p. 639, 2001.

[112] M. Kupryanov and V. Lukichev, "Temperature dependence of pair-breaking current in superconductors," *Sov. J. Low Temp. Phys.(Engl. Transl.);(United States)*, vol. 6, no. 4, 1980.

[113] Z. Wang, A. Kawakami, Y. Uzawa, and B. Komiyama, "Superconducting properties and crystal structures of single-crystal niobium nitride thin films deposited at ambient substrate temperature," *Journal of applied physics*, vol. 79, no. 10, pp. 7837–7842, 1996.

[114] B. Shinozaki, S. Ezaki, T. Odou, T. Asano, and K. Makise, "Anomalous electron inelastic scattering rate probed via superconducting fluctuation in epitaxial nbn thin films," *Physica C: Superconductivity and its Applications*, vol. 567, p. 1353547, 2019. [Online]. Available: http://www.sciencedirect.com/science/article/pii/S0921453418304428

[115] Y. Zou, X. Wang, T. Chen, X. Li, X. Qi, D. Welch, P. Zhu, B. Liu, T. Cui, and B. Li, "Hexagonal-structured ε-NbN: ultra-incompressibility, high shear rigidity, and a possible hard superconducting material," *Scientific reports*, vol. 5, p. 10811, 2015.

[116] D. Destraz, K. Ilin, M. Siegel, A. Schilling, and J. Chang, "Superconducting fluctuations in a thin NbN film probed by the Hall effect," *Physical Review B*, vol. 95, no. 22, p. 224501, 2017.

[117] S. Chockalingam, M. Chand, J. Jesudasan, V. Tripathi, and P. Raychaudhuri, "Superconducting properties and Hall effect of epitaxial NbN thin films," *Physical Review B*, vol. 77, no. 21, p. 214503, 2008.

[118] S. Ezaki, K. Makise, B. Shinozaki, T. Odo, T. Asano, H. Terai, T. Yamashita, S. Miki, and Z. Wang, "Localization and interaction effects in ultrathin epitaxial NbN superconducting films," *Journal of Physics: Condensed Matter*, vol. 24, no. 47, p. 475702, 2012.

[119] Y. Pellan, G. Dousselin, J. Pinel, and Y. Sohn, "Temperature and magnetic field dependence of NbN film resistivity: 3D weak localization effects," *Journal of Low Temperature Physics*, vol. 78, no. 1-2, pp. 63–77, 1990.

[120] R. Cabanel, J. Chaussy, J. Mazuer, and J. Villegier, "From localization to superconductivity in granular niobium nitride thin films," *Journal de Physique*, vol. 49, no. 5, pp. 795–802, 1988.

[121] D. Rall, P. Probst, M. Hofherr, S. Wünsch, K. Il'in, U. Lemmer, and M. Siegel, "Energy relaxation time in NbN and YBCO thin films under optical irradiation," in *Journal of Physics: Conference Series*, vol. 234, no. 4. IOP Publishing, 2010, p. 042029.

[122] A. A. Balandin and D. L. Nika, "Phononics in low-dimensional materials," *Materials Today*, vol. 15, no. 6, pp. 266 – 275, 2012. [Online]. Available: http://www.sciencedirect.com/science/article/pii/S1369702112701177

[123] S. P. Chockalingam, M. Chand, J. Jesudasan, V. Tripathi, and P. Raychaudhuri, "Superconducting properties and hall effect of epitaxial nbn thin films," *Phys. Rev. B*, vol. 77, p. 214503, Jun 2008. [Online]. Available: https://link.aps.org/doi/10.1103/PhysRevB.77.214503

[124] A. A. Balandin and D. L. Nika, "Phononics in low-dimensional materials," *Materials Today*, vol. 15, no. 6, pp. 266–275, 2012.

[125] V. E. Gmurman, *Fundamentals of probability theory and mathematical statistics*. Iliffe Books Limited, 1968.

[126] U. Fano, "Ionization yield of radiations. II. The fluctuations of the number of ions," *Physical Review*, vol. 72, no. 1, p. 26, 1947.

[127] A. Jeffrey and D. Zwillinger, *Table of integrals, series, and products*. Elsevier, 2007.

[128] M. Sidorova, A. Semenov, A. Kuzmin, I. Charaev, S. Doerner, and M. Siegel, "Intrinsic jitter in photon detection by straight superconducting nanowires," *IEEE Transactions on Applied Superconductivity*, vol. 28, no. 7, pp. 1–4, 2018.

[129] D. Y. Vodolazov, Y. P. Korneeva, A. Semenov, A. Korneev, and G. Goltsman, "Vortex-assisted mechanism of photon counting in a superconducting nanowire single-photon detector revealed by external magnetic field," *Physical Review B*, vol. 92, no. 10, p. 104503, 2015.

[130] M. G. Tanner, S. D. Dyer, B. Baek, R. H. Hadfield, and S. Woo Nam, "High-resolution single-mode fiber-optic distributed raman sensor for absolute temperature measurement using superconducting nanowire single-photon detectors," *Applied Physics Letters*, vol. 99, no. 20, p. 201110, 2011.

[131] O. Butov, K. Golant, A. Tomashuk, M. Van Stralen, and A. Breuls, "Refractive index dispersion of doped silica for fiber optics," *Optics Communications*, vol. 213, no. 4-6, pp. 301–308, 2002.

[132] J. M. Senior and M. Y. Jamro, *Optical fiber communications: principles and practice*. Pearson Education, 2009.

[133] M. Gnyba, J. Smulko, A. Kwiatkowski, and P. Wierzba, "Portable raman spectrometer-design rules and applications," *Bulletin of the Polish Academy of Sciences: Technical Sciences*, vol. 59, no. 3, pp. 325–329, 2011.

[134] M. Cubison and J. Jimenez, "Statistical precision of the intensities retrieved from constrained fitting of overlapping peaks in high-resolution mass spectra," *Atmospheric Measurement Techniques (Online)*, vol. 8, no. 6, 2015.

[135] S. J. Choquette, E. S. Etz, W. S. Hurst, D. H. Blackburn, and S. D. Leigh, "Relative intensity correction of raman spectrometers: NIST SRMs 2241 through 2243 for 785 nm, 532 nm, and 488 nm/514.5 nm excitation," *Applied spectroscopy*, vol. 61, no. 2, pp. 117–129, 2007.

List of publications

- **Mariia Sidorova**, Alexej Semenov, Heinz-Wilhelm Hübers, Konstantin Ilin, Michael Siegel, Ilya Charaev, Maria Moshkova, Natalia Kaurova, Gregory N. Goltsman, Xiaofu Zhang, Andreas Schilling, "Electron energy relaxation in disordered superconducting NbN films", *arXiv:1907.05039*, 2019, (submitted to Phys. Rev. B)

- Kuzmin, Artem, Steffen Doerner, **Mariia Sidorova**, Stefan Wuensch, Konstantin Ilin, Michael Siegel, and Alexey Semenov, "Geometrical jitter and bolometric regime in photon detection by straight superconducting nanowire", *IEEE Transactions on Applied Superconductivity* 29, no. 5, 2019.

- **Mariia Sidorova**, Alexej Semenov, Heinz-Wilhelm Hübers, Artem Kuzmin, Steffen Doerner, K. Ilin, Michael Siegel, Ilya Charaev, Denis Vodolazov, "Timing jitter in photon detection by straight superconducting nanowires: Effect of magnetic field and photon flux", *Phys. Rev. B* 98, 134504, 2018.

- **Mariia Sidorova**, Alexej Semenov, Artem Kuzmin, Ilya Charaev, Steffen Doerner, M. Siegel, "Intrinsic Jitter in Photon Detection by Straight Superconducting Nanowires", *IEEE Transactions on Applied Superconductivity*, Vol. 28, No. 7, 2018.

- E.M. Baeva, **M.V. Sidorova**, A.A. Korneev, K.V. Smirnov, A.V. Divochy, P.V. Morozov, P.I. Zolotov, Yu.B. Vakhtomin, A.V. Semenov, T.M. Klapwijk, V.S. Khrapai, G.N. Goltsman, "Thermal properties of NbN single-photon detectors", *Phys. Rev. Applied*, Vol. 10, No. 6, 2018.

- **Mariia V. Sidorova**, A. G. Kozorezov, A. V. Semenov, Yu. P. Korneeva, M. Yu. Mikhailov, A. Yu. Devizenko, A. A. Korneev, G. M. Chulkova, and G. N. Goltsman, "Nonbolometric bottleneck in electron-phonon relaxation in ultrathin WSi films", *Phys. Rev. B* 97, 184512, 2018.

- Xiaofu Zhang, Adriana E. Lita, **Mariia Sidorova**, Varun B. Verma, Qiang Wang, Sae Woo Nam, Alexei Semenov, and Andreas Schilling, "Superconducting fluctuations and characteristic time scales in amorphous WSi", *Phys. Rev. B* 97, 174502, 2018.

- E. Baeva, **M. Sidorova**, A. Korneev, and G. Goltsman, "Precise measurement of the thermal conductivity of superconductor", *AIP Conference Proceedings* 1936, 020003, 2018.

122

- **Mariia Sidorova**, Alexej Semenov, Heinz-Wilhelm Hübers, Ilya Charaev, Artem Kuzmin, Steffen Doerner, and Michael Siegel, "Physical mechanisms of timing jitter in photon detection by current-carrying superconducting nanowires", *Phys. Rev. B* 96, 184504, 2017.

- X Zhang, Andreas Engel, Q Wang, Andreas Schilling, Alexey Semenov, **Maria Sidorova**, H-W Hübers, Ilya Charaev, Konstantin Ilin, Michael Siegel, "Characteristics of superconducting tungsten silicide W_xSi_{1-x} for single photon detection", *Phys. Rev. B* 94 (17), 174509, 2016.

- KV Smirnov, AV Divochiy, YB Vakhtomin, **MV Sidorova**, UV Karpova, P. V. Morozov, V. A. Seleznev, A. N. Zotova, and D. Yu. Vodolazov, "Rise time of voltage pulses in NbN superconducting single photon detectors", *Applied Physics Letters* 109 (5), 052601, 2016.

- Yu Korneeva, **M Sidorova**, A Semenov, S Krasnosvobodtsev, K Mitsen, A Korneev, G Chulkova, G Goltsman, "Comparison of Hot-Spot Formation in NbC and NbN Single-Photon Detectors", *IEEE Transactions on Applied Superconductivity* 26 (3), 1-4, 2016.

- **MV Sidorova**, AV Divochiy, YB Vakhtomin, KV Smirnov, "Ultrafast superconducting single-photon detector with a reduced active area coupled to a tapered lensed single-mode fiber", *Journal of Nanophotonics* v. 9, 2015.

Acknowledgments

Statutory Declaration

I declare that I have completed the thesis independently using only the aids and tools specified. I have not applied for a doctor's degree in the doctoral subject elsewhere and do not hold a corresponding doctor's degree. I have taken due note of the Faculty of Mathematics and Natural Sciences PhD Regulations, published in the Official Gazette of Humboldt-Universität zu Berlin no. 42/2018 on 11/07/2018.

Mariia Sidorova

June 2, 2020